Eclipses, Bursts and Outflows in Highly Inclined X-ray Binaries

Amy H. Knight

Christ Church College
University of Oxford

A Thesis Submitted for the Degree of
Doctor of Philosophy

Trinity 2023

Abstract

Accretion, the capture of nearby material by the strong gravitational pull of an object, is ubiquitous throughout the universe and is often observed around newly forming stars, planets or compact objects like neutron stars (NSs) and black holes (BHs). X-ray binaries are transient systems in which a NS or BH heats material accreted from a companion star and thus glows brightly in X-rays. These bright X-rays are easy to observe with existing X-ray telescopes. Therefore, X-ray binaries serve as unique laboratories for fundamental physics, allowing us to test different gravitational regimes, probe the state of the ultra-dense matter in the cores of NSs and determine the maximum possible NS mass.

In this thesis, I pioneer the X-ray TRansit and EClipse model, X-TREC to provide a novel and precise way of measuring NS masses, thus informing on the equation of state of ultra-dense matter and the classification of merging compact objects. My model exploits eclipsing X-ray binaries, in which the binary inclination, i, and mass ratio, q relate via the duration of totality, $t_{\rm e}$, thus the degeneracy between i and q is disentangled through accurate mapping of the eclipse profile. I demonstrate the abilities of X-TREC by applying it to archival observations of two eclipsing low-mass X-ray binaries, EXO 0748 – 676 and *Swift* J1858.6 – 0814, precisely determining the i and q for both systems. Furthermore, the novel consideration of the companion star's outflow by X-TREC allows it to diagnose the source of any absorbing material within the systems. For EXO 0748 – 676 and *Swift* J1858.6 – 0814, I use this modelling technique to diagnose an irradiation-driven ablated outflow in both systems, suggesting they are related to spider pulsars. I thoroughly explore this relation, infer that these two binaries are *false widows*, and predict that the ablated material in EXO 0748 – 676 leads to Type-I X-ray bursts being observable *during* the X-ray eclipses.

Eclipses, Bursts and Outflows in Highly Inclined X-ray Binaries

Amy H. Knight
Christ Church College
University of Oxford

A thesis submitted for the degree of
Doctor of Philosophy

Trinity 2023

Acknowledgements

I'll begin by thanking my supervisor, Dr Adam Ingram, whose expertise, ideas and enthusiasm have been unmatched, even when I diverted the research away from the solace of X-ray binaries towards pulsar astronomy. He has encouraged me to explore every thought and theory I've had, even the more unconventional ideas, which ultimately led to some exciting results. Thank you for the insightful conversations and words of wisdom over the last four years. Also, I'd like to give a special shout-out to my secondary supervisor, Dr Matt Middleton, for his continued support, motivation, and light-hearted pestering for a Nature paper.

I thank Prof. Rob Fender and the transient astrophysics group at the University of Oxford. The weekly group meetings have introduced me to different ways to study compact objects and facilitated collaborations and friendships that have made for an incredible PhD experience. Also, I express my gratitude to Prof. Roger Davis, Prof. Stephan Smartt and the Hintze Centre for Astrophysical Surveys for their ongoing support, and the Hintze Family Charitable Foundation for funding my research.

To my good friends and teammates at Oxford Powersports Olympic Weightlifting Club, thank you for keeping me sane and asking: *what's new in the world of physics?* at the start of every training session. In particular, to Ashleigh, Nicole and Courtney, thank you for the hilarious conversations, bottomless brunches, and for being the best weightlifting hype squad, and the OXP coaches for always encouraging me to *do it again, but better.*

Thank you to my family and friends for their unwavering encouragement, despite repeatedly telling me they don't understand what I'm doing. To my sisters, Han and Jenn, the ketchup is still orbiting the mayo. Finally, thank you to my partner, Chris, for his continued love, support and motivation.

Abstract

Accretion, the capture of nearby material by the strong gravitational pull of an object, is ubiquitous throughout the universe and is often observed around newly forming stars, planets or compact objects like neutron stars (NSs) and black holes (BHs). X-ray binaries are transient systems in which a NS or BH heats material accreted from a companion star and thus glows brightly in X-rays. These bright X-rays are easy to observe with existing X-ray telescopes. Therefore, X-ray binaries serve as unique laboratories for fundamental physics, allowing us to test different gravitational regimes, probe the state of the ultra-dense matter in the cores of NSs and determine the maximum possible NS mass.

In this thesis, I pioneer the X-ray TRansit and EClipse model, X-TREC to provide a novel and precise way of measuring NS masses, thus informing on the equation of state of ultra-dense matter and the classification of merging compact objects. My model exploits eclipsing X-ray binaries, in which the binary inclination, i, and mass ratio, q relate via the duration of totality, $t_{\rm e}$, thus the degeneracy between i and q is disentangled through accurate mapping of the eclipse profile. I demonstrate the abilities of X-TREC by applying it to archival observations of two eclipsing low-mass X-ray binaries, EXO 0748 – 676 and *Swift* J1858.6 – 0814, precisely determining the i and q for both systems. Furthermore, the novel consideration of the companion star's outflow by X-TREC allows it to diagnose the source of any absorbing material within the systems. For EXO 0748 – 676 and *Swift* J1858.6 – 0814, I use this modelling technique to diagnose an irradiation-driven ablated outflow in both systems, suggesting they are related to spider pulsars. I thoroughly explore this relation, infer that these two binaries are *false widows*, and predict that the ablated material in EXO 0748 – 676 leads to Type I X-ray bursts being observable *during* the X-ray eclipses.

Contents

List of Figures

List of Tables

Chapter 1

Introduction

1.1 X-ray Binaries

In this thesis, I pioneer the X-ray TRansit and EClipse model, X-TREC, to determine the masses of compact objects in eclipsing X-ray binary systems. I introduce X-ray binaries and their properties in this section.

1.1.1 Compact Objects

Stars spend the majority of their life on the main sequence. This stage of stellar evolution is ubiquitous and powered by hydrogen fusion in the star's core. Beyond the main sequence, the fate of a star depends on its mass. For massive stars, the result is a supernova explosion which leaves behind a compact stellar remnant. If the degenerate neutron pressure interrupts the complete collapse of the core during this explosion, the resulting object is a neutron star (NS). For sufficiently massive progenitors, the degenerate neutron pressure is overwhelmed by the gravitational collapse of the core and a black hole (BH) forms (Kippenhahn et al., 2012).

Astrophysical BHs, formed through the collapse of a massive star, are expected to have a neutral charge. Therefore, the two properties that describe a BH are its mass and spin. The event horizon of a BH is the point at which the escape velocity is equivalent to the speed of light. For a non-spinning (Schwarzschild) BH, this boundary is $R_{\rm S} = 2GM/c^2$, twice the gravitational radius of the compact object

$R_{\rm S} \equiv 2R_{\rm g}$ (Schwarzschild, 1916). Here G is the gravitational constant. A spinning BH (Kerr) is described by a dimensionless spin parameter, a_* (Kerr, 1963; Bardeen et al., 1972). In this case, the event horizon is generalised to $R_{\rm H}/R_{\rm g} = 1 + \sqrt{1 - a_*^2}$. Another fundamental radius of accreting systems is the innermost stable circular orbit (ISCO), defined as the smallest radius at which a test mass can follow a circular and stable orbit around a compact object ($R_{\rm ISCO} = 6R_{\rm g}$ for a Schwarzschild BH). Beyond this, the orbits are unstable, and the mass spirals inwards towards the event horizon. In contrast, the ISCO for an accreting NS is approximately the radius of the NS. Therefore, the gravitational field experienced by the accretion flow is similar for both types of compact objects.

The fundamental difference between a NS and a BH is that the former has a solid surface, but the latter does not. As shown in Figure 1.1, the surface of a NS is described as an atmosphere containing hydrogen, helium and carbon that surrounds an outer crust of ions and free electrons. Beyond the surface, the pressure and density increase giving rise to more exotic states of matter, such as the superconducting protons comprising the outer core. The exact composition of the inner core is the primary source of uncertainty, as it represents the final state of matter that can resist gravitational collapse (Sen, 2019). Identifying this unique state of matter is highly sought-after and motivates some of the work presented in this thesis.

The structure of NSs and their mass-radius relations are determinable by integrating the Tolman-Oppenhiemer-Volkoff (TOV) equations (Oppenheimer & Volkoff, 1939; Tolman, 1939) (relativistic structure equations). A pressure-density curve appropriate for NS matter, known as the NS equation of state (EoS), is required to complete these equations. This relation is the key to determining the macroscopic properties of a NS from the TOV equations since each set of solutions uniquely maps to a mass-radius relation (Özel & Psaltis, 2009; Özel & Freire, 2016). In principle, reverse-engineering this mapping enables the determination of the EoS from the

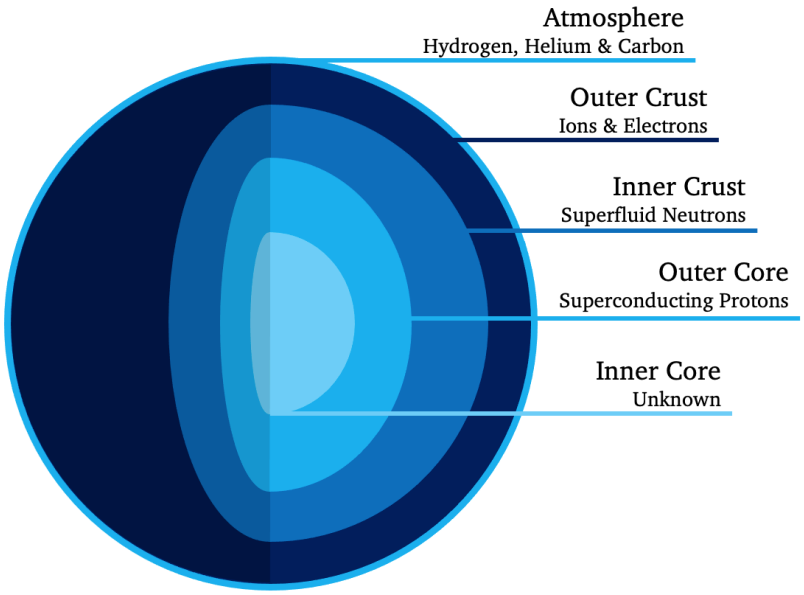

Figure 1.1: Schematic showing the interior composition of a neutron star (NS). The atmosphere of light elements surrounds an outer crust of ions and electrons. Below this, superfluid neutrons form the inner crust. The high density and pressure deep within the NS give rise to an outer core of superconducting protons and an inner core of unknown composition, which hosts one of many possible states of exotic matter. Figure adapted from visulisation by NASA's Goddard Space Flight Center.

masses and radii of astrophysical NSs (Lindblom 1992; see Fig 10 of Voisin et al. 2020 for some up-to-date examples). However, thorough sampling of the mass-radius relation is necessary to translate between the mass-radius relation and the pressure-density relation. Constraints are still possible with sparse sampling as some characteristics, like the maximum NS mass, determined by the EoS behaviour at high densities, make it possible to distinguish between the relations (Özel & Psaltis, 2009; Özel & Freire, 2016). Therefore, the EoS can be constrained solely by the measured masses of astrophysical NSs.

Many theories for the EoS of nuclear matter exist and their corresponding mass-radius relations are depicted in Figure 1.2. Here, we also see the constraints on the NS EoS made possible by measurements of the macroscopic properties of astrophysical NSs. The horizontal yellow and blue shaded regions are the 1σ confidence intervals on the NSs mass for two pulsars PSR J0740+6620 ($M_{\rm NS} \sim 2.1 M_{\odot}$) (Cromartie et al.,

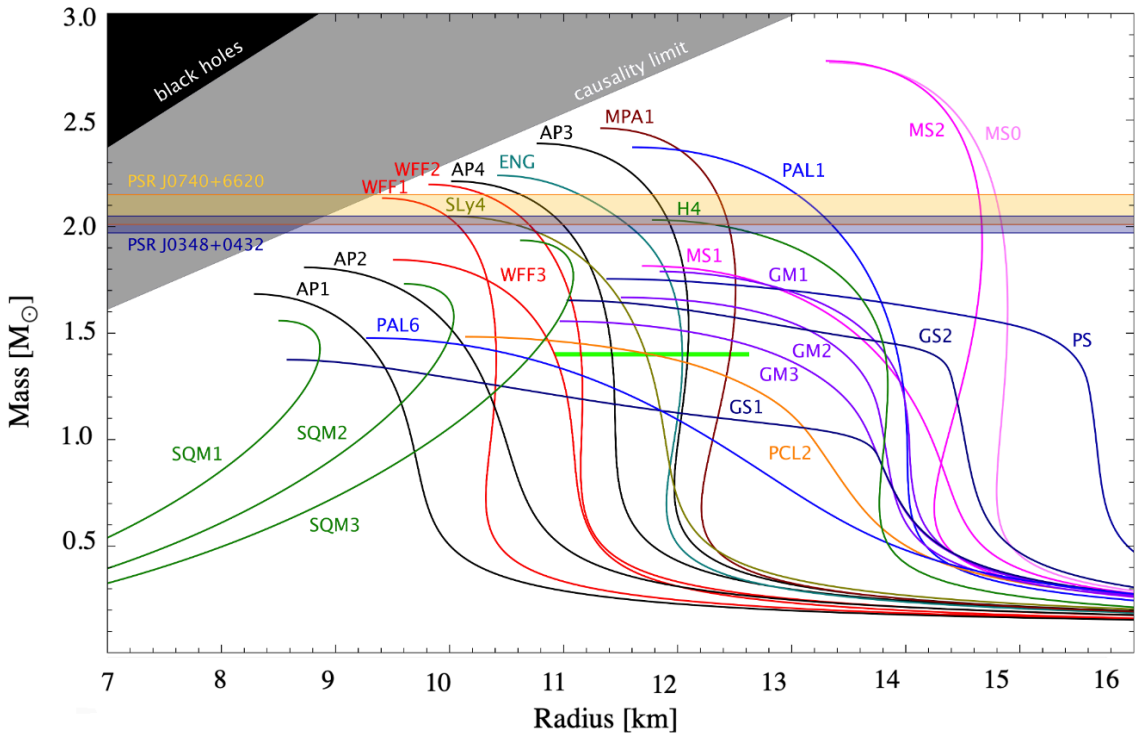

Figure 1.2: The mass-radius relations for the different equations of state (EoS) named in the figure. The blue and yellow shaded regions correspond to the 1σ confidence intervals for the masses of two pulsars. Multimessenger constraints on the neutron star (NS) radius, assuming a $1.4M_{\odot}$ canonical NS mass are given by the green bar (Dietrich et al., 2020).
This figure was created by Norbert Wex and published online by Paulo Freire. EOSs tabulated in Lattimer & Prakash (2001) and provided to the figure creators by the authors. Included with permission.

2020; Fonseca et al., 2021; Miller et al., 2021) and PSR J0348+0432, respectively. Based on these measurements, any EoS with a maximum possible NS mass below the yellow and blue shaded regions is disfavoured. Multimessenger constraints on the NS radius, assuming a $1.4M_{\odot}$ canonical NS mass are given by the green bar (Dietrich et al., 2020). Therefore, our understanding of the type of exotic matter comprising the cores of NSs is advancing with new observations of astrophysical NSs.

The maximum mass of a NS is confinable by the fundamental properties of matter and the assumed theory of gravity. The type of inner core material assumed (e.g. quarks, bosons, hyperons) specifies the density and the rotation rate of the NS sets

the gravitational regime. Combining these properties predetermines the maximum NS mass for each EoS, resulting in the causal mass limit (see Figure 1.2; Astashenok et al. 2021. Causality is a strict limit and would disobey fundamental laws of physics if violated (Van Oeveren & Friedman, 2017; Astashenok et al., 2021). BHs, however, are more massive than NSs, as they form from more massive progenitors (Kippenhahn et al., 2012), but there is uncertainty regarding the exact range of masses these compact objects occupy. Generally, a compact object of unknown type is assumed to be a BH if its mass is greater than $3M_{\odot}$, and objects less massive than this are tentatively classed as NSs. However, since the EoS of matter comprising the inner cores of NSs is unknown, the maximum mass of NSs cannot be more precisely defined than the causal limit. A caveat of this is that compact objects with masses in the range $3 - 5M_{\odot}$ are occasionally observed. This gap is understood through the bifurcation of the stellar processes creating compact objects (Belczynski et al., 2012), although, as shown in Figure 1.3, a tiny fraction of known compact objects do fall into this range. The BHs and NSs detected through gravitational waves (*LIGO-Virgo-KAGRA*) are more massive than those detected through the electromagnetic radiation (*EM*) emitted by X-ray binaries or pulsars. The gravitational wave sources GW190425 (Abbott et al., 2020b) and GW190814 (Abbott et al., 2020a) contest this. Respectively these events are classified as the coalescence of two NSs with a primary mass of $\sim 2.5M_{\odot}$ and the merger of a $\sim 2.6M_{\odot}$ mystery compact object with a $\sim 23M_{\odot}$ BH. No electromagnetic signatures coincided with either event, so it wasn't possible to confirm whether the compact objects involved were BHs or NSs. However, these events raise questions regarding the evolutionary processes that create very low-mass BHs or more massive NSs, and if they are NSs, what that means for the fundamental physics governing causality.

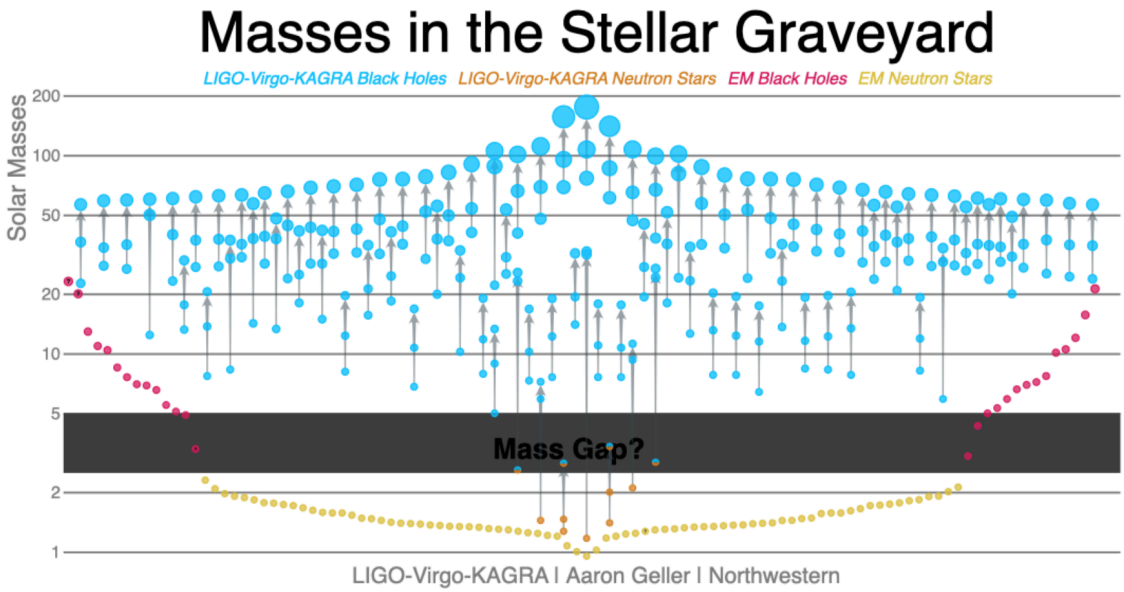

Figure 1.3: A graphic of the masses of black holes (BHs) and neutron stars (NSs) discovered through gravitational wave detections (*LIGO-Virgo-KADRA*) and electromagnetic (*EM*) observations. The $3 - 5M_{\odot}$ compact object mass gap hosts only a few sources.
Image credit: LIGO-Virgo / Aaron Geller / Northwestern University.

1.1.2 Mass Transfer Processes

Many NSs and BHs are identified through their interactions with a companion star or compact object if they display bright electromagnetic radiation or gravitational waves. A binary system consists of two stars orbiting a common centre of mass. In an X-ray binary (XRB), one component is instead a NS or BH and material transfer from the companion star to the compact object occurs. The infalling material efficiently converts its lost gravitational energy into electromagnetic emission, peaking in the X-ray band (van der Sluys, 2006). Therefore, these systems are referred to as XRBs and are the primary focus of this thesis. For gravitational wave sources, on the other hand, both binary components are compact objects. The two components orbit one another at an ever-decreasing separation until they merge and emit gravitational waves.

XRBs can host NSs or BHs, creating two broad groups. As NS XRBs are more numerous than BH XRBs, the results presented here focus on NS XRBs. The mass

of the companion star further classifies XRBs. A high mass X-ray binary (HMXB) hosts a companion star with a mass above $10M_{\odot}$. These high-mass stars are young (less than 10^7 yrs), highly luminous and typically of spectral class O or B (Tan, 2021). In contrast, a low-mass X-ray binary (LMXB) hosts a companion star with a mass less than $1M_{\odot}$ (Bahramian & Degenaar, 2022). These low-mass stars are older [1] and less luminous, falling into spectral classes K or M. Intermediate mass X-ray binaries (IMXBs) have companion stars with masses in the range $1.5 - 8.0M_{\odot}$. IMXBs are relatively uncommon compared to HMXBs or LMXBs, as they likely represent a prior stage of LMXB evolution (Bahramian & Degenaar, 2022). In other words, most LMXBs have descended from IMXBs after an epoch of mass loss. Beyond this, NS XRBs are sub-categorized by their spectral evolution, which I discuss in Section 1.1.4.

Most XRBs are transient sources, meaning they exist in X-ray quiescence for most of their lives. During this time, they are either barely detectable or undetectable in the X-ray band. Occasionally, these sources undergo X-ray outbursts when their mass accretion rate and therefore, their X-ray luminosity increases by more than an order of magnitude for a short time. X-ray outbursts last a few weeks to a few years, depending on the source, after which the system will return to a quiescent state. Persistent sources, on the other hand, experience stable and long-lived mass transfer epochs and thus are always bright in X-rays. These sources do not typically exhibit the drastic luminosity changes observed in transient sources but will show luminosity variations due to varying mass accretion rates (Done et al., 2007).

For most X-ray binaries, mass transfer occurs when the companion star fills its Roche lobe, either by radiation-induced expansion, stellar evolution or contraction of the binary orbit. Regardless of how the star fills its Roche lobe, it enables material to pass through the first Lagrange point (L1) and fall onto the compact object. The L1 point is shown in Figure 1.4 as the central Lagrange point on the Roche equipotential

[1] The main-sequence lifetime of low-mass stars is significantly longer than high-mass stars. Therefore, a low-mass star is likely older than a high-mass star, when observed on the same day.

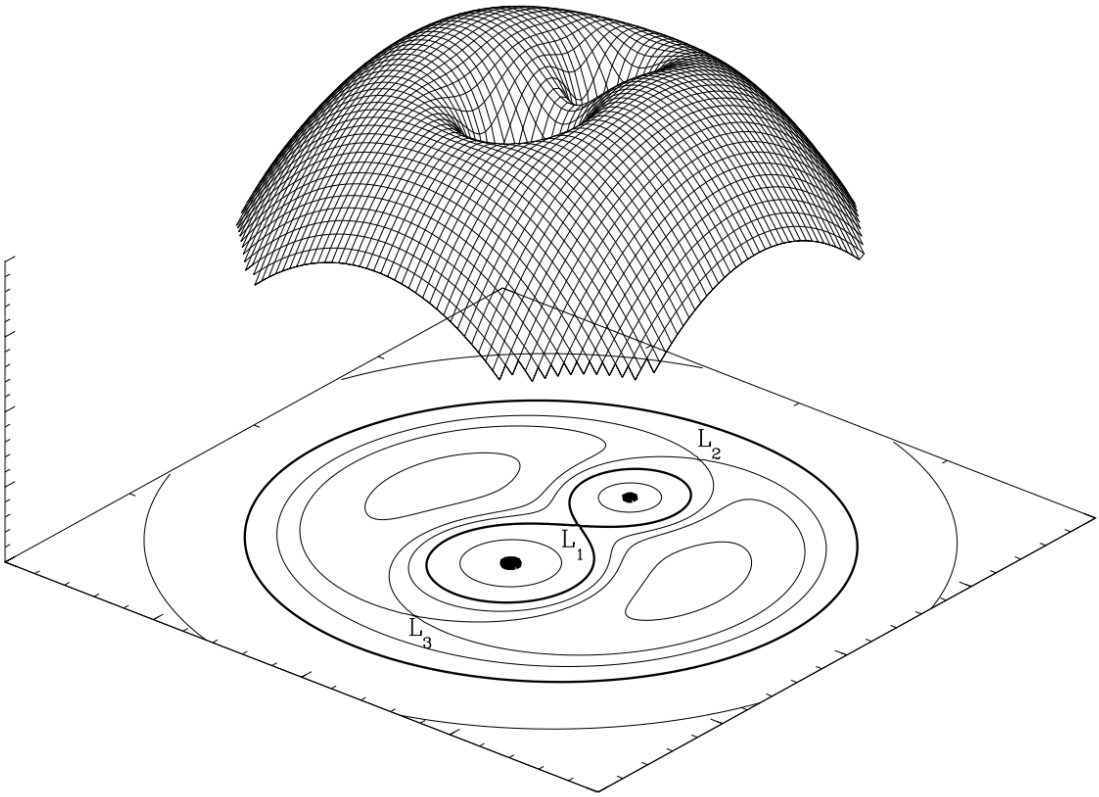

Figure 1.4: A three-dimensional view of the Roche equipotential surface for a binary system. Two teardrop-shaped regions, corresponding to the Roche lobe of each binary component, form the binary equipotential surface. The more massive star is in the foreground, and the system has a mass ratio of $q = 2$. The 3 Lagrangian points, L1, L2 and L3, are the points in the equipotential surface where the forces cancel. Matter can be transferred through L1 or lost through L2 or L3.
Figure from van der Sluys (2006). Included with permission.

surface. The equipotential surface forms from two teardrop-shaped Roche lobes, each corresponding to the Roche potential of one component, that intersect at L1. Further Lagrange points, L2 and L3, allow the mass to exit the system to infinity or a circumbinary disc (CBD) (van der Sluys, 2006). Mass transfer through L1 caused by a star filling its Roche lobe (Roche lobe overflow; RLOF) is the dominant process contributing to the accretion flow in LMXBs. Since material *within* a star's Roche lobe is gravitationally bound to that star, overflowing material is necessary to facilitate the mass transfer. The precise shape of Roche lobes depends on the mass ratio of the binary system. By defining a binary mass ratio of $q = M_1/M_2$, the radius of the Roche lobe of M_1 is given as (Eggleton, 1983),

$$\frac{R_{\rm L}}{a} = \frac{0.49q^{\frac{2}{3}}}{0.6q^{\frac{2}{3}} + \ln(1 + q^{\frac{1}{3}})}, \tag{1.1}$$

when approximating the Roche lobe to be a sphere of the same volume. Here M_1 and M_2 are the masses of the primary and secondary stars, and a is the separation between the two components. In HMXBs, mass transfer via RLOF can still occur. However, accretion could also result from a large-scale wind from the high-mass companion. A wind mass transfer mechanism is notably less efficient than RLOF. In this thesis, I focus on XRBs transferring mass via RLOF.

Material passing through the L1 point cannot fall directly onto the compact object as it possesses some angular momentum. Instead, the material forms circular orbits (minimum energy configuration) around the accretor, creating an accretion disc. The gas particles slowly spiral inwards as the turbulent effective viscosity in the disc erodes the angular momentum of their orbits, and due to the conservation of angular momentum, the created disc is flat and well described by the thin disc model (Shakura & Sunyaev, 1973).

Consider some material of mass m, following a Keplerian orbit about a compact

object of mass M at a distance r; the angular velocity of this material is

$$\omega = \left(\frac{GM}{r^3}\right)^{\frac{1}{2}} \tag{1.2}$$

The angular momentum travels outwards, causing m to lose some gravitational energy as it falls towards the compact object. This change in gravitational potential energy is

$$dE_p = \frac{GMm}{r^2}dr, \tag{1.3}$$

thus the rate of change of gravitational potential energy within a disc annulus of width dr is,

$$\frac{dE_p}{dt} = \frac{GM\dot{M}}{r^2}dr, \tag{1.4}$$

where $\dot{M}$ is the mass transfer rate. Some of this released gravitational potential energy is transferred to kinetic energy, thus increasing the angular velocity of the orbiting material closer to the compact object. The lost gravitational potential energy balances the gained kinetic energy,

$$E_k = \frac{1}{2}mv^2 = \frac{1}{2}mr^2\omega^2 = \frac{1}{2}\frac{GMm}{r} = \frac{1}{2}E_p \tag{1.5}$$

so half of the lost gravitational potential energy radiates away. The luminosity of the annulus is then,

$$dL = \frac{GM\dot{M}}{2r^2}dr, \tag{1.6}$$

and assuming $r_{\rm out} >> r_{\rm in}$ the luminosity of the entire disc is,

$$L = \int_{r_{\rm in}}^{r_{\rm out}} \frac{GM\dot{M}}{2r^2}dr = \frac{GM\dot{M}}{2r_{\rm in}}. \tag{1.7}$$

This can be rewritten as,

$$L = \eta\dot{M}c^2, \tag{1.8}$$

where η is the efficiency with which the disc rest mass energy is converted to radiation (the accretion efficiency), and from Equation 1.7, we see that

$$\eta = \frac{GM}{2r_{\rm in}c^2} = \frac{R_g}{2r_{\rm in}}. \tag{1.9}$$

The remaining disc rest mass energy is available to grow the mass of the compact object.

1.1.3 X-ray Bursts

X-ray bursts manifest as rapid and sudden increases in the observed X-ray flux of accreting NSs, typically to a level several times brighter than the level of persistent X-ray emission (Galloway et al., 2008; Lewin et al., 1993). X-ray bursts are one of the few observables to uniquely identify the compact object in an accreting system as a NS rather than a BH since the process requires an accretor with a solid surface (Bahramian & Degenaar, 2022). The mass accreted by the compact object in an XRB contributes to the growth of the compact object and is

$$\dot{M}_{\rm acc} = (1 - \eta)\dot{M}. \tag{1.10}$$

In the case of an accreting BH, $\dot{M}_{\rm acc}$ effectively disappears into the singularity. However, for a NS, this accreted material builds up on its solid surface resulting in X-ray bursts. There are two categories of X-ray bursts: type I and type II. Examples of type I X-ray bursts from the LMXB EXO 0748–676 are shown in Figure 1.5, where we see the characteristic burst profile of a fast rise followed by an exponential decay. These bursts are thermonuclear flashes from the surface of the NS and are thus often referred to as thermonuclear bursts (Galloway et al., 2008). type II bursts are due to accretion instabilities (Lewin et al., 1993; Masetti et al., 2000) and exhibit abrupt start-stop profiles without a decay, as in Figure 1.6, which depicts type II X-ray bursts observed from MXB 1730-335 (the rapid burster). Hereafter, I solely discuss type I X-ray bursts and thus do not explicitly specify the burst type.

X-ray bursts, triggered by the unstable ignition of accreted fuel on the surface of NSs, were first detected in 1975 from the ultracompact binary 3A 1820-30 (Grindlay et al., 1976). Since then, X-ray bursts have become an observational priority for many X-ray observatories as they diagnose the nature of the compact object in newly

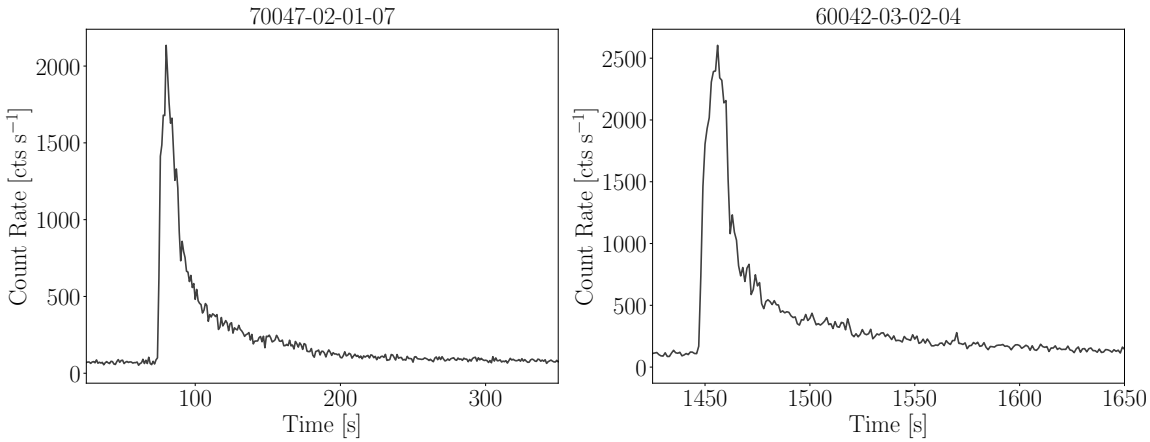

Figure 1.5: Two examples of type I X-ray bursts observed by the Rossi X-ray Timing Explorer (*RXTE*) from the LMXB EXO 0748–676. Both panels show the characteristic fast-rise, exponential-decay profile of a type I X-ray burst. The observation ID number for each event is in the figure.

discovered XRBs. In addition, an ever-growing population of *bursters* are exploited to probe the fundamental properties of NSs and their accretion environments, making them valuable sources.

The fuel for X-ray bursts originates from the outer layers of a binary companion star and, therefore, is typically primarily a combination of hydrogen and helium. The material is transferred via RLOF to the accretion disc before slowly drifting towards the NS. When the material reaches the NS, it spreads rapidly across the surface due to the lateral pressure gradients imposed by the strong surface gravity. The consistent flow of accreted material onto the surface of the NS allows the fuel layer to grow, until it is a sufficient depth for ignition. As more fuel reaches the surface of the NS, the preexisting layers become compressed, increasing the density and temperature of the fuel layer. The continuous flow of material causes the temperature and density to rise further until the conditions are sufficient for thermonuclear fusion. At this point, nuclear fusion reactions ignite a few metres below the NS surface, within the fuel layer. The fusion rate in the fuel increases with the temperature, so conditions for thermonuclear runaway are rapidly achieved, and the entire fuel layer ignites. All

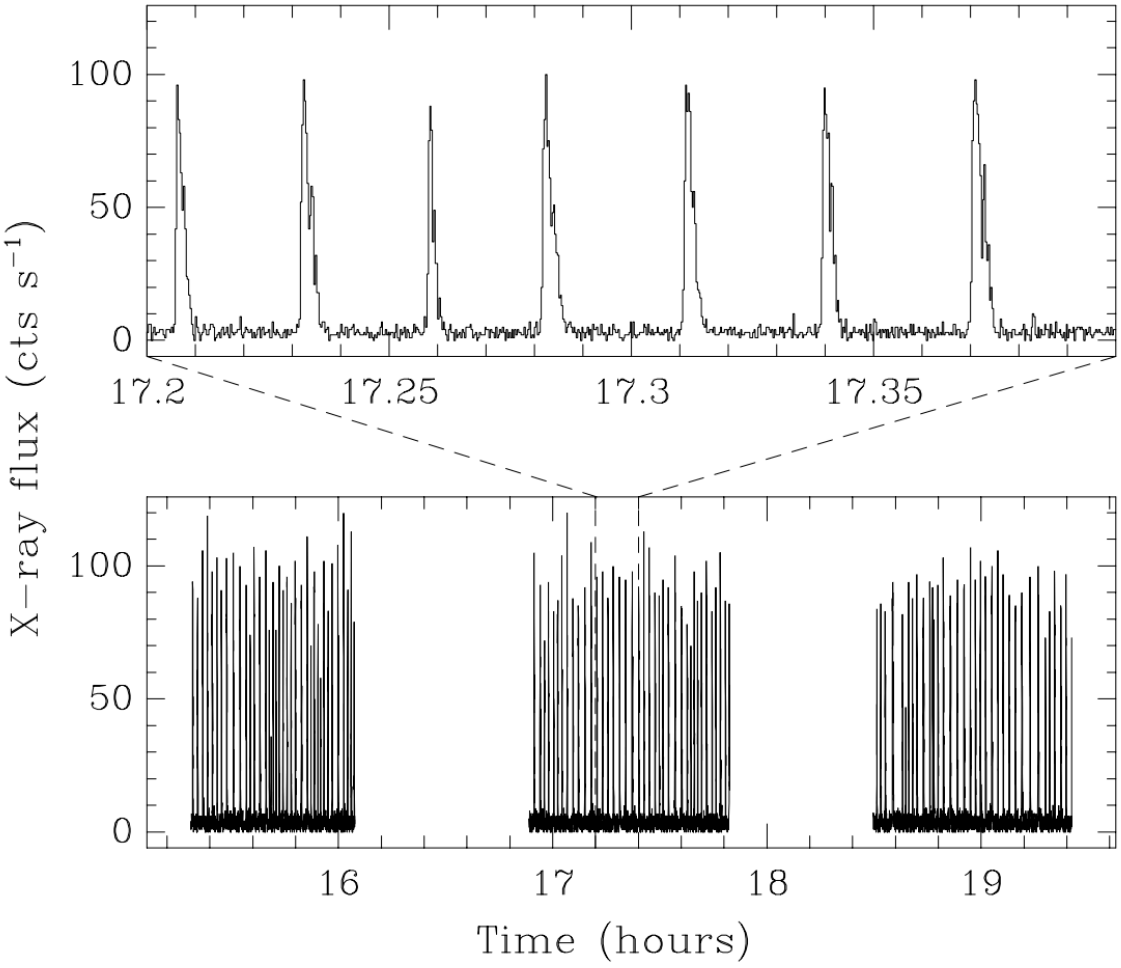

Figure 1.6: Type II X-ray bursts observed by the medium energy concentrator spectrometer (MECS) on board the *BeppoSAX* satellite. The figure shows the $2-10$ keV light curve of the Rapid Burster while it exhibited recurrent type II X-ray bursts. The profiles of type II X-ray bursts lack evidence of an exponential decay tail. The times are in hours from 0 UT of February 18 1998. The top panel enlarges the central part of the lower light curve.
Figure from Masetti et al. (2000) A&A, 363, 188, reproduced with permission ©ESO.

the surface material burns within a second, and this ignition results in an observable X-ray burst (Strohmayer & Bildsten, 2006; Galloway et al., 2008; Galloway & Keek, 2021).

X-ray bursts repeat, with any one source showing multiple X-ray bursts during an outburst. After one X-ray burst, there is a wait time until the next event because the fuel layer needs time to reform. The exact wait time depends on the mass accretion rate, $\dot{M}_{\rm acc}$. Some bursters, however, show consecutive bursts with a minimal wait time. The LMXB EXO 0748–676 exhibits such events as shown in Figure 1.7, where we see an example of a burst triplet. In these cases, a fraction of the fuel layer may be unburned and ignites soon after the previous burst. Turbulent mixing is required to transport the material to a depth where the conditions are sufficient for thermonuclear fusion. Successive bursts typically display progressively lower peaks and shorter decay tails than previous bursts (Galloway et al., 2008; Galloway & Keek, 2021).

The X-ray spectrum of an X-ray burst is a Planck (blackbody) distribution. Initially, the X-ray burst rises to its peak flux within the first few seconds of the X-ray burst, determined by the nuclear burning and flame-spreading timescales. During this phase, the blackbody temperature rises to its maximum value ($2-3$ keV) before gradually decreasing in the subsequent decay phase described by the burst's tail. In the decay phase, the temperature drop is a function of the cooling timescale and typically lasts $10-100$ s. The presence of this prolonged decay phase uniquely identifies a type I X-ray burst, while the absence of a decay phase indicates a type II burst.

In addition to X-ray bursts, other *surface processes* can confidently identify the presence of a NS. For example, NSs can exhibit regular pulsations of high energy radiation due to the misalignment of the NSs rotation axis and its magnetic axis (Alpar et al., 1982; Bahramian & Degenaar, 2022). Such NSs are called pulsars and generate the high energy radiation by channelling surface material along its magnetic

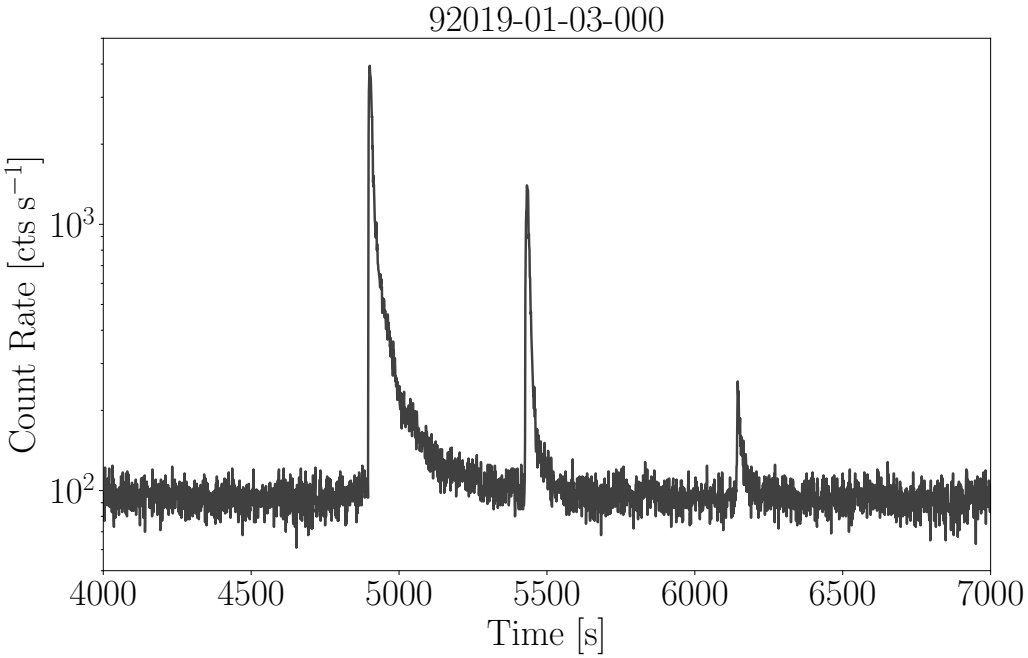

Figure 1.7: A type I X-ray burst triplet observed by *RXTE* from the LMXB EXO 0748–676. As shown, successive type I X-ray bursts have lower peak fluxes and shorter exponential decay phases than the previous bursts. The observation ID is in the figure and the y-axis is in log scale.

field lines towards the NSs magnetic poles, from which it emits the pulsations. I introduce pulsars in Section 1.2. Exhibiting pulsations requires a supply of surface material and a magnetic field. Magnetic fields cannot exist beyond the event horizon, so neither criteria are satisfied for a BH.

1.1.4 X-ray Spectral Properties

While in outburst, an XRB displays different spectral and timing behaviours, promoting the use of spectral states which broadly describe the observed spectrum of the source depending on its position on a hardness-intensity diagram (HID) (Fender et al., 2004; Belloni et al., 2005; Belloni, 2010; Fender & Muñoz-Darias, 2016; Ingram & Motta, 2019). These diagrams, such as Figure 1.8, allow us to categorise the various stages of an X-ray outburst using the total observed flux (intensity) and the X-ray hardness. Here, the latter is always the ratio of high energy to low energy flux, but

the energy bands are not strictly defined and depend on the instrument's bandpass.

The HID in Figure 1.8 describes the spectral evolution of the BH LMXB GX 339–4 during its prototypical outburst, showing that the source follows a q-shaped, anticlockwise track (Belloni et al., 2005). The q-shape and direction are consistent across all transient XRBs, and changes to the accretion flow govern their spectral evolution. This behaviour is roughly independent of the nature of the compact object within the system, but persistent sources do not trace out the full q-shaped path since they do not experience quiescent phases.

Following the spectral evolution in Figure 1.8, we see the source initially exiting quiescence and rising up the right-hand side of the HID into the hard state (HS). This spectral state, the most common for a source to reside in, describes a source with low intensity, an X-ray spectrum dominated by a power law with a hard photon index ($1.6 - 2.0$) and a high energy cut-off (red in Figure 1.9). The corresponding X-ray light curve would typically show a large amount of intrinsic variability, and a compact radio jet may be present (Fender & Gallo, 2014). There is likely a weak thermal contribution, but the observed spectrum is dominated by processes producing a hard X-ray spectrum.

When the system reaches its maximum luminosity, it initially maintains a hard spectrum. Subsequently, it transitions through the hard-to-soft intermediate state while upholding its luminosity. During this phase, known as the hard intermediate state (HIMS), the thermal component becomes hotter and more luminous, and the power law component weakens. The observed spectra in the intermediate state are thus a combination of the hard and soft states, with the ratio of thermal and non-thermal emission changing as the source migrates right-to-left along this track.

If the source successfully navigates through the HIMS, it enters the soft intermediate state (SIMS) before transitioning into the soft state (SS). Here, the source displays much less intrinsic variability than in hard states, due to the thermal compo-

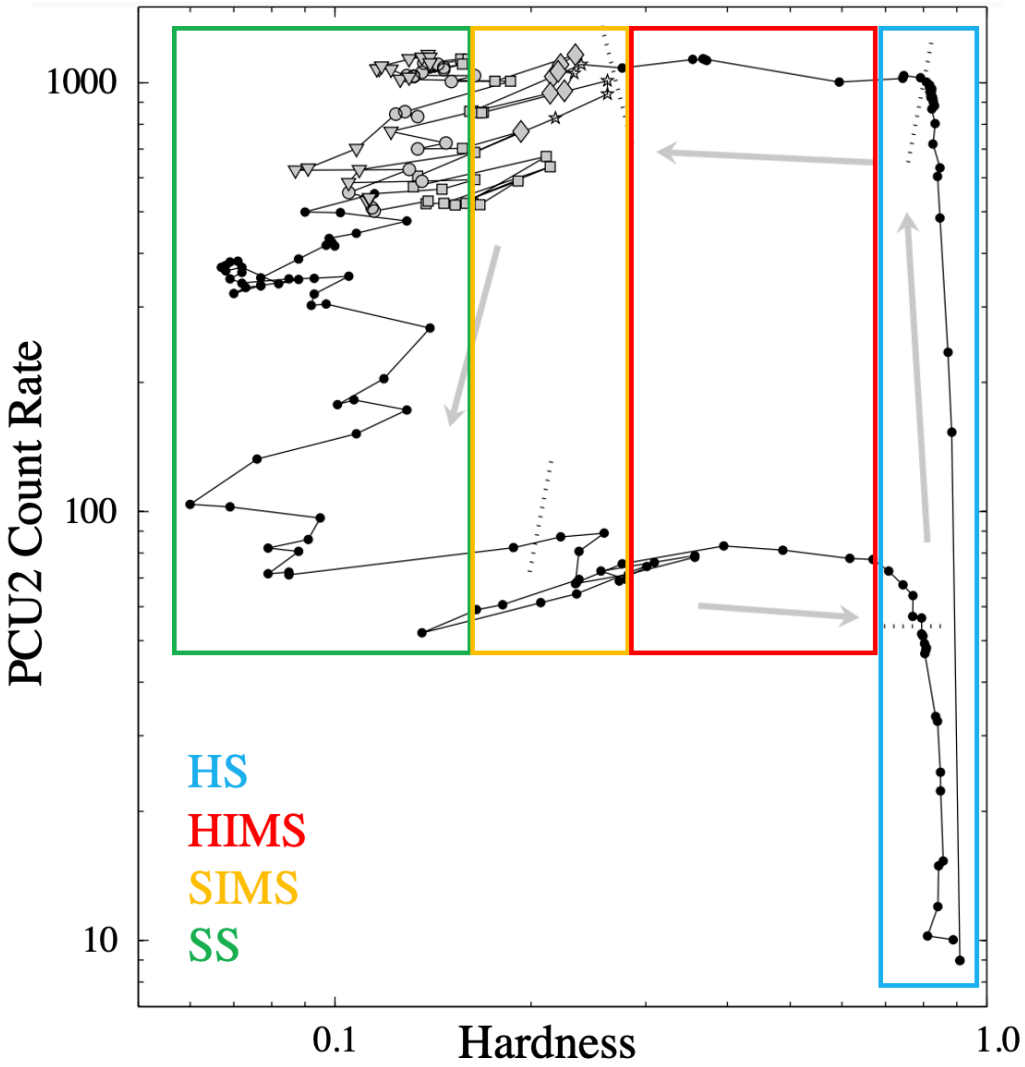

Figure 1.8: Hardness-intensity diagram (HID) for the black hole (BH) low mass X-ray binary (LMXB) GX 339–4. The motion along the q-shaped hysteresis is anticlockwise. Coloured boxes indicate the relationship between the position of the source on the HID and the spectral states described in this subsection; hard-state (HS, blue), hard-intermediate state (HIMS, red), soft intermediate state (SIMS, yellow) and soft-state (SS, green).
Figure adapted from Belloni et al. (2005), A&A, 440, 207, reproduced with permission ©ESO.

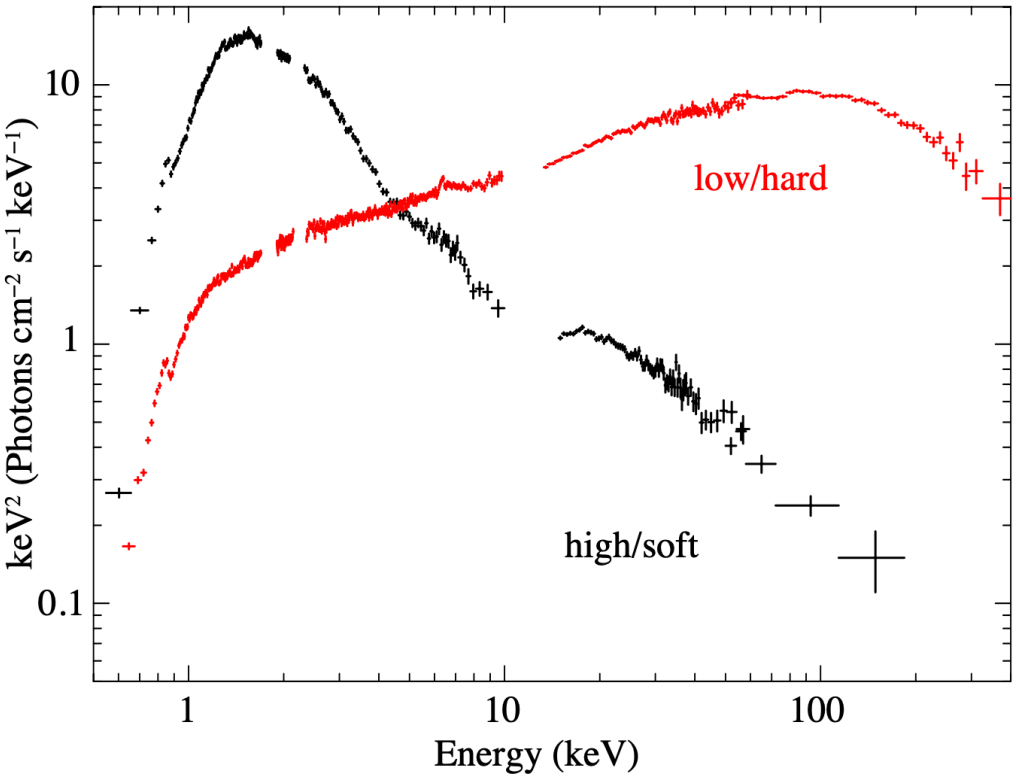

Figure 1.9: Response removed *Suzaku* spectra of the black hole (BH) high mass X-ray binary (HMXB) Cygnus X-1. The black data show the source in the high/soft state, while the red data show the source in the low/hard state.
Figure from Yamada et al. (2013). Included with permission from C. Done.

nent dominating the spectrum, creating a peak in the soft X-rays (black, Figure 1.9). Overall, the observed spectrum is soft. Some weak non-thermal emission remains and the radio jets will quench (Fender & Gallo, 2014). Gradually the source fades, falling down the left-hand side of the HID and transitioning through the soft-to-hard intermediate state before returning to quiescence until the source undergoes another outburst. If a source remains in the hard state or only enters the hard-to-soft intermediate state briefly before entering X-ray quiescence, then the source is said to have undergone a failed outburst (Tetarenko et al., 2016; Alabarta et al., 2021).

As shown in Figure 1.10, the hysteresis in NS XRBs is the same as in BH XRBs. The motion is always anticlockwise, the sources follow a q-shaped track, and the brightest phase is the transition from hard to soft (Muñoz-Darias et al., 2014). The

durations of hysteresis cycles are consistent between BHs and NSs, typically lasting a few months to a year. Their observed spectra are slightly different since NS XRBs require an additional thermal component to describe emission from the NS's solid surface, while BHs do not (Done & Gierliński, 2003; Burke et al., 2017). Thus, the spectral evolution of a NS XRB is further understood using a colour-colour diagram (CCD), showing the hard X-ray colour (high energy hardness ratio) against the soft X-ray colour (low energy hardness ratio).

The tracks shown in these diagrams give rise to two classes; atoll sources and Z-sources (see Figure 1.11) (van der Klis, 1989, 2004). Z-sources display a characteristic three-branch pattern on a CCD, resembling the letter Z (Figure 1.11C) (Church, M. J. et al., 2006). The three branches of this pattern are the horizontal branch, the normal branch, and the flaring branch, and each represents a different spectral state. The mass accretion rate governs the movement between branches (Hasinger & van der Klis, 1989; Mondal et al., 2017). $\dot{M}_{\rm acc}$ is highest while the source is on the normal branch and decreases as it moves towards the horizontal branch. This transition coincides with a decrease and subsequent increase in the Comptonised emission. The flaring branch is attributed to unstable nuclear burning, resulting in X-ray flares (Mondal et al., 2017). Z-sources do not jump between branches and will follow the Z pattern (Church, M. J. et al., 2006). Figure 1.10 highlights the similarity between the ultraluminous state (ULS) in BH XRBs and the high luminosity state (normal branch) of Z-sources (Ingram & Motta, 2019). These phases are comparatively short-lived, lasting weeks to months, and only a few sources will enter these states after the SS. These very high luminosity states have high mass accretion rates, a thermally dominated spectrum and low variability. In contrast, atoll sources show an elongated curved branch (banana state) surrounded by isolated clusters (island states) (Figures 1.11A and B). Atoll sources evolve slowly in comparison to Z sources. While Z sources can move through the pattern in a few days, atolls gradually move from right to left

along the elongated branch before jumping across to a surrounding island (van der Klis, 1989, 2004). These sources are analogous to a typical BH XRB, as in Figure 1.10.

1.1.5 Radiative Processes

The observed spectrum of an XRB strongly depends on the X-ray luminosity and, therefore, the mass accretion rate. Figure 1.9 demonstrates this for the BH HMXB Cygnus X-1 where we see the striking difference between the source in the SS (red) and the HS (black) (Yamada et al., 2013; Belloni et al., 2005; Belloni, 2010). While in the SS, a thermal accretion disc component dominates the spectrum. However, in the HS, a steep power-law component dominates. The accretion disc component is still present in the HS but is comparatively weak. In the HS, however, the presence of an X-ray corona containing energetic electrons near the disc can Compton upscatter photons from the accretion disc giving rise to the power law (Gierliński et al., 1999; Gierliński et al., 2002; Gierliński & Poutanen, 2005). A fraction of the photons emitted from the corona will then reflect off the accretion disc resulting in a reflection spectrum often identified by the strong iron Kα line at 6.4 keV. The intermediate states contain a combination of hard and soft spectral components. The observed spectra are also subject to absorption features arising from the interactions between the source and the interstellar medium (ISM). Therefore, four radiative processes describe the observed spectra of an XRB in any state: Comptonisation, Reflection and Absorption and Thermal Emission. For NS XRBs, the same four radiative processes will describe their spectra, but an extra thermal component originating from the solid surface is required. I discuss these radiative processes in the remainder of this subsection.

1.1.5.1 Thermal Disc Emission

A typical picture of accretion assumes a Shakura-Sunyaev disc (Shakura & Sunyaev, 1973), in which gas particles transferred through the L1 point form nearly Keplerian

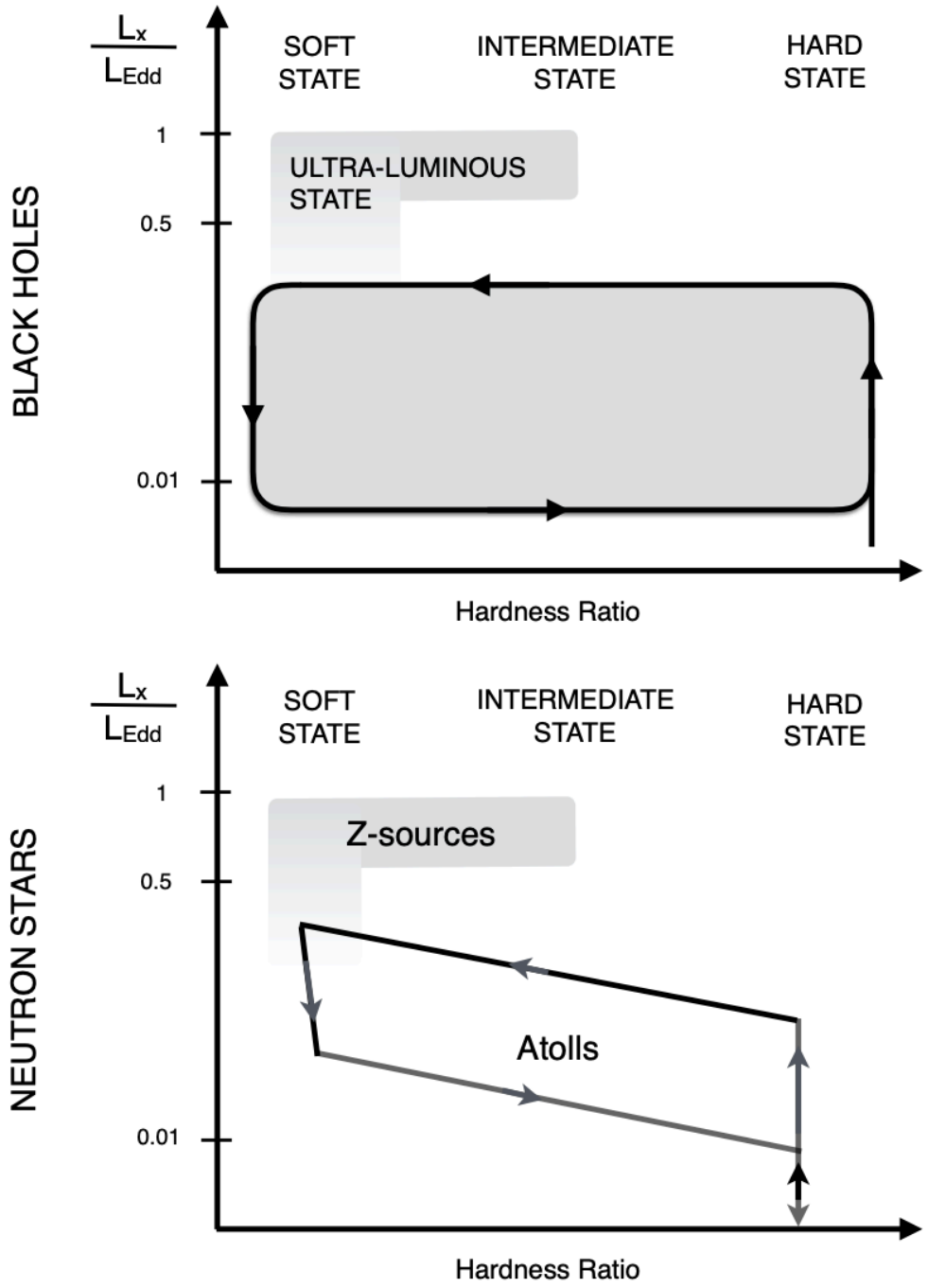

Figure 1.10: Hardness-intensity diagrams for black hole (BH) and neutron star (NS) X-ray Binaries (XRBs). The hysteresis in NS XRBs is the same as in BH XRBs. The motion is always anticlockwise, the sources follow a q-shaped track, and the brightest phase is the transition from hard to soft.
Figure adapted from Ingram & Motta (2019).

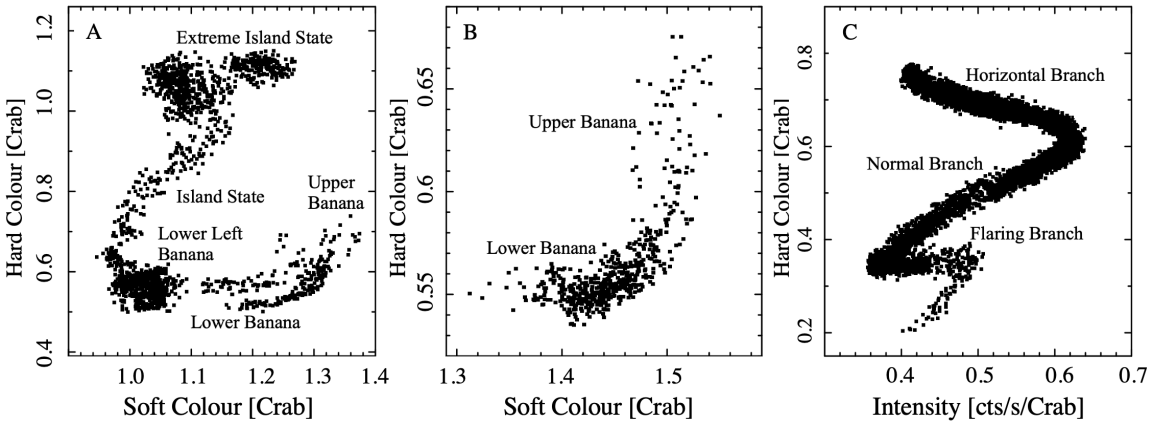

Figure 1.11: Colour-Colour Diagrams (CCDs) of atoll sources 4U 1608–52 (panel A) (van Straaten et al., 2003), GX 9+1 (panel B (van der Klis, 2004)) and Z-source GX 340+0 (panel C) (Jonker et al., 2000). Here, the soft colour is defined as $3.5 - 6.0/2.0 - 3.5$ keV and the hard colour is $9.7 - 16.0/6.0 - 9.7$ keV. The intensity is given in the $2 - 16$ keV band and all axes are normalized to Crab.
Figure adapted from van der Klis (2006).

orbits around the compact object and are influenced solely by the gravity of the compact object. As previously mentioned, angular momentum is slowly transported outwards due to the viscosity in the disc such that the gas particles have a small inward velocity, and the disc is considered geometrically thin. Recall from section 1.1.2, the luminosity of a disc annulus of width dr is

$$dL = \frac{GM\dot{M}}{2r^2}dr. \tag{1.11}$$

Each annulus radiates like a blackbody from the top and bottom of the accretion disc, so the radiating area is

$$dA = 2 \times 2\pi r dr, \tag{1.12}$$

and the corresponding flux is

$$F(r) = \frac{GM\dot{M}}{8\pi r^3}. \tag{1.13}$$

Subsequently, we recall the Stefan-Boltzmann law to show that the blackbody temperature radiated from a disc annulus is

$$T(r) = \left(\frac{GM\dot{M}}{8\pi\sigma r^3}\right)^{\frac{1}{4}}, \tag{1.14}$$

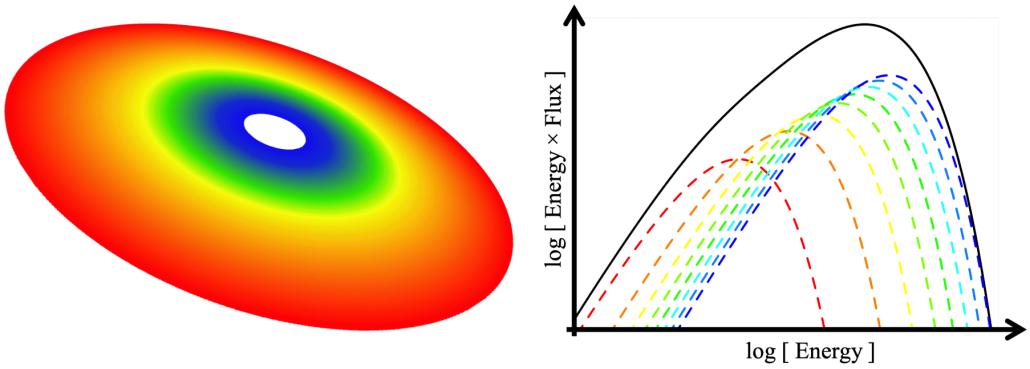

Figure 1.12: A schematic showing more energy is liberated from the accretion disc at smaller radii, resulting in the temperature of the accretion disc increasing closer to the compact object. The overall disc spectrum is the sum of the individual blackbody spectra radiated from each disc annuli.
Figure from Nathan (2022). Included with permission.

where σ is the Stefan-Boltzmann constant. The total disc spectrum is thus the sum of the individual blackbody contributions from each disc annulus, as shown in Figure 1.12. Here, we see the peak temperature of the blackbody radiated from disc annuli increases for smaller disc radii, resulting in a multi-temperature (often called multi-coloured) blackbody spectrum. As the disc material moves inwards, it gains more energy and becomes more luminous, causing the temperature of the material to increase as it gets closer to the compact object. That is to say, the temperature of the disc material is hotter at smaller radii because the gravitational potential energy gradient is larger. Therefore, the spectrum of an accretion disc is thermal, summarised as a quasi-thermal, multicolour blackbody spectrum with $T(r) \propto r^{-3/4}$. When considering angular momentum conservation, Equation 1.14 becomes, (Frank et al., 2002)

$$T^4(r) = \frac{3GM\dot{M}}{8\pi R^3}\left(1 - \sqrt{\frac{r_{\text{in}}}{R}}\right), \tag{1.15}$$

due to the stress-free inner boundary condition, which says that there is no viscosity beyond the inner disc radius, r_{in}. There are also some relativistic effects, although these result in fairly small corrections (Novikov & Thorne, 1973).

1.1.5.2 Comptonisation

Alongside the thermal accretion disc component, a higher energy component is commonly observed in XRB spectra and is the dominant spectral component for a source in the hard state. This high-energy component arises from the Compton scattering of low-temperature photons from the accretion disc, with electrons from a hot plasma close to the compact object known as the X-ray corona (Done, 2014). Understanding the exact geometry of the X-ray corona is beyond the scope of this thesis but is an active area of investigation (Poutanen, Juri et al., 2018; Gianolli et al., 2023). It is necessary, however, to discuss the population of hot electrons provided by the X-ray corona. These electrons undergo Compton scattering with comparatively cool accretion disc photons, resulting in the aforementioned high energy (power law) component in the observed spectra of XRBs (Gierliński et al., 2002; Gierliński & Poutanen, 2005). Compton scattering transfers energy between a photon and an electron via a collision. After the collision, the electron and photon recoil, with energy being transferred between the two. Note that Compton upscattering describes a scattering in which the photons gain energy and should not be confused with Compton down-scattering, in which the photons lose energy.

Consider a population of photons with a frequency, ν, and an energy, E. This population of photons are upscattered by a population of hot, relativistic electrons with velocity βc (and Lorentz factor $\gamma = (1-\beta^2)^{-0.5}$). The average fractional energy transferred from the electrons to the photons averaged over all scattering angles is (Longair, 2011; Rybicki & Lightman, 1979)

$$\frac{\Delta E}{E} = \frac{4}{3}\beta^2\gamma^2 - \frac{h\nu}{m_e c^2}. \tag{1.16}$$

Here, the first term results from the classical Thomson scattering (the low energy limit of Compton scattering) and the second term relates to the quantum recoil. If the population of electrons within the X-ray corona are in thermal equilibrium,

they are describable by the (dimensionless) electron temperature $\Theta = kT_e/m_ec^2$ and random velocity $v^2 \sim 3kT_e/m_e$, thus the average velocity is $\beta^2 = 3\Theta$, assuming $\gamma = 1$. Alternatively, we can consider the relativistic kinetic energy of the population of electrons, $E_{\rm k} = 0.5\gamma^2 mv^2$. In this case we get $v^2 = 3kTe/(m_e\gamma^2)$, and thus $\gamma^2\beta^2 = 3\Theta$.

Assuming isotropic distributions of electrons and photons, the average energy change from upscattering (averaged over all angles) is $\Delta E = E_{\rm out} - E_{\rm in} = 4\Theta E_{\rm in}$, where $E_{\rm in}$ and $E_{\rm out}$ are the input and output energies of a photon undergoing a scattering event, and we see from Equation 1.16 that the average fractional energy gain is 4Θ. This approximation is valid for $E_{\rm out} \lesssim 3\Theta$, as the photon cannot gain more energy than the electron started with and beyond this, the effects of quantum recoil cannot be ignored.

For this energy transfer to occur, a collision must happen and thus depends on the likelihood of a collision. In the Thomson limit, electrons have a cross-section for interactions with photons of σ_T, the Thomson cross-section. The optical depth is the number of electrons in the volume swept out by a photon travelling a distance R and is given as

$$\tau = nR\sigma_T, \tag{1.17}$$

where n is the electron density. The probability of a Compton upscattering event is then $1 - e^{-\tau}$. For a typical X-ray corona $\tau \sim 1 - 3$, while in the limit where $\tau << 1$, the scattering probability reduces to $\sim \tau$.

For seed photons with initial energy, $E_{\rm in}$, a fraction τ of these are up-scattered by the optically thin X-ray corona to an energy $E_{\rm out,1st} = (1 + 4\Theta)E_{\rm in}$. Photons that have undergone one scattering event are subsequently available to undergo a second scattering experiencing a change in energy of, $E_{\rm out,2nd} = (1 + 4\Theta)E_{\rm out,1st} = (1 + 4\Theta)^2 E_{\rm in}$. These photons can then scatter a third time and so forth until they reach the limit of the electron energy, $E_{\rm out,N} = (1 + 4\Theta)^N E_{\rm in} \sim 3\Theta$. The constant

energy increase thus gives rise to a power law,

$$F(E) \approx E^{-\alpha} \quad \Longrightarrow \quad \alpha = \frac{\ln \tau}{\ln(1+4\Theta)}, \tag{1.18}$$

with a low energy cut-off at $E_{\rm in}$ and a high energy cut-off at $\sim 3\Theta$. Here $F(E)$ is the specific energy flux.

1.1.5.3 Reflection and Absorption

A fraction of the flux emitted from the Comptonising corona will be incident on the optically thick accretion disc. Therefore, there is some probability that this emission is reflected into our line of sight, giving rise to the so-called *reflection hump* in the observed spectrum. Commonly, we identify reflection through the fluorescent iron Kα line at 6.4 keV, which results from an electron dropping energy levels to occupy a space in a lower energy shell (García et al., 2013).

The likelihood of photons undergoing reflection into our line of sight depends on the relative importance of scattering and photoelectric absorption, which in turn depends on the ionisation, $\xi = L/nr^2$, of the medium photons are passing through. Here L is the source luminosity, and n is the number density for an absorber illuminated by an isotropic emitter a distance r away (Fabian et al., 2000; Done, 2014). Reflection is a form of scattering that occurs when a photon encounters an optically thick medium, such that it bounces off of the outer layers of the medium rather than passing through it. Scattering events can also occur in optically thin mediums, whereby the photon travels some distance through the medium before encountering an electron to undergo a scattering event.

In neutral material, photoelectric absorption is the dominating process at low energies ($\leq$ 10 keV), as soft X-ray photons are more readily absorbed than hard X-ray photons. Therefore, the fraction of reflected photons is small because fewer photons are available to undergo scattering events at lower energies. The photoelectric absorption cross-sections decrease with energy, so the reflected fraction increases. At

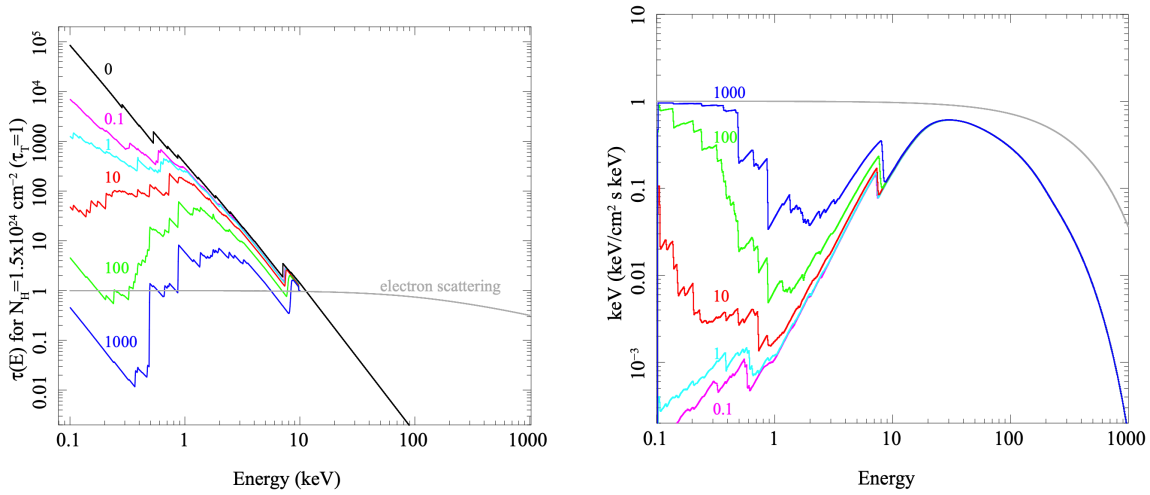

Figure 1.13: Panel A: The ionised absorption cross section for material with solar abundance and $N_{\rm H} = 1.5 \times 10^{24}$ cm^{-2}. The ionisation, ξ, is labelled on each curve, and the Klein-Nishima electron scattering cross-section is grey. Panel B: The corresponding reflection spectra for the same material and ionisations (the colours are consistent between panels). Higher ionisation results in decreased opacity at lower energies, thus more reflection. However, at high energies, reflection is insensitive to ionisation.

higher energies (≥ 10 keV), the observed spectrum is dominated by the scattering of electrons, and thus a reflection component is observed. In contrast, strongly ionised material hosts more free electrons than neutral material. Therefore, the importance of scattering increases, so more photons will get reflected into our line of sight at lower energies (see Figure 1.13). For less ionised material, the importance of absorption increases at lower energies as there are fewer free electrons in the medium. Therefore, more flux will get absorbed and reemitted at longer wavelengths (Done, 2014) in less ionised material than strongly ionised material at lower energies.

Edges and emission lines are broader at higher ξ as scattering, and therefore, reflection increases. Since the reflector (accretion disc) is rapidly spinning, we must consider the effects of this on the lines observed in the source spectra. An observer will see part of the disc moving towards them and the other side moving away. The approaching emission is blue-shifted, and the receding emission is redshifted by the

Doppler effect, resulting in a 'two horn' profile. The combination of Doppler boosting of the blue wing and length contraction in the line of sight leads to a skewed profile, while gravitational redshift acts to lower the energy. The result is the observed emission line being relatively broad, even if it is narrow in the rest frame and can be used to diagnose the inner radius of the accretion flow (Fabian et al., 1989, 2000).

Photoelectric absorption alters intrinsic emission via interactions between photons and the ISM or material local to the binary system, leaving behind an ion and a free electron. The electrons in the resulting ion are more tightly bound, so the binding energy is higher, and any free electrons typically recombine with an ion before the subsequent absorption interaction. For systems in which the X-ray irradiation is very intense, there may be more absorption events than time for the ions to recombine. Therefore, collisions between photons and ions dominate the absorption cross-section rather than photons and neutral atoms. The absorption cross-section thus depends on the ratio of ionisation and recombination. If the ionisation is high, the atoms are more likely to be stripped of their electrons, lowering the absorption cross-section and vice versa. The optical depth, τ, of the absorbing medium governs the absorption; a fraction $e^{-\tau}$ of the intrinsic emission is transmitted, and $1 - e^{-\tau}$ is absorbed. The total absorption cross-section is a sum of the cross-section for each element, weighted by relative abundance. Heavier elements have a higher energy absorption edge but lower abundance. Therefore, they have less influence on the total cross-section, while higher abundance elements have a greater effect.

1.2 Pulsars

A pulsar is an astrophysical source of electromagnetic radition that has a regular periodicity. The emission is observed as short bursts, which orginate from the magnetic poles of the NS and recur on the spin period of the NS. These pulses of stable, periodic

emission gave pulsars their name (Beskin et al., 2015). In this section, I introduce various classes of pulsars and their connections to XRBs.

1.2.1 Radio Pulsars

Pulsars, discovered in 1967 (Hewish et al., 1967), are magnetised NSs that continuously emit beams of radio radiation from their magnetic poles (see Figure 1.14), and the rotational energy of the NS powers the pulsar. Analogous to a lighthouse, the radio beam sweeps across the observers' line of sight, resulting in observations of short flashes of radio radiation each time the beam passes, as shown in Figure 1.15 (Lorimer & Kramer, 2004; Lyne & Graham-Smith, 2006; Condon & Ransom, 2016). These flashes are the radio pulsations that give pulsars their name and it was the discovery of pulsars that confirmed earlier theoretical predictions of the existence of NSs. The period on which the radio pulses recur is equal to the rotation period of the NS. However, the emission mechanism for the radio beams is not well understood. Let us assume a spherical NS of mass M and radius R rotates with an angular velocity $\Omega \equiv 2\pi/P$. Assuming that equilibrium rotation is sub-Keplerian (i.e. the rotational velocity of the NS is constant), we can write (Condon & Ransom, 2016),

$$\Omega^2 R < \frac{GM}{R^2} \quad \therefore \quad P^2 > \left(\frac{4\pi R^3}{3}\right)\frac{3\pi}{GM}. \tag{1.19}$$

Expressing this in terms of the mean density we obtain,

$$\bar{\rho} \equiv M\left(\frac{4\pi R^3}{3}\right)^{-1} \quad \Longrightarrow \quad \rho > \frac{3\pi}{GP^2}, \tag{1.20}$$

enabling a lower limit of the mean density of a NS through the measured pulse period, P. P is simply the time between successive pulses of radio emission, which for Figure 1.15, would be the time between the two pulse peaks. For a millisecond pulsar, $\rho > 10^{14}$ g cm^{-3}, indicating that the cores of NSs contain a stable form of highly dense matter.

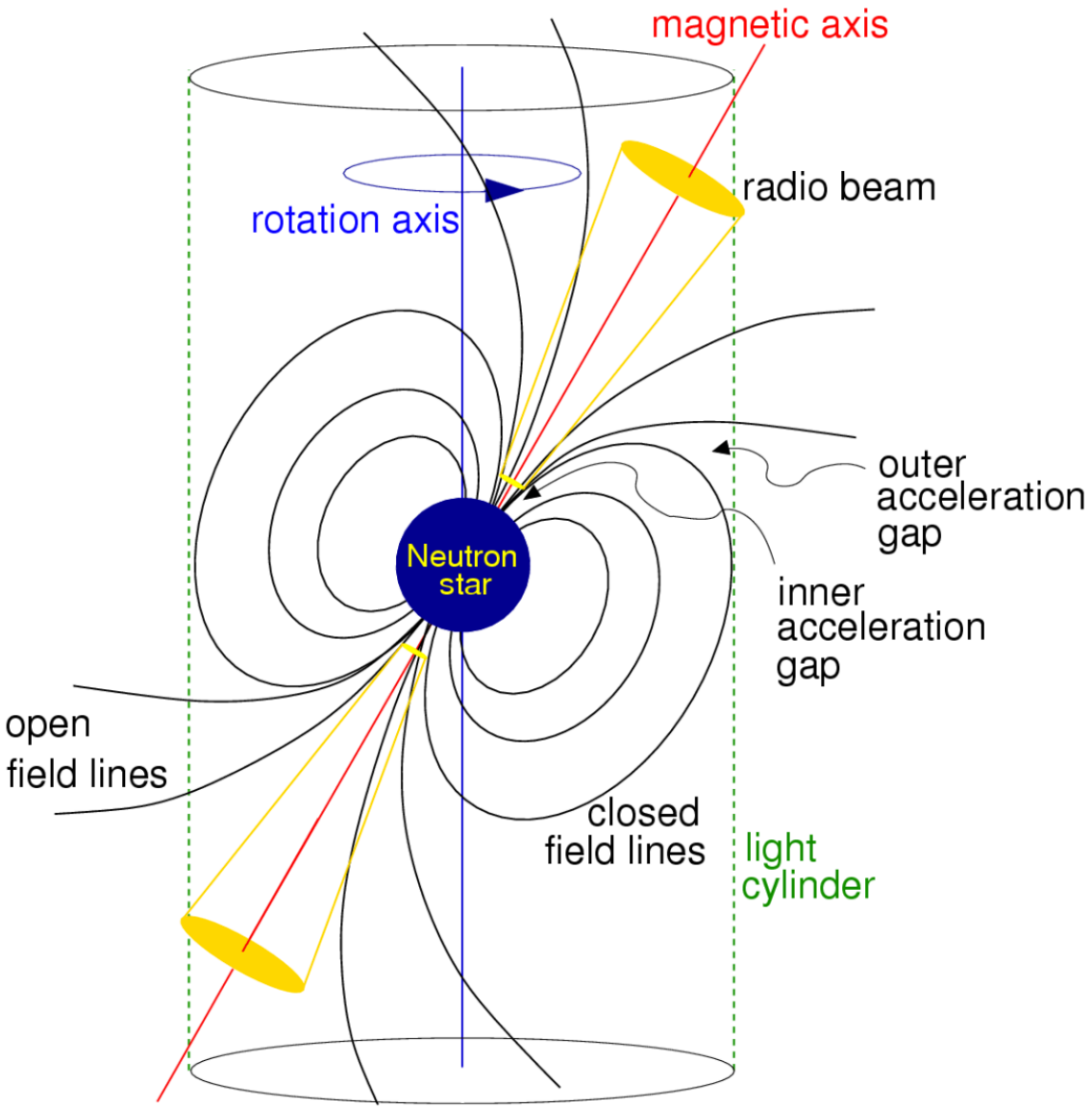

Figure 1.14: A schematic of the magnetic dipole of a neutron star (NS). Charged particles are accelerated in an outer acceleration gap before being chanelled along the open magnetic field lines towards the NS, enabling the emission of coherent radiation.
Figure from Condon & Ransom (2016), originally from The Handbook of Pulsar Astronomy, Lorimer & Kramer (2004), ©D. R. Lorrimer and M. Kramer 2005. Published by Cambridge University Press.
Reproduced with permission of The Licensor through PLSclear.

Radio pulsars are the most numerous class of pulsating NSs, and observations of these objects occupy a multidimensional parameter space summarised by P and its time derivative $\dot{P}$ (Beskin et al., 2015; Condon & Ransom, 2016). A $P\dot{P}$ diagram, as in Figure 1.16, is used to follow the lives of pulsars and encodes a vast amount of information about the pulsar population and its properties. Each point in Figure 1.16 represents one radio pulsar. The position of the point indicates the following properties of a pulsar: the spin period, P, the period derivative, $\dot{P}$, the characteristic age, $\tau_{\rm age}$, the magnetic field strength, B and the spin-down luminosity $-\dot{E}$ of the pulsar. In the remainder of this subsection I discuss these properties and the different clusters of pulsars that appear in Figure 1.16 (Condon & Ransom, 2016).

Figure 1.14 shows a canonical picture of a pulsar where the magnetic field is assumed to be dipolar. Note that recent results from the Neutron Star Interior Composition ExploreR (*NICER*) suggest that NSs may possess higher-order magnetic fields (Riley et al., 2019; Miller et al., 2019). Charged particles, constrained to move along magnetic field lines, are accelerated in the 'gap' regions of the NS's magnetosphere before streaming along the open magnetic field lines, generating coherent emission (Lorimer & Kramer, 2004). If the magnetic dipole and NS rotation axis are misaligned (see Figure 1.14), the NS emits this radiation at the rotation frequency of the NS. The power of this so-called magnetic dipole radiation is given by

$$L = \frac{2}{3c^3}(BR^3 \sin\alpha)^2 \left(\frac{2\pi}{P}\right)^4, \tag{1.21}$$

where $m = BR^3$ is the magnitude of the magnetic dipole moment (Jackson, 1998), B is the magnetic field strength, R is the radius of the NS and α is the angle between the magnetic and rotation axes.

As the NS emits dipole radiation, it loses rotational kinetic energy and spins down. We can calculate the rate at which rotational energy is lost (the spin-down luminosity) by writing the rotational kinetic energy in terms of the moment of inertia, I of the

NS,

$$E = \frac{I\Omega^2}{2} = \frac{2\pi^2 I}{P^2}. \tag{1.22}$$

For a spherical NS with mass M, radius R, and an average, uniform density ρ (Equation 1.20), the moment of inertia of the NS is,

$$I = \frac{2MR^2}{5}. \tag{1.23}$$

Differentiating Equation 1.22 with respect to time gives the spin-down luminosity (Salvo & Sanna, 2022),

$$-\dot{E} = -I\Omega\dot{\Omega} = \frac{4\pi^2 I\dot{P}}{P^3}. \tag{1.24}$$

Subsequently, stating $L \approx -\dot{E}$ allows us to derive some fundamental properties of the NS. Firstly, the minimum magnetic field strength is,

$$B > (\frac{3c^3 I}{8\pi^2 R^6})^{\frac{1}{2}}\ (P\dot{P})^{\frac{1}{2}}, \tag{1.25}$$

where the inequality arises from the factor of $1/\sin\alpha$. Combining this and Equation 1.23 with measurements or reasonable assumptions for M and R enables the minimum magnetic field to be determined (Condon & Ransom, 2016). Additionally, assuming the initial period was much shorter than the current period, the characteristic age of a pulsar is

$$\tau_{\text{age}} = \frac{P}{2\dot{P}}. \tag{1.26}$$

The initial NS formation mechanism, a supernova, creates rapidly rotating NSs with a spin period of a few milliseconds and strong magnetic fields of $\sim 10^{12}$ G. During the core collapse, a dynamo effect may generate even stronger magnetic fields of the order of $10^{14} - 10^{15}$ G, giving rise to magnetars, powered by magnetic field decay. The conservation of angular momentum means that rotation rates increase by $\sim 10^{10}$ during the core collapse, as does the magnetic field. Therefore, the youngest pulsars, with rapid rotation rates and strong magnetic fields, occupy the upper middle section of Figure 1.16. These pulsars are typically associated with supernovae remnants and

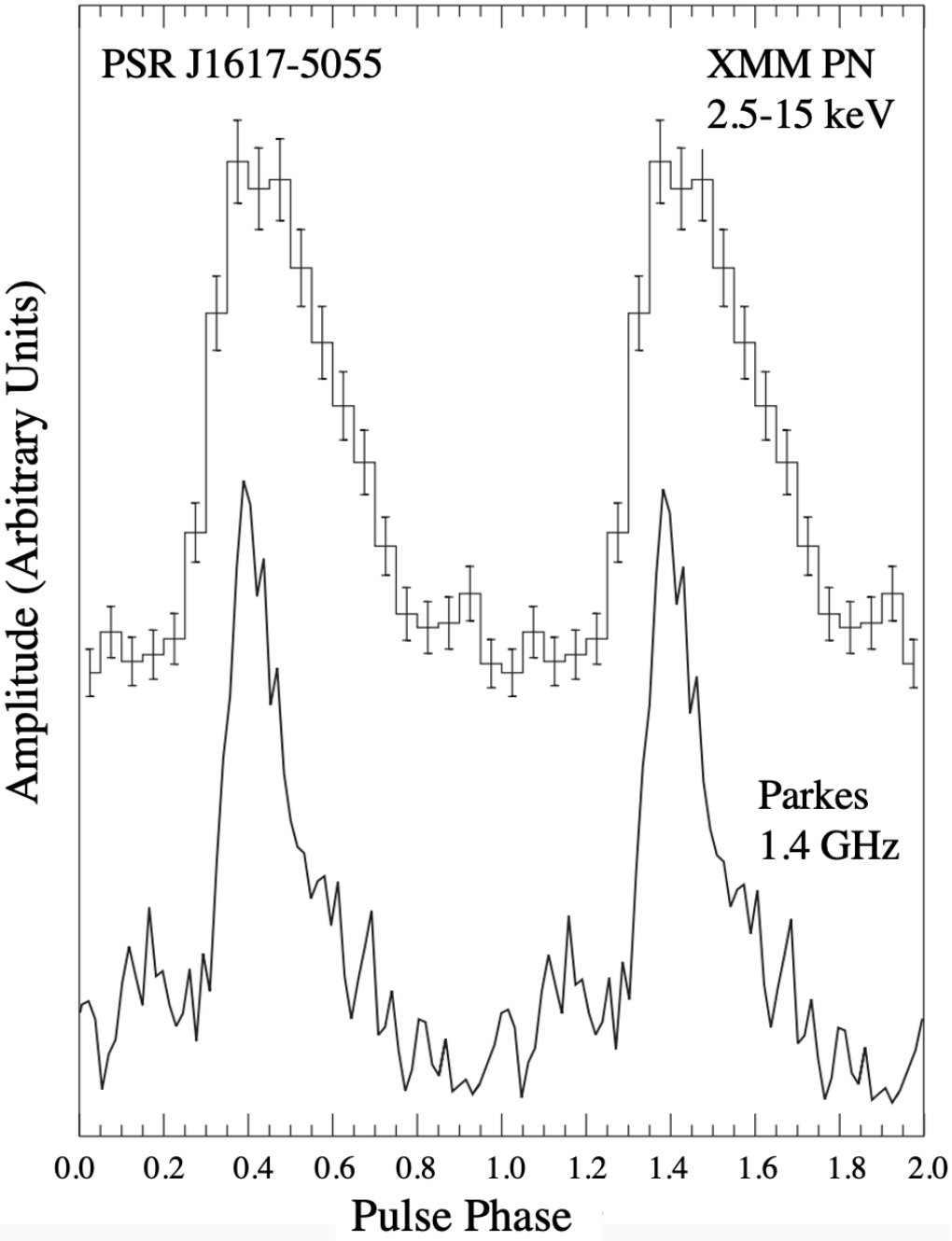

Figure 1.15: X-ray and radio pulsations from PSR J1617–5055 observed in the 2.5–15 keV band with the *XMM-Newton* and at 1.4 GHz with the Parkes Radio Telescope respectively.
Figure adapted from Becker (2009), X-Ray Emission from Pulsars and Neutron Stars, Springer eBook, 357, 91-140, 2009, Springer Berlin Heidelberg. Reproduced with permission from Springer Nature.

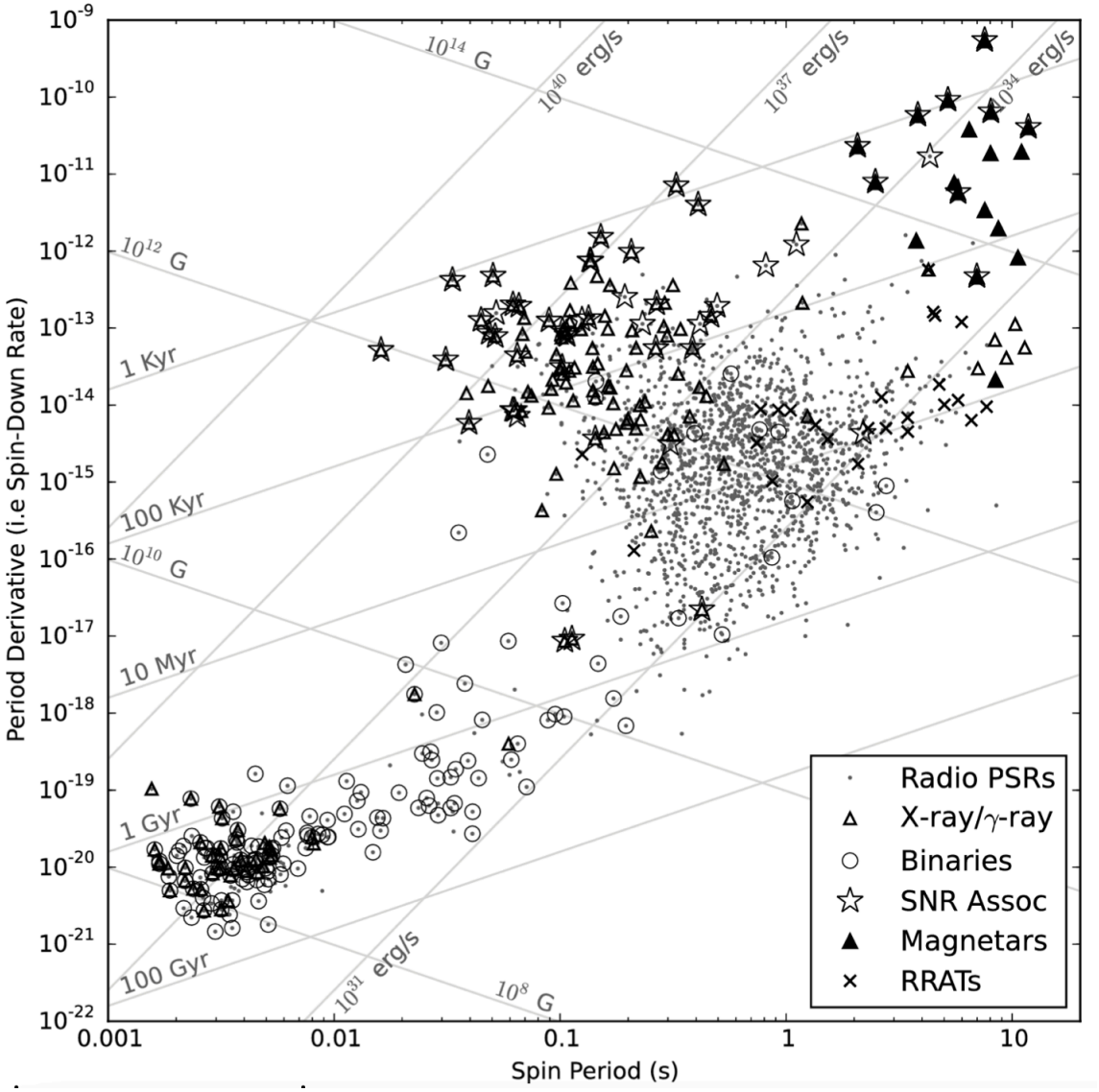

Figure 1.16: A $P\dot{P}$ diagram, which follows the lives of pulsars. Each point represents one pulsar and encodes its spin period, P, the time derivative of its spin period, $\dot{P}$, its characteristic age $\tau_{\rm age}$, its minimum magnetic field strength, B, and its spin-down luminosity, $-\dot{E}$, through the axes and contour lines. Young pulsars with higher magnetic field strengths and faster rotation rates occupy the upper middle of the diagram. More evolved pulsars with periods of $\sim$ seconds occupy the large, central population, and the oldest pulsars are in the lower left of this diagram. The older pulsars have rapid rotation rates, suggesting that they result from the recycling scenario (Wang, J. et al., 2011). Rotating Radio Transients (RRATs) are pulsars that sporadically emit single pulses instead of continuous pulse trains.
Figure from Condon & Ransom (2016). Included with permission from S. Ransom.

emit high-energy radiation. Pulsars' rotation rates reduce and evolve over millions of years until they become 'slow' or 'ordinary' pulsars with spin periods of a few seconds (large, central population in Figure 1.16). Eventually, their rotation rate is too slow to power the radio emission mechanism and they become unobservable.

The oldest pulsars in Figure 1.16 (lower left) are mostly millisecond pulsars (MSP), which exhibit rapid rotation rates and weaker magnetic fields ($10^8 - 10^9$ G). Many of these pulsars are in binaries and are reborn via the accretion of matter from a companion star. Accretion spins up the NS to millisecond spin periods and provides sufficient rotational energy to activate the pulsation mechanism again. This rejuvenation is known as the recycling scenario (Bhattacharya & van den Heuvel, 1991; Wang, J. et al., 2011) and gains support from the discoveries of millisecond X-ray pulsars (Wijnands & van der Klis, 1998) (Section 1.2.2) and transitional millisecond pulsars (Archibald et al., 2009) (Section 1.2.4). In contrast, several MSPs are solitary. Previously, these pulsars will have been part of binary systems but have since destroyed their companion star, akin to the ablation mechanism in spider pulsars (Fruchter et al., 1988) (Section 1.2.3).

1.2.2 X-ray and γ-ray Pulsars

Analogous to radio pulsars, X-ray and γ-ray pulsars appear to emit periodic pulses of X-ray and γ-ray radiation, respectively, that recur on the rotation rate of the NS. γ-ray pulsars are the rarer of the two and are usually associated with young NSs with strong magnetic fields or highly energetic, recycled MSPs (Hui & Li, 2019; Clark et al., 2023). The strength of the γ-ray radiation from these pulsars varies significantly, and some tentative correlations between the luminosity of the γ-ray radiation and the spin-down of the NS are beginning to emerge (Marsden & White, 2001).

In contrast, X-ray pulsars are commonly found in accretion-powered XRBs, hosting highly magnetised NSs (Poutanen, 2006; Patruno & Watts, 2021). Analogous to

radio pulsars, accreted material travels along the magnetic field lines and is accelerated towards the poles, giving rise to X-ray pulsations. Here, the inclination of the NSs rotation axis is misaligned with its magnetic axis, causing the emission to appear pulsated to a distant observer. X-ray pulsars have a range of rotation rates. The slower spinning NSs ($\sim$ seconds) have higher magnetic field strengths ($B \sim 10^{12}$ G), similar to ordinary radio pulsars, while NSs with rapid rotation rates ($\sim 10^{-3}$ s) generally have weaker magnetic fields ($B \sim 10^{9}$ G), like radio MSPs (see Figure 1.16) (Patruno & Watts, 2021; Salvo & Sanna, 2022). Respectively, these systems are known as accreting X-ray pulsars (AXPs) and accreting millisecond X-ray pulsars (AMXPs) (Bildsten et al., 1997). Typically, AXPs are located in wider binaries and therefore are unlikely to experience the prolonged period of mass transfer needed to spin the NS up to millisecond periods.

In AXPs and AMXPs, the accretion flow towards the NS can be interrupted by the NS's magnetosphere if the strength of the magnetic field is sufficient (Patruno & Watts, 2021). For a dipolar magnetic field, the magnetic energy ($B^2/8\pi$) increases at small radii allowing it to overcome the kinetic energy of infalling material at the magnetospheric radius, r_B. Inside r_B, charged particles flow along the magnetic field lines towards the NS's magnetic poles, where they are accreted (Poutanen, 2006; Salvo & Sanna, 2022). Thus r_B is approximately the inner boundary of the accretion disc. The magnetospheric radius is within a factor of a few of the Alfvén radius (Ghosh & Lamb, 1991; Burderi & King, 1998; Salvo & Sanna, 2022):

$$r_B \approx r_A = \left(\frac{\mu^4}{2GM\dot{M}^2} \right)^{\frac{1}{7}}, \tag{1.27}$$

where μ is the magnetic dipole moment. Therefore, we see that the strength of the magnetic field governs the radius of the inner disc boundary; the stronger the field, the larger the inner disc radius. If the inner disc radius is inside the corotation radius (the radius at which material corotating with the NS will be at its Keplerian velocity),

then the rotation rate of the NS increases (spin up) because the inner disc will rotate faster than the magnetosphere and exert a positive torque on the NS (Ghosh & Lamb, 1979; Patruno & Watts, 2021; Salvo & Sanna, 2022). If the inner disc radius is larger than the corotation radius, the NS experiences a spin-down torque. Due to this, NSs with weak magnetic field tend to be fast rotators, and those with strong magnetic fields tend to spin slower (Sanna, A. et al., 2018; Patruno & Watts, 2021; Salvo & Sanna, 2022).

The first detection of millisecond X-ray pulsations was from the LMXB SAX J1808.4–3658 in 1998 (Wijnands & van der Klis, 1998), which identified LMXBs as progenitors for MSPs and confirmed the pulsar recycling scenario. The transfer of angular momentum through accretion from a companion star is responsible for spinning up the NS and activating the pulsar mechanism in otherwise dormant NSs. These observations capture SAX J1808.4–3658 undergoing this process. Subsequently, X-ray pulsations were uncovered in several NS LMXBs (Bildsten et al., 1997; Casella et al., 2008; Patruno et al., 2008; Papitto, A. et al., 2011), growing the population of AMXPs, and all experience mass transfer from a low mass companion via RLOF. All AMXPs are transient systems with orbital period $\lesssim 1$ day. They are typically fainter than typical XRBs when in outburst, suggesting lower mass accretion rates and X-ray pulsations are not exhibited while in X-ray quiescence (Salvo & Sanna, 2022).

1.2.3 Spider Pulars

Depending on their properties, radio MSPs in binary systems can align with one of the three sub-classes of spider pulsars. These sub-classes are redback, black widow and huntsman pulsars and are distinguished by the companion star's mass or spectral classification, or the binary's orbital period. Huntsman Pulsars have orbital periods $\gtrsim 5$ days and host evolved non-degenerate companions. They are γ-ray MSPs and

could be the progenitors of binary MSPs with white dwarf companions (Swihart et al., 2018). Redback pulsars host companion stars with masses $M_{\rm CS} \sim 0.2 - 0.4 M_{\odot}$, while black widows host less massive companion stars $M_{\rm CS} << 0.1 M_{\odot}$ (Roberts, 2012a; Chen et al., 2013). Redbacks and black widows have short orbital periods < 1 day, often as short as hours (Roberts et al., 2017). The first black widow and redback pulsars are PSR B1957+20 (Fruchter et al., 1988) and PSR J1023+0038 (Archibald et al., 2009; Roberts, 2012b), respectively. Redback and black widow pulsars occupy the lower left corner of Figure 1.16, implying that they are older pulsars and represent part of the population of recycled pulsars. Their discovery thus provides evidence for the recycling scenario.

Characteristically, the companion stars in redback and black widow pulsars undergo ablation driven by the pulsar wind (particles) and irradiation (high energy photons) from the NS (Kluzniak et al., 1988; Ruderman et al., 1989a,b). The pulsar wind and radiation incident on the companion star liberates its outer layers, resulting in ablated material around the system. This so-called cannibalistic behaviour is where the naming of redbacks and black widows originated. Conversely, huntsman pulsars, who take after their larger, non-aggressive namesake, do not experience ablation and are weakly irradiated. Ablation was previously considered unique to spider pulsars, but recent studies have uncovered evidence that X-ray irradiation can drive ablation in X-ray binaries (Knight et al., 2022a,b, 2023). In such cases, the ablated outflow may present as an extended companion star atmosphere rather than a vast clumpy wind like those often associated with spider pulsars.

The material forced off the companion star in redback and black widow pulsars 'collides' with pulsar wind, giving rise to an intrabinary shock, as in Figure 1.17 (Arons & Tavani, 1993; Venter et al., 2015). The shock forms at the radius at which the pressure balance points of the pulsar wind and abalted material conincide. Interactions and particle acceleration occuring at the shock front give rise to X-ray and

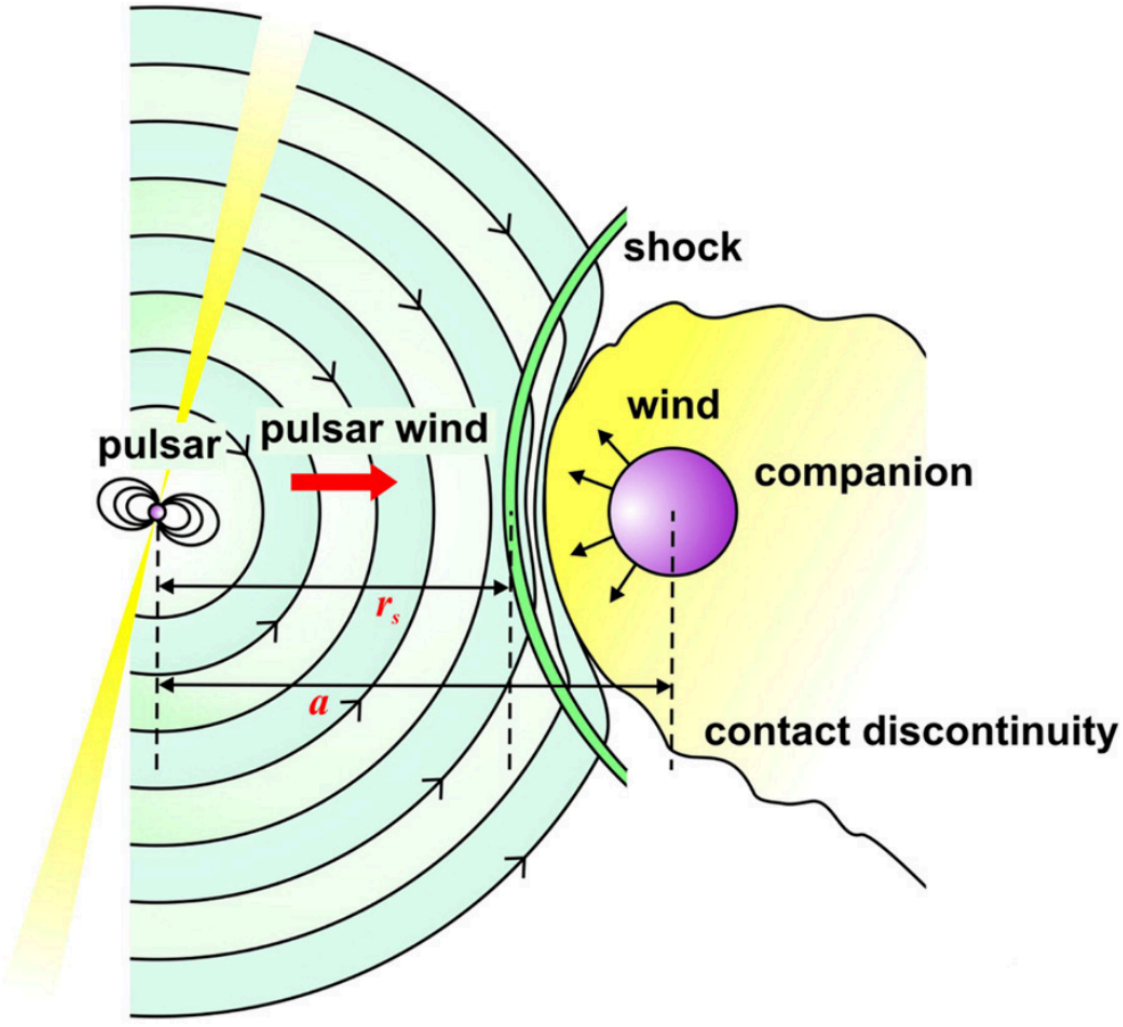

Figure 1.17: A schematic of a shock front in a spider pulsar (redback or black widow), showing how the pulsar wind from the neutron star (NS) interacts with the ablated outflow (wind) from the comapnion star.
Figure from Cosmic-Ray Positrons from Millisecond Pulsars, Venter et al. (2015), The Astrophysical Journal, 807, 130, Jul 2015. ©AAS. Reproduced with permission.

γ-ray emissions (Roberts et al., 2017) and contribute to the heating of the companion's surface, thus creating a day and night side of the star. The day side faces the pulsar and thus gets significantly heated, while the night side is comparatively cool, creating orbital modulations in the optical light curves.

Ablated material remains gravitationally bound to the binary, thus introducing characteristic observable properties like delayed pulse arrival times (Polzin et al., 2018) and a material trail behind the companion star (Fruchter et al., 1988). Furthermore, sufficiently inclined redbacks and black widows can exhibit radio eclipses which are frequency-dependent, extended and asymmetric due to absorption by the ablated material (Polzin et al., 2018, 2020), an example of which is in Figure 1.18. These eclipses arise when the companion star (and ablated material) obscure an observer's view of the pulsar and have longer durations at lower frequencies. Eclipses are frequently observed in spider pulsars as there is so much ablated material around the system that it is opaque to radio emission, and eclipses are visible at moderate inclinations. γ-ray eclipses in spider pulsars are also common and can identify new spider pulsars (Clark et al., 2023). Ablation also increases mass loss from the companion star. Therefore, redback and black widow pulsars may comprise part of the evolutionary pathway towards isolated MSPs. Given sufficient time, the ablation process could reduce the mass of a redback companion so that it classifies as a black widow. If ablation continues beyond this, the companion may be entirely *devoured* by ablation, resulting in an isolated MSP, as suggested for PSR B1957+20 (Fruchter et al., 1988). This scenario is similar to the dissolution or evaporation of the donor star, which is considered a likely scenario for the formation of isolated MSPs (Bildsten, 2002). In this case, the donor star must remain hot (e.g. irradiated) while losing mass, and the donor star may expand. Therefore, spider pulsars could explain the populations of binary and solitary MSPs.

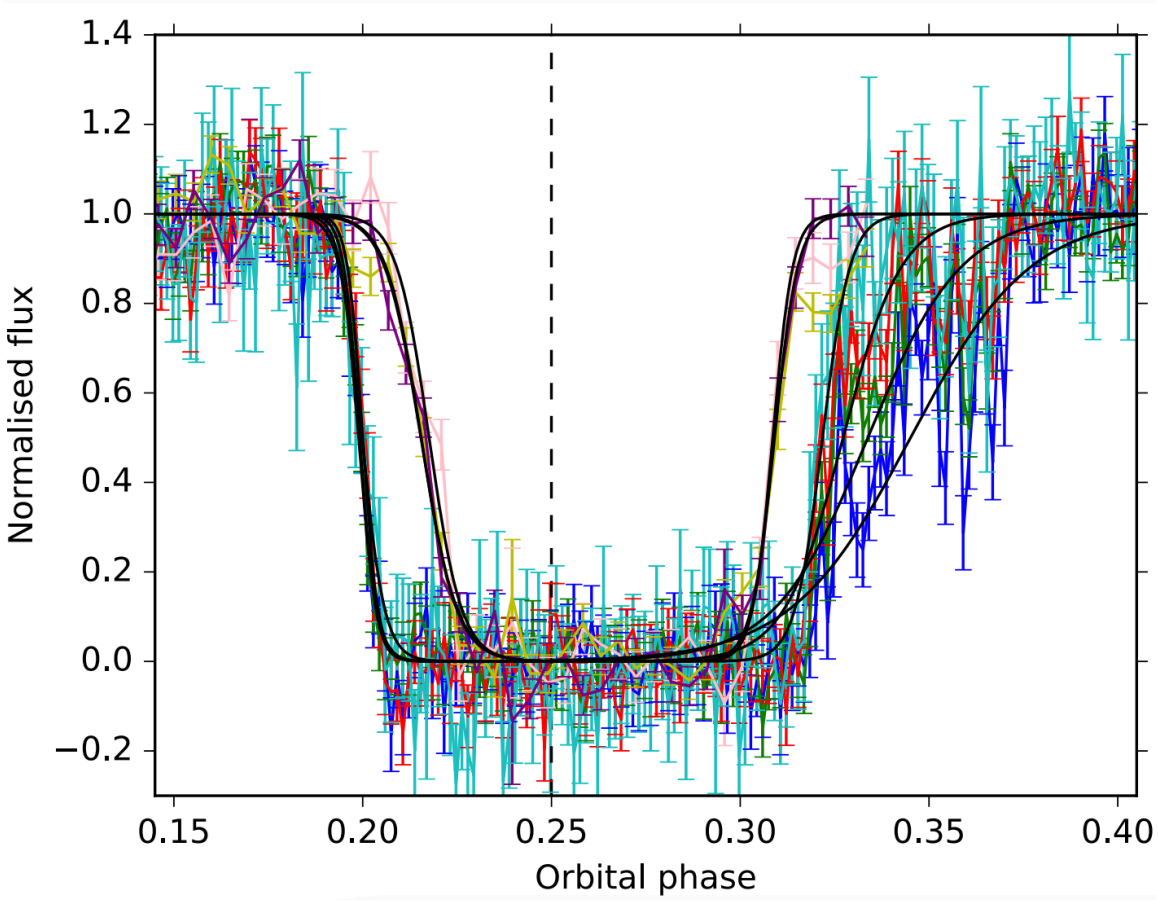

Figure 1.18: Radio eclipses from the black widow PSR J1810+1744. The frequency bands shown are 118 (blue), 134 (green), 154 (red), 176 (cyan), 321 (pink), 344 (yellow) and 369 MHz (purple). The eclipses occur when the companion star and ablated material pass in front of the pulsar. These eclipses are longer in duration and have more pronouced asymmetries at lower frequencies. The eclipses are modelled (black lines) with least squares fits of Fermi-Dirac functions.
Figure from Polzin et al. (2018). Included with permission from R. Breton.

1.2.4 Transitional Millisecond Pulsars

Further confirmation of the recycling scenario came from the discovery of transitional millisecond pulsars (tMSPs) (Archibald et al., 2009; Papitto et al., 2013). TMSPs switch between exhibiting accretion-powered X-ray pulsations and rotation-powered radio pulsations on timescales as short as weeks, thus confirming that older radio MSPs form in LMXBs. During the accretion-powered phase, a tMSP exists like an AMXP and emits intense, high-energy radiation like an XRB. When accretion ceases, the binary transitions to a rotation-powered state in which the pulsar wind prevents the in-fall of matter onto the NS, and the system presents as a radio MSP (Papitto & Martino, 2022). The initial transition from AMXP to radio MSP could take several years, but the transitional phase is expected to be an extended stage of binary pulsar evolution (Archibald et al., 2009; Papitto et al., 2013; Bahramian et al., 2018).

TMSPs bridge several classes of MSPs. Frequently, redback pulsars are identified as tMSPs (see Linares 2014 for discussion of the transitional redback pulsars PSR J1023+0038, PSR J1824–24521 and XSS J12270–4859). Therefore, studying the X-ray loud phase of transitional redback pulsars can inform us of their prior evolution and probe the mass loss processes that deplete the companion stars in spider pulsars. For PSR J1023+0038, the transition from rotation to accretion power in 2013 was accompanied by the onset of X-ray and γ-ray emission, suggesting that transitional and/or spider pulsars represent a fraction of the transient γ-ray sources. Recently, spider γ-ray pulsars provided precise NS mass measurements and a technique for identifying elusive eclipsing spider pulsars (Clark et al., 2023).

The interplay between the gravitational field of the NS and the outward pressure of the pulsar wind determines whether the system is rotation or accretion powered. In turn, this depends on the binary's orbital period and if the conditions for RLOF are satisfied. All known tMSPs have shown at least one rotation-powered state in which they emit radio pulsations - this is necessary to classify a system as transitional.

Two other distinct states of tMSPs are the accretion state, with X-ray luminosities $> 10^{36}$ erg s^{-1} and high variability, and the sub-luminous disc state, where the X-ray luminosities are $10^{33} - 10^{34}$ erg s^{-1}, and the source appears stable. Rapid transitions between these two accretion states are typical (Papitto & Martino, 2022).

1.3 Neutron Star Mass and Radius Measurments

Since the postulation of NSs in 1934 (Baade & Zwicky, 1934), our understanding of these ultra-compact objects has rapidly evolved due to the discovery of hundreds of pulsars and the development of precise pulsar timing techniques. The high-quality data provided by new generations of radio, X-ray and γ-ray telescopes have enabled measurements of the macroscopic properties of NSs and, therefore, constraints on their internal composition. The masses of ~ 70 NSs are known, many of which are in Figure 1.19, and NS radii are generally constrained to $9 - 13$ km. When combined, these measurements limit the possible EoS of nuclear matter and often favour a harder NS EoS.

Most advances to our knowledge of the EoS come from measurements of the masses and radii of astrophysical NSs, as terrestrial experiments cannot recreate the conditions within the cores of NSs. Such advances originated from different populations of NSs and observations at all wavelengths. Precise mass measurements, for example, come from radio observations of pulsars, while radius measurements predominantly come from X-ray observations of NS LMXBs. Even so, the NS EoS remains one of the big, unanswered questions and motivates the work presented in this thesis. Furthermore, astrophysical measurements of NS properties enable tests of general relativity in the strong-field regime and probe the explosive or transient events governed by the maximum mass of NSs. In this section, I describe some current techniques to infer the masses and radii of astrophysical NSs.

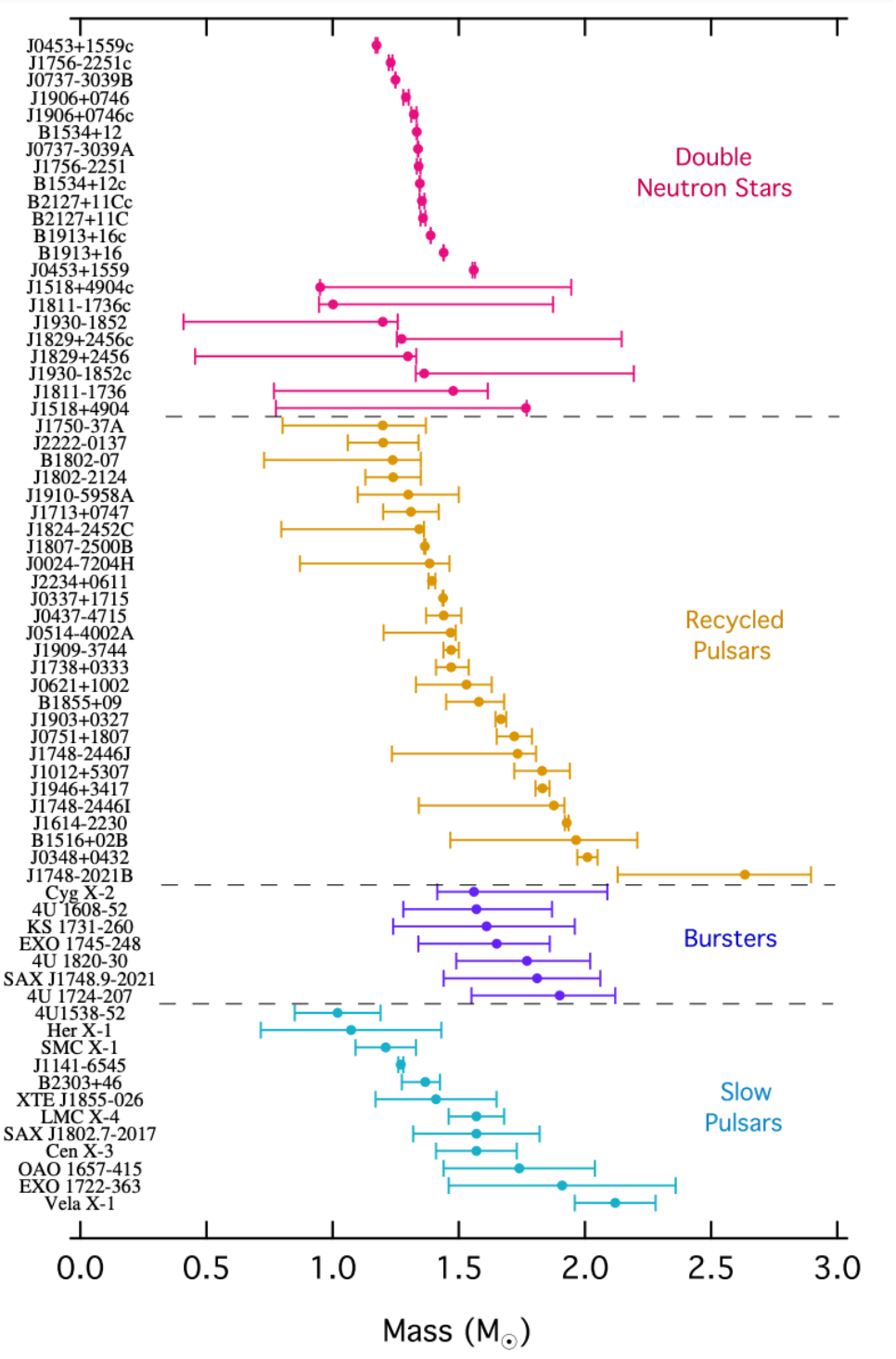

Figure 1.19: A distribution of measured neutron star (NS) masses from different classes of NS system.
Figure From Özel & Freire (2016), included with permission of Annual Reviews, Inc. from Masses, Radii, and the Equation of State of Neutron Stars Özel, Feryal; Freire, Paulo, 54, 401-440, Copyright 2016; permission conveyed through Copyright Clearance Center, Inc.

1.3.1 Dynamical Mass Measurements

The masses of NSs in XRBs can be measured dynamically using the Doppler shifts caused by the orbital motion of one of the binary components. Dynamical methods are the most direct techniques since they only assume Kepler's laws. For pulsars, measurements of the Doppler shifts come from the orbital phase-dependent shifts to the pulse frequency (Chakrabarty & Morgan, 1998) and for quiescent XRBs, they are from the orbital phase-dependent shifts to the wavelength of emission lines in the spectrum of the companion star (the radial velocity curve, Figure 1.20; e.g. Casares et al. 2014). In both cases, the actual observable is the binary mass function, which depends on the component masses ($M_{\rm NS}$ and $M_{\rm CS}$) and binary inclination angle, i.

The long-term stability of recycled pulsars, and their rapid rotation rates, make them ideal candidates for pulsar timing. Therefore, for recycled pulsars, which are often in binary systems, precise timing can meticulously measure the pulsar's orbital motion. Assuming Newtonian gravity, the binary period, P, the projection of the semi-major axis, a onto the observer's line of sight, $x \equiv a \sin i/c$, the time of periastron, and the longitude of periastron govern the orbital motion of the pulsar. Collectively, these are the Keplerian parameters and are determinable by fitting a radial velocity model to the observed spin period of the pulsar, which is Doppler shifted by its orbital motion. The pulsar binary mass function,

$$f_{\rm pulsar} = \frac{(M_{\rm CS} \sin i)^3}{M_{\rm tot}^2} = \frac{4\pi^2 a^3 \sin^3 i}{GP^2}, \tag{1.28}$$

where $M_{\rm tot} = M_{\rm CS} + M_{\rm NS}$, is then determined from the Keplerian orbital parameters, enabling the pulsar's mass to be constrained.

The approach for quiescent XRBs is similar and often utilises X-ray observations of the system while in outburst to determine the orbital period, P, and the semi-major axis of the NSs orbit. While in quiescence, optical observations of the companion star give the radial velocity semi-amplitude from a measured curve (Figure 1.20), projected

rotational velocity and the amplitude of ellipsoidal modulations. The fundamental parameters of the NS, including its mass, are subsequently determinable from the X-ray binary mass function,

$$f_{\rm opt} = \frac{PK^3}{2\pi G} = \frac{M_{\rm NS} \sin^3 i}{(1+q)^2}, \tag{1.29}$$

where K is the semi-amplitude of the radial velocity curve.

Both approaches require knowledge of the binary inclination angle, i. There are several ways to determine the binary inclination angle independently of the mass ratio; the inclination of material close to the compact object can be determined by comparing the properties of two sides of the jet (Hjellming & Johnston, 1981), or through modelling the Doppler and gravitational shifts on the X-ray spectrum, typically via the iron line (Fabian et al., 1989) but also potentially from the thermal disc spectrum if high-quality data exist (Parker et al., 2019). Further from the compact object, optical and X-ray disc winds can suggest the inclination of the disc from which they originate (Ponti et al., 2012; Higginbottom et al., 2018). The inclination angle of the orbital plane is determinable from ellipsoidal modulations arising from tidal distortion of the companion star (Casares et al., 2014). Alternatively, the inclination angle is determinable through X-ray eclipse mapping, which models the shape and duration of the ingress, egress and totality to self-consistently determine the binary mass ratio, q, the binary inclination, i and the totality duration t_e, thus breaking the degeneracy between mass, mass ratio and inclination (the model developed in this thesis; Knight et al. 2022a,b). The NS's mass in an eclipsing system with a measured binary mass function (radial velocity curve) is simply a function of q if the companion star is filling its Roche-Lobe (Horne, 1985).

X-ray eclipse mapping requires the system to have a sufficiently high inclination to the observer to result in the characteristic drop in X-ray flux that arises from the occultation of the compact object by the companion star. At lower inclination angles,

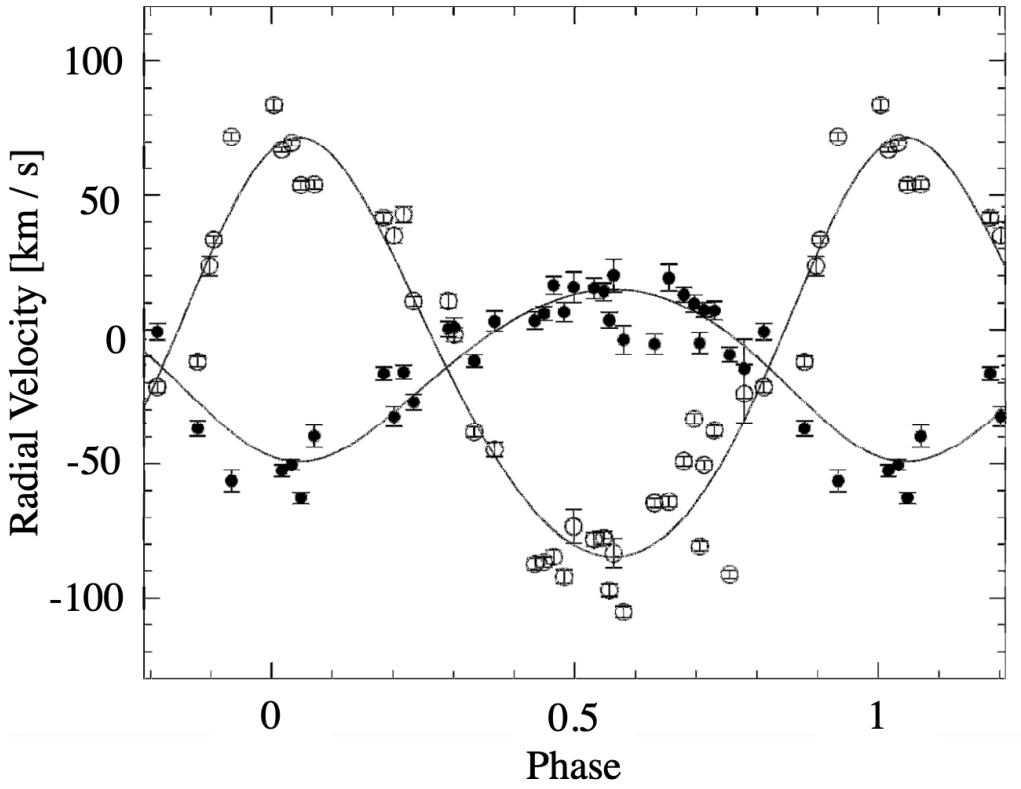

Figure 1.20: A radial velocity curve of a Be XRB. Here, Be refers to the spectral class of the companion star. The solid circles indicate the velocities of the Be star, obtained from the Fe II line at 4583 Å, and the open circles represent the velocities of the compact companion, extracted from the He II line at 4686 Å. The measured velocities are shown with error bars of 1 standard deviation and folded on the photometric ephemeris.
Figure Adapated From Casares et al. (2014), A Be-type star with a black-hole companion, Nature, 505, 378, Springer Nature. Reproduced with permission from Springer Nature.

the companion star can partially block the X-ray emitting region, creating grazing eclipses. X-ray observations of eclipsing systems yield the orbital period, eccentricity, semi-major axis and duration of the eclipse, while optical observations provide the projected rotational velocity, velocity semi-amplitude and amplitude of ellipsoidal variations. Combining these observables in Equation 1.29 enable constraints on the NS mass and properties of the companion star.

1.3.2 Waveform Modelling

Modelling the periodic waveform modulations of pulsations or thermonuclear burst oscillations from either isolated (MSPs) or accreting NSs (AMXPs, bursters) provides constraints on the NS mass and radius because the waveform (see Figure 1.21) gets distorted by Doppler shifts from NS rotation and gravitational redshift (van Paradijs, 1979; Fujimoto & Taam, 1986; Sztajno et al., 1987; Poutanen & Gierliński, 2003; Riley et al., 2019; Miller et al., 2019).

MSPs are rotation-powered pulsars, so the observed emission is largely non-thermal and dominated by their magnetospheres. Despite this, several MSPs show a thermal component in the soft X-ray band (Grindlay et al., 2002; Zavlin, 2006; Zavlin, 2007; Bogdanov et al., 2006). Therefore, exploiting X-ray observations of MSPs can constrain the macroscopic properties of NSs. The observed waveform depends on the location and size of the hotspots, the beaming pattern of the emitted radiation and the angle between the observer's line of sight and the rotation axis. Such analysis first subtracts the non-thermal magnetospheric emission from the total observed emission to isolate the thermal components - the pulsar's hotspots (Miller et al., 2019; Riley et al., 2019). The hotspots are each modelled with a shape (e.g. circular or oval), size, temperature and surface location to recreate the observed waveform from the radiation beaming (Özel, 2013), typically assuming a hydrogen atmosphere (Zavlin, 2006; Bogdanov et al., 2007). In AMXPs, the thermal emission comes from the bases of the accretion columns. Here, the accretion column refers to the funnelling of accreted material along the NSs magnetic fields towards its magnetic poles. The material subsequently free-falls towards the NSs surface (the base of the accretion column), thus forming material columns at the NSs magnetic poles. The locations of these column bases wobble about the spin axis, enabling NS mass and radius measurements by modelling the observed modulation.

The amplitude and spectra of the waveform also depend on the NS's gravitational field, which determines the strength of the gravitational self-lensing experienced by the photons as they travel to an observer (Pechenick et al., 1983). Therefore, waveform modelling also probes the strong-gravity regime. Developing theoretical models for the gravitational fields of NSs leads to more precise calculations of the lensing effects on the surface photons used to analyse the waveform. Simple approximations for non-spinning NSs, supplemented with Doppler modulations, aberration effects (Miller & Lamb, 1998; Muno et al., 2002) and frame dragging (Braje et al., 2000) are reasonable, first order calculations for slower spinning pulsars. For AMXPs, fully numerical solutions for the gravitational effects are necessary (Cook et al., 1994; Cadeau et al., 2007; Psaltis & Özel, 2014), as is consideration of the NS's oblateness.

The mass and radius of PSR J0030+0451 were determined using modulated waveform modelling of data taken by *NICER*, shown in Figure 1.21. Riley et al. (2019) assume two distinct hot regions based on two pulsed components and explore several morphologies and topologies for each hotspot. They strongly favour a model in which both hotspots are in the same rotational hemisphere and hotspots with a temperature gradient. The inferred shape of the two hotspots are dramatically different - one is small and approximately circular, and the other is azimuthally extended and forms a narrow arc. Their inferred NS mass and radius are, respectively, $1.34^{+0.15}_{-0.16} M_{\odot}$ and $12.71^{+1.14}_{-1.19}$ km (Riley et al., 2019).

During type I X-ray bursts, periodic flux oscillations, originating from the NS surface (Strohmayer et al., 1996), arise from surface temperature non-uniformities during the nuclear burning stage of burst ignition (see Section 1.1.3 or Watts 2012). Modelling the profiles of these burst oscillations provides constraints on the NS's compactness (Strohmayer et al., 1997). Specifically, the amplitude of the burst oscillations, the deviations from a sinusoidal waveform, and the dependence on photon energy are the properties of the oscillation's profile that probe the NS's mass and

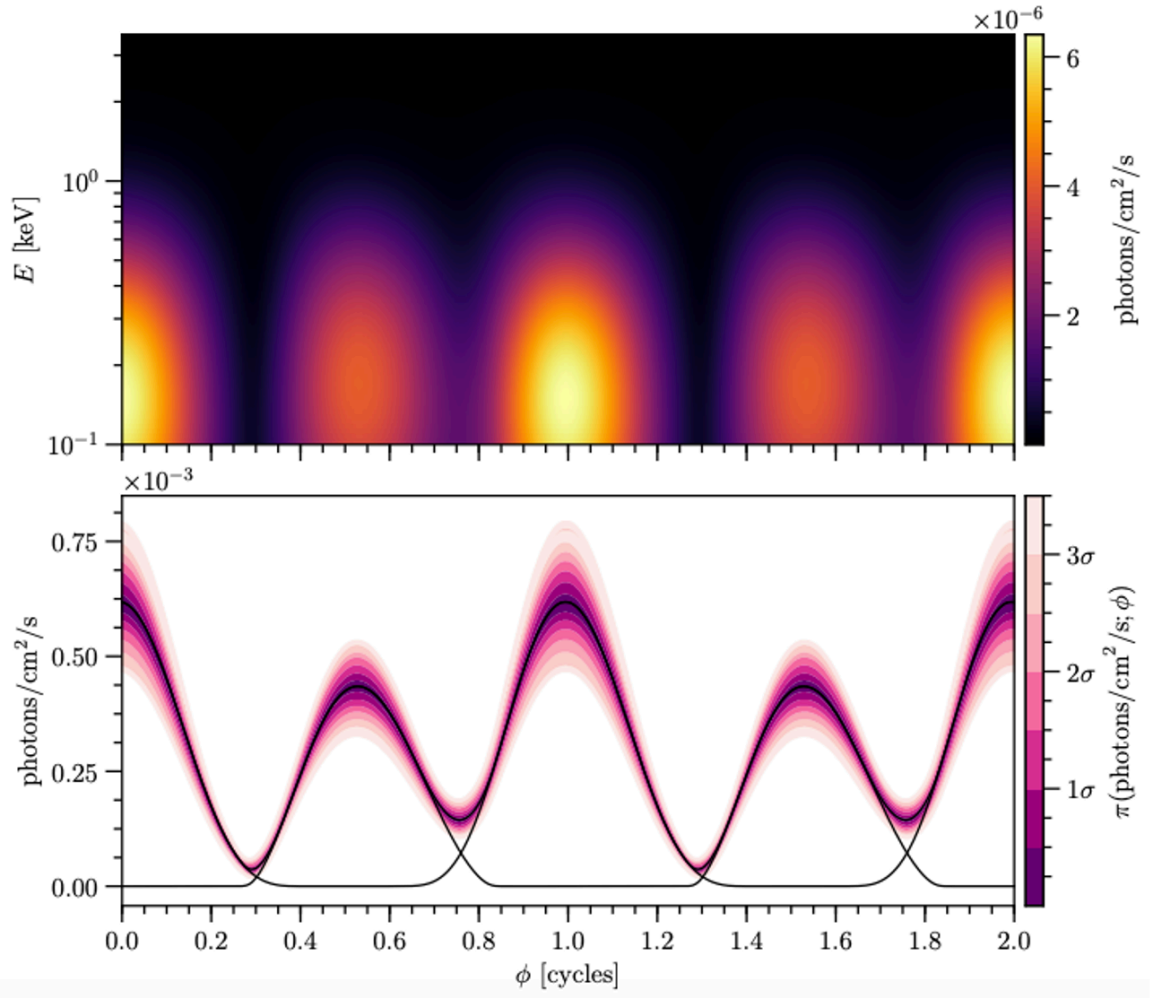

Figure 1.21: The expected modulated X-ray waveform from the X-ray pulsar PSR J0030+0451, incident on *NICER*, integrated over the linearly-spaced instrument energy intervals. The signal is effectively proportional to the specific photon flux. Top: The phase-dependent modulation as a function of photon energy. Bottom: the phase-dependent signal as a function of photon count rate.
Figure Adapated from Riley et al. (2019), A NICER View of PSR J0030+0451: Millisecond Pulsar Parameter Estimation, The Astrophysical Journal Letters, 887, L21, Dec 2019. ©AAS. Reproduced with permission.

radius.

1.3.3 Spectral Methods

Spectroscopic measurements of NS radii come from thermal flux measurements, obtained by modelling the spectrum of the source to determine the effective surface temperature, $T_{\rm eff}$. Combining this with a distance, D, we can calculate the apparent radius,

$$\frac{R_{\rm obs}}{D} = \left(\frac{F_{\rm bol}}{\sigma_B T_{\rm eff}^4}\right)^{\frac{1}{2}} \tag{1.30}$$

where σ_B is the Stefan-Boltzmann constant. However, there are several complications to this. Firstly, due to their extreme density, NSs gravitationally lens their surface emission, thus introducing mass-dependent corrections to their apparent radii (Pechenick et al., 1983; Psaltis et al., 2000). Therefore, the physical radius of a NS is related to the observed radius as,

$$R_{\rm obs} = R\left(1 - \frac{2GM}{Rc^2}\right)^{-\frac{1}{2}}, \tag{1.31}$$

providing that the radius is larger than the photon orbit ($3GM/c^2$). For spinning NSs, additional spin-dependent corrections to their angular size are necessary (Bauböck et al., 2015). Secondly, non-thermal emission from the NS's magnetosphere or its accretion disc contaminates the thermal NS surface emission. For NSs with strong magnetic fields, temperature non-uniformities on the surface can impact the inferred radius. Finally, determining distances to NSs is challenging and thus the distance is often not accurately known. Detailed modelling of the emission from NSs with full consideration of the general relativistic effects can mitigate some of the challenges associated with distance measurements. Alternatively, selecting a source that resides in a globular cluster of known distance avoids this complication. Combining multiple observations, thus breaking the inherent measurement degeneracies, can improve the reliability of spectroscopic mass and radius measurements.

For some MSPs, particularly those with short orbital periods, the companion star is optically bright, enabling reliable mass measurements for both components by analysing the Balmer lines produced by hydrogen in the companion star's atmosphere. The width of the Balmer lines depends on the local gravitational acceleration, $g = GM_{\rm CS}/R_{\rm CS}^2$. Phase-resolved spectroscopy measures the line shifts with the orbital phase, thus determining the projected orbital velocity, v. This projected velocity is related to the orbital velocity of the pulsar, $v_{\rm PSR} = 2\pi x/P$, determined through pulsar timing and subsequently the binary mass ratio, $q \equiv M_{\rm NS}/M_{\rm CS} = v/v_{\rm PSR}$. Reasonable assumptions regarding the relationship between the mass and radius of the companion are thus used to obtain q and $M_{\rm NS}$ from g. This is commonly used for pulsars with white dwarf companions (Callanan et al., 1998; Bassa, C. G. et al., 2006).

Spectral studies of thermonuclear X-ray bursts provide simultaneous measurements of NS mass and radius, generating valuable insights (Damen et al., 1990; Lewin et al., 1993; Özel, 2006; Güver et al., 2010b). In a subset of thermonuclear bursts, the luminosity reaches the Eddington luminosity such that the radiation forces exceed the gravitational forces and lift the photosphere off the NS surface. Characteristically, these photospheric radius expanion (PRE) bursts cause the photosphere to rise to several times the NS radius, raising the temperature in the process (Lewin et al., 1993). This characteristic behaviour enables measurements of NS radii through two methods. The first approach determines the apparent angular size of the NS during the decay phase of the PRE burst, using the cooling tail to constrain the mass-radius relation (van Paradijs, 1979; Nättilä, J. et al., 2017). The second approach breaks the degeneracy between the mass and radius using the spectral evolution of the source during the decay phase (Fujimoto & Taam, 1986; Damen et al., 1990; Özel, 2006).

Güver et al. (2010a) measured the apparent angular size of the NS in 4U 1608–52, using the flux and temperature obtained from time-resolved spectroscopy. They com-

bined these with the assumption that the NS's luminosity is exactly Eddington when the photosphere touches back down to the surface after expansion. The Eddington flux is related to the mass and radius of the NS as,

$$F_{\rm Edd} = \frac{GMc}{R^2\kappa_e}(1+z), \tag{1.32}$$

where $\kappa_e = \sigma_T N_e/\rho$ is the opacity. Here, σ_T is the Thomson cross-section, N_e is the electron number density, ρ is the gas density and $(1+z)$ is the gravitational redshift. Interpretation of the spectra of PRE bursts requires knowledge of the NS's atmospheric composition and a reliable measurement of the effective temperature. Any deviations from a black body spectra at the presumed effective temperature of the atmosphere are quantifiable by the colour correction factor, $f_c = T_c/T_{\rm eff}$ and incorporated into the spectral analysis. Further corrections to the angular size of the NS due to general relativistic effects arising from the rapid rotation rates of the NS, oblateness of the NS and rotational broadening of the thermal spectra are necessary and of the order of 10 per cent (Bauböck et al., 2015). The resulting mass and radius of the NS in 4U 1608–52 were $1.74^{+}_{-}0.14 M_\odot$ and $9.3^{+}_{-}1.0$ km, respectively, which can be achieved by many EoS.

The second approach obtained radius measurements from the spectral evolution of the colour correction factor during PRE bursts (Majczyna & Madej, 2005; Suleimanov, V. et al., 2011). The spectral distribution depends on the effective surface gravity of the NS and the emitted flux. Thus, the colour correction factor changes with luminosity as the burst cools, providing a measurement of the NS mass and radius. However, the resulting radii are often unreliable and heavily limited by the quality of the available data and sampling rate. For example, the application of this method to 4U 1728–34 (Majczyna & Madej, 2005) resulted in radius measurements that are far too small and incompatible with measured NS masses and EoS possibilities.

Chapter 2

The X-ray TRansit and EClipse Model (X-TREC)

2.1 Introduction

Observations of XRBs enable the development of binary evolution models (Steiner et al., 2010; Podsiadlowski, 2014; Postnov & Yungelson, 2014; Providência, 2019) and the study of accretion processes (Done, 2014; Zhang et al., 2014; Ponti et al., 2014). Studying NS LMXBs, in particular, provides an opportunity to constrain the EoS of matter at extreme densities. Since the EoS (the pressure-density relation) uniquely predicts the NS mass-radius relation (Section 1.1.1; Lindblom 1992, Voisin et al. 2020), it can be constrained from measurements of the mass and radius of astrophysical NSs. The NS mass alone can be highly constraining as each EoS predicts a maximum possible NS mass, which informs stellar evolution models (Antoniadis et al., 2016; Sukhbold et al., 2018; Raithel et al., 2018) and the interpretation of gravitational wave observations (Yang et al., 2018; Essick & Landry, 2020; Chen & Chatziioannou, 2020).

Several methods are employed to infer the masses of astrophysical NSs (see Section 1.3 for an overview). However, observations of eclipsing NS X-ray binaries are fundamental when determining the NS EoS and the maximum NS mass. In these systems, periodic X-ray eclipses occur by the occultation of the X-ray emitting region by

the companion star (Cominsky & Wood, 1984; Parmar et al., 1986). Eclipses demand a sufficiently high binary inclination, but determining the exact inclination requires knowledge of the binary mass ratio, $q = M_{\rm cs}/M_{\rm ns}$, and the physical properties of the companion star. The mass ratio further dictates the minimum inclination for which eclipses are observable. Fortunately, we can disentangle the binary inclination, i, and q if the system undergoes X-ray eclipses since they are related via the duration of totality if the companion star is filling its Roche-Lobe (Horne, 1985). Therefore, the NS mass in an eclipsing system is determined using measured values of i and q within the binary mass function, Equation 1.29. X-ray eclipse mapping is the modelling technique that does exactly this and produces precise, self-consistent measurements of q, i and the totality duration, t_e (Knight et al., 2022a,b).

This chapter is adapted from Knight et al. (2022a), Knight et al. (2022b) and Knight et al. (2023), in which we describe the details of our XSPEC compatible eclipse mapping model for X-ray eclipses and its applications. The X-ray TRansit and EClipse model, X-TREC, is publically available [1] and is unique in its consideration of companion star outflows, thus providing a way to probe stellar outflows and investigate ablation and irradiation processes (Knight et al., 2022b,a). As such, X-TREC can capture the shape and duration of the ingress, egress and totality, even for extended and asymmetric X-ray eclipse profiles. Ultimately, accurate eclipse models reduce the propagated uncertainty on subsequent NS mass measurements leading to invaluable constraints on the NS EoS.

2.2 X-TREC Version 1.0

The initial release of X-TREC assumes a point-like X-ray source is in orbit with a secondary star exhibiting a stellar wind or material outflow. An X-ray point source is a reasonable assumption since it will be indistinguishable from an extended source

[1] https://xtrec.bitbucket.io/

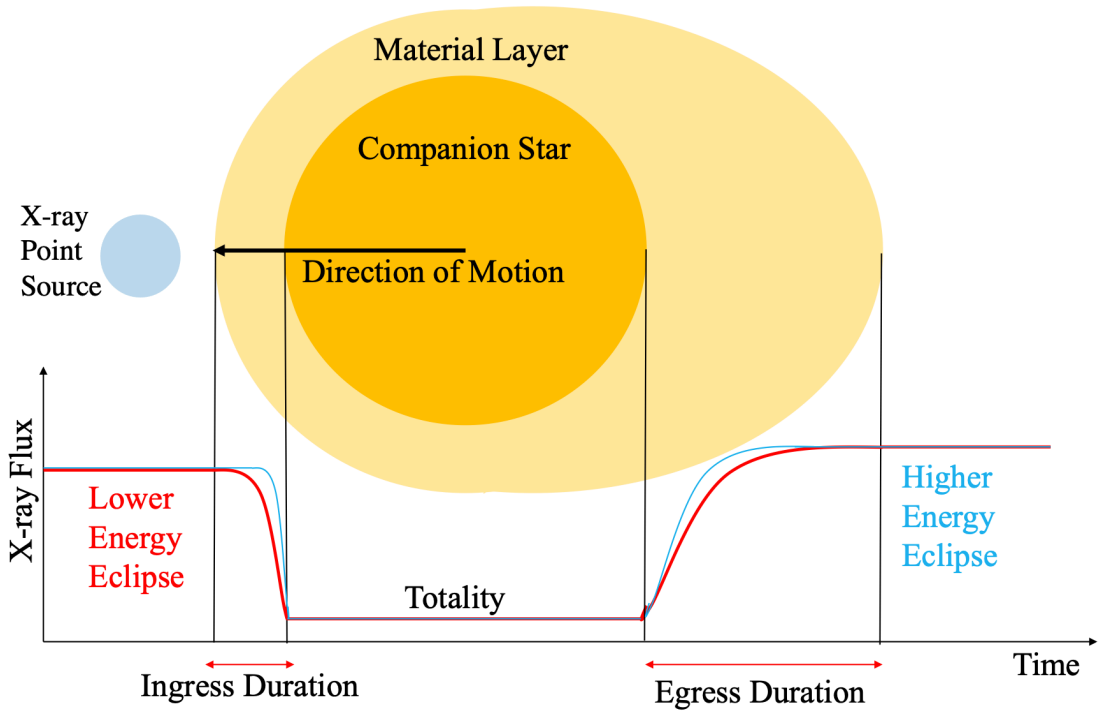

Figure 2.1: A schematic of showing how X-TREC models energy dependent and asymmetric X-ray eclipses profiles. The compact object and accretion disc are modelled as an X-ray point source. The eclipses are the occulation of the X-ray point source by the companion star and surrounding material. This diagram is not to scale.

unless it has a diameter exceeding a few hundred kilometres. In this scenario, the outflowing material, which is optically thin, is the first structure to obscure the view of the X-ray source from the observer. Only a fraction of the X-rays emitted by the source are absorbed, creating a gradual transition into the eclipse (ingress). Typically softer X-rays are absorbed more efficiently than the hard X-rays at the start of the ingress. The column density of our sightline through the outflow increases with proximity to totality until the material is effectively optically thick - this is totality. The gradual transition is mirrored for the egress as the harder X-rays emerge first. Figure 2.1 depicts this and shows how an asymmetric eclipse may form. Here it is assumed that the companion star's outflow trails behind the companion star as it orbits such that the egress is longer than the ingress, which is common in many X-ray eclipses (Wolff et al., 2009; Parmar et al., 1991).

2.2.1 Geometry

Consider a perfectly circular binary system with orbital period, P, separation, a, and inclination angle to the observer, i. For a given orbital phase, $\phi = (2\pi/P)(t - t_0)$, where t_0 is the time of superior conjunction, the projected distance on the image plane between the X-ray point source and the centre of the companion star is,

$$b_\star(\phi) = a\sqrt{1 - \sin^2 i \ \cos^2 \phi}. \tag{2.1}$$

It is convenient to define all distances in units of the companion star's radius, $R_{\rm cs}$: $x \equiv r/R_{\rm cs}$. In these units, the companion star radius is at $x = 1$ and the outer radius of the outflow is at $x = x_{\rm out}$. The *impact parameter*, $b_\star$, in units of $R_{\rm cs}$ ($b \equiv b_\star/R_{\rm cs}$) is,

$$b(\phi) = \frac{a}{R_{\rm cs}}\sqrt{1 - \sin^2 i \ \cos^2 \phi}. \tag{2.2}$$

Assuming the companion star is filling its Roche Lobe, the ratio $R_{\rm cs}/a$ is (Horne 1985; Ratti et al 2012),

$$\frac{R_{\rm cs}}{a} = h(q) = \frac{0.49q^{2/3}}{0.6q^{2/3} + \ln(1 + q^{1/3})}. \tag{2.3}$$

The *eclipse condition*, thus follows from Equations 2.2 and 2.3,

$$\left(\frac{R_{\rm cs}}{a}\right)^2 = h(q)^2 = 1 - \cos^2\left(\frac{\pi t_e}{P}\right) \ \sin^2 i, \tag{2.4}$$

and we can calculate the inclination angle from the above equations as,

$$\sin i = \frac{\sqrt{1 - h(q)^2}}{\cos(\pi t_e/P)}. \tag{2.5}$$

The model is, therefore, independent of $M_{\rm NS}$ and does not depend on a or $R_{\rm cs}$, only on the ratio $R_{\rm cs}/a$. Therefore, for known $t_{\rm e}$, P and t_0, the only parameter required to calculate $b(t)$ is q.

2.2.2 Companion Star Outflow

We assume a spherically symmetric companion star with a radial hydrogen number density profile $n_\star(r)$. The photospheric radius of the companion is $R_{\rm cs}$, defined such that in the region $r < R_{\rm cs}$, $n_\star(r)$ is large enough for the optical depth to be effectively infinite. Therefore, totality occurs whenever the projected separation between the centre of the companion star and the X-ray point source is less than $R_{\rm cs}$ on the image plane. The *impact parameter*, $b(t)$, is defined as this projected separation in units of $R_{\rm cs}$, which means that totality occurs for all times when $b(t) \leq 1$. For $b(t) > 1$, we compute the hydrogen column density for a sight line through the outflowing material as

$$\mathrm{N_H(t)} = \int_{-\infty}^{+\infty} \mathrm{n_\star(r)ds}. \tag{2.6}$$

Here, s is the distance a ray has travelled along a given sight line, and $s = 0$ occurs when the ray passes closest to the centre of the companion star. Thus, a ray travelling along a sight line that starts behind the star and points towards the observer extends from $s = -\infty$ to $s = +\infty$, and it can be shown that $(s/R_{\rm cs})^2 = x^2 - b^2$. Therefore, re-write the above integral as

$$\mathrm{N_H(t)} = 2\mathrm{N_{H,0}} \int_{\mathrm{b(t)}}^{\mathrm{x_{out}}} \mathrm{n(x)} \frac{\mathrm{x}}{\sqrt{\mathrm{x^2 - b^2(t)}}} \mathrm{dx}, \tag{2.7}$$

where $n(x) \equiv n_\star(r)/n_0$ such that $n_0 = n_\star(r = R_{\rm cs})$ and $N_{\rm H,0} = R_{\rm cs} n_0$ is the column density of a sight-line of length $R_{\rm cs}$ through material with constant density n_0. Here, the outermost radius of the absorbing medium with non-negligible density is $x_{\rm out}$.

Within X-TREC, there are currently five options for the radial density profile, $n(x)$, of the outflowing material. The first option assumes no outflow from the companion star and envokes a sharp transition between out-of-eclipse and totality. The second is a power law model,

$$n(x) = x^{-m}, \tag{2.8}$$

typically used to model weak stellar winds from low or intermediate-mass stars. Setting $m = 2$ in Equation 2.8 corresponds to a stellar wind with constant velocity. The third is a radial density profile corresponding to an accelerating wind (Puls et al., 2008),

$$n(x) = x^{-2}\ (1 - x^{-1})^{-\beta}, \tag{2.9}$$

where β is a parameter that describes the acceleration. This radial density profile is most applicable to HMXBs as massive stars, like those of OB spectral type, are required to drive these fast-flowing stellar winds. In this case, the constant $N_{\mathrm{H},0}$ from Equation 2.7 is related to the mass loss rate of the wind, $\dot{M}_{\mathrm{out}}$, as:

$$N_{H,0} = \frac{\dot{M}_{\mathrm{out}}}{4\pi\bar{m}\sqrt{GM_{\mathrm{cs}}R_{\mathrm{cs}}}}, \tag{2.10}$$

where $\bar{m}$ is the mean molecular weight of the wind material. Note that $\beta \leq 1.0$ is typical for an OB star (Puls et al., 2008).

In LMXBs, the low-mass companion star is unlikely to launch a stellar wind. As such, an extended or bloated stellar atmosphere may be a more appropriate outflow model. For these cases, we include a Gaussian radial density profile, characterised by the fractional width of the material layer, Δ. This profile is a steeper function of distance than the two stellar wind profiles, as the density of the outflow must increase rapidly over a comparatively short distance. We express this form of density profile as:

$$n(x) = \exp\left[-\frac{(x-1)^2}{2\Delta^2}\right], \tag{2.11}$$

The fifth option is an exponential radial density profile which describes an outflow driven by incident irradiation liberating the outer layers of the companion star. Hereafter this is referred to as X-ray-driven ablation or an ablated outflow and is expected to occur in short-period binaries since the incident flux from the compact object onto the companion star will have a greater effect than in wider binaries. This

profile is given as

$$n(x) = \exp\left[\frac{1-x}{h}\right], \tag{2.12}$$

where h is the scale height of the material in units of $R_{\rm cs}$. Therefore, the column density of the outflowing material as a function of time through the eclipse transitions $\mathrm{N_H(t)}$ can be calculated by assuming an appropriate radial density function, $n(x)$, with q as the only other model parameter.

As illustrated in Figure 2.2, each radial density profile behaves differently as a function of column density and time through the eclipse transitions. Therefore, for eclipsing systems in which the nature of the companion star outflow is unknown, X-TREC acts as a fantastic diagnostic tool for inferring the origin of any outflowing material in these systems.

2.2.3 Absorption and Scattering Model: ABSSCA

Photons originating from the X-ray source can be absorbed and scattered by the material outflowing from the companion star. Similarly, the scattering can be both into and out of the line of sight. The effect of photons scattered into the line of sight is typically negligible since the material outflowing from the companion star likely subtends a small solid angle according to the X-ray source. This is in contrast to the commonly considered case of a spherical shell of absorbing material surrounding a central X-ray source, in which photons scattered into the line of sight will exactly cancel those scattered out of the line of sight. To account for these interactions, we introduce a local XPSEC model called ABSSCA, required by X-TREC to model eclipse transitions in systems where a stellar outflow is present but can be used separately for spectral modelling (Knight et al., 2022a,b).

Within ABSSCA, the total transmitted specific intensity, when considering absorption and scattering, is given as

$$I_{\rm E} = I_{\rm E}^{0}\Big\{\mathrm{f_{cov}}\exp\{-\mathrm{N_H}[\sigma(E) + (\mathrm{n_e}/\mathrm{n_H})\sigma_{\rm T}]\} + 1 - \mathrm{f_{cov}}\Big\}, \tag{2.13}$$

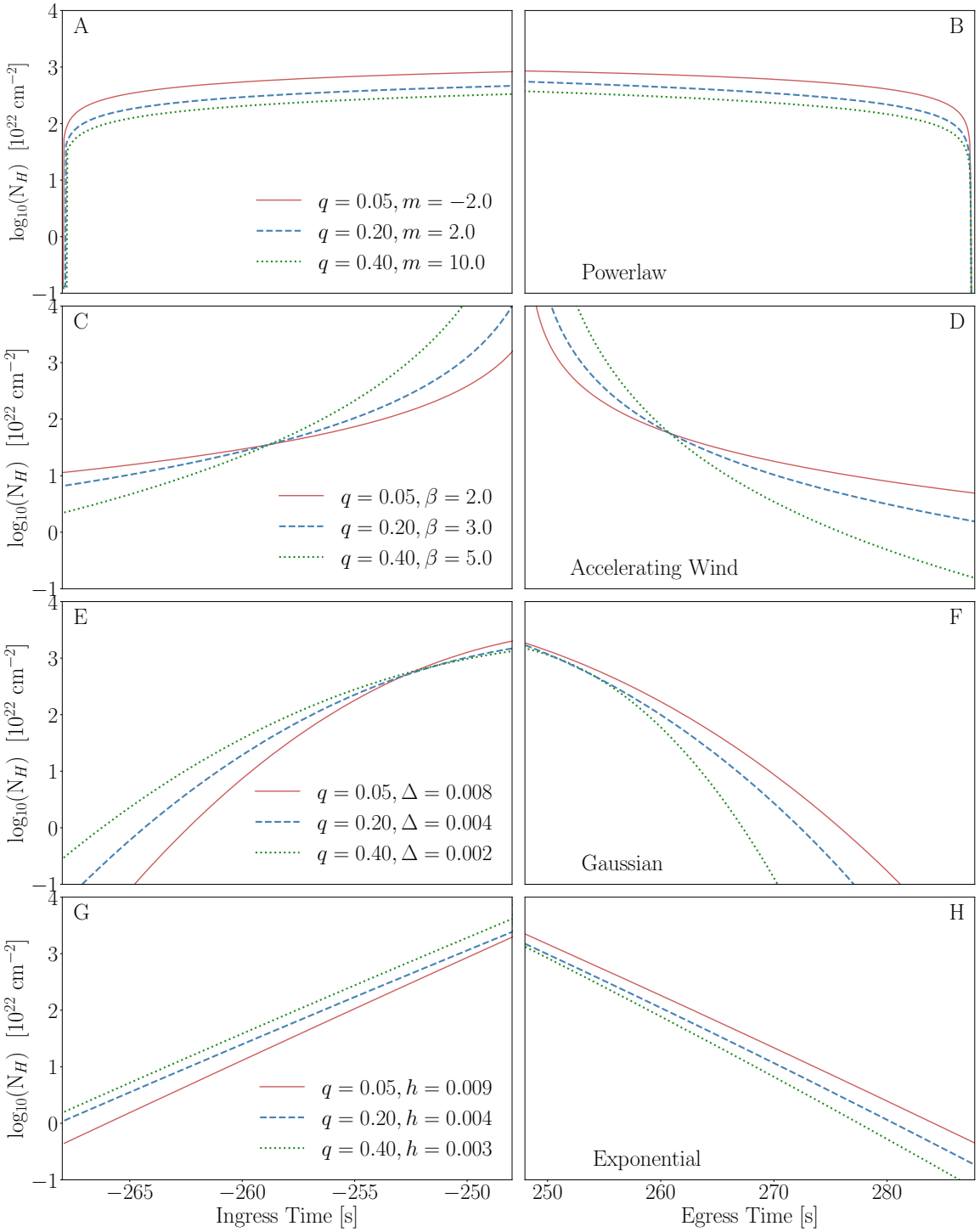

Figure 2.2: The coulumn density as function of time through the ingress and egress for each of the four material radial density profiles available within X-TREC. For each profile, three combinations of characteristic parameter and binary mass ratio are selected to demonstrate the profile's behaviour.

where $I_{\rm E}^0$ is the out-of-eclipse specific intensity, predetermined from a fit to the out-of-eclipse spectrum of the source. The covering fraction is $\rm f_{cov}$, $\rm N_H$ is the material hydrogen column density. $\sigma_{\rm T}$ is the Thomson electron scattering cross-section, and $\sigma(E)$ is the absorption cross-section, calculated using the XSPEC model ZXIPCF (Miller et al., 2006) and depends on the ionization parameter, $\xi = L/(nR^2)$, where L is the luminosity of the irradiating source, n is the number density of the irradiated material and R is the distance between the source and the irradiated material. The ratio of free electrons to hydrogen nuclei in the material is $\rm n_e/n_H$ and the redshift is z.

The three model parameters introduced by ABSSCA each create a subtly different change to the spectra and can be used to infer properties of the material and diagnose its origin. The material hydrogen column density, $N_{\rm H}$, alters the transmission factor such that higher values of $N_{\rm H}$ increase the material optical depth by an energy-independent factor. Since the absorption cross-section typically decreases with energy, increasing $N_{\rm H}$ tends to suppress soft X-rays. The log of the ionization parameter, $\log(\xi)$, impacts the number of bound atomic species in the absorber, thus impacting the energy dependence of the absorption cross-section. The covering fraction, $\rm f_{cov}$, changes the absorption fraction such that lower covering fractions allow more photons to pass through and increase the spectrum's peak. These effects are depicted in Figure 2.3, where we notice how slight each is. Therefore, partial parameter degeneracies must be investigated when using ABSSCA in spectral fitting, outside of X-TREC (see Knight et al. 2023 for further details).

2.2.4 Eclipse Profile Model

The time dependent specific photon flux, $S(E,t)$, is the product of an energy dependent transmission factor, $\alpha(E)$, and the out-of-eclipse spectrum, $S_0(E)$. Our absorption and scattering model ABSSCA (Knight et al., 2022a) is used to calculate $\alpha(E)$ (not to be confused with the absorption coefficient), thus introducing the ionisa-

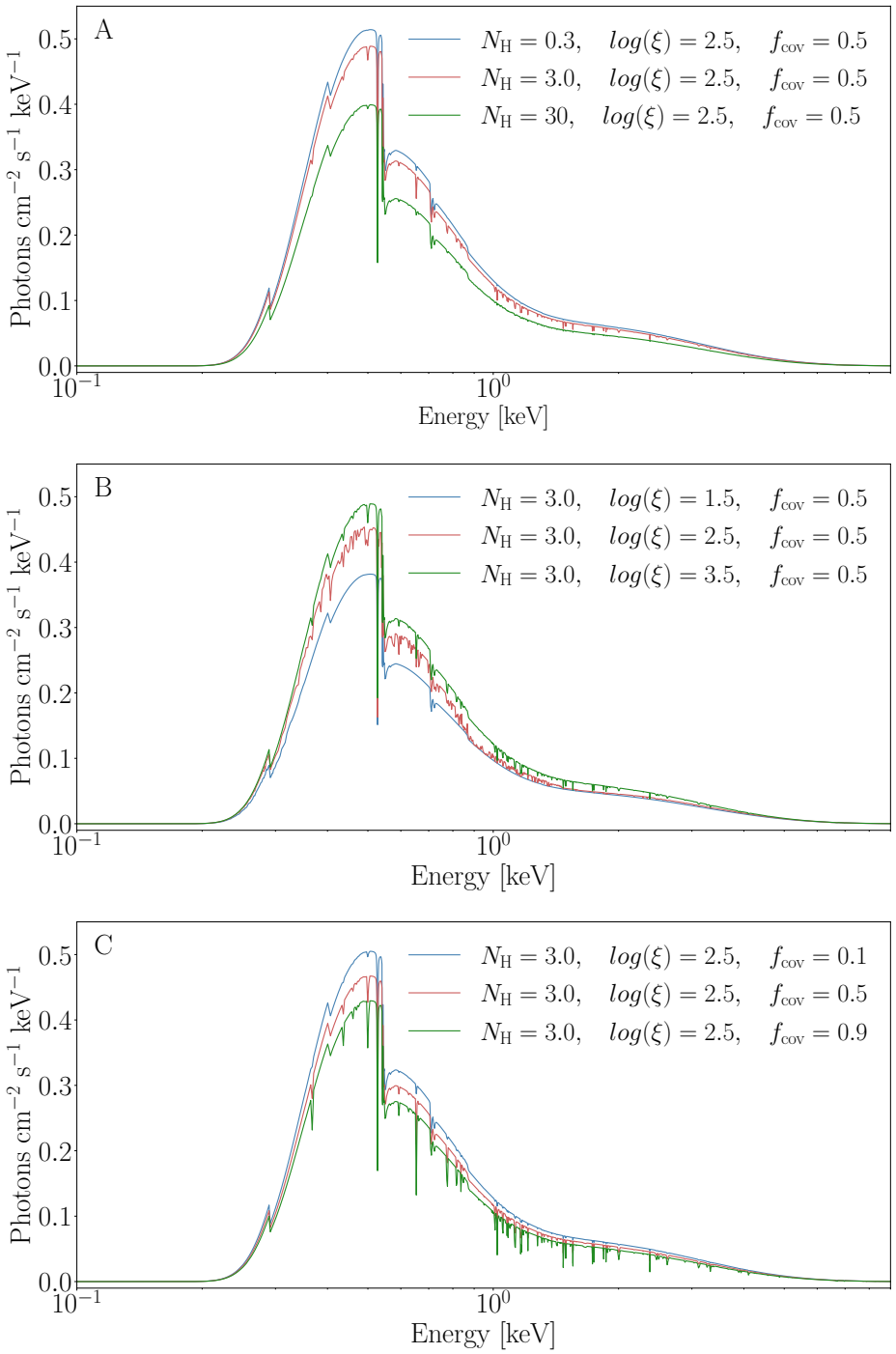

Figure 2.3: The transmitted spectrum of a typical neutron star X-ray binary when photons from the X-ray source are intercepted by outflowing material of with different properties. The emitted spectrum is formed from a blackbody from the neutron star's surface, a multi-temperature blackbody from the accretion disc and a comptonised component from the corona. The properties of the outflowing material considered are the material covering fraction f_{cov}, the hydrogen column density, N_H, and the log of the ionisation $\log(\xi)$.

tion parameter (ξ) and covering fraction (f_{cov}) as properties of the companion star's outflow. These material properties are model parameters, and their values for the ingress ($t < t_0$), ξ_{in} and $f_{cov,in}$, are allowed to be different from those corresponding to the egress ($t > t_0$), ξ_{eg} and $f_{cov,eg}$. We calculate column density as a function of time $N_H(t)$, from Equation (2.7), which depends on mass ratio, q, the *surface column density*, $N_{H,0}$, and an assumed parameterisation of the stellar radial density profile, $n(x)$. Each form of $n(x)$ is characterised by a key parameter: the power-law index, m, for the power-law profile, the acceleration parameter, β, for the accelerating wind profile, the fractional width of the outflowing material, Δ, for the Gaussian profile and the apparent scale height of the outflowing material, h, for the exponential profile. Each characteristic parameter can take different values for the ingress and egress to enable the modelling of eclipse asymmetries. The integral in Equation (2.7) is only calculated for orbital phases with $1 \leq b(\phi) \geq x_{out}$, since $b(\phi) < 1$ corresponds to totality and $b(\phi) > x_{out}$ to out-of-eclipse. The orbital period, P, is often known for eclipsing systems and can be set before fitting, while the totality duration t_e should remain a free model parameter. Finally, we correct the time-dependent count rate for the instruments' energy response. For example, the time-dependent count rate in an energy range translated to channels ranging from I_1 to I_2 is

$$C(I_1, I_2, t) = \int_0^\infty A_{\text{eff}}(E, I, I_2)\ S(E, t)\ dE, \tag{2.14}$$

where

$$A_{\text{eff}}(E, I_2, I_2) = \sum_{I=I_1}^{I_2} R_D(I, E), \tag{2.15}$$

is the effective area of the combined instrument channels I_1 to I_2 (analogous to a photometry filter), and $R_D(I, E)$ is the effective area of channel I, commonly referred to as the *instrument response* (see Rapisarda et al. 2016). In practice, the instrument response is quantised into the response matrix stored in the rmf and arf files produced during data reduction and is read into X-TREC. For convenience when fitting, both

the data and model in each energy band are divided by the mean out-of-eclipse count rate such that the out-of-eclipse count rate is approximately 1.0 and the totality level is close to 0.0.

2.3 X-TREC Version 2.0

The initial release of X-TREC (version 1.0), which I implement throughout this thesis, assumes circular binary orbits. However, this is not always a valid assumption (Zasche, P. et al., 2021). Thus, it is prudent to enable the modelling of eclipses exhibited by eccentric XRBs, especially since the binary mass function depends on the binary's orbital eccentricity (Orosz et al., 2007). This section details the ongoing updates to the geometric formalism required to include non-zero eccentricities within X-TREC and is intended for release later this year.

2.3.1 Eccentric Orbits

If there is a non-zero eccentricity, the impact parameter becomes

$$b(\phi) = \frac{r_a(\phi)}{R_{\rm cs}}\sqrt{1 - \sin^2 i \cos^2 \phi_*}, \tag{2.16}$$

where $\phi_* \equiv \phi - \phi_0$. At the pericenter, the orbital phase is $\phi = 0$ and at the centre of the eclipse, $\phi = \phi_0$. The new model parameters are the orbital phase at the centre of totality, ϕ_0, and the orbital eccentricity ϵ. The separation now depends on the orbital phase as

$$r_a(\phi) = \frac{a(1-\epsilon^2)}{1 + \epsilon\cos\phi}. \tag{2.17}$$

What happens to the Roche potential in an eccentric orbit is unclear. Therefore, we make the simple assumption that the ratio $h(q) = R_{\rm cs}/r_a(\phi)$ stays constant. In this case, the eclipse condition becomes

$$\sin i = \frac{\sqrt{1-h^2(q)}}{\cos\phi_*(t_{\rm eg})} = \frac{\sqrt{1-h^2(q)}}{\cos\phi_*(t_{\rm in})}, \tag{2.18}$$

where $\phi_*(t_{\rm in})$ is the value of $\phi_* = \phi - \phi_0$ at the start of totality and $\phi_*(t_{\rm eg})$ is the same at the end of totality. We see that we still have the symmetry in terms of orbital phase such that $\phi_*(t_{\rm in}) = -\phi_*(t_{\rm eg})$ with the centre of totality at $\phi_* = 0$. Where we *lose* symmetry is in time: $t_0 - t_{\rm in}$ is no longer necessarily equal to $t_{\rm eg} - t_0$, where t_0 is the time at the centre of totality. The method for determining $N_H(t)$, the column density of the outflowing material as a function of time through the eclipse transitions, will also be modified.

To determine ϕ, we make the first-order approximation that the angular velocity of the orbit does not change very much during the eclipse, which allows us to set the orbital angular velocity as a constant equal to its value at the eclipse centre:

$$\frac{d\phi}{dt} \approx \frac{d\phi}{dt}(\phi = \phi_0) = \frac{[1 + \epsilon\cos\phi_0]^2}{[1-\epsilon^2]^{3/2}}\frac{2\pi}{P}. \tag{2.19}$$

We can therefore write

$$\phi_*(t) \approx \frac{[1 + \epsilon\cos\phi_0]^2}{[1-\epsilon^2]^{3/2}}\frac{2\pi}{P}(t - t_0) \tag{2.20}$$

and

$$\phi_{\rm eg} \approx \frac{[1 + \epsilon\cos\phi_0]^2}{[1-\epsilon^2]^{3/2}}\frac{\pi}{P}t_e. \tag{2.21}$$

Subsequently, the eclipse condition becomes,

$$\sin i = \frac{\sqrt{1 - h^2(q)}}{\cos(\phi_{\rm eg} - \phi_0)}. \tag{2.22}$$

For zero eccentricity X-TREC reverts to the more computationally efficient geometry routine described in Section 2.2.1.

A more exact implementation determines the impact parameter, $b(t)$, from Equation (2.16). This requires a solution to

$$t - t_0 = \frac{P}{2\pi}f(\epsilon, \phi), \tag{2.23}$$

where

$$f(\epsilon,\phi) \equiv \left\{\frac{-\epsilon\sqrt{1-\epsilon^2}\sin\phi}{1+\epsilon\cos\phi} - 2\arctan\left[-\sqrt{\frac{1-\epsilon}{1+\epsilon}}\tan(\phi/2)\right]\right\}, \tag{2.24}$$

such that ϕ is known. This is achieved by calculating the eclipse profiles on a ϕ grid and re-binning onto a given time grid, using linear interpolation. Alternatively, we can numerically solve Equation 2.23 for each time interval across the eclipse profile. While these approaches are under development, we utilise the above first-order approximation for eccentric orbits (Equations 2.19 - 2.22).

Chapter 3

Eclipse Mapping of the X-ray Binary EXO 0748 − 676

This chapter, adapted from Knight et al. (2022a), models the X-ray eclipse profiles of the NS LMXB EXO 0748–676 in multiple energy bands, using archival *XMM-Newton* data and X-TREC version 1.0. Modelling the energy-dependent eclipse profiles EXO 0748–676 requires a narrow and asymmetric layer of absorbing material to surround the companion star. This outflow, driven by X-ray irradiation, appears consistent with EXO 0748–676 being a transitional redback system. Finally, I utilise prior radial velocity measurements to constrain $M_{\rm NS}$ using my measured value of q.

3.1 The History of EXO 0748 − 676

In 1985, EXO 0748–676 entered an accretion-powered X-ray outburst phase enabling its discovery by the European X-ray Observatory Satellite (*EXOSAT*) (Parmar et al., 1986). EXO 0748–676 remained in X-ray outburst for ~ 24 years before entering X-ray quiescence in late 2009 (Degenaar et al., 2011). During its outburst, EXO 0748–676 was regularly monitored by the Rossi X-ray Timing Explorer (*RXTE*) (Wolff et al., 2009) and the X-ray Multi-Mirror Misson (*XMM-Newton*). These observations uncovered eclipses lasting $t_e \approx 500$ s that recur on the orbital period of $P = 3.824$ hrs (Parmar et al., 1986; Wolff et al., 2009). These X-ray eclipses arise from the occultation of the NS and accretion disc by the $\sim 0.4 M_{\odot}$ M-dwarf companion (Parmar

et al., 1991) and are known to vary greatly in duration on both long and short timescales (Parmar et al., 1991; Wolff et al., 2009; Knight et al., 2023). Specifically, the ingress, egress and totality durations are all observed to vary between successive orbits, with the ingress and egress durations ranging from less than 1.0 s more than 30 s (Parmar et al., 1991; Knight et al., 2023).

The discovery of Type I X-ray bursts from EXO 0748–676 confirmed that the accretor is a NS (Galloway et al., 2010), and the subsequent detection of Type I burst oscillations revealed the NS's spin frequency to be within a few Hertz of the measured 552 Hz burst oscillation frequency (Galloway et al., 2010). To date, no searches for X-ray or radio pulsations at this frequency are published. The determination that EXO 0748–676 is a NS LMXB prompted multiple investigations into the mass and radius of the NS. Özel (2006) used PRE bursts (e.g. Wolff et al. 2005) to estimate the mass and radius of the NS to be $M_{\rm NS} = 2.10 \pm 0.28\ M_{\odot}$ and $R_{\rm NS} = 13.8 \pm 1.8$ km respectively. The authors subsequently showed that these values rule out softer equations of state for nuclear matter. Once EXO 0748–676 entered quiescence, the opportunity arose for this high NS mass to the confirmed dynamically. While absorption lines have never been detected directly from the companion star's surface, irradiation-driven emission lines have been observed and are found to be modulated on the orbital period (Pearson et al., 2006; Muñoz-Darias et al., 2009; Bassa et al., 2009). The radial velocity curve of such emission lines can thus provide a lower limit on the binary mass function since they originate from somewhere between the companion star and the binary system's centre of mass (Munoz-Darias et al., 2005). The resulting lower mass limit is $M_{\rm NS} > 1.27\ M_{\odot}$, which was determined by Bassa et al. (2009) using doppler tomography of the H_{α} emission line observed in their optical spectra. Similarly, Muñoz-Darias et al. (2009) used Doppler tomography on the broad He II feature, which originates from the irradiated face of the companion star to measure a radial velocity of $K_{\rm em} = 300$ km/s and constrain the mass of the NS to be $M_{\rm NS} > 1.50\ M_{\odot}$,

assuming the companion star is on the main sequence.

Ratti et al. (2012) attempted to constrain the binary mass ratio, q, by measuring the width of the phase-resolved companion star emission lines. Under the assumption that the star is tidally locked, fills its Roche-Lobe and that the width results entirely from rotational broadening, q can be derived from the line width and radial velocity (Wade & Horne, 1988). However, the emission lines were found to be much broader than expected, requiring a $> 3.5\ M_{\odot}$ NS, if rotational broadening dominates. Instead, they concluded that a stellar outflow, driven by a pulsar wind and/or X-ray heating, likely contributed to the extra broadening. The presence of a stellar outflow can also explain the lack of emission lines observed from an accretion disc one year into quiescence because the evaporation of material during extended outburst periods results in the lack of disc material, and thus emission lines (Ratti et al., 2012). It is worth noting that a non-detection of disc emission lines is incredibly unusual for LMXBs (Marsh et al., 1994).

A similar X-ray-induced evaporative wind was considered for EXO 0748–676 by Parmar et al. (1991) before this, to explain the aforementioned, drastic variability in the ingress and egress durations. Parmar et al. (1991) suggested that an X-ray-induced evaporative wind is required to sufficiently extend the eclipse transition durations, since the atmospheric scale height of the assumed main sequence companion would be $\sim$ 100 km, and have a negligible impact on the eclipse transitions. Additionally, the pulsar wind hypothesis is supported by the detection of a broad C IV emission line by Parikh et al. (2021), who draw similarities between their quiescent observations of EXO 0748–676 and the known transitional redback pulsar, PSR J1023+0038 in its rotation powered state. These scenarios are all reminiscent of so-called spider pulsars – radio MSPs with an under-massive companion star that is in the process of being ablated by an ionising pulsar wind. Therefore, if the ablation of the companion star begins in the accretion-powered LMXB binary phase, EXO

0748–676 may be a transitional redback pulsar [1]. Therefore, it is clear that understanding the companion star's outflow and improving the measurement of the binary mass ratio is necessary to advance our understanding of EXO 0748–676 and, more broadly, the evolution of short-period LMXBs.

3.2 Data Reduction and Analysis

We consider one archival *XMM-Newton* observation of EXO 0748–676 taken in April 2005 (Obs-ID 0212480501) when the source was in the soft spectral state (Ponti et al., 2014). The soft X-ray coverage offered by *XMM-Newton* enables us to test models of absorption in any structure surrounding the companion star. During the observation, the EPIC-pn (European Photon Imaging Camera) was in timing mode and captured four full X-ray eclipses (with a total exposure of 42.48 ks). Here we describe the data reduction procedure followed and our initial spectral and timing analysis.

3.2.1 Data Reduction

We used the *XMM–Newton* Science Analysis Software (SAS) version 18.0 to reduce data from the EPIC-pn in timing mode. We generated calibrated and concatenated event lists using EPPROC with the default settings for timing mode as of SAS v18.0 (`runepreject=yes withxrlcorrection=yes runepfast=no withrdpha=yes`). We filtered the event list for flaring particle background using the SAS routine ESPFILT, and barycentered using BARYCEN. The ingress of the first eclipse is heavily interrupted by the flaring particle background and is therefore filtered out. Two egresses are also impacted by this flaring, although this does not result in the total loss of either egress. We applied further standard filters to ignore bad pixels (`FLAG==0`), housekeeping events (`#XMMEA_EP`) and keep only single and double events (`PATTERN`

[1] Ratti et al. (2012) labelled EXO 0748–676 as *black widow - like* but, as was noted by Parikh et al. (2021), the name *redback-like* would have been more appropriate given the likely companion mass.

$\leq$ 4). For all products, we used a source region of 31 $\leq$ RAWX $\leq$ 45, all RAWY; and a background region of 3 $\leq$ RAWX $\leq$ 5, all RAWY. We extracted spectra and light curves using EVSELECT and generated response and ancillary files using RMFGEN and ARFGEN. We re-binned all spectra to have at least 25 counts per channel using SPECGROUP. We find that the source contributes 99.4 per cent of the total counts. We extracted light curves with 1 second time binning for a range of different energy bands: $0.2-10.0$ keV, $0.4-1.0$ keV, $1.0-2.0$ keV, $2.0-4.0$ keV, $4.0-6.0$ keV and $6.0-8.0$ keV. Since the source dominates over the background, we do not perform a background subtraction for the light curves. We consider the calibration accuracy of the instrument in timing mode, concluding that our time-domain analysis in broad energy ranges will be robust to any effects.

3.2.2 Eclipse Profiles

We fold the extracted light curves on the orbital period of 3.824 hours and divided through by the mean out-of-eclipse count rate. Figure 3.1 shows the resulting eclipse profiles that are normalised to have an out-of-eclipse count rate of 1.0 and a totality level of 0.0. The full $0.2-10.0$ keV band eclipse profile (Figure 3.1A) shows an initially gradual decline towards totality between the normalised count rate $0.8-1.0$ ct/s. This behaviour is mirrored in the egress, which shows a gradual rise out of totality between the normalised count rate $0.8-1.0$ ct/s. Figure 3.1B shows the eclipse profile for five energy bands, with the full band profile reproduced for comparison. To investigate the energy dependence of the eclipse profiles, we define the times t_{90} and t_{10} as those at which the count rate is first at 90 and 10 per cent of the mean out-of-eclipse level, respectively. Therefore, for the ingress, t_{90} marks the start and t_{10} the end, whereas for the egress, t_{10} marks the start and t_{90} the end. To account for stochastic variability, we define these times as the time when the average count rate first passes the desired percentage and stays past it for at least five seconds. The measured t_{90} and t_{10} values

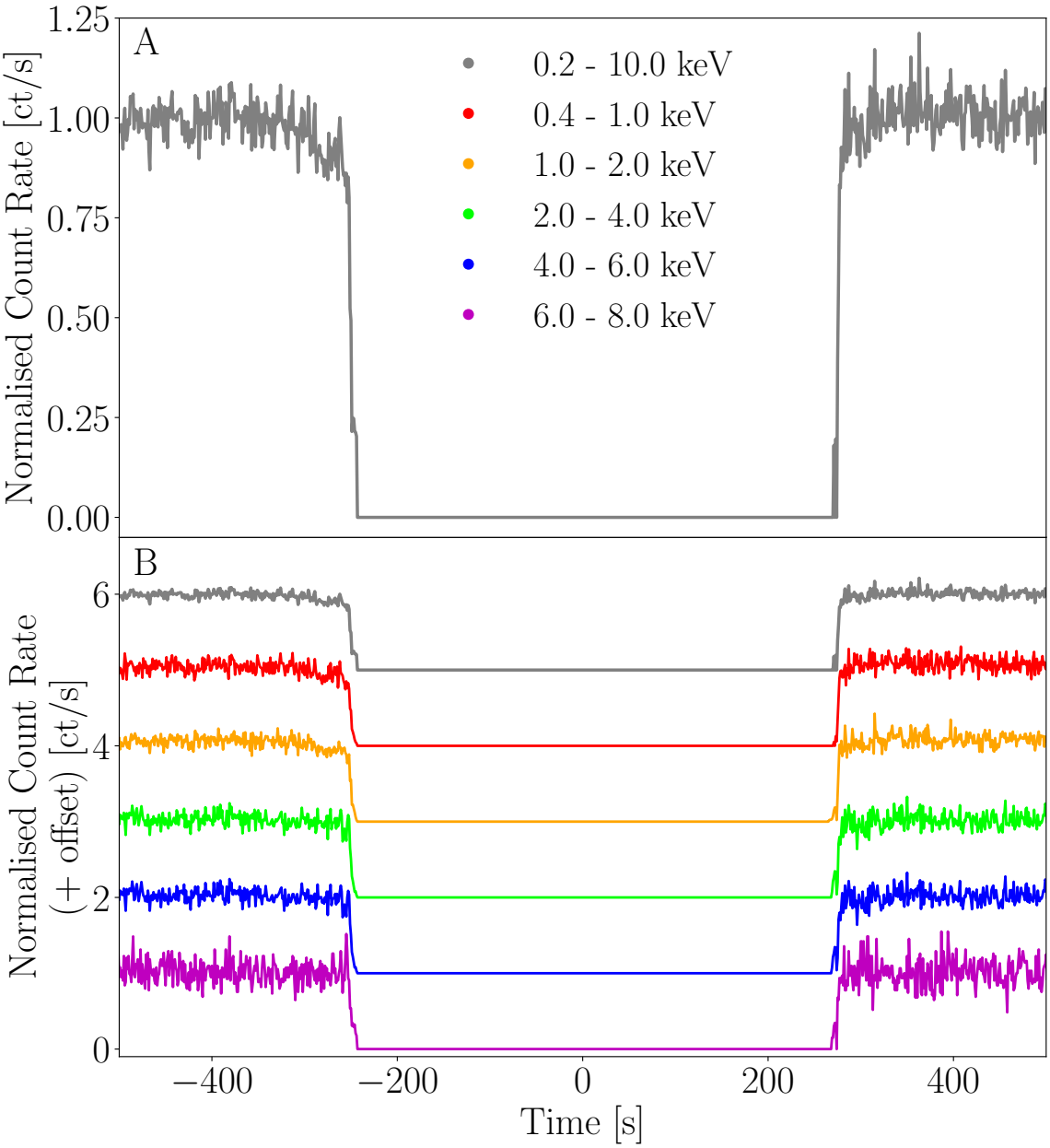

Figure 3.1: The folded eclipse profile of EXO 0748–676 in the soft-state, seen for the full energy range of *XMM*-Netwon ($0.2 - 10.0$ keV, grey) in Panels A and B, and for narrower energy ranges $0.4 - 1.0$ keV (red), $1.0 - 2.0$ keV (orange), $2.0 - 4.0$ keV (green), $4.0 - 6.0$ keV (blue) and $6.0 - 8.0$ keV (magenta) in Panel B. For all eclipse profiles, the count rate is normalised by dividing by the mean out-of-eclipse count rate such that the out-of-eclipse level is 1.0 and the count rate during totality is ~ 0.0. In Panel B, eclipse profiles are displayed with a vertical offset for visual clarity. These are +0.0 (magenta), +1.0 (blue), +2.0 (green), +3.0 (orange), +4.0 (red) and +5.0 (grey).

for the ingress and egress are shown in Figure 3.2, panels A and B respectively. For the ingress, we see that t_{90} increases with energy whereas t_{10} is approximately constant, indicating that the ingress begins later for higher photon energies, but totality starts at approximately the same time for all energies. This behaviour is mirrored in the egress: the end of totality is approximately independent of energy, but the egress ends later for softer X-rays. The ingress and egress durations, therefore, decrease with increasing photon energy. This is shown explicitly in Figures 3.2C and 3.2D. We see from these plots that the egress is longer in duration than the ingress. In the full band, the ingress duration is approximately $t_{10,\mathrm{in},0.2-10.0\mathrm{keV}} - t_{90,\mathrm{in},0.2-10.0\mathrm{keV}} = 15.2$ s and the egress duration is approximately $t_{90,\mathrm{eg},0.2-10.0\mathrm{keV}} - t_{10,\mathrm{eg}0.2-10.0\mathrm{keV}} = 17.5$ s.

3.2.3 Interpretation

The eclipses result from the companion star passing in front of the X-ray emitting region close to the NS. To explain the extended ingress and egress duration, we consider two limiting cases: 1) an extended X-ray emitting region eclipsed by an optically thick companion star with a sharp outer boundary. 2) a point-like X-ray source eclipsed by a companion star surrounded by a layer of absorbing material with some radial density profile.

3.2.3.1 Extended Source with an Optically Thick Companion

In this case, the ingress duration is the time it takes for the companion to move across our view of an extended X-ray-emitting region. For an edge-on, circular binary system, we can relate the radius of the assumed spherical X-ray emitting region, r_{x}, to the ingress duration, Δt_{in}, as $r_{\mathrm{x}} = \pi r_{\mathrm{a}} \Delta t_{\mathrm{in}}/P$, where P is the orbital period and r_{a} is the binary separation. Calculating r_{a} from Kepler's law and assuming a mass ratio of $q = 0.2$, we find that the observed ingress duration of $\Delta t_{\mathrm{in}} = 15.2$ s requires an X-ray emitting region radius of $r_{\mathrm{x}} \approx 3500$ km $\approx 1700\ r_{\mathrm{g}}$ for $M_{\mathrm{NS}} = 1.4\ M_{\odot}$ and

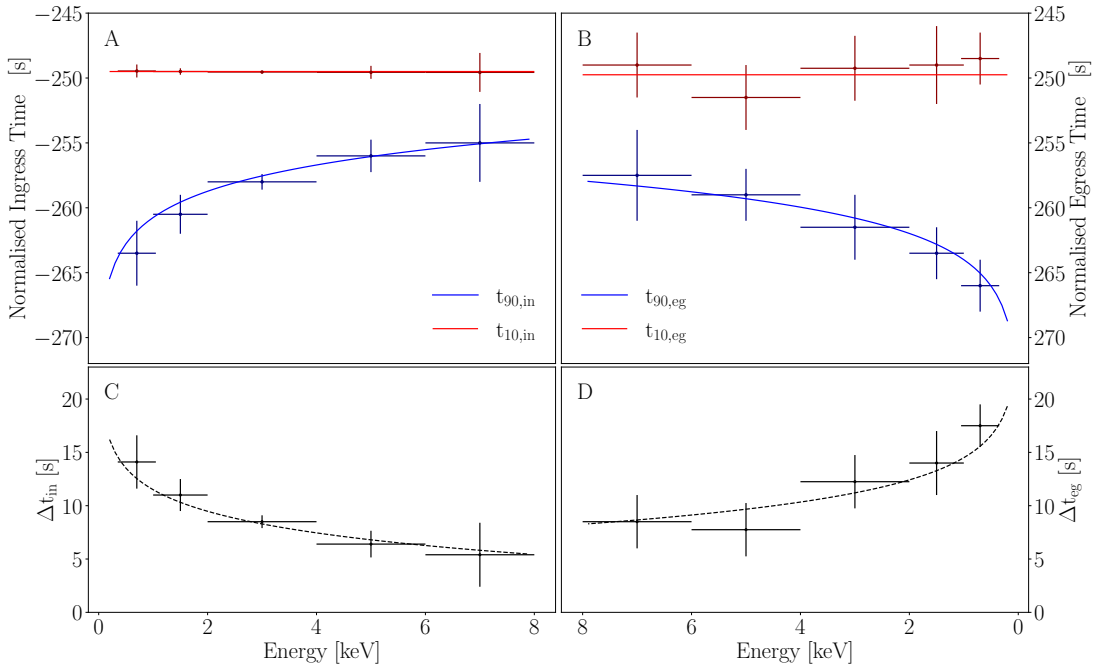

Figure 3.2: Measured eclipse times, t_{90} and t_{10}, as functions of energy for the ingress and egress; panels A and B respectively. We define the times t_{90} and t_{10} as, respectively, the time at which the count rate is first at 90 and 10 per cent of its mean out-of-eclipse level. Times are measured from each of the eclipse profiles in Figure 3.1 B. Panel A: Ingress start times ($t_{90,in}$) increase with energy indicating that eclipses start later for higher photon energies. Ingress end times ($t_{10,in}$), which mark the start of totality are independent of energy. Panel B: The end of totality that marks the start of the egress ($t_{10,eg}$) is approximately independent of energy, but the egress ends later for softer X-rays ($t_{90,eg}$). Note that both axes have been reversed to aid the comparison of the egress with the ingress. Panels C and D respectively show that the ingress and egress duration increases with photon energy.

$r_x \approx 4200$ km $\approx 1200\ r_g$ for $M_{NS} = 2.4\ M_\odot$; where $r_g = GM_{NS}/c^2$ is a gravitational radius.

In Appendix 3.7, we show that r_x and q can be inferred as a function of binary inclination angle from the ingress duration and totality duration, under the assumption that the companion is filling its Roche-Lobe (Figure 3.10). The minimum inclination for which there is a solution is $i \approx 69°$, corresponding to a mass ratio of $q = 1$. For a more realistic mass ratio of $q \lesssim 0.4$, we find $i \gtrsim 73°$. From the minimum possible inclination, we find a minimum X-ray emitting region size of $r_x \approx 1100$ km $\approx 550\ r_g$ for $M_{NS} = 1.4\ M_\odot$ and $r_x \approx 1400$ km $\approx 400\ r_g$ for $M_{NS} = 2.4\ M_\odot$. This large

minimum source size is incompatible with, e.g., the high blackbody temperature that we measure ($kT \approx 0.5$ keV, $T \approx 5.7 \times 10^6$ K; see Table 3.1), which would require a luminosity of ~ 50 times the Eddington limit, and for the system to be located outside of the Galaxy.

We observe the ingress and egress duration to decrease with increasing photon energy. This can be explained by the extended source model if the inner region of the source emits a harder spectrum than the outer region. In this case, the companion star starts to block the soft X-ray emitting region before it starts to cover the hard X-ray emitting region such that the hard X-ray ingress would begin after the soft X-ray ingress. However, this simple scenario predicts the hard X-ray ingress would end *before* the soft X-ray ingress. In contrast, we observe the start and end of totality to be roughly independent of energy, therefore this scenario cannot reproduce the energy dependence of the eclipse profiles. It also cannot reproduce the egress being longer in duration than the ingress, as we observe it to be.

3.2.3.2 Point Source with a Material Layer Surrounding the Companion

In the opposite limiting case, the ingress and egress occur when our view of a point-like X-ray source is blocked by a layer of absorbing material surrounding the companion star. In this picture, the surrounding material absorbs soft X-rays more efficiently than hard X-rays at the start of the ingress until the column density becomes very large at the end of the ingress, therefore, reproducing the observed energy dependence of the ingress and egress. If the absorbing material trails somewhat behind the companion star, this can explain why we observe the egress to be consistently longer than the ingress (as seen for many more eclipses: Wolff et al. 2009; Parmar et al. 1991). In this Chapter, I assume an X-ray point source, because in this model a point source is indistinguishable from an extended source unless the source is hundreds of km across or larger.

3.2.4 Fit to the Time-Averaged Spectrum

We fit the time-averaged spectrum using XSPEC V12.11.1 (Arnaud, 1996) and the model

$$\text{TBABS}*(\text{DISKBB} + \text{BBODY} + \text{NTHCOMP}) *\texttt{G}. \tag{3.1}$$

Here, TBABS accounts for absorption by the interstellar medium (we use the abundances of Wilms et al. 2000), and DISKBB is a multi-temperature accretion disk spectrum. We model the spectrum from the NS surface as a blackbody (BBODY) plus Comptonisation by a thermal population of electrons with temperature $kT_{\rm e}$ (NTHCOMP; Zdziarski et al. 1996). We tie the seed photon temperature to the blackbody temperature, physically corresponding to some fraction of the NS surface blackbody photons being Compton up-scattered. Finally, `G` represents eight Gaussian absorption lines (GABS). The first five of these correspond to astrophysical absorption lines, originally discovered in this observation by Ponti et al. (2014). We tie the widths of these five lines but leave their centroids and strengths as free parameters. Several calibration features are evident in the $E < 2.5$ keV region of the spectrum, as is common for the EPIC-pn (see e.g. Marco & Ponti 2016). These features motivated Ponti et al. (2014) to ignore energies below 2.5 keV. However, we wish to model the eclipse profile in soft X-rays, for which we need to extend our model for the out-of-eclipse spectrum to lower energies. We, therefore, account for the calibration features with three additional GABS components.

Figure 3.3 shows the total model (red) and its constituent components: the blackbody from the NS's surface (blue), the multi-temperature blackbody from the accretion disk (green) and the thermal Comptonisation component (magenta). We achieve an acceptable fit with a reduced χ^2 value of $\chi^2/\nu = 161.57/151$ and a null hypothesis probability, $p = 0.426$. The best-fitting parameters are reported in Table 3.1. Since the duration of the ingress and egress are only $\sim 0.01\%$ of the orbital period each,

Model Component	Parameter	Value	1σ Interval
`TBabs`	N_H [1×10^{22} cm^{-2}]	0.149	$\pm^{0.006}_{0.006}$
`diskbb`	T_{in} [keV]	0.218	$\pm^{0.006}_{0.006}$
`bbody`	kT [keV]	0.491	$\pm^{0.010}_{0.012}$
`NthComp`	Γ	2.091	$\pm^{0.026}_{0.053}$
	kT_e [keV]	3.469	$\pm^{0.418}_{0.310}$
Absorption lines	E_1 [keV]	6.687	$\pm^{0.009}_{0.008}$
	E_2 [keV]	7.021	$\pm^{0.030}_{0.021}$
	E_3 [keV]	2.639	$\pm^{0.021}_{0.020}$
	E_4 [keV]	3.111	$\pm^{0.018}_{0.018}$
	E_5 [keV]	3.979	$\pm^{0.229}_{0.127}$
	$\sigma_{1-5}[keV]$	0.007	$\pm^{0.005}_{0.005}$
Calibration lines	E_6 [keV]	0.990	$\pm^{0.004}_{0.004}$
	$\sigma_6[keV]$	0.070	$\pm^{0.002}_{0.002}$
	E_7 [keV]	2.002	$\pm^{0.016}_{0.016}$
	σ_7 [keV]	0.002	$\pm^{0.001}_{0.001}$
	E_8 [keV]	2.419	$\pm^{0.018}_{0.019}$
	σ_8 [keV]	0.016	$\pm^{0.002}_{0.001}$

Table 3.1: Best-fitting parameters from our fit to the time-averaged spectrum. Line energies quoted are centroid energies. Following (Ponti et al., 2014), the first 5 lines correspond to 1) a Fe XXIII-XXV Kα blend, 2) Fe XXVI Kα, 3) S XVI Kα, 4) a S XVI Kβ and Ar XVII Kα blend, 5) A Ca XIX-XX Kα blend. The final 3 lines account for calibration issues (see e.g. Marco & Ponti 2016). Reduced χ^2 is $\chi^2/\nu = 161.57/151$. Since the duration of the ingress and egress are only$\sim$ 0.01% of the orbital period each, and no counts are contributed during totality, the time-averaged spectrum is approximately the out-of-eclipse spectrum.

and no counts are contributed during totality, the time-averaged spectrum is approximately the out-of-eclipse spectrum and is subsequently used in our eclipse profile modelling.

3.3 Phase-Resolved Spectroscopy

To diagnose the nature of the absorbing material around the companion star, we fit the phase-resolved spectra of the ingress and egress with ABBSCA (see Section 2.2.3) which considers both the absorption and scattering of photons by the companion

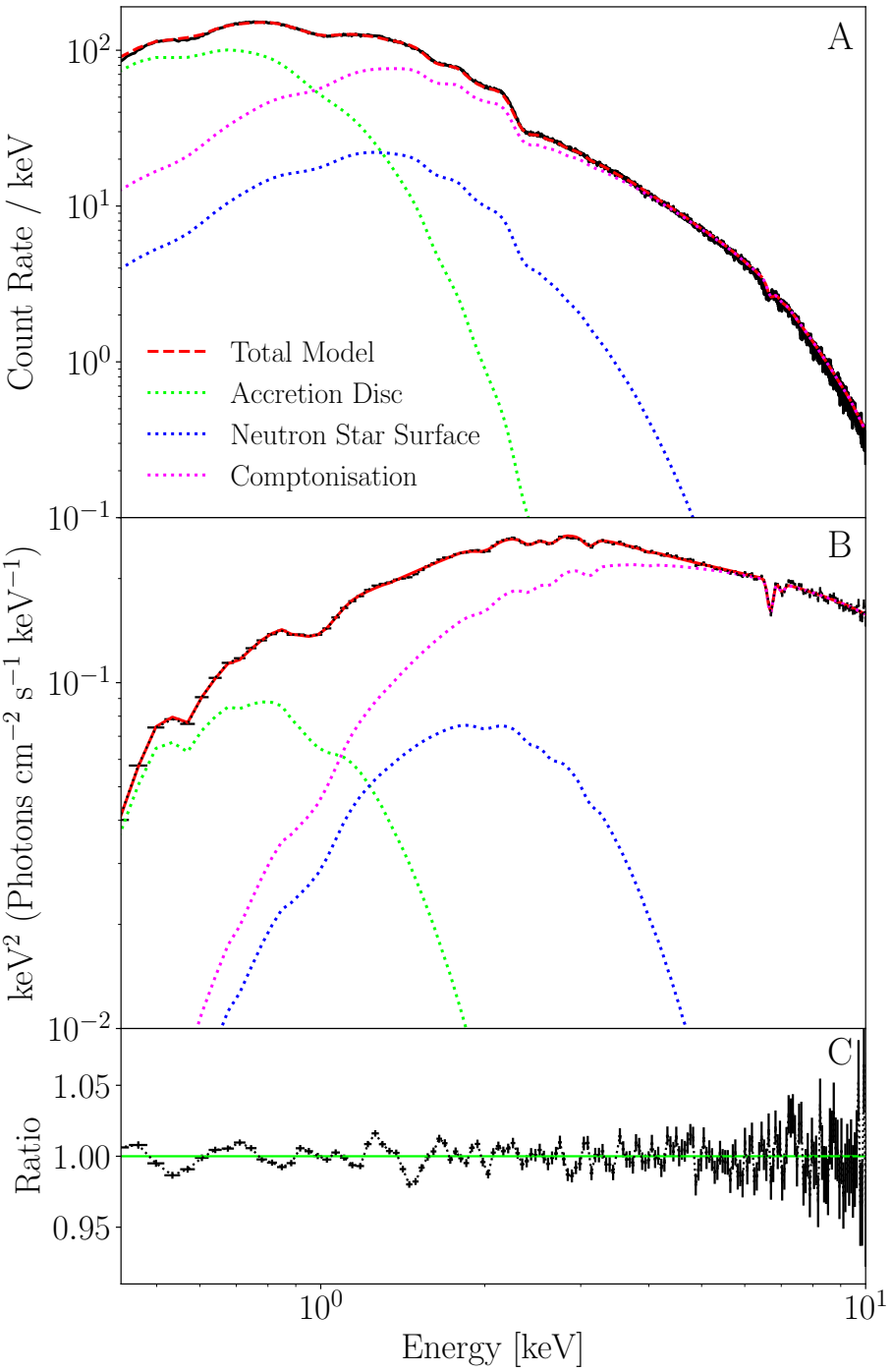

Figure 3.3: A fit to the time-averaged spectrum of EXO 0748–676 (black) using the multi-component model (red) described in Section 3.2.4. Also shown are the model components originating from the NS's surface (blue), the accretion disk (green) and the thermal Comptonisation component (magenta). Model parameters are summarised in table 3.1 Panel A shows the best-fitting folded spectrum, panel B shows the best-fitting unfolded spectrum and panel C shows the ratio: data/folded model.

star's outflow. We fix $n_e/n_H = 1.0$ and the redshift to $z = 0$.

3.3.1 Results

We extract phase-resolved spectra for the ingress and egress from the folded eclipse profiles in 6 energy bands: $0.2 - 0.5$ keV [2], $0.5 - 1.0$ keV, $1.0 - 2.0$ keV, $2.0 - 4.0$ keV, $4.0 - 6.0$ keV and $6.0 - 8.0$ keV (which were calculated following the procedure described in Section 3.2.2). Spectra are extracted using 2.5 second and 5.0 second time bins, respectively, for the ingress and egress, covering time ranges of t = −267.5s to t = −250.0s and t = 247.5s to t = 282.5s, producing a total of 14 spectra (seven for the ingress and seven for the egress). The time ranges are defined to ensure we fully encapsulate the times in which the absorbing material is influencing the eclipses and to account for the observed asymmetry in the eclipse profiles.

Because of the asymmetry in the eclipses, we allow the ingress and egress to have different values of covering fraction (f_{cov}), ionisation parameter (ξ) and column density (N_H). We initially allow the covering fractions and ionisation parameters to be free for each spectrum, finding their values to be approximately constant across the sets of ingress and egress spectra. We, therefore, tie the covering fractions and ionisation parameters for the sets of ingress and egress spectra (such that it is constant in both sets), but the column density remains a free parameter for each spectrum. The XSPEC fit results are shown in Table 3.2, where the column densities are listed chronologically. We find that $\log(N_H)$ increases linearly with time during the ingress and decreases linearly with time in the egress, as shown by the dashed black lines in Figure 3.4. The column density is found to change by several orders of magnitude over a short time, suggesting the absorbing material possesses a steep density profile.

Note that two fit statistics are considered here. Due to the low count rate in several

[2] We chose to include this energy band in the phase-resolved spectral analysis because soft X-ray photons appear to be most susceptible to absorption by the surrounding material. For the eclipse profile modelling, it is excluded due to high variability and a low count rate.

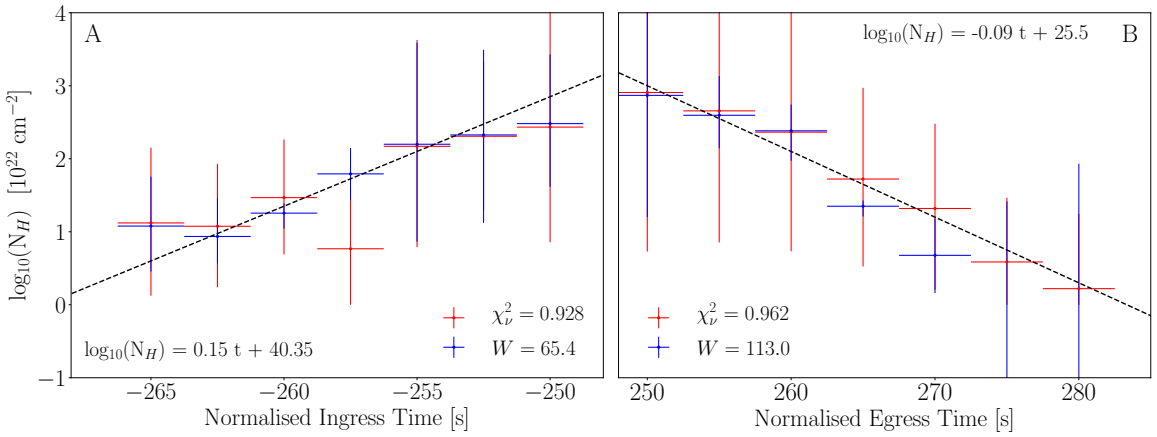

Figure 3.4: Hydrogen column densities as functions of time for the ingress (Panel A) and egress (Panel B), obtained by fitting our local absorption and scattering model `abssca` to 7 phase-resolved ingress spectra and 7 phase-resolved egress spectra. We present results obtained using two fit statistics - χ^2 (red), quantified by χ^2/ν and C-Stat (blue), quantified by the W statistic. As shown, the measured Hydrogen column densities are found to be independent of the chosen fit statistic but note that C-Stat is more appropriate here because of the low count rate in several of the spectra. The eclipse times are normalised such that the centre of the eclipse occurs at $t = 0$ s. In both A and B, the black dashed line shows the log-linear trend of the data. The corresponding equations for each line are given in their respective panels.

of the spectra, C-Stat [3] is more appropriate than χ^2. Within XSPEC, this requires a background spectrum and model to be defined because the difference between two Poisson variables is not another Poisson variable. Therefore, instead of subtracting the background from the source, the combined likelihood for the source and background are found and quantified with the *W-Statistic* (see Arnaud 1996 Appendix B for further details). The background spectrum is simply the totality spectrum and is well-modelled by an ISM absorption and power-law model: TBABS*PO. We present best-fitting model parameters for the ingress and egress spectra using both fit statistics (C-Stat and χ^2) in Table 3.2, to show that the best-fitting parameters are independent of the chosen fit-statistic. Table 3.2 also details the best-fitting parameters for the background spectral fit which was used in both the ingress and egress spectral fits.

[3] C-Stat is a likelihood-based statistic for low count-rate, Poisson distributed data.

Parameter	Ingress		Egress	
	$\frac{\chi^2}{\nu} = \frac{40.8}{44}$ $p = 0.77$	$W = 65.4$ $p = 0.67$	$\frac{\chi^2}{\nu} = \frac{42.3}{44}$ $p = 0.54$	$W = 113.0$ $p = 0.47$
f_{cov}	$0.99 \pm^{0.01}_{0.01}$	$1.00 \pm^{0.00}_{0.01}$	$0.99 \pm^{6\times10^{-3}}_{0.01}$	$1.00 \pm^{0.00}_{0.01}$
$\log(\xi)$	$2.81 \pm^{0.15}_{0.55}$	$3.21 \pm^{0.08}_{0.08}$	$2.57 \pm^{0.83}_{0.19}$	$2.80 \pm^{0.42}_{0.65}$
N_H	$13.2 \pm^{10.8}_{9.93}$	$12.0 \pm^{0.24}_{0.21}$	$808 \pm^{80.8}_{151}$	$739 \pm^{42.6}_{46.7}$
$[10^{22}cm^{-2}]$	$11.9 \pm^{7.16}_{6.84}$	$8.62 \pm^{0.42}_{0.30}$	$453 \pm^{145}_{63.4}$	$394 \pm^{3.45}_{2.83}$
	$29.4 \pm^{6.25}_{6.00}$	$18.0 \pm^{1.37}_{1.63}$	$231 \pm^{41.7}_{42.8}$	$242 \pm^{2.29}_{2.57}$
	$5.85 \pm^{6.35}_{5.85}$	$62.1 \pm^{2.25}_{2.27}$	$52.8 \pm^{17.8}_{15.8}$	$22.4 \pm^{1.20}_{1.38}$
	$148 \pm^{28.6}_{24.1}$	$158 \pm^{24.6}_{21.6}$	$20.8 \pm^{14.4}_{12.9}$	$4.75 \pm^{0.30}_{0.32}$
	$203 \pm^{10.6}_{10.4}$	$212 \pm^{14.7}_{16.0}$	$3.86 \pm^{7.58}_{3.86}$	$10^{-9} \pm 10^{-10}$
	$272 \pm^{54.7}_{37.8}$	$303 \pm^{8.87}_{7.37}$	$1.66 \pm^{10.6}_{1.66}$	$10^{-8} \pm 10^{-10}$
n_H $[10^{22}cm^{-2}]$		$0.56 \pm^{0.08}_{0.07}$		$0.56 \pm^{0.08}_{0.07}$
α		$2.68 \pm^{0.14}_{0.15}$		$2.68 \pm^{0.14}_{0.15}$

Table 3.2: Best fitting parameters obtained from fitting our local absorption and scattering model `abbsca` to the phase-resolved spectra of the ingress and egress. We present results obtained using two fit statistics - χ^2, quantified by χ^2/ν and C-Stat, quantified by the W statistic. Their values are given in the first and second columns respectively for both the ingress and egress, with corresponding null hypothesis probabilities below. The model parameters are found to be consistent between the two fit statistics, but C-Stat is more appropriate because of the low count rate in several of the spectra. Here, χ^2_ν provides a simple way to understand the goodness of fit. The rows are covering fraction, f_{cov}, ionisation parameter, $\log(\xi)$, and column density for each time bin, N_H. The column densities are listed chronologically. The bottom two rows detail the best-fitting parameters for the background spectral model, `TBabs*po`, which are the equivalent hydrogen column, n_H and the power-law index, α. All errors are 1σ and the same background spectral fit was applied to both the ingress and egress.

3.3.2 Inferring the Density Profile

Assuming a spherically symmetric companion star and the model geometry detailed in Section 2.2.2, the column density $N_H(t)$ can be calculated from an assumed radial density function, $n(x)$, with q as the only other model parameter.

We trial the all options for $n(x)$ available within X-TREC (see Section 2.2.2). The first is a power law (Equation 2.8). Setting $m = 2$ corresponds to a stellar wind with constant velocity. The companion star in EXO 0748–676 is a low mass M-dwarf star (Parmar et al., 1986) that would typically drive a weak solar-like wind with a mass-loss rate of the order of $10^{-13} M_\odot$ yr^{-1} or less (e.g., Wargelin & Drake, 2002). Such a wind is too low-density to yield significant absorption at X-ray wavelengths: a wind velocity of 500 km s^{-1}, for example, corresponds to a particle density at the base of the wind of 6×10^6 cm^{-3} for the typical M-dwarf radius of $R_{cs} = 0.43 R_\odot$, and a column density through the wind of 2×10^{17} cm^{-2}. In this case, however, a much denser wind could be driven by irradiation from the NS and accretion flow.

We trial power-law indices of $m = -2$, $m = 0$, $m = 2$ and m = 10. For each index, we also explore mass ratios of $q = 0.05$, $q = 0.2$ and q = 0.4, corresponding to inclination angles of $i = 82.8$, $i = 76.9$ and i = 73.6 degrees respectively. Here, $q = 0.05$ translates roughly to the canonical NS mass, $1.4 M_\odot$. As seen in the top row of Figure 3.5, the power-law density profile results in an $N_H(t)$ that overwhelmingly disagrees with observations, for both the ingress and egress. We find higher values of m and q to be the most consistent with $m = 10$ and $q = 0.4$ providing $\chi^2/\nu = 464.2/44$ for the ingress and $\chi^2/\nu = 332.4/44$ for the egress. The null hypothesis probabilities for both are of the order 10^{-30}. We conclude that the asymptotic nature of the power-law function trialled will not easily reproduce the observed, steep $N_H(t)$.

The data require a density profile that drops off more steeply with radius rather than a constant velocity wind. We, therefore, consider a density profile corresponding to an accelerating wind (Equation 2.9; Puls et al. 2008), where β describes the accel-

eration of the outflow. Equation (2.9) is typically applied to massive stars for which the wind is driven by the radiation of the star itself. Puls et al. (2008) quote $\beta \leq 1.0$ for an OB star, however, we require much higher values to obtain consistency with the data. With a parameter combination of $\beta = 3.0$ and $q = 0.2$, $\chi^2/\nu = 85.1/44$, while a parameter combination of $\beta = 5.0$ and $q = 0.4$ gives $\chi^2/\nu = 64.9/44$ for the ingress. For the egress these are, respectively, $\chi^2/\nu = 140.1/44$ and $\chi^2/\nu = 74.9/44$. Panels C and D of Figure 3.5 show this consistency for parameter combinations of $\beta = 2.0,\ q = 0.05,\ \beta = 3.0,\ q = 0.2,$ and $\beta = 5.0,\ \mathrm{q} = 0.4$, with the latter providing the best overall agreement. This could indicate that there is very fast-moving material surrounding the companion, or that this, an M-dwarf star within a LMXB, is an inappropriate context for this functional form of $n(x)$ (Equation 2.9), especially since it is usually applied to hot, massive stars.

We consider the possibility that the absorbing material may behave less like a stellar wind and more like an extended atmosphere. Therefore we trial a Gaussian density profile (Equation 2.11) characterised by the fractional width of the material layer, Δ, which is a steeper function of distance, and therefore should be more consistent with the observed $\mathrm{N_H(t)}$. We try values of $\Delta = 0.008,\ \Delta = 0.005$ and $\Delta = 0.003$ for the set of mass ratios detailed above. As seen in Panels E and F of Figure 3.5, we achieve better agreement with the observed $\mathrm{N_H(t)}$, particularly for the ingress, where the parameter combination $\Delta = 0.003$ and $q = 0.4$ gives the most consistent result $\chi^2/\nu = 64.3/44$. The eclipse timings (see Section 3.2.2) suggested that there might be material trailing behind the companion star as it orbits, therefore, it is unsurprising that a larger fractional width, $\Delta = 0.008$, is most consistent with the egress data ($\chi^2/\nu = 64.4/44$, with $q = 0.05$), further supporting the presence of an asymmetric eclipse.

We additionally trial the exponential density profile (Equation 2.12) for the material, where h is the scale height of the material in units of R_{cs}. For the ingress we

consider $h = 0.004$, $h = 0.002$ and $h = 0.001$, and for the egress $h = 0.009$, $h = 0.004$ and $h = 0.003$. It is clear that the $N_H(t)$ functions predicted from this density profile provide the best description of the data, as seen in Panels G and H of Figure 3.5. For the ingress, the most consistent parameter combination is $h = 0.002, q = 0.2$ giving $\chi^2/\nu = 52.0/44$, and for the egress the most consistent parameter combination is $h = 0.004, q = 0.2$ giving $\chi^2/\nu = 44.6/44$.

Overall, the exponential radial density profile (Equation 2.12) is most consistent with the observed $N_H(t)$, but using the results from all density profiles, we can infer some properties of the absorbing material. The Gaussian density profile requires small fractional widths (Δ), the exponential profile requires small scale heights (h), and the accelerating profile requires high values for β, indicating that the density of material must drop off quickly with distance from the companion star's surface in all three cases. The Gaussian and exponential profiles also highlight the asymmetry of the eclipse profiles. When using the Gaussian density profile, the parameter combination $\Delta = 0.003$ and $q = 0.4$ yields $\chi^2/\nu = 64.3/44$ for the ingress, but yields a notably worse fit of $\chi^2/\nu = 277/44$ for the egress. Similarly, when using the exponential density profile with $q = 0.2$, a scale height of $h = 0.004$ is needed for the egress to produce $\chi^2/\nu = 44.6/44$, while $h = 0.002$ for the ingress is required to give the comparable $\chi^2/\nu = 52.0/44$. These results imply that more material is present in our line of sight during the egress than the ingress thus we consider a scenario in which the absorbing material trails behind the companion as it orbits, perhaps similar to a comet-tail. This could explain the 2.3 s asymmetry we observed in the folded eclipse profiles (Section 3.2.2). The phase-resolved spectral fits also provide useful insights. The ingress and egress both require high ionisation parameters, with the ingress being slightly more ionised than the egress. Such levels of ionisation could be driven by irradiation from the NS itself, perhaps being collisionally ionised by a pulsar wind. The difference in ionisation and covering fraction are likely due to the

orbital motion of the companion around the NS; denser, less extended material on the ingress side of the star is more susceptible to ionisation than the lower density material trailing behind the star.

3.4 Eclipse Mapping

Using XSPEC v12.1.1, we simultaneously fit the eclipse profiles of EXO 0748–676 in the five narrow energy bands presented in Figure 3.1B with X-TREC version 1.0. We ignore the majority of the phase bins corresponding to out-of-eclipse and totality, leaving only a small number of bins surrounding the ingress and egress. This ensures the best-fitting parameters and statistics refer to the portions of the eclipse profiles that contain the energy-dependent behaviour. Due to the abundance of observations of EXO 0748–676, the eclipse duration, t_e of ~ 500 s is well-known but is also observed to vary (Wolff et al., 2009; Parmar et al., 1991). Therefore, we apply a Bayesian prior on $t_{\rm e}$ assuming a Gaussian peaking at 500s with a width of 5s. We trial all four forms of $n(x)$ considered in Section 3.3.2, and allow $N_{H,0}$ and each of the $n(x)$ parameters (m, β, Δ or h, depending on the model being used) to take different values for ingress and egress. We fix the orbital period to $P = 3.824$ hrs and leave the totality duration t_e as a free model parameter.

We first trial X-TREC with no absorbing material surrounding the companion. This model simply invokes a sharp transition between out of eclipse and totality. This model produces a poor fit to the observed eclipse profiles (see row 1 of Table 3.3), demonstrating the need for the layer of absorbing material. We further trial the four density profiles presented in Equations 2.8 - 2.12. Table 3.3 compares the resulting fit statistics from our eclipse model for each density profile. As anticipated, the power-law density profile, with reasonable power-law indices of $m = 2$ and $m = 10$, are unable to describe the data, respectively yielding $\chi^2/\nu = 17700/818$ and $\chi^2/\nu = 15600/818$. Interestingly, if the power-law index is allowed to vary during the fits and

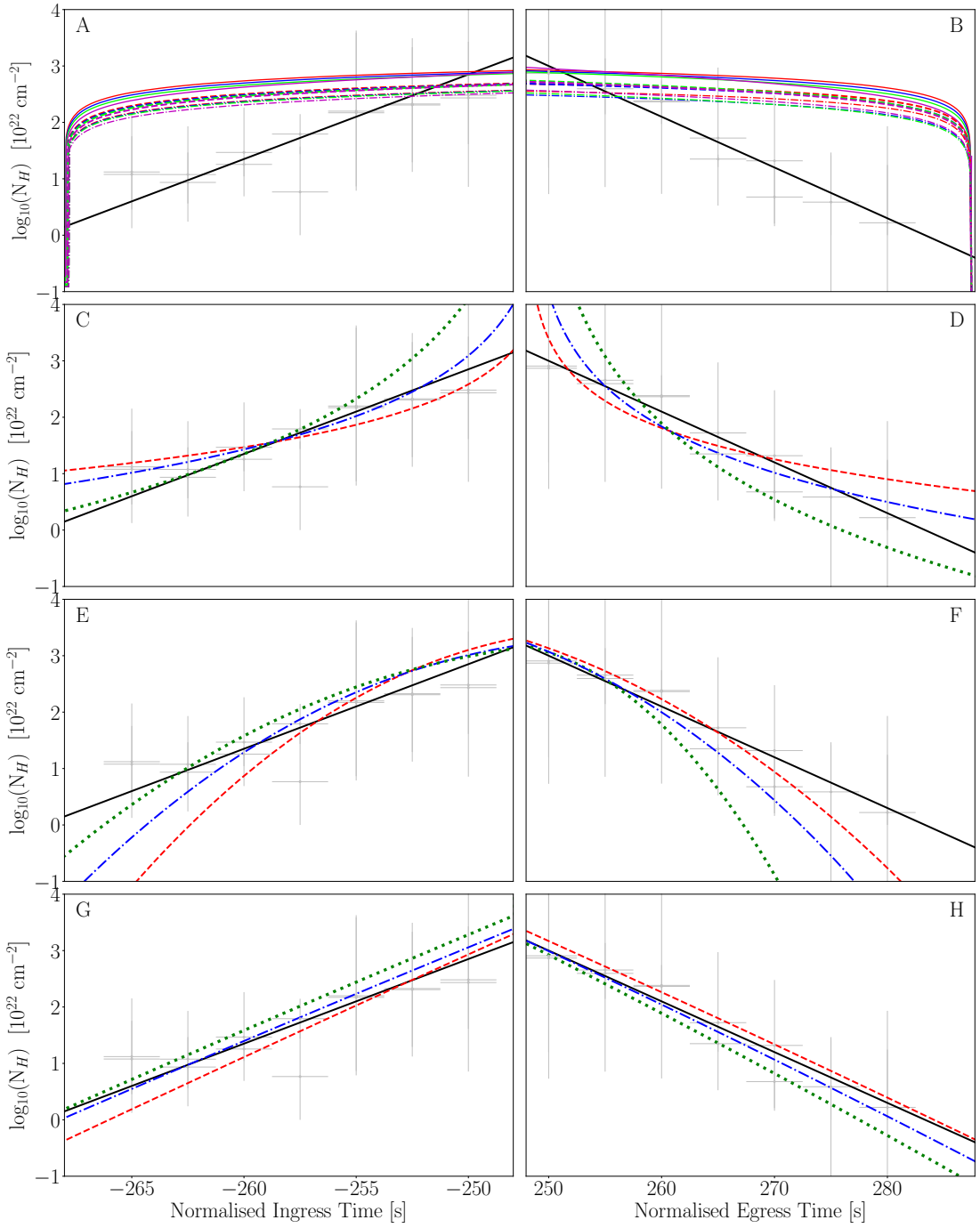

Figure 3.5: Panels A-H: Hydrogen column density of the absorbing material as a function of time during the ingress and egress. Measured $N_{\rm H}$ values are shown in grey with a log-linear best-fit function in black. Panels A and B assume the power law density profile (Equation 2.8). We use mass ratio q = 0.05 (solid), q = 0.2 (dashed) and q = 0.4 (dot-dashed); which correspond to i = 82.8 , i = 76.9 and i = 73.6 degrees respectively. We explore a power law index of m = -2 (red), m = 0 (blue), m = 2 (green) and m = 10 (magenta). (Continued on next page)

Figure 3.5: (Continued from previous page) Panels C and D assume the accelerating wind profile (Equation 2.9) with parameter combinations of $q = 0.05, \beta = 2.0$ (red), $q = 0.2, \beta = 3.0$(blue) and $q = 0.4, \beta = 5.0$ (green). Panels E and F assume the Gaussian density profile (Equation 2.11). We use mass ratio and fractional width parameter combinations of $q = 0.05, \Delta = 0.008$ (red), $q = 0.2, \Delta = 0.004$ (blue) and $q = 0.4, \Delta = 0.003$ (green) for the ingress and combinations of $q = 0.05, \Delta = 0.008$ (red), $q = 0.2, \Delta = 0.004$ (blue) and $q = 0.4, \Delta = 0.003$ (green) for the egress. Panels G and H assume the exponential density profile (Equation 2.12). We use mass ratio and scale height parameter combinations of $q = 0.05, h = 0.004$ (red), $q = 0.2, h = 0.002$ (blue) and $q = 0.4, h = 0.001$ (green) for the ingress and combinations of $q = 0.05, h = 0.009$ (red), $q = 0.2, h = 0.004$ (blue) and $q = 0.4, h = 0.003$ (green) for the egress. Panels C-H: We trial $q = 0.05, q = 0.2$ and $q = 0.4$ for each value of β, Δ and h but only plot three in each panel for visual clarity.

be different for the ingress and egress, they rise to the high values of $m_{\rm in} \approx 410.0$ and $m_{\rm eg} \approx 760.0$. At such high values of m, the power-law function behaves similarly to the exponential function (Equation 2.12), so based on our previous inferences, it is not surprising that these values yield a much lower fit statistic ($\chi^2/\nu = 1352/816$). As such high indices are nonphysical, we subsequently discard the power-law density profile. The remaining three profiles yield reasonable fits to the eclipse profiles, as alluded to by the phase-resolved spectroscopy. However, we discard the accelerating wind profile because 1) the associated $\chi^2_\nu = 1.288$ is notably higher than assuming the Gaussian ($\chi^2_\nu = 1.009$) or exponential ($\chi^2_\nu = 1.000$) density profiles and 2) the associated null-hypothesis probability, $p = 10^{-39}$, indicates that this model does not reproduce the data.

When assuming the Gaussian ($\chi^2/\nu = 822.95/816$) or exponential ($\chi^2/\nu = 816.01$ /816) density profiles are difficult to separate statistically, therefore, we consider both profiles going forward. The resulting eclipse profiles are shown in Figure 3.6, where panels A(i)–A(iv) assume the Gaussian density profile and panels B(i)–B(iv) assume an exponential density profile. Associated best-fitting parameters can be found in Table 3.4, with 1σ confidence intervals obtained through a Markov-Chain Monte Carlo (MCMC) simulation (see Appendix 3.9 for full details). The best-fitting

parameters from either profile lead to a similar inference regarding the absorbing material – the fractional widths and scale heights are both small, confirming that the material doesn't extend far out from the star's surface. Both profiles show asymmetry here, with larger fractional widths and scale heights for the egress than for the ingress. When assuming the exponential density profile, our fits suggest there is $\sim 20\%$ more material in the egress than the ingress while assuming the Gaussian density profile increases this to $\sim 40\%$. This further supports the hypothesis that some material is trailing behind the companion as it orbits. We find consistent ionisation parameters between the two density profiles, with both profiles finding the ingress to be more ionised than the egress, thus suggesting an incident wind or irradiation from the NS more strongly affects the ingress side of the star. The two models show variations in covering fraction, with the Gaussian model indicating the ingress side of the star is less covered by absorbing material than the egress side of the star, although the larger errors associated with $f_{cov,in}$ mean that the two sides could have similar coverings. In comparison, the exponential model shows the covering fractions to be consistent between the two sides of the star. The best-fitting mass ratio, q, and inclination angle, i, are found to be independent of the assumed radial density profile; we, therefore, have increased confidence in these values and our subsequent inference of the NS mass. Nonetheless, the energy-dependent eclipse timings strongly depend on the chosen density profile, so it is necessary to understand the density of the material to model the features of the eclipses caused by absorption. When comparing the eclipses modelled with the Gaussian density profile to the eclipses modelled with the exponential density profile (i.e. comparing panels A(iii) and A(iv) with panels B(iii) and B(iv) of Figure 3.6), we see the energy bands are more dispersed at the start ($t_{10,in}$) and end ($t_{10,eg}$) of totality when modelled with the Gaussian density profile. As a result, the Gaussian model does not capture the energy independence of the observed t_{10} times as well as the exponential model. Both models are capable of

Density Profile	Parameter(s)	χ^2	ν	χ^2_ν	p
No Material	-	4546.74	818	5.56	10^{-256}
Power-law	m = 2.00 *	17700	818	21.61	
	m = 10.0 *	15400	818	18.81	
	m_{in} = 413.6	1352.1	816	1.65	10^{-167}
	m_{eg} = 764.9				
Accelerating	$\beta_{in} = 5.48$	1050.6	816	1.288	10^{-39}
	$\beta_{eg} = 6.20$				
Gaussian	$\Delta_{in} = 0.0035$	822.95	816	1.009	0.581
	$\Delta_{eg} = 0.0047$				
Exponential	$h_{in} = 0.0023$	816.01	816	1.000	0.610
	$h_{eg} = 0.0027$				

Table 3.3: Fit statistics and characteristic density profile parameters obtained from modelling the eclipses profiles of EXO 0748–676 in five energy bands simultaneously with X-TREC, for each assumed density profile. From left to right: the assumed density profile of the absorbing material, key parameters governing the density profile, chi-squared, number of degrees-of-freedom, reduced chi-squared. The key density parameters are the power-law index, m, acceleration parameter, β, fractional width of the material, Δ and scale height, h, for the power-law, accelerating, Gaussian and exponential density profiles respectively.
* Parameter fixed for the duration of the fit.

reproducing the observed $t_{90,in}$ and $t_{90,eg}$.

3.4.1 Neutron Star Mass

We can calculate the NS mass from the binary mass function by rearranging Equation (1.29) to get

$$M_{\rm NS} = \frac{PK_{\rm em}^3}{2\pi G}\frac{1}{(K_{\rm em}/K)^3}\frac{(1+q)^2}{\sin^3 i}, \tag{3.2}$$

where $K_{\rm em}$ is the semi-major amplitude of the radial velocity curve of the observed stellar emission lines. Since emission lines originate from the irradiated face of the companion, they do not trace the centre of mass of the companion, but instead a region of the companion that is closer to the centre of mass of the binary. Therefore $K_{\rm em} < K$, and a *K-correction* $(K_{\rm em}/K) < 1$, is required in order to infer K from $K_{\rm em}$. Munoz-Darias et al. (2005) derive physical upper and lower limits for the K-correction as a function of mass ratio. The upper limit ($K_{\rm em}$ closest to K) corresponds to the

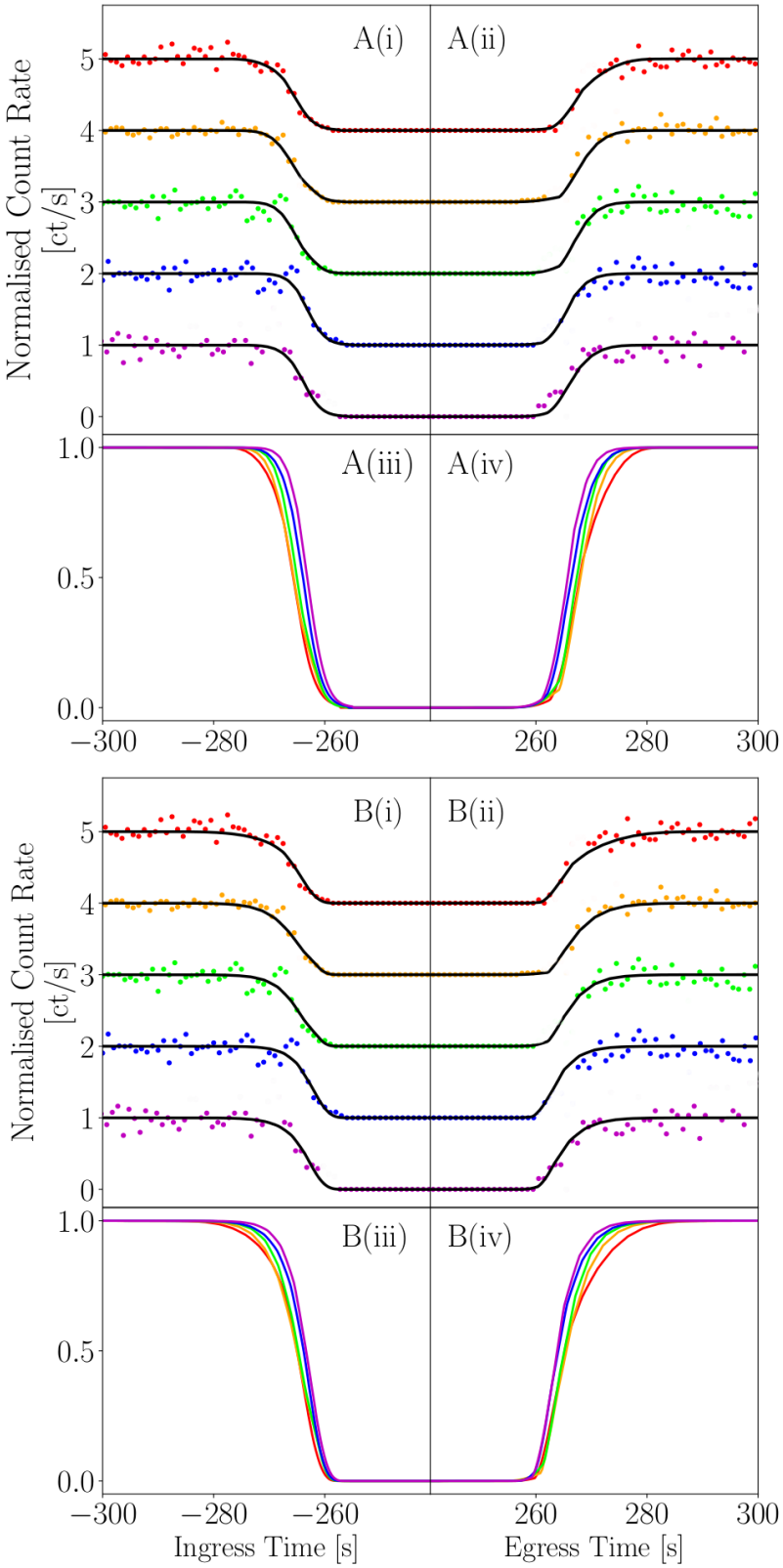

Figure 3.6: Eclipse profiles resulting from fitting the eclipses of EXO 0748–676 (continued on next page)

Figure 3.6: (Continued from previous page) in five energy bands with X-TREC version 1.0, assuming the Gaussian density profile (panels A(i)–A(iv)) and the exponential density profile (panels B(i)–B(iv)). Colours represent the 5 narrow energy bands used in our modelling and are consistent with Figure 3.1. In each set of four panels, i and ii show the resulting fits to each energy band, each with vertical offsets for visual clarity. These are +0.0 (magenta), +1.0 (blue), +2.0 (green), +3.0 (orange) and +4.0 (red). In each set of four panels, iii and iv show the resulting model in each energy band without a vertical offset to clearly show the energy-dependent behaviour of the best-fitting eclipse profiles. Fit statistics achieved are $\chi^2/\nu = 822.95/816$ and $\chi^2/\nu = 816.01/816$ for the Gaussian (A) and exponential (B) models respectively.

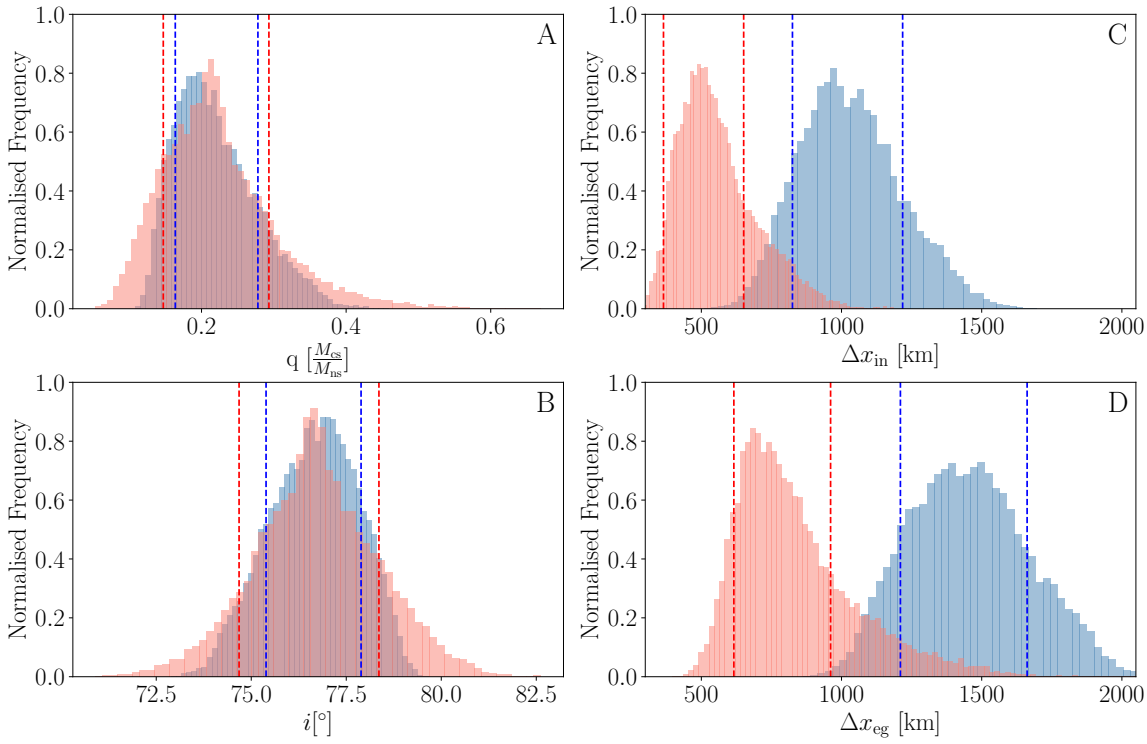

Figure 3.7: Distributions of mass ratio (A), inclination angle (B), the width of absorbing material during ingress (C) and width of the absorbing material during egress (D), from the X-TREC fits to the eclipses of EXO 0748 – 676. The distributions are obtained through a Markov Chain Monte Carlo simulation with 256 walkers, 307200 steps and a burn-in of 92160 steps assuming the Gaussian density profile (blue) and the exponential density profile (red). Corresponding 1σ confidence intervals are shown by blue and red dashed lines respectively.

Parameter	Gaussian Density Profile	Derived Values
$t_{\rm e}$	$503.21\ \pm^{1.62}_{1.48}$	$i = 76.52\pm^{1.37}_{1.13}$
q	$0.221\ \pm^{0.057}_{0.057}$	$M_{\rm NS} = 2.01\pm^{0.22}_{0.21}$
$N_{H0,\rm in}$	$2364.32\ \pm^{682.7}_{666.8}$	
$N_{H0,\rm eg}$	$4842.15\ \pm^{506.2}_{543.3}$	
$\log(\xi)_{\rm in}$	$3.49\ \pm^{0.460}_{0.084}$	
$\log(\xi)_{\rm eg}$	$2.82\ \pm^{0.009}_{0.043}$	
$\rm f_{cov,in}$	$0.897\ \pm^{0.064}_{0.062}$	
$\rm f_{cov,eg}$	$0.995\ \pm^{0.002}_{0.002}$	
$\Delta_{\rm in}$	$0.0035\ \pm^{0.0006}_{0.0006}$	$\Delta x = 1033\pm^{194}_{186}$ km
$\Delta_{\rm eg}$	$0.0049\ \pm^{0.0008}_{0.0007}$	$\Delta x = 1446\pm^{216}_{236}$ km
Parameter	Exponential Density Profile	Derived Values
t_e	$504.11\ \pm^{0.56}_{0.62}$	$i = 76.47\pm^{1.89}_{1.79}$
q	$0.222\ \pm^{0.070}_{0.075}$	$M_{\rm NS} = 2.02\pm^{0.29}_{0.27}$
$N_{H0,\rm in}$	$3819.7\ \pm^{1023.9}_{1040.2}$	
$N_{H0,\rm eg}$	$4320.3\ \pm^{881.3}_{972.4}$	
$\log(\xi)_{\rm in}$	$3.30\ \pm^{0.349}_{0.013}$	
$\log(\xi)_{\rm eg}$	$2.76\ \pm^{0.081}_{0.125}$	
$\rm f_{cov,in}$	$0.998\ \pm^{0.002}_{0.001}$	
$\rm f_{cov,eg}$	$0.996\ \pm^{0.005}_{0.009}$	
$\rm h_{in}$	$0.0023\ \pm^{0.0012}_{0.0001}$	$\Delta x = 679\pm^{222}_{107}$ km
$\rm h_{eg}$	$0.0027\ \pm^{0.0004}_{0.0009}$	$\Delta x = 797\pm^{104}_{251}$ km

Table 3.4: Best fitting parameters obtained when fitting the eclipse profiles of EXO 0748–676 in five energy bands with X-TREC. We implement both the Gaussian (top table) and exponential (bottom table) density profiles for the absorbing material around the companion star. From top to bottom, the model parameters are totality duration, mass ratio, surface column density for the ingress and egress, ionisation parameter for the ingress and egress, and covering fraction for the ingress and egress. The final two parameters are the fractional widths of the surrounding material layer for the ingress and egress in the case of the Gaussian density profile and the surrounding material's scale height for the ingress and egress in the case of the exponential density profile. The third column details values that have been derived from the model parameters in that row. Here, $M_{\rm NS}$ is the NS's mass, i is the binary inclination angle in degrees and Δx is the physical width of absorbing material from the companion star's surface.

emission line originating entirely from the point on the companion's Roche-Lobe surface that is furthest from the NS whilst still being visible to it, giving

$$K_{\rm em}/K = 1 - 0.2134q^{2/3}(1+q)^{1/3}. \tag{3.3}$$

The lower limit corresponds to the line originating entirely from the L1 point. In reality, most systems fall in between these two limits.

Different emission lines that originate predominantly from different parts of the irradiated face of the companion star will produce different measured $K_{\rm em}$ and will disappear at orbital phases ~ 0 (i.e. during or close to eclipse). Higher $K_{\rm em}$ values correspond to lines emitted furthest from the NS and therefore will have a K-correction closer to unity. For EXO 0748–676 there have been four independent studies resulting in radial velocity measurements from five emission features, all of which appear to be associated with the companion star. In outburst Muñoz-Darias et al. (2009) obtain 310 ± 10 km/s from HeII and Mikles & Hynes (2012) find 329 ± 26 km/s from the Bowen blend (CIII - NIII). In quiescence Bassa et al. (2009) used a Doppler mapping (DM) technique to obtain 345 ± 5 km/s and 410 ± 5 km/s respectively for HeII and H_α. By applying a Gaussian fitting technique to the same H_α emission, Bassa et al. (2009) find 333 ± 5 km/s. The authors favour the DM-derived values since this technique does not require symmetric line profiles, and consider the Gaussian model to be too simplistic to reproduce the complex shape of the H_α emission. Finally, Ratti et al. (2012) found 308.5 ± 3.9 km/s from a weighted average of H_β and H_γ.

We first chose to implement the H_α velocity measurement of $K_{\rm em} = 410 \pm 5$ km/s from Bassa et al. (2009) because it is the largest value, corresponding to a line emitted further from the NS than any other detected lines and therefore has a K-correction closer to unity ($K_{\rm em}$ closest to K). For a conservative approach, we use the upper limit of the K-correction (Equation 3.3), meaning that our mass measurement will be an under-estimate. We use the mass ratio measured from our eclipse profile fits,

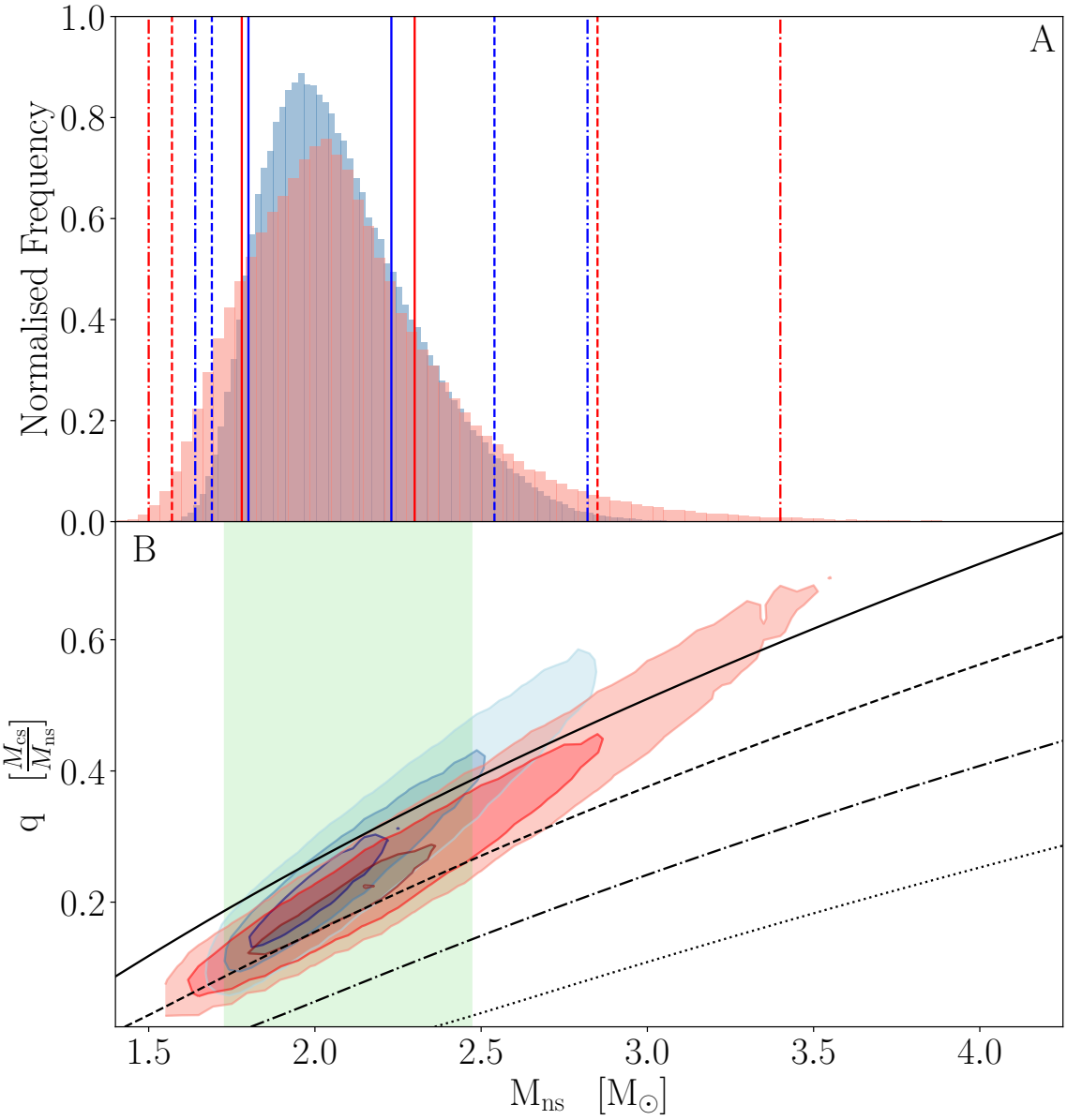

Figure 3.8: Panel A: Distributions of $M_{\rm NS}$ assuming the Gaussian (blue) and exponential (red) density profiles within the X-TREC. Distributions are obtained through a Markov Chain Monte Carlo simulation with a length of 307200, 256 walkers and a burn-in length of 92160 steps. Vertical lines show 1σ (solid), 2σ (dashed) and 3σ (dot-dashed) contours in blue and red, for the Gaussian and exponential density profiles respectively, which peak at $2.01M_\odot$ and $2.02M_\odot$. Panel B: Comparison between our measurements of $M_{\rm NS}$ assuming the Gaussian density profile (blue) and the exponential density profile (red), and the measurement from Özel 2006 (green). Dark, mid and light shades of blue and red correspond to 1, 2 and 3σ contours respectively for the Gaussian and exponential density models. Black lines show the relationship between, $M_{\rm NS}$ and q, for K-corrections of 1.0 (solid), 0.9 (dashed), 0.8 (dot-dashed) and 0.7 (dotted). K-corrections closer to unity yield a lower NS mass.

implementing the results of both the Gaussian and exponential models. For each model, we obtain a posterior probability distribution for $M_{\rm NS}$ by running an MCMC simulation with 256 walkers for a total of 307200 steps after a burn-in period of 92160 steps (see Appendix 3.9 for full details). For each step in the chain, we calculate i from q and t_e (Equation 2.5), draw a value of $K_{\rm em}$ from a Gaussian distribution with centroid 410 km/s and width 5 km/s, and finally calculate $M_{\rm NS}$ from Equations (3.2) and (3.3). Figure 3.7 shows the resulting posterior distributions of mass ratio, inclination and surrounding material width for the ingress and egress. Figure 3.8A shows the resulting $M_{\rm NS}$ distribution, with 1 (solid), 2 (dashed) and 3 σ (dot-dashed) confidence levels. For both figures 3.7 and 3.8, the Gaussian and exponential models are coloured blue and red respectively.

We see that the inferred NS mass is independent of the assumed density profile. We find $M_{\rm NS} = 2.01 \pm^{0.22}_{0.21} M_\odot$ and $M_{\rm NS} = 2.02 \pm^{0.29}_{0.27} M_\odot$ when we model the absorbing material with a Gaussian or exponential density function respectively. Note that for both models, the canonical NS mass of 1.4 $M_\odot$ falls outside of the 3σ contours. We infer this high value for the mass despite employing the most conservative possible K-correction (Equation 3.3). Applying a more realistic K-correction would increase the peak posterior mass values. Figure 3.8B demonstrates how our mass measurement depends on the mass ratio and K-correction. Solid, dashed, dot-dashed and dotted lines correspond to $K_{\rm em}/K = $ 1, 0.9, 0.8 and 0.7 (for comparison, Equation 3.3 gives $K_{\rm em}/K \approx 0.92$ for $q = 0.2$). We see that employing a reasonable value of $K_{\rm em}/K = 0.8$ (see Figure 4 of Munoz-Darias et al. 2005) pushes the mass measurement to $M_{\rm NS} \approx 2.8\ M_\odot$ (see Figure 3.9A-C), which is more massive than the most massive confirmed NS to date ($\sim 2.1\ M_\odot$: Cromartie et al. 2020). The distributions can also extend into the $3.0 - 5.0 M_\odot$ compact object mass gap, where it becomes uncertain if the compact object would be a NS or a BH. Since the primary in EXO 0748–676 is confirmed to be a NS by the presence of Type I X-ray burts with associated burst

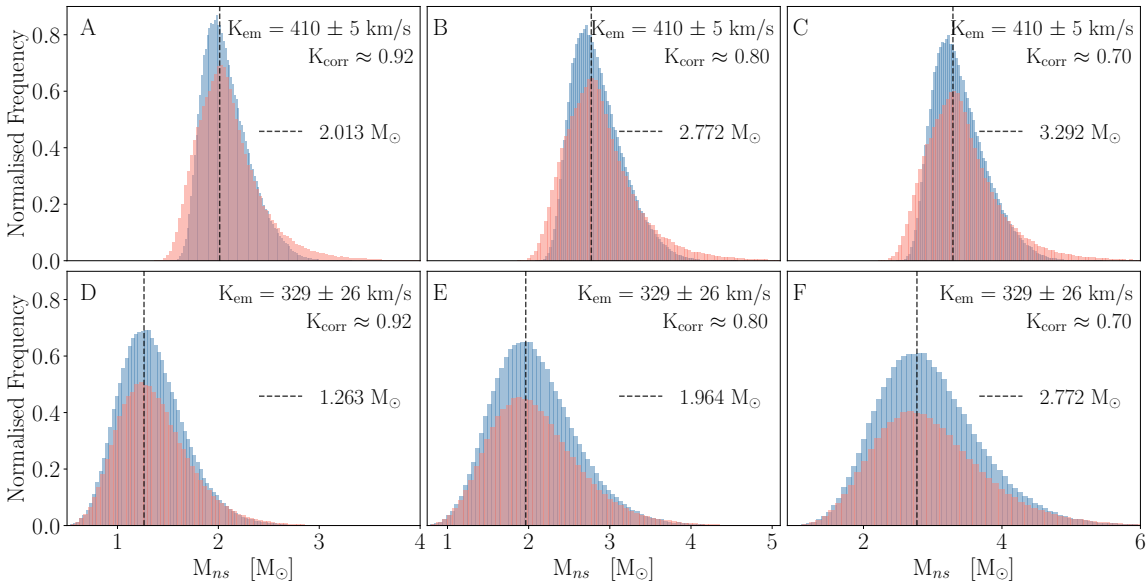

Figure 3.9: Distributions of $M_{\rm NS}$ assuming the Gaussian (blue) and exponential (red) density profiles within X-TREC, calculated using a different combination of $K_{\rm em}$ and K-Correction (as labelled). Also shown is a black dashed line corresponding to the peak-posterior NS mass. The K-correction in A and D corresponds to the most conservative value calculated using the mass-ratio dependent relation of Munoz-Darias et al. (2005) (Equation 3.3) for our best fitting value $q = 0.222$. Column 2 (B and E) and column 3 (C and F) assume the reasonable K-corrections of 0.8 and 0.7 respectively. Emission lines considered are H_α, $K_{\rm em}$ =410 ± 5 km/s (Bassa et al., 2009) and CIII–NIII blend, $K_{\rm em}$ =329 ± 26 km/s (Mikles & Hynes, 2012). We see that the peak-posterior is above the canonical NS mass unless we discard the H_α measurement *and* employ the maximum (closest to unity) possible K-correction (panel D).

oscillations (Özel, 2006; Galloway et al., 2010), future direct measurements of K may even inform on the observational lower bound of the mass gap. Furthermore, our consistency with the mass measurement presented by Özel (2006) ($M_{\rm NS} = 2.10 \pm 0.28 M_\odot$ and $r_{\rm NS} = 13.8 \pm 1.8$km) is encouraging for boths their PRE burst method and X-TREC. Our findings improve confidence in their conclusion, agreeing that a harder EoS is required for nuclear matter.

The difference in each measured $K_{\rm em}$ arises because each line will trace a different spatial zone between the irradiated face of the companion star and the L1 point, and since the highest value H_α = 410 ± 5 km/s (Bassa et al., 2009) is thought to

originate closer to the companion, it is reasonable to assume that this line is the most constraining. However, it is important to consider the caveats associated with this particular K_{em} measurement. Firstly, the approach taken by Bassa et al. (2009) is more typical of outburst studies, when the lines are assumed to be formed by irradiation. At the time EXO 0748–676 had just entered quiescence, making the detection of H_α unusual. Furthermore, the author's favoured result of $K_{em} = 410 \pm 5$ km/s obtained via a well-tested but indirect DM technique differs substantially from their result of $K_{em} = 333 \pm 5$ km/s, obtained directly from Gaussian fits to the same emission line. While Bassa et al. (2009) justify their preference for the velocities obtained via DM by suggesting that the DM method accounts for the shape of the emission line not being Gaussian, we highlight that $K_{em} = 410 \pm 5$ km/s is inconsistent with all other radial velocity measurements for this source, including the other values presented by Bassa et al. (2009). Additionally, our conservative approach towards the K-correction (i.e. $K_{em} / K \sim 1$) implies that the emitting area of the companion star is very small which is difficult to reconcile with the strong H_α emission component that is observed (Bassa et al., 2009). As shown in Figures 3.8 and 3.9, a more reasonable K-correction easily increases the peak of the distributions to $> 3M_\odot$. These high masses are inconsistent with a number of possible EoS and are substantially higher than any observed NS mass to date.

Another problem with assuming $K_{em} = 410 \pm 5$ km/s is the small error (~ 1 per cent). Underestimated uncertainties are often a problem associated with DM techniques, and in the case of Bassa et al. (2009), the error is assigned from the variation in the centroid velocity of the large spot seen in the DM, but only considers the effect of using the wrong systematic velocity. Recently, Wang et al. (2016) and Jiménez-Ibarra et al. (2017) tackled the issues with the errors in DM spots, using a newly developed code that computes the error using bootstraps DMs, obtaining more realistic errors on the radial velocities of $6-8$ per cent from very significant DM spots.

We note that if $K_{\rm em} = 410 \pm 5$ km/s Bassa et al. (2009) is trusted, the error is likely more significant than the one quoted and therefore, may not rule out the canonical NS mass. We also note that assuming $K_{\rm em}$= 410 $\pm$ 5 km/s violates the assumption that the disk rim orbits at Keplerian velocities (Mikles & Hynes, 2012). This does not provide a definitive reason to discard H_α because sub-Keplerian disk rim velocities have previously been measured (Somero, A. et al., 2012), but when combined with the other caveats presented here, provides reason to consider the other measured $K_{\rm em}$ values.

We additionally consider $K_{\rm em}$= 329 $\pm$ 26 km/s from Mikles & Hynes (2012). This measurement is robust, using a standard technique, and the value is consistent with all others except for the DM H_α measurement from Bassa et al. (2009). Note that this value is consistent with their H_α velocity derived via Gaussian fitting. Figure 3.9 shows how our mass posterior changes when we consider these two different $K_{\rm em}$ values for three different values of the K-correction (as labelled). Here $K_{\rm corr} \approx 0.92$ corresponds to the conservative, mass ratio-dependent K-correction calculated using our MCMC simulations and Equation 3.3. The K-corrections used in Panels B, C, E and F are found by drawing a value from Gaussian distributions peaking at 0.80 and 0.70 respectively with widths of 0.025. We chose this Gaussian width as it's comparable to the width of the calculated K-correction distribution peaking at $\sim$ 0.92. For the larger $K_{\rm em}$ (panels A-C), the distribution peaks at $M_{\rm NS} \sim 2\ M_\odot$ even for the largest possible K-correction value (panel A), and the canonical NS mass is ruled out with $> 3\sigma$ confidence. For the smaller $K_{\rm em}$ (panels D-F), the distribution peaks at $M_{\rm NS} \sim 2\ M_\odot$ for the most realistic K-correction ($K_{\rm corr} = 0.8$: panel E). For the Gaussian and exponential model respectively these distributions peak at $M_{\rm NS} = 1.95 \pm^{0.60}_{0.50}\ M_\odot$ and $M_{\rm NS} = 1.97 \pm^{0.53}_{0.49}\ M_\odot$. However, the distribution is broader due to the larger error bar on the $K_{\rm em}$ measurement, meaning that the canonical NS mass is not ruled out. Moreover, pushing the K-correction to its highest

possible value moves the peak to $M_{\rm NS} \sim 1.3\ M_{\odot}$ (panel D). As such, our modelling favours a $M_{\rm NS} \gtrsim 2\ M_{\odot}$ NS, but does rule out the canonical value of $M_{\rm NS} \sim 1.4\ M_{\odot}$ when considering the robust radial velocity amplitude measurement from the Bowen blend.

3.5 Discussion

We have modelled the energy-dependent X-ray eclipse profiles of EXO 0748–676 from which we have inferred an inclination of $i \sim 77°$, mass ratio $q \sim 0.2$ and thus NS mass $M_{\rm NS} \gtrsim 2\ M_{\odot}$. We infer the presence of a narrow ($\sim 500 - 1500$ km) region of ionised material around the low-mass companion star which absorbs soft X-rays more efficiently than hard X-rays. The presence of such a region explains the energy dependence of the extended ingress and egress profiles. In particular, ingress and egress are longer for softer X-rays, but the start and end times of totality are more or less independent of energy. The egress is ~ 2.3 s longer than the ingress. This can be explained if the absorbing material trails slightly behind the companion star during its orbit. Our fits require the layer of material to be $\sim 20-40$ per cent thicker behind the star than it is in the direction of orbital motion. The spectroscopic mass of the M-dwarf companion star is estimated to be $\sim 0.45 M_{\odot}$ (Parmar et al., 1986), assuming it to be on the main sequence; our eclipse mapping analysis returns a consistent value of $M_{\rm cs} \sim 0.44\ M_{\odot}$. Such a star would not typically launch a wind, therefore we explore other possible origins for the absorbing material.

Rapidly rotating M-dwarf stars are known to exhibit strong magnetic fields, of the order of a few kilo-Gauss (kG) (Johns-Krull & Valenti, 1996; Shulyak, D. et al., 2019; Kochukhov, 2020). For a tidally locked binary system, the secondary star will have a rotation period equal to the binary period, which for EXO 0748–676 is a few hours. Therefore, it is possible that the companion star could have a sufficiently strong magnetic field to induce a *slingshot prominence* (Collier Cameron, 1991; Evans

& Wood, 1996; Ferreira, 2000). This occurs when strong, active magnetic regions on the surface of the star interact with the forces of rotation which pull and distort the magnetic field lines from the star (Evans & Wood, 1996). The magnetic field lines loop out from the surface of the star, typically near the equator and carry stellar material along them. This could introduce absorbing material into our line-of-sight, but only for an ∼edge-on system. For our preferred inclination of $i \sim 77°$, our sight-line would miss such an equatorial prominence, and so we disfavour this interpretation.

The interaction between incident radiation from the NS, or a pulsar wind, and any outflow (not accretion flow) from the companion star are known to cause intra-binary shocks between the binary components (An et al., 2018). If an intra-binary shock is present, it could produce the necessary absorption. Here, the bow shock would channel any ionised stellar material into a parabolic shape around the companion star, causing extra absorption to occur close to the companion star. This scenario is well-motivated by observations with its effects being seen in pulse profiles (An et al., 2018; Polzin et al., 2020; Miraval Zanon, A. et al., 2021). We do not entirely rule out this possibility but cannot comment further as the complexities associated with modelling an intra-binary shock are beyond the scope of this paper. Note, however, that this scenario may not explain why the absorbing region is so narrow, as required by the data.

Our eclipse profile modelling measures $M_{\rm cs} \sim 0.44 M_{\odot}$ and $R_{\rm cs} \sim 300,000$ km ($0.43 R_{\odot}$), which are consistent with known mass and radius values of M2V - M3V main sequence stars (Kaltenegger & Traub, 2009), thus supporting Parmar et al. (1986), who suggested the companion is a main sequence M-dwarf. However, no absorption lines have ever been observed from the companion star in EXO 0748–676 and so we do not dismiss the possibility that the companion may not be a main sequence star, as is suggested by Mikles & Hynes (2012). In this case, we may simply be seeing the expanded outer layers of the star as it evolves off the main sequence, or

excess material from RLOF (Pols et al., 1998). This alternative scenario is plausible, particularly if the star is within the short-lived sub-giant phase. However, subsequent giant-branch phases can see the radius of low-mass stars increase by $100-10,000$ times ($L_{\rm cs} \propto R_{\rm cs}^2$) (Pols, 2011), thus requiring the absorbing material to extend further from the stellar surface than the narrow layer of material we infer.

The X-ray eclipse profiles observed here are reminiscent of the radio eclipse profiles observed for spider pulsars, which also feature extended, frequency-dependent eclipse profiles and egress/ingress asymmetry (Fruchter et al., 1988; Polzin et al., 2018). In these systems, incident radiation from the NS bombards and heats the outer layers of the companion star, resulting in their ablation from the surface of the companion. This process liberates and ionises material from the stellar surface, encasing the companion in a region of highly ionised material that trails somewhat behind the star due to the binary's orbital motion (Fruchter et al., 1990; Polzin et al., 2018). Therefore, given the similarities between the observations of eclipsing spider pulsars and those we present here, we consider the possibility that EXO 0748–676 is a progenitor to these pulsar systems. We find that the absorbing material around the companion star has a steep radial density profile and a characteristic width of only a few per cent of the companion star's radius, therefore, we invoke an *early ablation* scenario in which incident radiation from the NS or a pulsar wind has just started to ablate the outer layers of the companion. For EXO 0748–676 it is possible that kinetic energy from the disk wind (Ponti et al., 2014) is itself, sufficient to cause ablation or a contributing source of incident radiation that subsequently leads to ablation. Since EXO 0748–676 existed in an accretion-powered state for more than two decades, it is reasonable to consider that the disk wind may have contributed to the presence of the absorbing material. Assuming ablation to be driven by thermalisation, the response is the thermal (Kelvin-Helmholtz) timescale of the atmosphere ($\sim 10^{12}$ yrs). This is consistent with the lifetime of a $0.4 M_{\odot}$ M-star (Pols, 2011). Therefore, in the case of

our early ablation scenario, either not much material will have been ablated and/or the material has not had long enough to diffuse away from the star's surface. Both could explain why the absorbing region is so narrow. The highly ionised material inferred from our analysis ($2.8 \lesssim \log \xi \lesssim 3.5$) is consistent with it originating from an ablation process caused by irradiation from the NS (and accretion flow), and/or a pulsar wind (Fruchter et al., 1990; Miraval Zanon, A. et al., 2021), as is thought to be the case for spider pulsars.

Similar interpretations of EXO 0748–676 being a spider progenitor have been suggested by Ratti et al. (2012), who performed phase-resolved optical spectroscopy of the companion star's emission lines, and Parikh et al. (2021), who analysed UV spectroscopic data and quasi-simultaneous Swift X-ray observations of the source in quiescence. Ratti et al. (2012) attributed the broad emission lines to an outflow driven by a pulsar wind and/or X-ray heating from the stellar surface since broadening via tidally-locked rotation alone would indicate an unfeasibly heavy NS ($M_{\rm NS} \gtrsim 3.5\ M_{\odot}$, which though unlikely, is not entirely ruled out by our analysis). These authors noted that this scenario could also explain the lack of observed disk emission features and the observed variability in the g-band light curve. Parikh et al. (2021) notes that the broadening of the C IV line observed in EXO 0748–676 is similar to that of UV lines observed in PSR J1023+0038 (a known tMSP), which are thought to be broadened by a stellar outflow driven by the pulsar wind. Our results provide further evidence that EXO 0748–676 could be a *transitional redback pulsar*; i.e. a progenitor to a spider pulsar. Under this hypothesis, EXO 0748–676 will eventually transition to a redback pulsar, during which ablation will continue until it finally evolves into an isolated MSP. However, to date, no radio pulsations have been observed from this object so evidence for our interpretation remains circumstantial.

Similarities between the observed behaviour of EXO 0748–676 and the evaporation or disintegration of exoplanet atmospheres further suggest that the companion

star in EXO 0748–676 is undergoing ablation. In the context of planetary ablation, it is usual to consider the photo-thermal escape flow cycle (Moore & Horwitz, 2007). When incident radiation deposits energy into the geosphere, the outer layers of the atmosphere expand. This is known as *upflow*. With sufficient energy, the upflow becomes a material outflow, that can escape gravity but remains trapped by the planet's magnetosphere. In this context, ablation is then the process describing out-flowing material that has escaped the magnetospheric boundary (Moore & Horwitz, 2007). Any liberated atmospheric material then trails behind the exoplanet as it orbits, causing ingress/egress asymmetry in the observed transits (Lecavelier des Etangs, A. et al., 2010; Vanderburg et al., 2015). Typically, this is seen in systems where the planet is in a tight orbit with its host star, so a similar ablation process would, in theory, apply to short-period XRBs.

Interestingly, a similar evaporative wind scenario is considered by Parmar et al. (1991) to explain the heavily extended ingress and egress durations in EXO 0748–676 as observed by *EXOSAT* between 1985 and 1989. The ingress and egress durations are found to be as long as 40 s, are highly variable and show significant asymmetry. Since the atmospheric scale height for a star of the same type as the companion is ~ 100 km (Parmar et al., 1986, 1991), they conclude that the scale height must be enhanced, possibly by an X-ray induced evaporative wind, to explain the long durations and their variability. Our analysis infers a material layer $4 - 20$ times larger than their calculated scale height, supporting the notion that an extended atmosphere or layer of ablated material must be surrounding the companion and significantly extending the ingress and egress duration.

The early ablation scenario and the hypothesis that EXO 0748–676 is a redback tMSP can be tested through extended observations of this source. While currently in quiescence, the source should be rotationally powered, allowing us to search for radio and gamma-ray pulsations. The timescales of transitional pulsar phases are not

well established, so only extended, regular monitoring of EXO 0748–676 can confirm if it will transition back to an accretion-powered state. Similar monitoring will allow us to study the suspected ablation process and the predicted evolution of this source towards a black widow pulsar.

We combine the mass ratio and binary inclination inferred from our eclipse mapping analysis with the previously measured binary mass function (Muñoz-Darias et al., 2009; Bassa et al., 2009; Mikles & Hynes, 2012; Ratti et al., 2012) to yield an estimate for the NS mass. When implementing the H_α radial velocity amplitude of $K_{\rm em}$ =410 $\pm$ 5 km/s derived via DM (Bassa et al., 2009), we find $M_{\rm NS} = 2.01 \pm^{0.22}_{0.21} M_\odot$ and $M_{\rm NS} = 2.02 \pm^{0.29}_{0.27} M_\odot$ when we model the absorbing material with a Gaussian or exponential density function respectively. Under these conditions, we find that the canonical value of $M_{\rm NS} = 1.4 M_\odot$ falls outside of the 3σ contour for both models. For these measurements, we used a *lower limit* of the binary mass function, which was inferred from emission lines that originate from the irradiated face of the companion star (Bassa et al., 2009; Mikles & Hynes, 2012). The true binary mass function is calculated by applying a K-correction (Munoz-Darias et al., 2005). We have considered the most conservative (i.e. closest to unity) K-correction possible when implementing the radial velocity of H_α, such that a more realistic K-correction would *increase* the inferred mass. Indeed, a realistic K-correction of $\sim 0.7 - 0.8$ yields mass distributions that extend into the $3.0 - 5.0 M_\odot$ compact object mass gap.

However, the detection of H_α during quiescence is atypical and there are a number of caveats that require consideration before confidently implementing the DM-derived H_α velocity of 410 $\pm$ 5 km/s (Bassa et al., 2009). Crucial considerations are its inconsistency with all other $K_{\rm em}$ measurements for this source, including the H_α velocity measurement of $K_{\rm em}$ = 345 $\pm$ 5 km/s derived from direct Gaussian fits to the emission line rather than DM (Bassa et al., 2009), and the small associated error ($\sim$ 1 per cent). We therefore also implement the Bowen blend radial velocity

amplitude of $K_{\rm em}$ =329 ± 26 km/s (Mikles & Hynes, 2012) to explore the limits we get without relying on H_α. In this case (i.e. discarding the H_α measurement), assuming a realistic K-correction of $K_{\rm corr} = 0.8$ (Munoz-Darias et al., 2005) gives a NS mass of $M_{\rm NS} = 1.95 \pm^{0.60}_{0.50} M_\odot$ and $M_{\rm NS} = 1.97 \pm^{0.53}_{0.49} M_\odot$ for Gaussian and exponential radial density functions respectively. However, these distributions are broader and only rule out the canonical mass at 1σ level, and assuming the maximum possible K-correction yields a peak posterior below the canonical mass, although, the maximum possible K-correction is somewhat nonphysical. We, therefore, favour a NS mass $\gtrsim 2\ M_\odot$, but cannot definitively rule out the canonical $\sim 1.4\ M_\odot$ value. Future radial velocity measurements of lines originating directly from the companion star surface would dispense with the need for a K-correction and combined with our inclination and mass ratio constraints would yield a precise NS mass measurement. Our measurements are consistent with Özel (2006), who used PRE bursts to measure the mass and radius of EXO 0748–676 to be $M_{\rm NS} = 2.10 \pm 0.28 M_\odot$ and $r_{\rm NS} = 13.8 \pm 1.8$km respectively, thus ruling out soft EoS. Our findings improve confidence in their conclusion, agreeing that a harder EoS is required for nuclear matter.

3.6 Conclusions

We have studied archival *XMM-Newton* observations of X-ray eclipses from EXO 0748–676 in the soft state, finding that they display a gradual decline in-to and out-of-totality. Through timing analysis and phase-resolved spectroscopy, we uncover a narrow region of highly ionised material surrounding the companion star, which preferentially absorbs softer X-rays, creating energy-dependent eclipse profiles. The layer of material is found to be $\sim$ 20 - 40 per cent thicker behind the star than in the direction of orbital motion, thus explaining why the egress is observed to be $\sim$ 2.3 s longer than the ingress. Similar (albeit more extreme) asymmetries are present in radio-band observations of eclipsing spider pulsars, as are frequency-dependent

eclipses. Therefore, we favour an interpretation in which EXO 0748–676 is a spider pulsar progenitor. We invoke an *early ablation* scenario, which introduces a small amount of absorbing material around the companion star. The material is suggested to originate from the surface of the companion star, having been evaporated off by incident radiation from the NS (and accretion flow) or perhaps a pulsar wind. Similar interpretations of EXO 0748–676 have been suggested by Parmar et al. (1991), Ratti et al. (2012) and Parikh et al. (2021).

We model the energy-dependent eclipse profiles of EXO 0748–676 to estimate the mass ratio, $q \sim 0.2$ and the binary inclination angle $i \sim 77^{\circ}$. In eclipsing systems, these values are related via the duration of totality, $t_{\rm e}$; therefore we can combine our measurement of q with the previously measured binary mass function to constrain the NS mass. Using the DM-derived semi-amplitude of the Hα emission line, $K_{\rm em} \approx 410$ km/s (Bassa et al., 2009), yields $M_{\rm NS} \sim 2\ M_{\odot}$ even for the most conservative (closest to unity) K-correction possible to account for the fact that this line originates from the irradiated face of the companion (Munoz-Darias et al., 2005). In this case, the canonical NS mass of $M_{\rm NS} = 1.4\ M_{\odot}$ is outside of our 3σ confidence contour, and use of a more realistic K-correction ($K_{\rm corr} \sim 0.8$) even pushes the posterior NS mass distribution into the $3 - 5\ M_{\odot}$ mass gap. If we instead discard the $\rm H_{\alpha}$ line and rely on the Bowen blend (Mikles & Hynes, 2012), the canonical NS mass is permitted but the peak-posterior value for a realistic K-correction is still $M_{\rm NS} \sim 2\ M_{\odot}$. Future observations of spectral lines emitted directly from the whole companion star surface could be combined with our inclination and mass ratio constraints to yield a precision NS mass measurement.

3.7 Appendix 2A: The X-Ray Emitting Region

If we assume that the companion star is an optically thick sphere with no surrounding material, the ingress duration is the time it takes for the outer radius of the companion

star to cross the finite X-ray emitting region. In this scenario, we can calculate the radius of the (assumed spherical) X-ray emitting region by combining the ingress duration with the totality duration. Let us represent ϕ_1 as the orbital phase at the start of the ingress, ϕ_2 as the beginning of totality, ϕ_3 the end of totality and ϕ_4 the end of egress. Since the centre of totality is at $\phi = 0$, we have that $\phi_1 = -\phi_4$ and $\phi_2 = -\phi_3$ where ϕ_3 and ϕ_4 are positive. The phase duration of totality is therefore $\Delta\phi_{\rm e} = 2\pi\Delta t_{\rm e}/P = \phi_3 - \phi_2 = 2\phi_3$, and the phase duration of ingress is $\Delta\phi_{\rm in} = 2\pi\Delta t_{\rm in}/P = \phi_2 - \phi_1 = \phi_4 - \phi_3$. The projected separation between the centre of the NS and the centre of the companion star at orbital phase ϕ is $R_{\rm cs}b(\phi)$, where the impact parameter $b(\phi)$ is given by Equation (2.4). We can write $b(\phi_3) = 1 - r_x/R_{\rm cs}$ and $b(\phi_4) = 1 + r_x/R_{\rm cs}$ and solve for ϕ_3 and ϕ_4. After applying the small angle approximation ($\sin\phi \approx \phi$), we obtain

$$\Delta\phi_e = \frac{2}{\sin i}\sqrt{\left(\frac{R_{\rm cs} - r_x}{r_a}\right)^2 - \cos^2 i}, \tag{3.4}$$

and

$$\Delta\phi_{\rm in} = \phi_2 - \phi_1 = \frac{1}{\sin i}\sqrt{\left(\frac{R_{\rm cs} + r_x}{r_a}\right)^2 - \cos^2 i} - \frac{\Delta\phi_e}{2}. \tag{3.5}$$

Equations (3.4) and (3.5) are a pair of simultaneous equations with three unknowns: $R_{\rm cs}/r_a$, r_x/r_a and i. We can re-arrange these two equations to find

$$2\frac{r_x}{r_a} = \sqrt{(\Delta\phi_{\rm in} + \Delta\phi_e/2)^2\sin^2 i + \cos^2 i} - \sqrt{(\Delta\phi_e/2)^2\sin^2 i + \cos^2 i}. \tag{3.6}$$

and

$$2\frac{R_{\rm cs}}{r_a} = \sqrt{(\Delta\phi_{\rm in} + \Delta\phi_e/2)^2\sin^2 i + \cos^2 i} + \sqrt{(\Delta\phi_e/2)^2\sin^2 i + \cos^2 i}. \tag{3.7}$$

Therefore, for a given inclination angle, we can calculate r_x/r_a and $R_{\rm cs}/r_a$. We can then assume that the companion fills its Roche-Lobe in order to calculate the mass ratio q from $R_{\rm cs}/r_a$ (Equation 2.3). In order to calculate r_x as a function of i, we then only need to assume a NS mass and calculate r_a from Kepler's law.

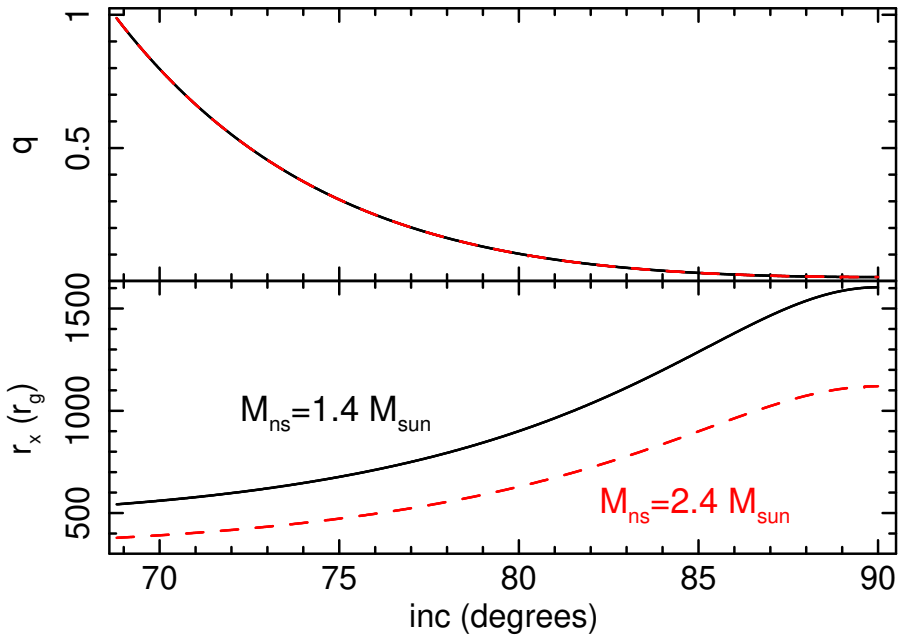

Figure 3.10: Radius of the X-ray emitting region (bottom) and mass ratio (top) inferred from the ingress duration and totality duration assuming that the companion star is an optically thick sphere with no surrounding material. Black solid and red dashed lines correspond to an assumed NS mass of 1.4 $M_\odot$ and 2.4 $M_\odot$ respectively.

Figure 3.10 shows the resulting inferred values of r_x and q as a function of inclination angle for two values of NS mass. We see that r_x increases with i, and recover the simple equation $r_x(i = 90°) = \Delta\phi_{\rm in} r_a/2$ from the main text. For inclination lower than $\sim 69°$, there is no solution for q. The smallest possible X-ray region under our assumptions is therefore $r_x \sim 400\ r_g$. This is implausibly large and adds to the argument that the ingress duration must instead be dominated by an extended stellar atmosphere and/or a layer of ablated material.

3.8 Appendix 2B: Neutron Star Mass

Figure 3.11 is provided to show the posterior NS mass distributions obtained using $K_{\rm em}$ values from Bassa et al. 2009, Ratti et al. 2012 and Muñoz-Darias et al. 2009. Panels A, B and C assume $K_{\rm em} = 345 \pm 5$ km/s (Bassa et al., 2009). This value is subject to the same uncertainties as $K_{\rm em} = 410 \pm 5$ km/s (Bassa et al., 2009), which

is presented in the main text and therefore, is not included in our primary analysis. Panels D, E and F assume $K_{\rm em} = 308.5 \pm 3.9$ km/s (Ratti et al., 2012). Panels G, H and I assume $K_{\rm em} = 310 \pm 10$ km/s (Muñoz-Darias et al., 2009). The latter two radial velocity measurements were not considered in the main text as they are lower than other measured radial velocities, indicating that they originated from a spatial zone further from the centre of mass of the companion and are, therefore, less constraining.

3.9 Appendix 2C: Markov Chain Monte Carlo

To further understand the parameter space of X-TREC, we run a Markov Chain Monte Carlo (MCMC) simulation within XSPEC using the Goodman-Weare algorithm. We run 4 chains using the intrinsic routine `chain`, two assuming the Gaussian density profile and two assuming the exponential density profile. Each chain is run individually, ensuring that the chains assuming the same radial density profile are not correlated. We use a chain length of 307200 with a burn-in period of 92160. Each chain uses 256 walkers and starts, respectively, from their best fits presented in Table 3.4.

Our model assumes a constant out-of-eclipse spectrum so only parameters governing the eclipse profiles are variable during the fits. Therefore, we have 12 free parameters. Two of the parameters are simply normalisations of the eclipse profiles such that the out-of-eclipse count rate equals 1.0 and the time at the centre of totality equals 0.0, so there are 10 key parameters we explore here: t_e, q, $N_{H0,\rm in}$, $N_{H0,\rm eg}$, $\log(\xi)_{\rm in}$, $\log(\xi)_{\rm eg}$ $\rm f_{cov,in}$, $\rm f_{cov,in}$, $\Delta_{\rm in}$, $\Delta_{\rm eg}$ (for the Gaussian density profile only), $\rm h_{in}$ and $\rm h_{eg}$ (exponential density profile only). Figures 3.12 and 3.13 show the output distributions for the Gaussian and exponential models respectively.

When using X-TREC with the Gaussian radial density profile, we see evidence of a positive correlation between $\Delta_{\rm in}$ and$\Delta_{\rm eg}$. Assuming a spherically symmetric system, it can be expected that the amount of material accumulating around the star to increase

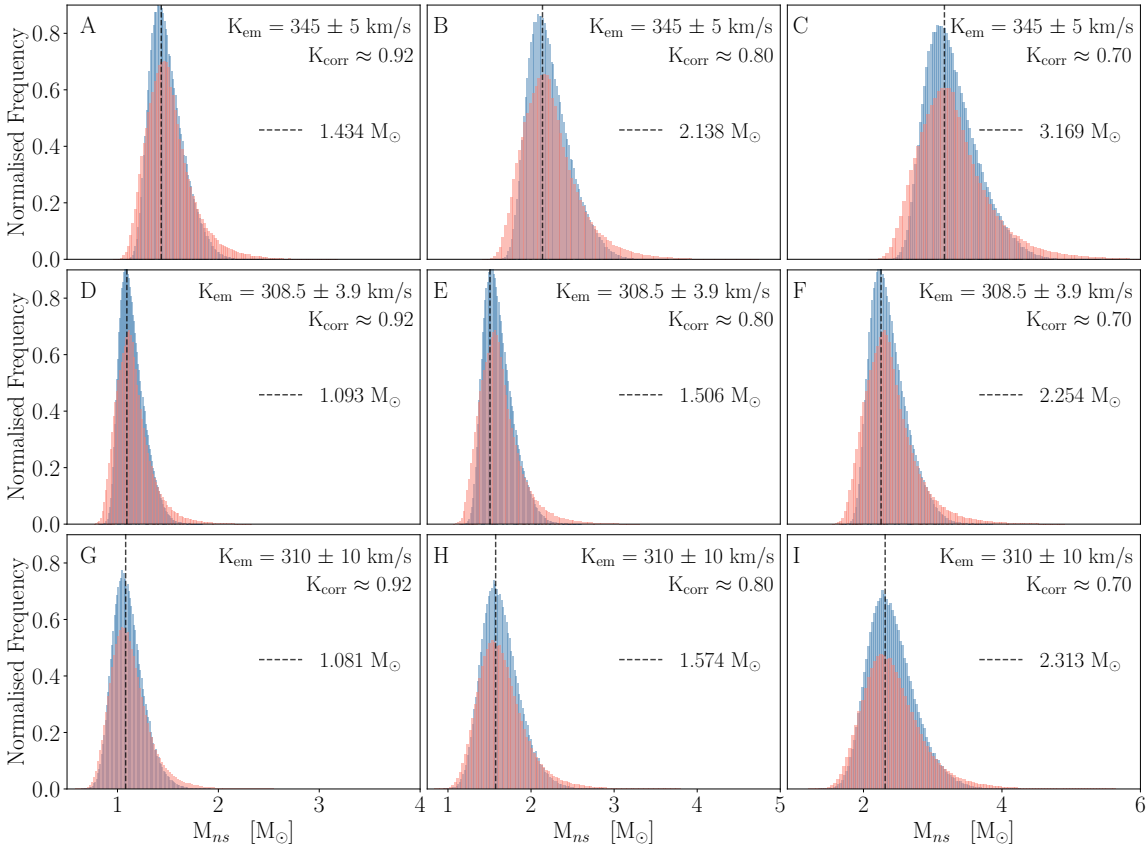

Figure 3.11: Panels A-I: Distributions of $M_{\rm NS}$ assuming the Gaussian (blue) and exponential (red) density profiles within X-TREC calculated using a different combination of $K_{\rm em}$ and K-Correction, which are detailed in each panel. Also shown is a black dashed line corresponding to the mean peak NS mass. The K-correction in A, D and G corresponds to the most conservative value calculated using the mass ratio-dependent relation of Munoz-Darias et al. (2005) (Equation 3.3) for our best fitting value $q = 0.222$. Column 2 (B, E and H) and column 3 (C, F and I) assume the reasonable K-corrections of 0.8 and 0.7 respectively. Emission lines considered are 345 ± 5 km/s from He$_{\rm II}$ (Bassa et al., 2009), 310 ± 10 km/s from He$_{\rm II}$ (Muñoz-Darias et al., 2009) and 308.5 ± 3.9 km/s from a weighted average of H$_\beta$ and H$_\gamma$ (Ratti et al., 2012).

similarly on both sides. The mass ratio is anti-correlated with both $\Delta_{\rm in}$ and$\Delta_{\rm eg}$ which is expected from our formalism presented in Sections 3.3 and 3.4. Similarly, the scale heights, $h_{\rm in}$ and $h_{\rm eg}$ within the exponential radial density profile display a slightly positive correlation. Similar physical arguments to those presented above can explain this relationship. No other correlations are present for these models.

The convergence of each chain is tested using the Geweke convergence measure which compares the mean of each parameter in two intervals of the chain, one shortly after the burn-in period and one towards the end of the chain. These correspond to the first 10% and the last 50% of the chain. For all chains, all parameters measured between ± 0.2, indicating that convergence has been achieved. One parameter remains an exception to this: $N_{H0,\rm eg}$ within the exponential density profile. This parameter is 0.545 and 0.551 for the two chains. The higher Geweke values here are likely a result of an upper limit on the parameter of 5500, which is in place to prevent the walkers from venturing into nonphysical parts of parameter space. Therefore, we remain confident in the convergence of the chain despite this result.

To increase our confidence in the convergence of the chains, we use the Rubin-Gelman convergence test to compare the variances of each parameter in the chain between two chains of the same length. For this test, we implement a stringent bound of $R_c < 1.1$ as an indication of convergence, with higher values indicating parameters are varying too much and have not yet converged. For both models, all parameters give $R_c < 1.05$, therefore we are confident in the convergence of the chains.

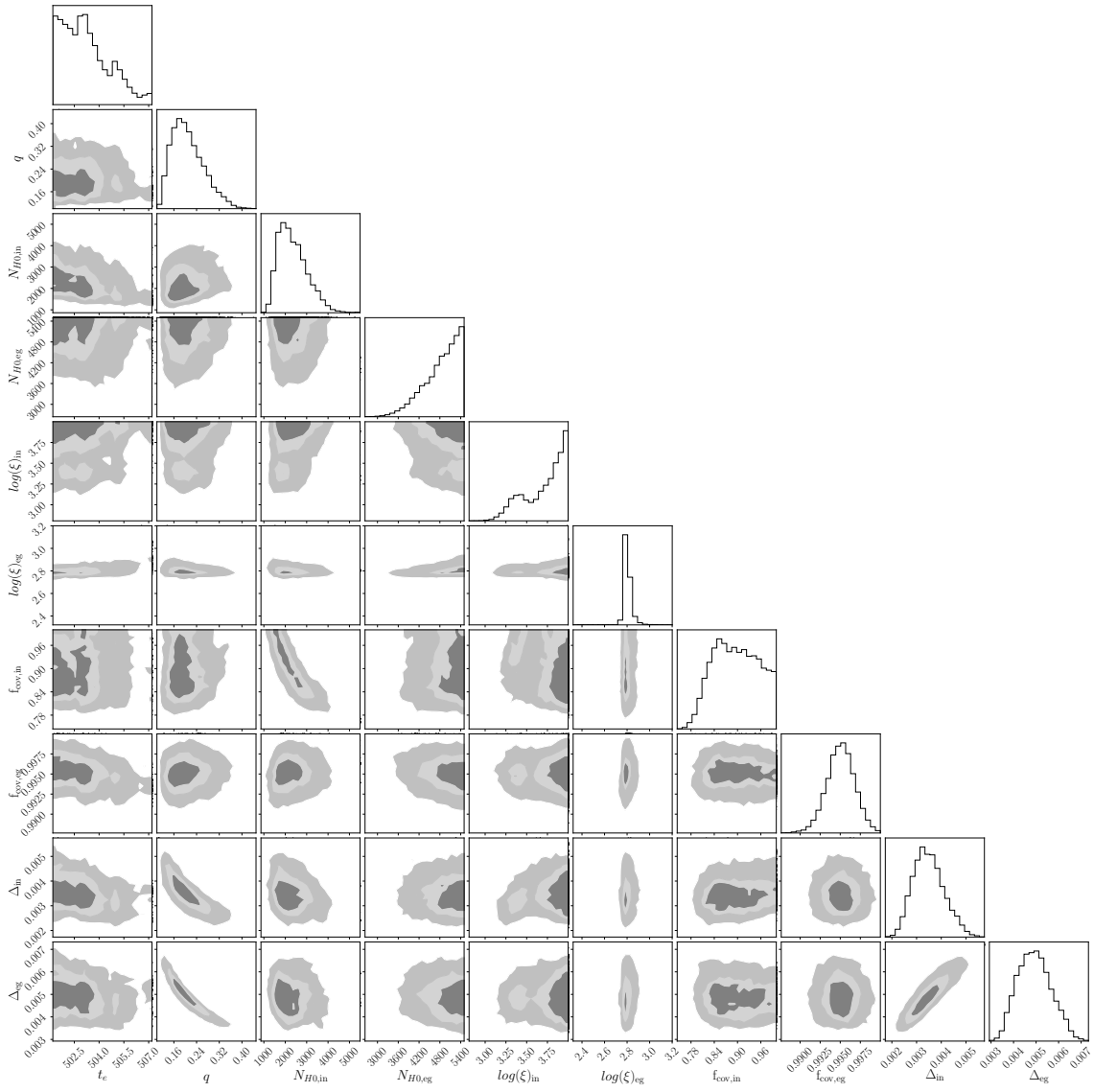

Figure 3.12: Output distributions from the MCMC simulation of X-TREC with the Gaussian density profile with a chain length of 307200, a burn-in period of 92160 and 256 walkers. Hard upper limits of 5500 are used for the surface column densities, $N_{H0,\mathrm{in}}$ and $N_{H0,\mathrm{eg}}$ to prevent the walkers entering non-physical parts of parameters space. For the same reason the ionisation parameters, $\log(\xi)_{\mathrm{in}}$ and $\log(\xi)_{\mathrm{eg}}$, had an upper limit of 4.0. The lines and shading, dark to light, on the 2D histograms, represent 1σ, 2σ and 3σ contours respectively. The y-axes for the 1D histograms are in arbitrary units.

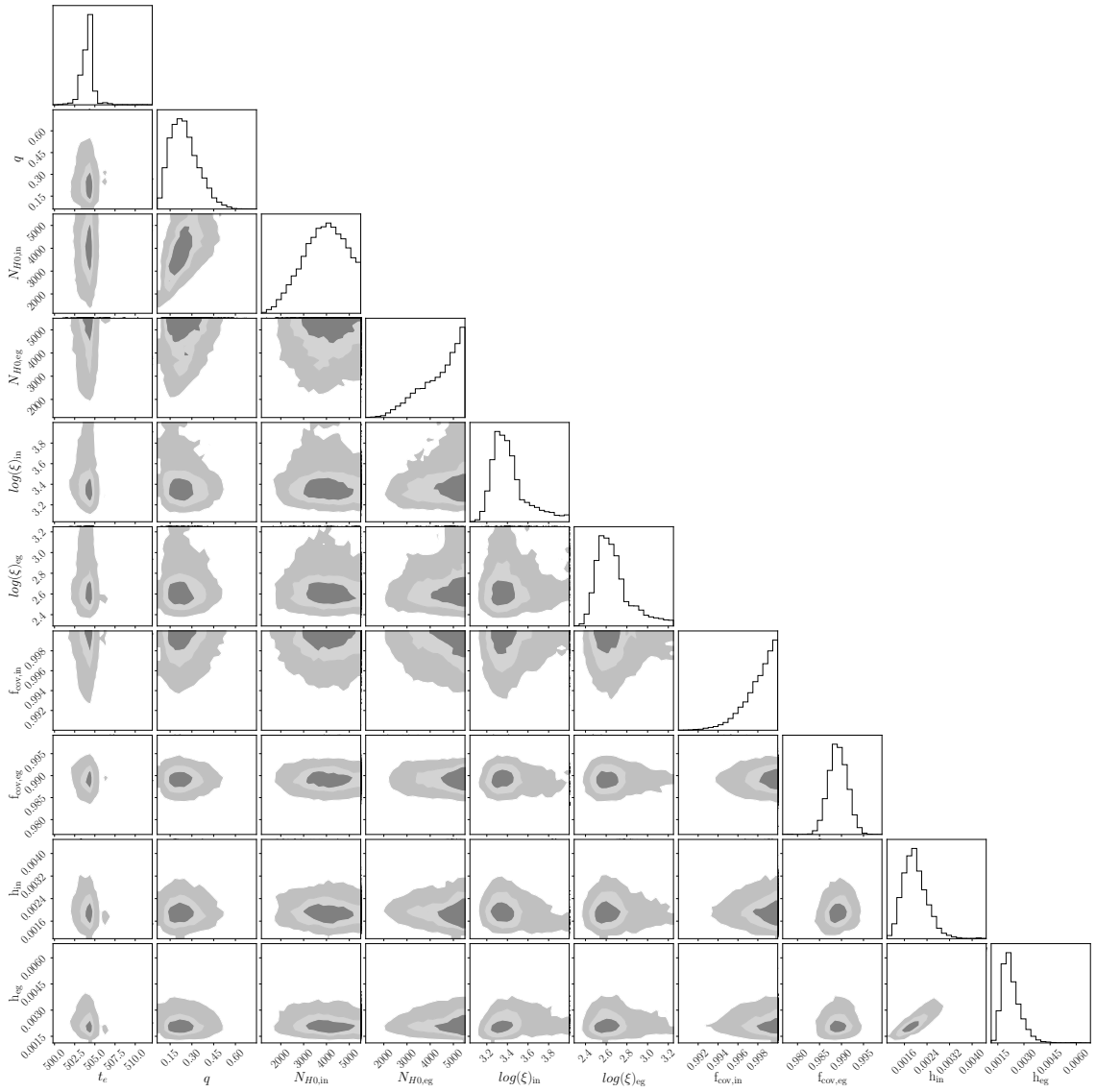

Figure 3.13: Output distributions from the MCMC simulation of X-TREC with the exponential density profile with a chain length of 307200, a burn-in period of 92160 and 256 walkers. Hard upper limits of 5500 are used for the surface column densities, $N_{H0,\mathrm{in}}$ and $N_{H0,\mathrm{eg}}$ to prevent the walkers entering non-physical parts of parameters space. For the same reason the ionisation parameters, $\log(\xi)_{\mathrm{in}}$ and $\log(\xi)_{\mathrm{eg}}$, had an upper limit of 4.0. The lines and shading, dark to light, on the 2D histograms, represent 1σ, 2σ and 3σ contours respectively. The y-axes for the 1D histograms are in arbitrary units.

Chapter 4

Eclipse Mapping of the X-ray Binary *Swift* J1858.6 – 0814

This chapter is adapted from Knight et al. (2022b), in which we apply X-TREC to archival observations of the NS LMXB, *Swift* J1858.6–0814. Our modelling enabled tight constraints on q and i which will lead to a precise NS mass measurement once a radial velocity curve is available. I discuss the possible prior evolution of the binary and suggest the companion star is a highly irradiated sub-giant with a substantial ablated outflow.

4.1 The History of *Swift* J1858.6 – 0814

Swift J1858.6–0814 is a NS LMXB known to exhibit X-ray eclipses once per orbital period that appear heavily extended in time and asymmetric (Buisson et al., 2021). For all observed eclipses, the egress is longer than the ingress. *Swift* J1858.6–0814 was originally discovered as an X-ray transient in October 2018 (Krimm et al., 2018) with a variable counterpart observed at optical (Vasilopoulos et al., 2018; Baglio et al., 2018) and radio (van den Eijnden et al., 2020) wavelengths. Initially, *Swift* J1858.6–0814 displayed significant X-ray variability, with the observed flux changing by factors of hundreds within a few hundred seconds (Hare et al., 2020). As a result, *Swift* J1858.6-0814 was described as an analogue of the BH sources V4641 Sgr and V404 Cyg, which showed similarly strong X-ray variability during their outbursts

(Wijnands & van der Klis, 2000; Revnivtsev et al., 2002; Walton et al., 2017; Motta et al., 2017). *Swift* J1858.6–0814 transitioned from this so-called flaring outburst state (2018 - 2019) to a steady outburst state (2020) with a more persistent X-ray flux. The first half of 2020 saw the steady-state flux decline, and the source has been in quiescence since May 2020 ($\sim$ 58970 MJD) (Saikia et al., 2020; Parikh et al., 2020).

During the steady-state, several Type I X-ray bursts were detected (Buisson et al., 2020), thus identifying *Swift* J1858.6-0814 as a NS LMXB. Currently, there are no detections of X-ray or radio pulsations from the source. The steady-state enabled the discovery of extended and asymmetric eclipses, which appear to depend on energy (Buisson et al., 2021). Analysis by Buisson et al. (2021) of all available *NICER* observations uncovered an average ingress duration of $\sim$ 100 s and an average egress duration of $\sim$ 200 s. By simultaneous calculations of the totality duration and orbital period, they determined the totality duration, $t_{\rm e} \sim 4100$ s and the orbital period $P \sim 21.3$ hrs. Furthermore, the ratio of the eclipse duration to the orbital period constrained the inclination to be $i > 70^{\circ}$. Buisson et al. (2021) utilised their calculated orbital period to determine the companion's mass as a function of radius, concluding that the companion must be a sub-giant due to the large inferred stellar radius and inconsistency with the main sequence mass-radius relation of Demircan & Kahraman (1991).

4.2 Data Reduction and Analysis

We consider all available archival *NICER* observations of *Swift* J1858.6–0814 during outburst; these are all ObsIDs beginning with 120040, 220040, 320040 or 359201. These observations occurred between November 2018 and July 2020, thus containing detections from both the flaring and steady outburst states.

4.2.1 Data Reduction

The data are reduced using the *NICER* data reduction software NICERDAS V008 (HEASoft V6.29, CALDB 20210707), keeping most filtering criteria to their default values (e.g Buisson et al. 2021). We include data taken at low Sun angle by following the procedure of Buisson et al. (2021) and relax the undershoot rate limit to allow up to 400 cts/s (per FPM). At low Sun angles, optical loading is relatively high, which can deteriorate the response and raise the background at energies $\lesssim 0.4$ keV. This does not impact our timing analysis or modelling of eclipses between $0.4 - 10.0$ keV. We again follow Buisson et al. (2021) to carefully remove any achromatic dips arising from occultation of the detector plane by parts of the ISS as there are some instances in which these are not filtered out by the *NICER* pipeline. We apply barycentric corrections and use `xselect` to extract $0.4 - 10.0$ keV time-averaged spectra and light curves with 1 second time bins, in seven energy bands; $0.4 - 10.0$ keV, $0.4 - 1.0$ keV, $1.0 - 2.0$ keV, $2.0 - 4.0$ keV, $4.0 - 6.0$ keV, $6.0 - 8.0$ keV and $8.0 - 10.0$ keV.

4.2.2 Eclipse Profiles

To obtain eclipse profiles in each energy band, we fold the data on the orbital period $P = 76841.3^{+1.3}_{-1.4}$ s (≈ 21.3 hours) (Buisson et al., 2021) and divide through by the mean out-of-eclipse count rate. Fig. 4.1 shows the resulting eclipse profiles for all seven energy bands, displayed with vertical offsets for visual clarity. Note that the eclipse profile in Fig. 4.1 arises from partial eclipses only since the eclipse duration of ~ 4100 s (Buisson et al., 2021) is too long to be observed in full by *NICER*. We find 5 ingresses ($\sim$ orbital cycles 39, 43, 47, 52 and 56) and 7 egresses ($\sim$ orbital cycles 28, 32, 38, 42, 50, 51 and 55), where the zeroth orbital cycle is defined to coincide with the onset of the steady state at ~ 58885 MJD (Buisson et al., 2021). Since we divide through by the mean out-of-eclipse count rate, the stacked eclipse profile for each energy band reaches unity during out-of-eclipse phases. The totality, however,

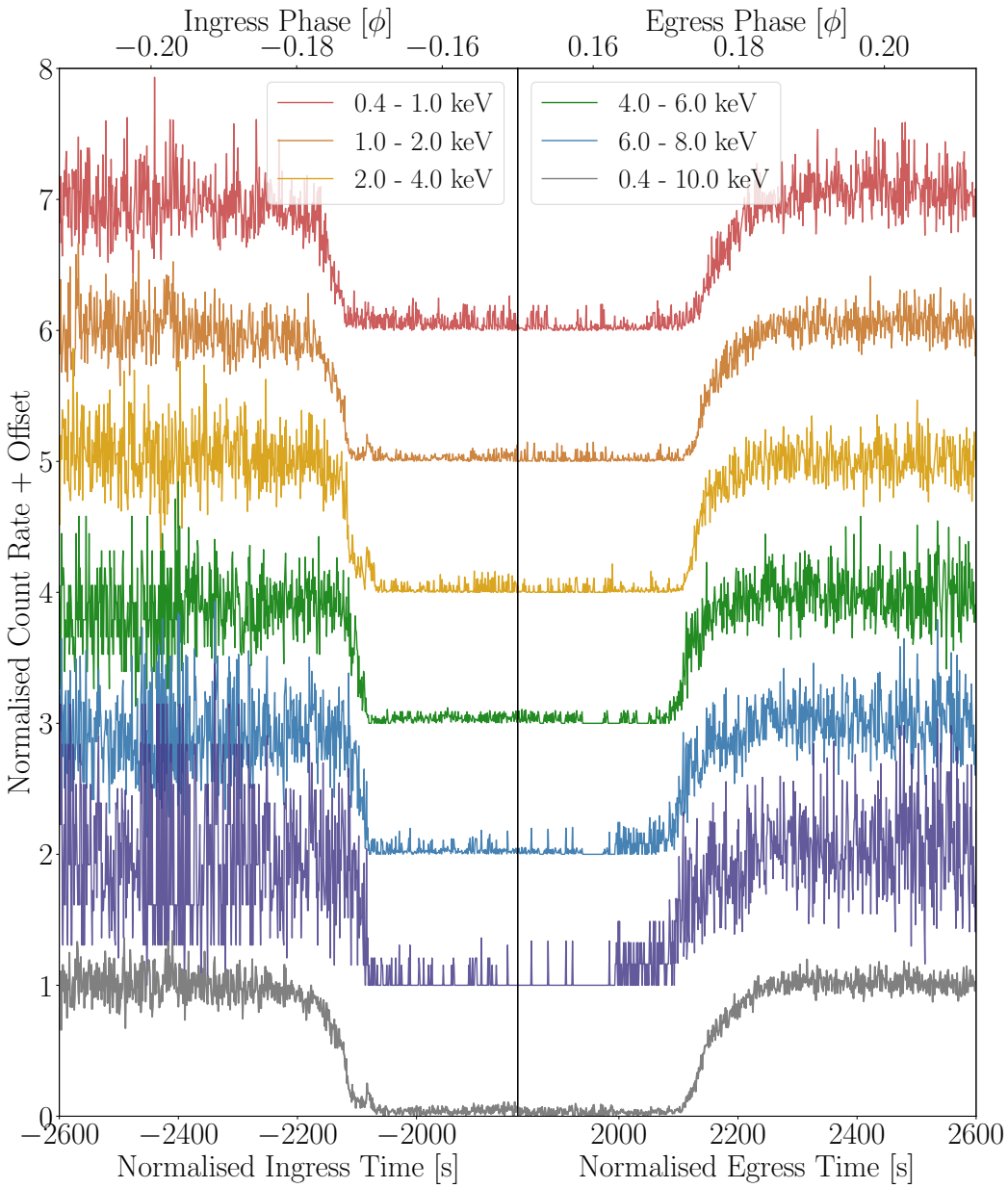

Figure 4.1: Folded eclipse profiles of *Swift* J1858.6-0814 shown for seven energy bands; $0.4-1.0$ keV (red), $1.0-2.0$ keV (orange), $2.0-4.0$ keV (yellow), $4.0-6.0$ keV (green), $6.0-8.0$ keV (blue), $8.0-10.0$ keV (magenta) and $0.4-10.0$ keV (grey). These have been obtained by folding the extracted light curves on the orbital period $P = 76841.3$ s (Buisson et al., 2021) and dividing through by the mean out-of-eclipse count rate. Note that *NICER* only observed partial eclipses (5 ingresses and 7 egresses). All eclipse profiles are normalised to have a mean out-of-eclipse level of 1.0 and a mean totality level of ~ 0.05 (the totality level is not 0.0 due to a low in-eclipse background count rate). The light curves are shifted such that the time at the centre of the eclipse is at 0.0 seconds ($\phi = 0.0$). The eclipse profiles are shown with a vertical offset. These are +0.0 (grey), +1.0 (magenta), +2.0 (blue), +3.0 (green), +4.0 (yellow), +5.0 (orange) and +6 (red).

is ~ 0.05 and not zero due to a background contributed, low in-eclipse count rate. The eclipse profiles are also shifted such that the time at the centre of the eclipse is 0.0 s (orbital phase $\phi = 0.0$).

Swift J1858.6-0814 shows two distinct outburst states - the flaring state and the steady-state divided at MJD 58885 (see in Fig. 1 of Buisson et al. 2021). The eclipses are only readily apparent in the light curves of the more recent (2020) steady-state, which show partial eclipses in the form of 5 ingresses and 7 egresses. However, the flaring state observations are also consistent with including eclipses at the orbital phases expected from analysing the steady state. The extreme flaring and frequent telemetry drop-outs make it difficult to identify eclipses in the light curves during the flaring state, but folding all observations on the orbital period derived from the steady-state observations reveals that the flaring state count rate is always consistent with the background during expected totality phases (Buisson et al., 2021). Despite this, there are no clear ingresses or egresses in the flaring state data since they all happen to occur within telemetry gaps.

We see from Fig. 4.1 that the eclipse ingress and egress are both heavily extended in time, with the egress appearing to be longer in duration than the ingress (consistent with the analysis of Buisson et al. 2021). We also see the eclipse profile shape, and therefore ingress and egress duration appears to depend on photon energy. To investigate this further, we plot estimates of the start and end times of ingress and egress as a function of energy in Fig. 4.2. Here, following Knight et al. 2022a, a time during an eclipse transition, t_x, is defined as the time at which the count rate first passes x per cent of the mean out-of-eclipse level and remains past it for ~ 5 s. Therefore, when applied to the ingress and egress, $x = 90$ measures the ingress start time and the egress end time, while $x = 10$ measures the totality start and end times.

The t_{90} times depend strongly on energy. For the ingress, t_{90} increases with photon energy and the egress t_{90} mirrors this, decreasing with photon energy. This

behaviour is well described by a logarithmic equation (solid blue trend line in Figs. 4.2A and 4.2B). For both the ingress and egress, t_{10} is approximately independent of energy, although some variations are observed. These variations likely result from the presence of a background contributed, fluctuating, low in-eclipse count rate. The t_{10} and t_{90} behaviour is equivalent to the duration of both the ingress and egress decreasing with increasing energy. This is shown explicitly in Figs. 4.2C and 4.2D respectively for the ingress and egress. These plots additionally confirm that the egress is longer in duration than the ingress. We measure the ingress duration to be $t_{10,in,0.4-10.0keV} - t_{90,in,0.4-10.0keV} \approx 106$ s and the egress duration to be $t_{90,eg,0.4-10.0keV} - t_{10,eg0.4-10.0keV} \approx 174$ s.

These extended, asymmetric, energy-dependent eclipse transitions are similar to those observed in EXO 0748–676 by *EXOSAT* (Parmar et al., 1991), *RXTE* (Wolff et al., 2009) and *XMM-Newton* (Knight et al., 2022a), and can be explained by the presence of an ionised layer of material around the companion star (Knight et al., 2022a). As our sight-line passes closer to the companion star, the column density of the material layer increases thus causing an energy-dependent drop in flux during the ingress. A sufficiently high column density is, therefore, achieved close to the companion's surface and results in energy independence at the start and end of totality. The eclipse asymmetry can be explained if the absorbing medium trails behind the companion star as a result of the star's orbital motion.

4.2.3 Fit to the Time-Averaged Spectrum

Using XSPEC V12.12.0 (Arnaud, 1996), we fit the time-averaged spectrum with the model

$$\text{TBABS*(LAOR+DISKBB+BBODY)*E*A*G}. \tag{4.1}$$

Here, DISKBB and BBODY respectively describe the multi-temperature spectrum originating from the accretion disc and a blackbody spectrum originating from the NS

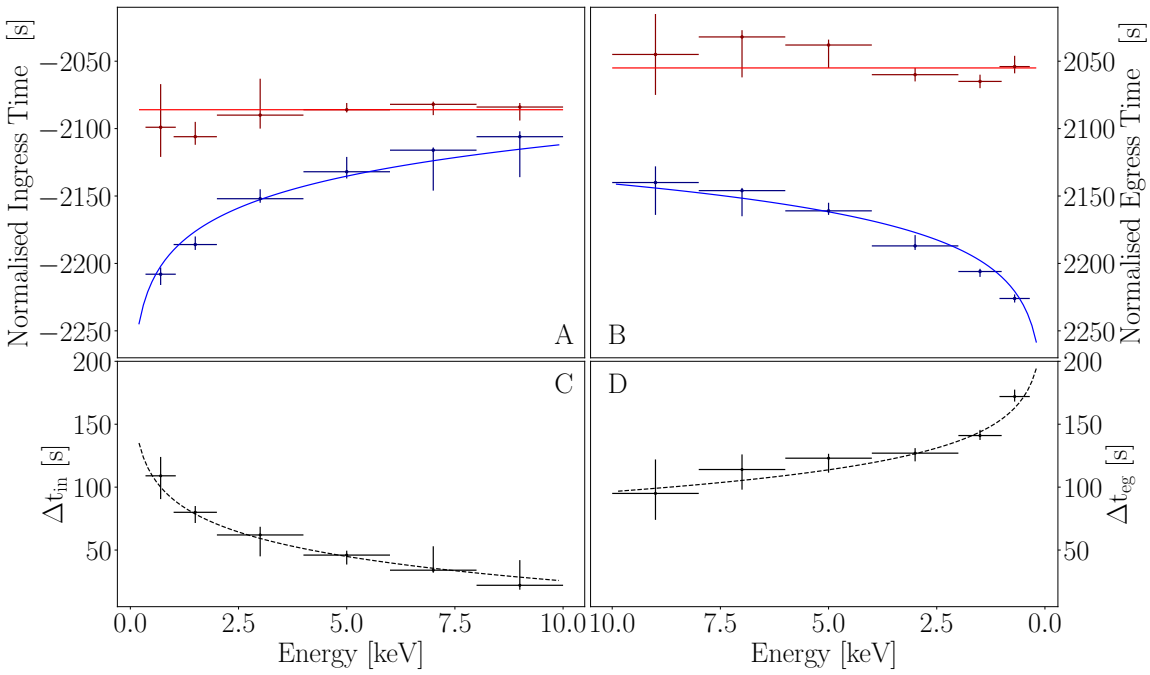

Figure 4.2: Eclipse transition times, t_{90} and t_{10}, as functions of energy. A time during the eclipse transition, t_x, is defined as the time at which the count rate first passes x per cent of the mean out-of-eclipse level (e.g. Knight et al. 2022a). Panel A: t_{90} (blue) represents the start of the ingress, which starts earlier for lower energies. The start of totality, t_{10} (red), is approximately independent of energy. Panel B: The end of totality (red) is approximately independent of energy, but the end of the egress (blue) depends on energy, ending later for softer X-rays. For the ingress and egress, t_{90} and t_{10} have been measured from the folded eclipse profiles in Fig. 4.1. Panels C and D: The eclipse transition duration as a function of energy. The duration decreases with increasing photon energy and the egress is consistently longer in duration than the ingress. Note that both sets of axes have been reversed to assist the comparison between the ingress and egress.

surface. Absorption by the interstellar medium is accounted for by TBABS and assumes the abundances of Wilms et al. (2000).

The spectrum requires an emission contribution from Fe Kα which is modelled as a LAOR emission line with $E = 6.57$ keV (Laor, 1991). The LAOR component models the Fe Kα line as a relativistically smeared line, assuming a delta function in the rest frame. It would be more precise to instead use a full X-ray reflection model such as RELXILL (García et al., 2014), which also accounts for effects such as electron scattering and absorption edges. We attempted spectral fits using RELXILL, XILLVER

and XILLVERCP (flavours of the RELXILL model), but found that these models were not well suited to modelling the softer X-ray components of the spectrum. Nonetheless, the LAOR component captures the asymmetrically broadened shape of the line indicative of relativistic smearing from a highly inclined disc.

There are 3 further components in our spectral model: `E`, `A` and `G`. Here, `E` corresponds to two absorption edges (EDGE) at 0.48 keV and 2.22 keV. These features likely arise from *NICER* calibration systematics as they could be attributed to Oxygen ($\sim$ 0.5 keV) and a gold M edge (2.1–4.5 keV complex) (Wang et al., 2021). `A` corresponds to three Gaussian absorption lines (GABS) at energies 2.37 keV, 2.79 keV and 6.97 keV. The first two are likely associated with the aforementioned gold M absorption while the third physically corresponds to Fe XXVI Kα. Lastly, `G` represents four Gaussian emission lines (GAUSS) at energies 1.77 keV (Si VIII Kα), 0.718 keV (Fe XVIII Lβ), 1.47 keV (Al Kα) and 2.10 keV (P XIV Kβ). These are assumed to be real features except for Al Kα which may arise from *NICER* calibration systematics (Wang et al., 2021).

We show the resulting model (red) in Fig. 4.3. The individual components, respectively, are coloured green, magenta and blue which correspond to the Laor iron line profile, the NS surface blackbody and the multi-temperature blackbody originating from the accretion disc. The astrophysical emission lines at 0.718 keV (Fe Lβ), 1.77 keV (Si Kα), and 2.10 keV (P kβ) are shown in cyan and the 1.47 keV (Al Kα) emission line, suspected to be present as a result of *NICER* calibration systematics is shown in orange. Our fit returns the parameters listed in Table 4.1, a reduced χ^2 of $\chi^2/\nu = 834.42/815$ and the corresponding null hypothesis probability is $p = 0.414$. The eclipse duration (the sum of the duration of the ingress, totality and egress) is $\sim$ 4400 s, corresponding to $\sim$ 0.06% of the orbital period. Also, the in-eclipse count rate is low. As such, it is reasonable to assume the out-of-eclipse can be approximated by the time-averaged spectrum. Therefore, we use the time-averaged

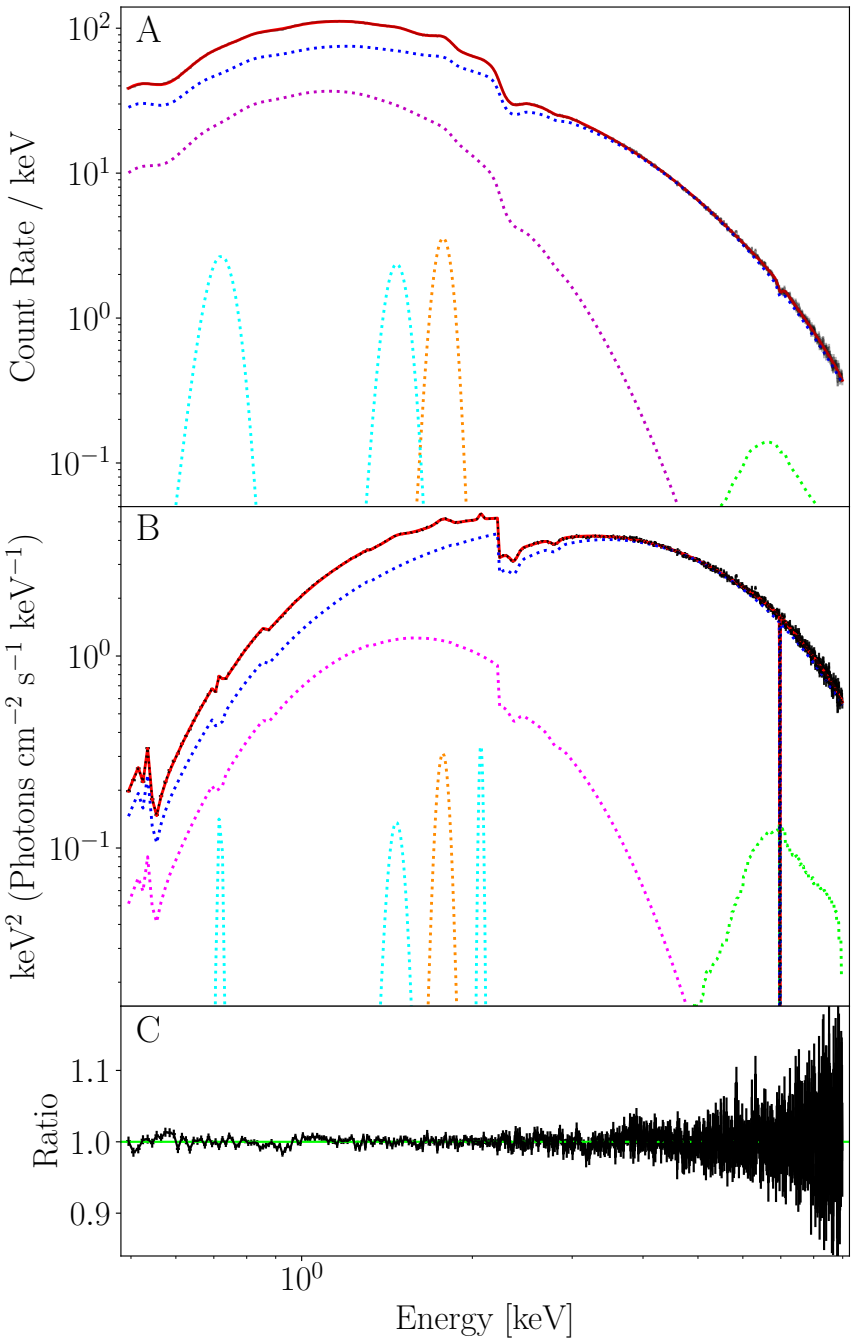

Figure 4.3: Panels A (best-fitting folded spectrum) and B (best-fitting unfolded spectrum): The time-averaged spectrum of *Swift* J1858.6-0814 (black) fit with the multi-component model (red) detailed in Section 4.2.3. The individual components coloured blue and magenta originate from the accretion disc and the NS surface respectively. Also shown are the Laor iron line profile (green), astrophysical emission lines (cyan) and an emission line likely originating from *NICER* calibration systematics (orange). These emission lines correspond to 0.718 keV (Fe XVIII Lβ), 1.47 keV (Al Kα, orange) , 1.77 keV (Si VIII Kα), and 2.10 keV (P XIV Kβ). Model parameters are summarised in Table 4.1. Panel C: The ratio data/folded model.

Model Component	Parameter	Value
TBABS	N_H [10^{22} cm^{-2}]	$0.233 \pm^{0.002}_{0.002}$
DISKBB	T_{in} [keV]	$1.186 \pm^{0.006}_{0.002}$
BBODY	kT [keV]	$0.356 \pm^{0.003}_{0.003}$
LAOR	E [keV]	$6.573 \pm^{0.057}_{0.060}$
	Γ	$2.376 \pm^{0.177}_{0.177}$
	R_{in} [GM/c^2]	$4.892 \pm^{0.636}_{0.853}$
	R_{out} [GM/c^2]	400.0 [a]
	i [deg]	$86.20 \pm^{0.323}_{0.028}$
Absorption Edges (E)	E_1 [keV]	$2.224 \pm^{0.001}_{0.001}$
EDGE	$\tau_{max,1}$ [keV]	$0.368 \pm^{0.005}_{0.006}$
	E_2 [keV]	$0.482 \pm^{0.043}_{0.059}$
	$\tau_{max,2}$ [keV]	$0.803 \pm^{0.006}_{0.002}$
Absorption Lines (A)	E_1 [keV]	$2.369 \pm^{0.003}_{0.004}$
GABS	σ_1 [keV]	$0.038 \pm^{0.007}_{0.007}$
	E_2 [keV]	$2.797 \pm^{0.006}_{0.007}$
	σ_2 [keV]	$0.048 \pm^{0.010}_{0.011}$
	E_3 [keV]	$6.974 \pm^{0.008}_{0.008}$
	σ_3 [keV]	$0.002 \pm^{0.043}_{0.001}$
Emission Lines (G)	E_1 [keV]	$1.772 \pm^{0.004}_{0.004}$
GAUSS	σ_1 [keV]	$0.042 \pm^{0.007}_{0.004}$
	E_2 [keV]	$0.7181 \pm^{0.004}_{0.004}$
	σ_2 [keV]	$0.006 \pm^{0.012}_{0.001}$
	E_3 [keV]	$1.466 \pm^{0.007}_{0.006}$
	σ_3 [keV]	$0.043 \pm^{0.009}_{0.009}$
	E_4 [keV]	$2.071 \pm^{0.007}_{0.007}$
	σ_4 [keV]	$0.016 \pm^{0.019}_{0.002}$

Table 4.1: Best-fitting parameters from our fit to the time-averaged spectrum of *Swift* J1858.6 -0814, achieving a reduced χ^2 is $\chi^2/\nu = 834.42/815$. The absorption edges at centroid energies E_1 and E_2 are likely features arising from *NICER* calibration systematics, as they could be associated with oxygen and a gold M edge (2.1–4.5 keV complex) respectively (Wang et al., 2021). Gaussian absorption lines (GABS) at energies 2.37 keV and 2.79 keV also fall within this absorption complex. The (GABS) component at 6.97 physically corresponds to Fe XXVI Kα. The four Gaussian emission lines are at energies 0.718 keV (Fe XVIII Lβ), 1.47 keV (Al Kα) , 1.77 keV (Si VIII Kα), and 2.10 keV (P XIV Kβ). These are assumed to be real features except for Al Kα which may also arise from *NICER* calibration systematics.
[a] Parameter fixed for the duration of the fit.

spectrum within X-TREC. Note that X-TREC is not sensitive to the X-ray spectral model used, but simply requires a reasonable fit to the observed spectrum (see Knight et al. 2022a). Since we assume an X-ray point source, any spectral decomposition that fits the observed spectrum would have the same time dependence. Therefore, the X-ray spectral model is not critical to the results obtained via eclipse mapping. As such we are content with our spectral model including a LAOR iron line profile and we do not pursue a more complex reflection model.

4.3 Eclipse Mapping

In Section 4.2 we demonstrated that the observed eclipse profiles of *Swift* J1858.6 – 0814 have many of the same characteristics (extended in time, asymmetric and energy-dependent) as those of EXO 0748–676 (Parmar et al., 1991; Wolff et al., 2009; Knight et al., 2022a). Furthermore, an orbital phase-resolved spectral analysis of the ingress and egress regions in *Swift* J1858.6-0814, returns similar results to our previous analysis of EXO 0748–676 (Knight et al., 2022a). As such, it seems sensible to use the same modelling approach for *Swift* J1858.6-0814 as we used for EXO 0748–676. Therefore, we model the eclipses using X-TREC version 1.0 and consider all available radial density profiles for the companion's outflow (see Section 2.2). We fix the obrital period to the known value of $P = 76841.3^{+1.3}_{-1.4}$ s (≈ 21.3 hours) (Buisson et al., 2021), the redshift is $z = 0$ and $\mathrm{n_e/n_H} = 1.0$.

4.3.1 Results

We simultaneously fit the eclipse profiles of *Swift* J1858.6 -0814 in five energy bands; $0.4 - 1.0$ keV, $1.0 - 2.0$ keV, $2.0 - 4.0$ keV, $4.0 - 6.0$ keV and $6.0 - 10.0$ keV using XSPEC v12.12.0 and X-TREC version 1.0. All eclipse profiles are obtained following the procedure described in Section 4.2.2. Note the $6.0 - 10.0$ keV band is preferred to separate $6.0 - 8.0$ keV and $8.0 - 10.0$ keV bands as the former has a higher number of

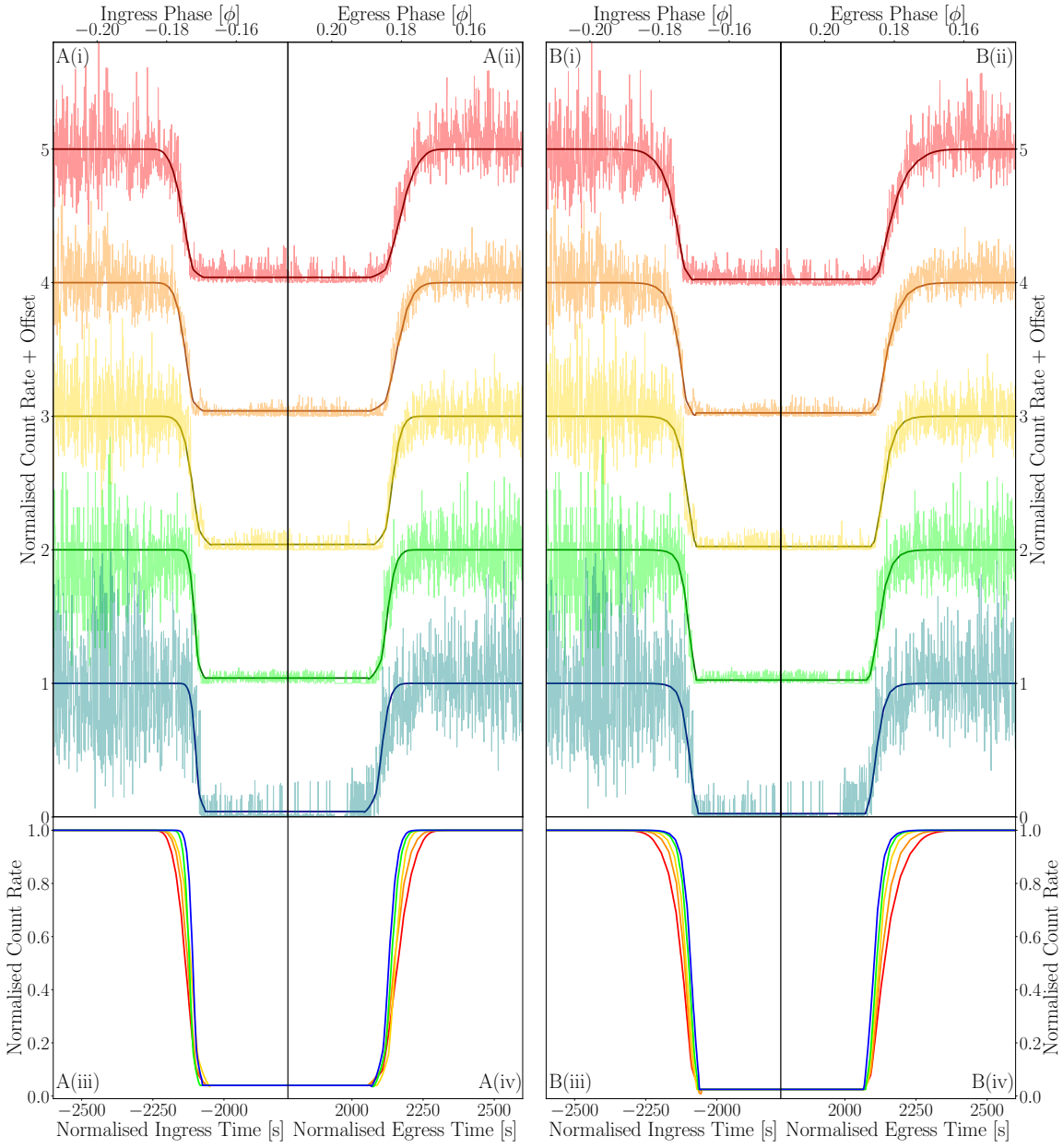

Figure 4.4: Eclipse fits obtained by simultaneously fitting the eclipse profiles of *Swift* J1858.6–0814 with X-TREC in five energy bands ($0.4-1.0$ kev: red, $1.0-2.0$ kev: orange, $2.0-4.0$ kev: yellow, $4.0-6.0$ kev: green and $6.0-10.0$ kev: teal) with X-TREC, assuming the Gaussian radial density profile (A(i–iv)) and the exponential radial density profile (B(i–iv)). Panels A(i–ii) and B(i–ii): the resulting fits to each energy band, displayed with vertical offsets (+0.0 (teal), +1.0 (green), +2.0 (yellow), +3.0 (orange) and +4.0 (red)). Panels A(iii–iv) and B(iii–iv): the resulting eclipse profiles without a vertical offset, thus clearly displaying the energy-dependent behaviour. For the Gaussian (A) and exponential (B) models respectively, $\chi^2/\nu = 2723.6/2673$ and $\chi^2/\nu = 2679.0/2673$.

Density Profile	Parameter(s)	χ^2	ν	p	q
No Material	-	104600	2675	-	-
Power-law	m = 2.00 [a]	99100	2675	-	-
	m = 10.0 [a]	32900	2675	-	-
	m_{in} = 198.2	2696.0	2673	10^{-102}	0.139
	m_{eg} = 178.9				
Accelerating	β_{in} = 6.12	4640.6	2673	10^{-136}	0.137
	β_{eg} = 7.68				
Gaussian	Δ_{in} = 0.0099	2723.6	2673	0.433	0.140
	Δ_{eg} = 0.0119				
Exponential	h_{in} = 0.0086	2679.0	2673	0.464	0.139
	h_{eg} = 0.0135				

Table 4.2: For each radial density profile, the characteristic density profile parameters and associated fit statistics are found by fitting X-TREC to the eclipse profiles of *Swift* J1858.6–0814 in multiple energy bands. The best-fitting values of the key density profile parameters (power-law index, m, acceleration parameter, β, fractional width of the material, Δ, and fractional scale height, h, for the power-law, accelerating, Gaussian and exponential density profiles respectively) are each presented with their associated chi-squared, χ^2, the number of degrees-of-freedom, ν, the null hypothesis probability, p, and the mass ratio, q for all fits where constraints were possible.
[a] Parameter fixed for the duration of the fit.

counts per bin, thus allowing the use of chi-squared fit statistics. We ensure the best-fitting model parameters primarily correspond to the eclipse transitions, which host the energy-dependent behaviour, by ignoring most of the out-of-eclipse and totality phase bins. Despite this, a systematic error of 15 per cent is applied to account for the variability in the remaining out-of-eclipse portion of the data. The eclipse duration has previously been measured as $t_e = 4098 \pm^{17}_{18}$ s (Buisson et al., 2021), therefore, we initially set $t_e = 4100$ s but keep it as an unconstrained free parameter during the fits.

Following the modelling approach of Knight et al. (2022a), we first trial X-TREC with no absorbing material surrounding the companion. Given the extended ingress and egress duration in the eclipse profiles, it is unsurprising that this model fits the data poorly ($\chi^2/\nu = 104600/2675$). Therefore, the data require some absorbing medium surrounding the companion star to recreate the extended and asymmetric

Parameter	Gaussian Density Profile	Exponential Density Profile
P [s]	76841.3	76841.3
$t_{\rm e}$	$4103.52\ \pm^{1.19}_{1.03}$	$4096.17\pm^{0.02}_{1.66}$
q	$0.1402\ \pm^{0.0028}_{0.0037}$	$0.1394\ \pm^{0.0021}_{0.0019}$
i°	$80.90\ \pm^{0.13}_{0.10}$	$80.96\ \pm^{0.08}_{0.09}$
$\log(\xi)_{\rm in}$	$1.935\ \pm^{0.010}_{0.007}$	$1.906\ \pm^{0.044}_{0.032}$
$\log(\xi)_{\rm eg}$	$1.953\ \pm^{0.016}_{0.004}$	$1.910\ \pm^{0.012}_{0.012}$
$\rm f_{cov,in}$	$0.999\ \pm^{0.001}_{0.0001}$	$0.980\ \pm^{0.009}_{0.016}$
$\rm f_{cov,eg}$	$0.997\ \pm^{0.003}_{0.005}$	$0.984\ \pm^{0.009}_{0.005}$
$\Delta_{\rm in}$ or $\rm h_{in}$	$0.0099\ \pm^{0.0004}_{0.0010}$	$0.0086\ \pm^{0.00004}_{0.00110}$
$\Delta_{\rm eg}$ or $\rm h_{eg}$	$0.0119\ \pm^{0.0003}_{0.0004}$	$0.0135\ \pm^{0.00092}_{0.00004}$

Table 4.3: Best-fitting model parameters, for both the Gaussian and exponential density profiles, found by fitting X-TREC to the eclipse profiles of *Swift* J1858.6–0814 in five energy bands simultaneously. The parameters are orbital period (fixed for the duration of the fitting), totality duration (t_e), the mass ratio (q), binary inclination (subsequently calculated using the best-fitting q and t_e), log of the ionisation parameter for the ingress and egress ($\log(\xi)_{\rm in}$ and $\log(\xi)_{\rm eg}$), covering fraction for the ingress and egress ($\rm f_{cov,in}$ and $\rm f_{cov,eg}$, and the characteristic density profile parameter for the ingress and egress. These characteristic parameters are the fractional widths of the material layer (Δ) for the Gaussian model and material scale heights (h) for the exponential model. Values are provided with a 1 σ error obtained via MCMC.

ingress and egress. We test the four radial density profiles detailed in Section 2.2.2 and present the resulting fit statistics in Table 4.2. Although the assumed form of the density profile has a large influence on fit quality, it has little effect on the inferred mass ratio, which is $q \sim 0.14$ for all fits where constraints are possible.

Assuming reasonable power-law indices of $m = 2$ and $m = 10$, the power-law radial density profile does not yield a good fit to the data. Respectively, the reduced chi-squared are $\chi^2/\nu = 99100/2675$ and $\chi^2/\nu = 32900/2675$, the associated null-hypothesis probabilities are negligible and the mass ratios are unconstrained. Allowing the power-law indices to be free during the fits yields unphysical values of $m_{\rm in} = 198.2$ and $m_{\rm eg} = 178.9$ for the ingress and egress respectively. While a statically better fit is achieved here ($\chi^2/\nu = 2969.0/2673$) than for the fits assuming power-law indices of $m = 2.0$ and $m = 10.0$, it is clear that the data require a steeper radial density function. Thus, we discard the power-law density profile.

The accelerating wind profile is a steeper function, with the density dropping off more quickly with distance from the companion star's surface, thus could improve upon the fits using the power-law density profile. However, this radial density function is simply too steep to model the heavily extended eclipse transitions we observe and is, therefore, discarded. The best-fitting acceleration parameters for the ingress and egress respectively are $\beta_{\rm in} = 6.12$ and $\beta_{\rm eg} = 7.68$, yielding $\chi^2/\nu = 4640.6/2673$, and the associated null-hypothesis probability is, $p = 10^{-136}$.

The remaining two density profiles yield acceptable fits to the observed eclipse profiles. We show the resulting eclipse profiles for both the Gaussian and exponential density profiles in Fig. 4.4A(i) - A(iv) and Fig. 4.4B(i) - B(iv) respectively. For the Gaussian and exponential density profiles we obtain $\chi^2/\nu = 2723.6/2673$ ($p = 0.433$) and $\chi^2/\nu = 2679.0/2673$ ($p = 0.464$) respectively. Since both fits are statistically similar, we consider both density profiles in our subsequent analysis and present the best fitting parameters from both models in Table 4.3.

The best-fitting model parameters obtained assuming the Gaussian radial density profile are found to be consistent with the best-fitting model parameters obtained assuming the exponential radial density profile within a 1σ error, thus increasing confidence in our constraints on q and subsequent constraints on i. We find consistent ionisation parameters between the ingress and egress side of the star, which is in contrast to EXO 0748–676 where the ingress appeared to be more heavily ionised (Knight et al., 2022a). Overall, the surrounding material is less ionised in *Swift* J1858.6–0814 where $\log(\xi) \sim 1.9$ than for EXO 0748–676 where $\log(\xi) \sim 3.0$. We further find consistent covering fractions between the ingress and egress, in contrast to EXO 0748–676, where the Gaussian model suggested the leading side of the companion to be less covered. The energy-dependent eclipse timings predicted by the model strongly depend on the density profile chosen, since this governs the X-ray absorption in the surrounding medium. We find both density profiles can recreate

both t_{90} and t_{10} behaviour presented in Fig. 4.2. The t_{10} behaviour is more difficult to model because it relies on a sufficiently high material density and a high material ionisation. Nonetheless, our modelling can reproduce this and the overall eclipse models are shown in Fig. 4.4.

4.3.2 Binary Inclination and Mass Ratio

Our fits to the observed eclipse profiles assuming a Gaussian and exponential density profile each return best-fitting values for model parameters t_e and q. The binary inclination i can then be found from these parameters and Equation 2.5. We constrain posterior distributions of i and q by running a Markov Chain Monte Carlo (MCMC) simulation within XSPEC using 256 walkers, a total of 768000 steps and a burn-in period of 742912 steps (see Appendix 4.6 for further details). For each step in the chain, we calculate i from q and t_e and present the resulting posterior distribution in Fig. 4.5 (side panel), in which the Gaussian and exponential models are coloured blue and red respectively. Corresponding 1σ contours are provided by the dashed lines of the same colours.

Our posterior distributions demonstrate tight constraints on both q and i finding, at 1σ, $q = 0.1402\pm^{0.0028}_{0.0037}$ and $i = 80.9°\pm^{0.13}_{0.10}$ when assuming Gaussian density profile and $q = 0.1394\pm^{0.0021}_{0.0019}$ and $i = 80.96°\pm^{0.08}_{0.09}$ when assuming the exponential density profile. We further demonstrate this in Fig. 4.5 where 1, 2 and 3σ regions of $q - i$ parameter space are shaded in light, medium and dark shades of blue and red for the Gaussian and exponential models respectively. The black line shows the relation between q and i assuming a totality duration of $t_e = 4100$ s. We see that the fit closely follows this line, but width is introduced into the 2D contour by statistical uncertainty on t_e. We can, therefore, combine these results with future radial velocity amplitude measurements for a precision NS mass measurement.

We note the 5-degree discrepancy between the inclination measured via eclipse

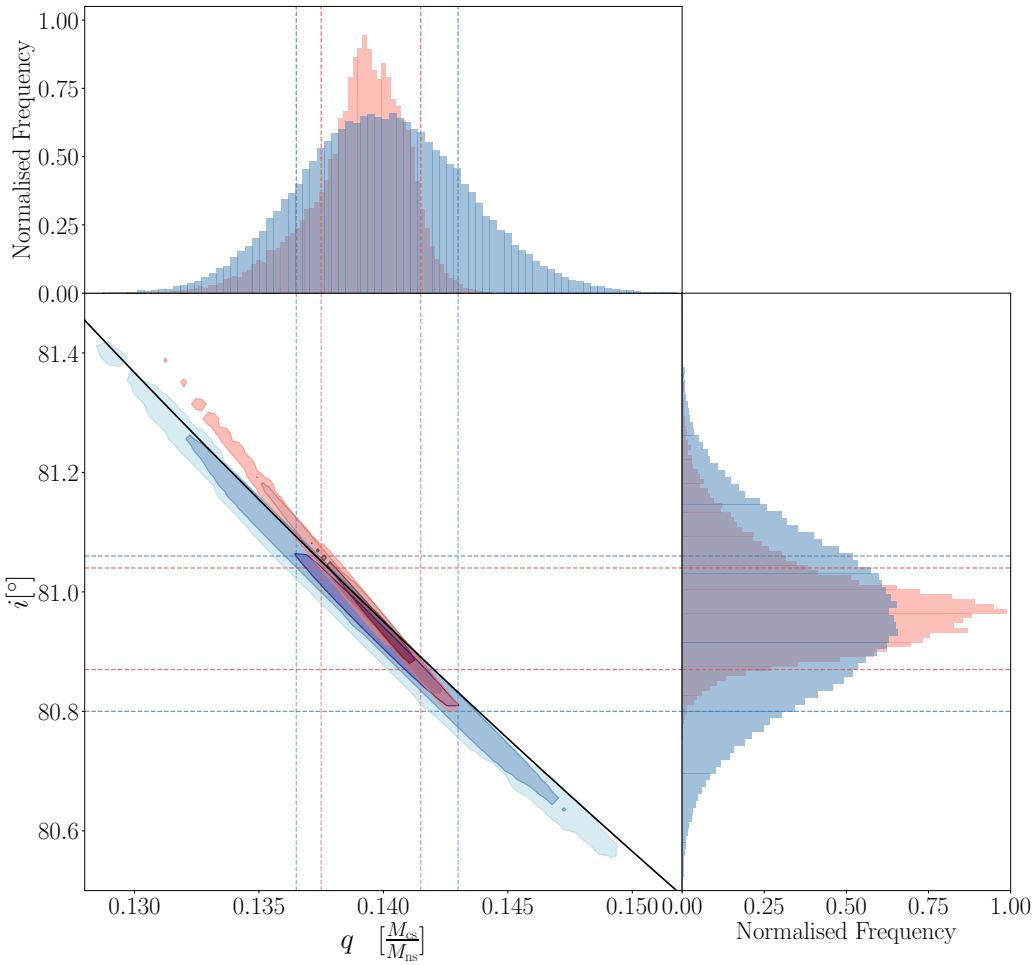

Figure 4.5: Posterior distributions for the mass ratio, q (top), and binary inclination, i (right). These are shown for both the Gaussian model (blue) and the exponential model (red). The distributions are obtained by running a Markov Chain Monte Carlo simulation with 256 walkers, 768000 steps and a burn-in length of 742912. Blue and red dashed lines show 1σ confidence intervals for the Gaussian and exponential models respectively. The centre plot shows a 2D projection of these posterior distributions for both density profile models, plotted with the theoretical $q - i$ relation (black). Dark, medium and light shades of blue and red highlight 1, 2 and 3σ contours in this 2D parameter space.

mapping ($\sim 81°$) and the preferred inclination of the LAOR iron line profile used in our spectral fitting ($\sim 86°$). This difference is very small when considering the modelling uncertainties and we consider their similarity encouraging. Although, eclipse mapping is measuring the inclination of the binary orbit itself while the LAOR model is measuring the inclination closer to the compact object. This could indicate that the inner disc is misaligned with the binary plane, but likely by a reasonably small amount (e.g. Fragos et al. 2010).

4.3.3 Nature of the Companion Star

We can make inferences about the companion star properties from the results of our model fits. The mass and radius can be constrained from our measured value of q. Given the (current) absence of a binary mass function, the mass estimate, $M_{\rm CS} = qM_{\rm NS}$, comes simply from assuming some reasonable range of possible NS masses. From Kepler's law, the radius and mass are related via the orbital period as (Buisson et al., 2021)

$$R_{\rm CS} = h(q) \left[\frac{G(M_{\rm NS} + M_{\rm CS})P^2}{(2\pi)^2} \right]^{1/3} . \tag{4.2}$$

The solid red and dotted teal lines in Fig. 4.6 show this relation for the orbital period of *Swift* J1858–0814, assuming respectively $M_{\rm NS} = 1.4\ M_\odot$ and $M_{\rm NS} = 2.5\ M_\odot$. We see that the assumed NS mass has little influence on the relation. The green shaded area shows the range of $M_{\rm CS}$ values corresponding to $1.4\ M_\odot \leq M_{\rm NS} \leq 2.5\ M_\odot$ and our measured 3σ contour on q (we use the distribution from our Gaussian model, which has larger uncertainties than the exponential model). This range of $0.183\ M_\odot \leq M_{\rm CS} \leq 0.372 M_\odot$ corresponds to $1.02\ R_\odot \leq R_{\rm CS} \leq 1.29\ R_\odot$ (dashed red lines). Following Buisson et al. (2021, see their Fig. 9), we also plot the theoretical mass-radius relation for an isolated main sequence star (Demircan & Kahraman, 1991) as a solid yellow line. It is clear that the companion star has a radius much larger than a main sequence star of the same mass. This was also noted by Buisson et al. (2021) but

is now definitively confirmed by our measurement of the mass ratio. For comparison, we also plot the same relation for the orbital period of EXO 0748–676 (solid blue line) as well as an eclipse mapping measurement of $R_{\rm CS}$ and $M_{\rm CS}$ (Knight et al., 2022a) for that source utilizing the known binary mass function (magenta cross). Interestingly the EXO 0748–676 companion star *is* consistent with being on the main sequence.

Evidence for irradiation-driven ablation of the companion star's outer layers is found through the requirement of an additional layer of absorbing material surrounding the companion star beyond the Roche lobe radius. This layer is modelled such that the material's density decreases with distance from the companion's surface, thus explaining the observed, extended and energy-dependent eclipses. The best-fitting parameters from our modelling, regardless of the assumed radial density profile, suggests this layer is asymmetric. In the case of the exponential density profile, our modelling yields scale heights of $h_{\rm in} = 0.0086$ and $h_{\rm eg} = 0.0135$ for the ingress and egress respectively. For the Gaussian density profile we obtain $\Delta_{\rm in} = 0.0099$ $\Delta_{\rm eg} = 0.0119$ for the ingress and egress respectively. This asymmetry is required by the data since the egress duration is more than 1.5 times the ingress duration. This can be understood if the material layer is elongated behind the companion star due to its orbital motion in a diffuse ambient medium.

To properly compare the height of the material layer around the companion predicted by the Gaussian and exponential models, we define a characteristic radius within which 68.27 per cent of the mass of the layer is contained. For the Gaussian model, this is simply $y_0 = \Delta$, and for the exponential model, it is $y_0 = -h\ln(1 - 0.6827)$. For the Gaussian and exponential density profiles, the characteristic size for the material on the leading side of the star is $y_0 \approx 0.00999$ and $y_0 \approx 0.00987$ respectively. For the egress side of the star, these respectively increase by ~ 1.21 times to $y_0 = 0.0119$ and by ~ 1.57 times to $y_0 = 0.0155$. The characteristic size of the material layer on the ingress side of the companion inferred from

the two density profiles is in remarkable agreement, both suggesting the size of the layer is $\sim 1\%\ R_{\rm CS}$. For the egress side of the companion, the characteristic size of the material layer differs between the two density profiles and lies within the range $1.2 - 1.56\%\ R_{\rm CS}$. Using the constraints on $R_{\rm CS}$ from the previous paragraph, this corresponds to a physical size in the range $\sim 8400 - 14000$ km for the trailing side of the companion and $\sim 7000 - 8900$ km for the leading side.

4.4 Discussion

We have applied our previously published eclipse profile model, X-TREC (Knight et al., 2022a), to archival X-ray eclipses of *Swift* J1858.6–0814 in multiple energy bands, from which we have measured a mass ratio of $q \sim 0.14$ and a binary inclination of $i \sim 81°$. Assuming the NS mass to be in the range $1.4\ M_\odot \leq M_{\rm NS} \leq 2.5\ M_\odot$ indicates that the companion star has a low mass in the range $0.183 M_\odot \leq M_{\rm CS} \leq 0.372 M_\odot$ and a radius in the range $1.02 R_\odot \leq R_{\rm CS} \leq 1.29 R_\odot$ (see Fig. 4.6). These radii are much larger than a main sequence star of the inferred mass. Buisson et al. (2021) concluded from similar arguments that the companion star is a sub-giant. Naively though, this seems unlikely since the sub-giant phase is a short-lived stage of stellar evolution and eclipsing LMXBs are very rare, implying that it should be vanishingly unlikely for us to observe such a system.

The apparent low likelihood of the sub-giant scenario could, however, be counteracted by a selection effect. Specifically, if mass transfer is triggered by the expansion of the companion star as it evolves off the main sequence, then the likelihood of a given LMXB containing an evolved star becomes greater than the likelihood of observing an isolated star in an evolved state. Indeed, radio pulsars observed to be in circular orbits with low mass functions have been suggested to be LMXBs with sub-giant companions (Verbunt, 1993). Expanded, sub-giant companions have also been suggested to drive mass transfer in LMXBs with an orbital period in excess

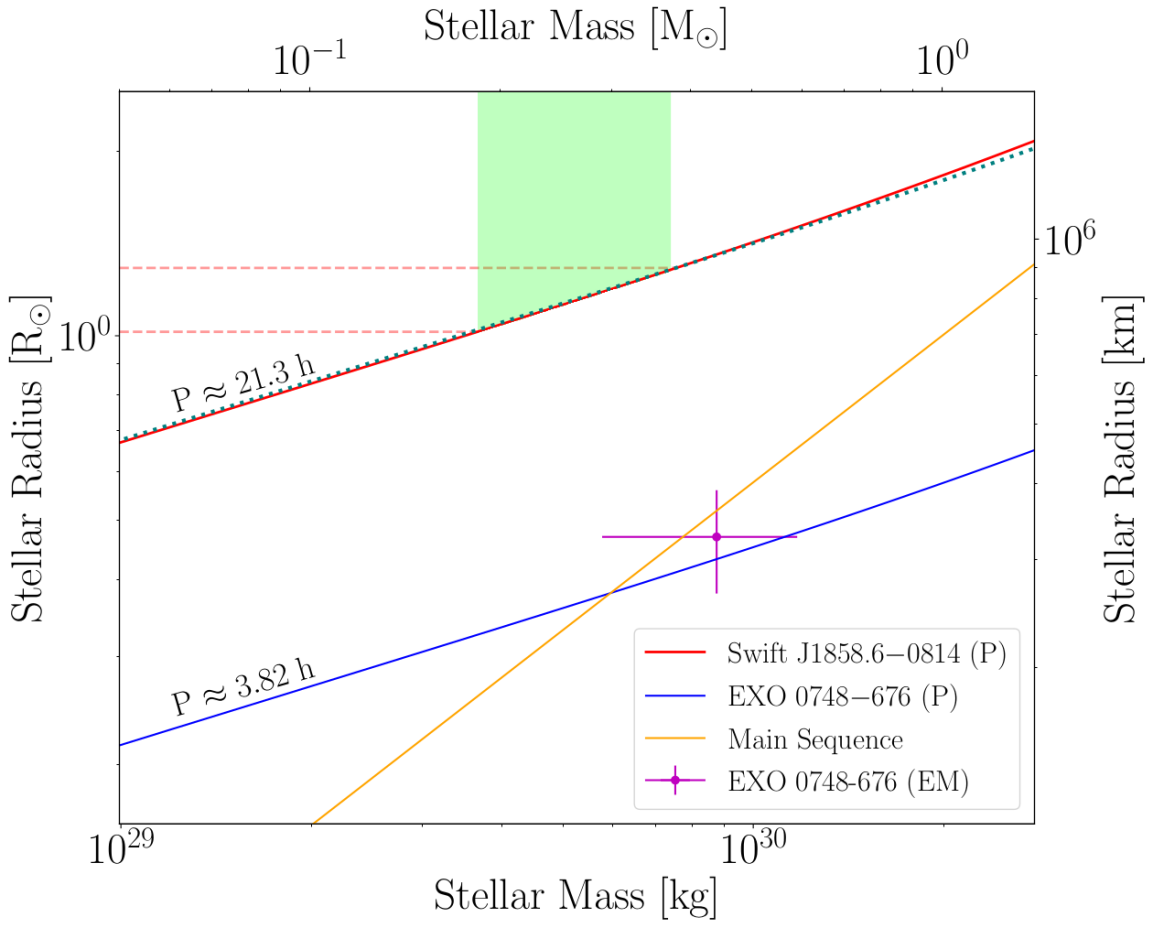

Figure 4.6: The mass-radius (M-R) relation for *Swift* J1858.6–0814 derived using the orbital period of 21.3 hrs, a range of mass ratios, and assuming the companion star fills its Roche lobe (e.g Buisson et al. 2021). We show this for both $M_{\rm NS} = 1.4 M_\odot$ (solid, red) and $M_{\rm NS} = 2.5 M_\odot$ (dotted, teal). We follow the same procedure to calculate the M-R relation for EXO 0748–676 (blue), assuming the orbital period of 3.82 hrs. For comparison, the main sequence M-R relation (yellow) from Demircan & Kahraman 1991 is provided. The companion in EXO 0748–676 is consistent with being on the main sequence but the companion in *Swift* J1858.6–0814 is inconsistent with being on the main sequence. The green band shows the range of possible companion star masses for *Swift* J1858.6–0814, found using the 3σ range of mass ratios ($0.131 \leq q \leq 0.149$) and $1.4 \leq M_{\rm NS} \leq 2.5 M_\odot$. The dashed red lines highlight the range of corresponding stellar radii. The companion in *Swift* J1858.6–0814, therefore, has a radius much larger than a main sequence star of the same mass.

of 0.5 days, e.g. Sco X-1 (Gottlieb et al., 1975). Since the orbital period of *Swift* J1858.6–0814 is just under a day, it fits into this class of systems.

However, the expected main sequence lifetime of an isolated $\sim 0.3 M_{\odot}$ star far exceeds a Hubble time, so the companion star simply wouldn't have yet evolved onto the giant branch unless its evolutionary path had been altered by binary interactions. We also note that the orbital period is short. Under the reasonable assumption that the NS evolved from an intermediate-high mass progenitor, the original orbital period would have been much larger. Therefore, the binary's evolution requires a mechanism to decrease the orbital separation while keeping the binary system intact. The latter could be avoided if the system formed via capture during a close encounter, as this allows the two components to evolve separately before forming a binary. A close encounter within a globular cluster is one of the formation scenarios considered for Sco X-1 (Mirabel, I. F. & Rodrigues, I., 2003). Like *Swift* J1858.6–0814, Sco X-1 has a low mass companion of $\sim 0.4 M_{\odot}$ (Steeghs & Casares, 2002) and a similar orbital period of $\sim$ 18.9 hrs (Gottlieb et al., 1975). Such a scenario would require *Swift* J1858.6–0814 to have a high proper motion from being kicked out of the globular cluster in which it formed.

It seems more likely that the system instead had its separation reduced by a common envelope phase (CE; see Podsiadlowski 2014 for a brief overview). This could have occurred before the formation of the NS if the intermediate-high mass progenitor overfilled its Roche lobe and led the system into a period of unstable mass transfer. Alternatively, the progenitor to the current companion could have been initially more massive, initiating the CE itself. Regardless of when the CE occurred, the system would have ejected mass and angular momentum during the CE phase, subsequently forming a short-period binary.

An evolutionary path, similar to that suggested for PSR J1952+2630 by Lazarus et al. (2013), seems plausible here if both binary components were initially of inter-

mediate mass. This scenario assumes the binary components evolved together and that the binary remained intact after the formation of the NS. Subsequently, there is a period of mass transfer as an intermediate-mass X-ray binary (IMXB), during which the secondary loses some mass through accretion and ablation processes. Such an IMXB phase has also been suggested to have occurred during the evolution of Sco X-1 (Chen, 2017). Towards the end of the IMXB phase, RLOF can lead to a period of dynamically unstable mass transfer and the creation of a CE (Lazarus et al., 2013). This assumes the intermediate-mass companion is on the tip of the red-giant or asymptotic-giant branch and the binary has a wide orbit. The wide initial orbit allows the system to survive the CE, emerging as a short-period binary consisting of a NS and a stripped He star.

The idea that the companion is a stripped He star is intriguing. Its formation through CE provides a means to significantly reduce the mass of the companion. Additionally, stripped helium stars are suggested to expand to giant dimensions as a result of a continuously growing shell (Dewi et al., 2002; Dewi & Pols, 2003; Yoon et al., 2012; Laplace, E. et al., 2020). This picture could therefore reconcile both the inferred low mass and large radius of the companion in *Swift* J1858.6–0814 if the expanding shell of the He star, due to the onset of shell He burning, was the trigger of the 2018-2020 outburst. This scenario can be tested by using spectroscopy to search for evidence of CNO enhancement of the companion.

Regardless of the prior evolution of *Swift* J1858.6–0814, our modelling requires the presence of an ionized layer of material around the companion star and is likely driven by X-ray ablation of the stellar surface. The inferred properties of this layer are very similar to those we inferred for EXO 0748–676, for which irradiation-driven ablation was also the expected origin (Knight et al., 2022a). X-ray ablation impacts the outermost layers of the stellar surface. The incident radiation from the NS and disc (see Castro Segura et al. 2022 for discussion on the disc wind in *Swift* J1858.6–

0814) bombard the companion, liberating material from its surface that builds up around the star. The radial profile of this collected material is what we measure in our modelling. The overall result of ablation is mass loss from the companion star in addition to that lost via RLOF. Ablation is not expected to be efficient enough to substantially reduce the companion's mass (e.g Ginzburg & Quataert 2020), so additional factors such as accretion or CE ejection are likely required to explain the extremely low inferred companion mass in *Swift* J1858.6–0814.

Ablation can, however, enhance the mass loss from the companion in LMXBs (Podsiadlowski, 2014). The incident irradiation causing ablation can also induce other effects on the companion star, changing the expected evolution of the system. As discussed by Podsiadlowski (1991), these are irradiation-driven winds and irradiation-driven expansion. If the envelope of the star is sufficiently irradiated by the incident X-ray flux, the star will try to expand by a factor of 2 to 4 to reach a new state of thermal equilibrium. This occurs as irradiation changes the degree of ionisation in the outer layers of the star and thus changes the star's effective surface boundary condition. Podsiadlowski (1991) shows that stellar expansion arising from X-ray irradiation is a function of the initial stellar radius and the incident X-ray flux. Using their calculations, we can infer that a $0.2 - 0.4 M_{\odot}$ main sequence companion would have a radius $\approx 0.6 - 1.0 R_{\odot}$ for an irradiating flux of $\log(F/\mathrm{ergs}^{-1}\mathrm{cm}^{-2}) \approx 11.6$. The X-ray flux incident on the companion from the NS can be estimated through the ratio $F_x/F_{\mathrm{det}} \approx D^2/r^2$, where F_x and F_{det} are the X-ray flux incident on the companion star from the NS and the X-ray flux incident on our detector respectively. The orbital separation is r and the distance to the source is D. The average X-ray flux incident on the detector is $F_{\mathrm{det}} \approx 7.4 \times 10^{-11}$ ergs/s/cm^2, which is calculated from the observed X-ray flux from 10 epochs as reported by van den Eijnden et al. (2020). The orbital separation is found through Kepler's law and assuming the distance to the source is $D = 13$ kpc (Buisson et al., 2020) we find $\log(F_x/\mathrm{ergs}^{-1}\mathrm{cm}^{-2}) \sim 12.1$.

Thus it appears plausible that the irradiation is driving the ablation and evolution of the companion star and could, therefore, be the origin of the inferred material layer around the companion. However, we note that the X-rays driving ablation are powered by accretion, therefore expansion via ablation cannot be the *cause* of RLOF, they can simply further increase the size of the companion once RLOF has already begun.

While there are many unknowns regarding the prior evolution of *Swift* J1858.6 – 0814, and we cannot favour any particular evolutionary scenario, we note that the *irradiation scenario* is capable of explaining the origin of the surrounding material layer, the under-massive companion and its larger radius. Despite this, we note that the inferred mass and radius of the companion are somewhat extreme, and additional evidence of X-ray irradiation is required to support this conclusion. In addition, we consider it likely that a prior CE phase occurred if the current binary components evolved together, thus explaining the origin of the short binary period and providing a route for substantial mass loss from the system. Future spectroscopic studies could uncover evidence of CNO enhancement of the companion, thus providing support for a prior CE phase and assisting in distinguishing between the possible formation scenarios.

4.5 Conclusions

We model the energy-dependent eclipse profiles of *Swift* J1858.6–0814 in multiple energy bands, placing constraints on the binary inclination, i and mass ratio, q. We find $i \sim 81°$, and $q \sim 0.14$ which are related by the duration of totality, $t_e \sim 4100$ s. We combine our measured mass ratio with NS masses in the range $1.4\ M_\odot \leq M_{\rm NS} \leq 2.5\ M_\odot$ to infer that the companion star has a low mass in the range $0.183 M_\odot \leq M_{\rm CS} \leq 0.372 M_\odot$ and a large radius in the range $1.02 R_\odot \leq R_{\rm CS} \leq 1.29 R_\odot$. Since an

isolated star with a mass in the inferred range would have a main sequence lifetime above the Hubble time, the large radius likely arises from binary interactions.

We consider it likely that a prior CE phase contributed to the ejection of mass from the system and the reduction in the orbital period, thus forming a short-period binary with a low-mass companion. If the companion emerged from the CE as a stripped star, it may swell to giant dimensions during later evolutionary stages. Future spectroscopic studies could confirm this possibility. An alternative scenario invokes irradiation of the companion star by the X-ray source, causing the companion star to expand (by a factor of 2-4 for low-mass stars) to reach a new state of thermal equilibrium. The incident irradiation can also lead to enhanced mass loss (Podsiadlowski, 1991). This scenario also explains the origin of the material layer found to surround the companion star by invoking irradiation-driven ablation of the stellar surface. The inferred material layer is ionised and asymmetric ($21 - 57\%$ thicker on the trailing side of the star than the leading side). This material layer is required by X-TREC to recreate the observed extended and asymmetric eclipses in *Swift* J1858.6–0814.

The extended and asymmetric eclipses in *Swift* J1858.6–0814 are among numerous similarities between *Swift* J1858.6–0814 and EXO 0748–676. We suggest that in both sources, the companion stars are ablated by X-ray irradiation from the NS and disc. I will discuss these similarities in detail in Chapter 5.

4.6 Appendix 4A: Markov Chain Monte Carlo

We run a Markov Chain Monte Carlo (MCMC) simulation of X-TREC within XSPEC. For each assumed density profile, we simulate with 256 walkers a chain length of 768000 and a burn-in period of 742912 steps using the Goodman-Weare algorithm. We start the chains from the best fitting parameters presented in Table 3.4. Figures 4.7 and 4.8 show the output distributions for each model parameter, assuming the Gaussian and exponential radial density profiles respectively.

We do not find evidence for strong parameter correlations in the resulting distributions in either density profile model with one exception - the mass ratio, q appears anti-correlated with egress ionisation $\log \xi_{\rm eg}$ when assuming the exponential density profile. In addition, there is some indication that the width of the material layer on the ingress side of the companion star is correlated with the material layer on the egress side of the companion star. This can be seen for both assumed density profiles.

The Geweke convergence measure was used to check that each of the MCMC simulations achieved convergence. This is carried out by comparing the mean of each parameter in the first 10% of the chain (i.e. shortly after the burn-in) and the last 50% of the chain. For both chains, we determined Geweke values in the range ± 0.2, which suggests that convergence has been reached.

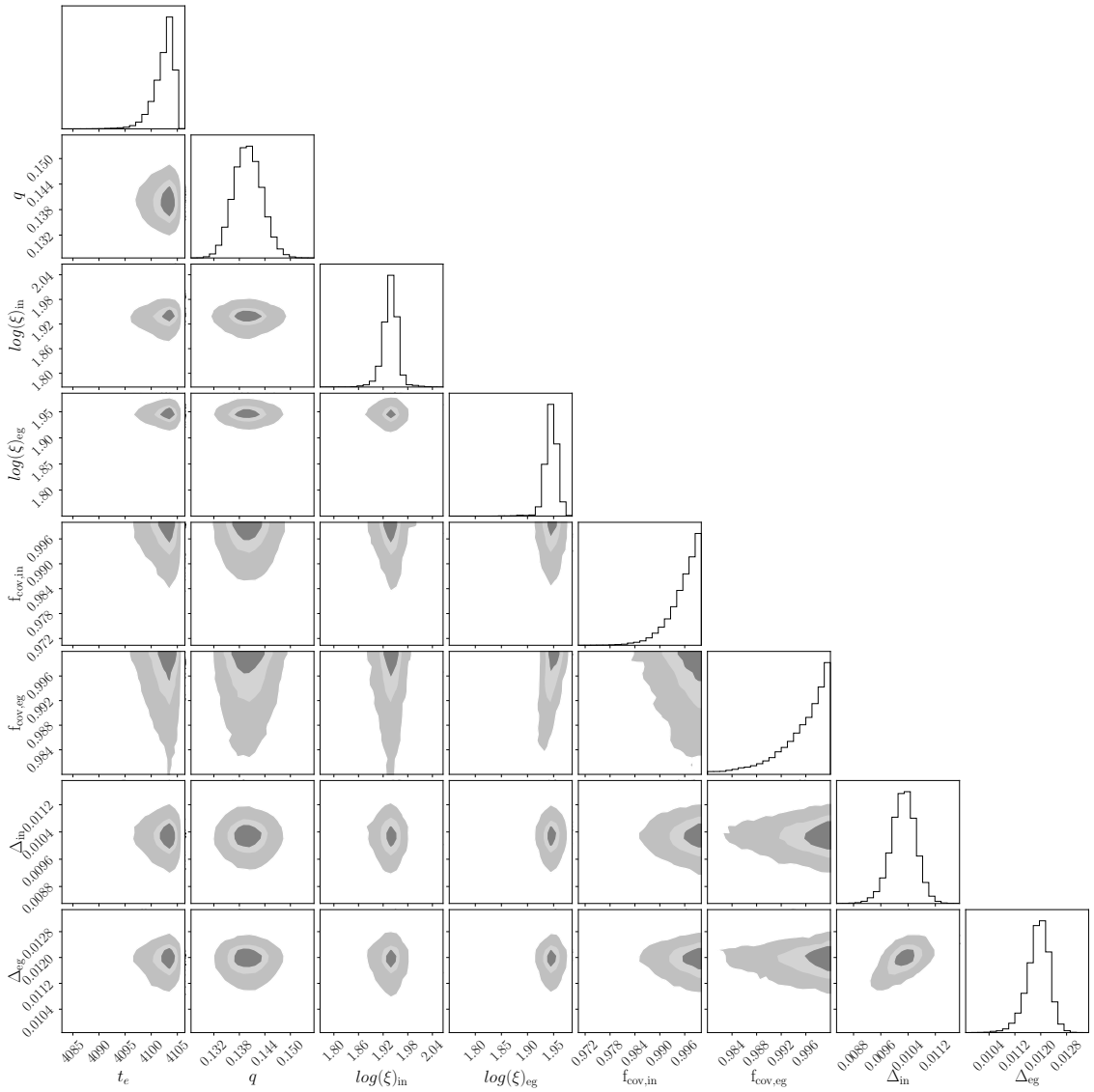

Figure 4.7: Parameter distributions obtained by running a Markov Chain Monte Carlo (MCMC) simulation of X-TREC assuming the Gaussian radial density profile. The MCMC is carried out within XSPEC and uses the Goodman-Weare algorithm. The chain has a length of 768000, 256 walkers and a burn-in period of 742912. For the 2D histograms, 1σ, 2σ and 3σ contours are respectively shaded in grey, silver and light grey. The 1D histograms are displayed with their y-axes in arbitrary units.

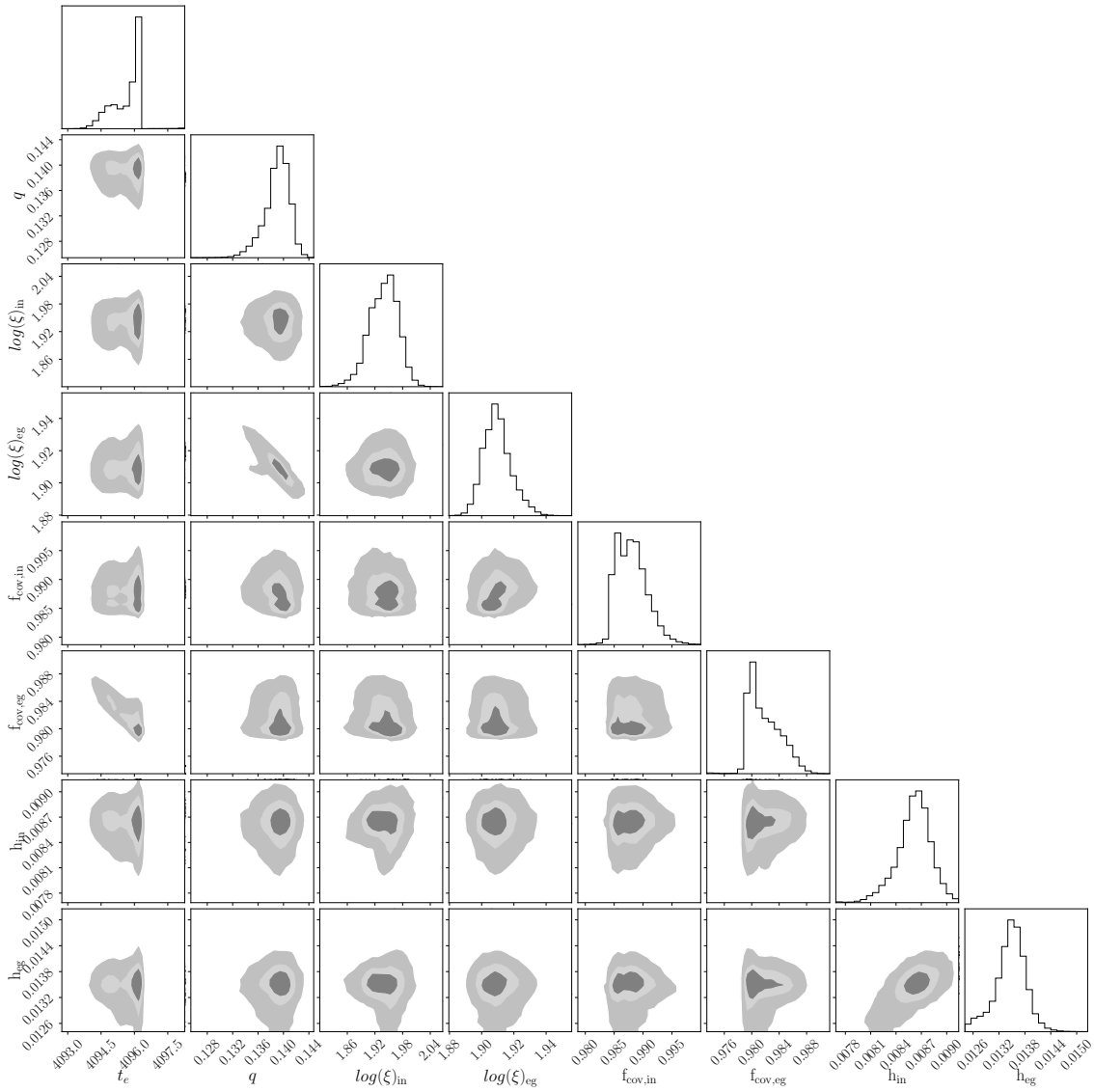

Figure 4.8: Parameter distributions obtained by running a Markov Chain Monte Carlo (MCMC) simulation of X-TREC assuming the exponential radial density profile. The MCMC is carried out within XSPEC and uses the Goodman-Weare algorithm. The chain has a length of 768000, 256 walkers and a burn-in period of 742912. For the 2D histograms, 1σ, 2σ and 3σ contours are respectively shaded in grey, silver and light grey. The 1D histograms are displayed with their y-axes in arbitrary units.

Chapter 5

The False Widow Link Between Neutron Star X-ray Binaries and Spider Pulsars

5.1 Introduction

Despite ablation typically being a property of the rotation-powered redback and black widow pulsars, I have uncovered evidence suggesting that it begins in the LMXB phase for some short period binaries (see Chapters 3 and 4). By modelling the X-ray eclipse profiles of EXO 0748–676 (hereafter EXO 0748), I inferred that a narrow region of ablated material surrounds the companion, extending $\sim 700 - 1500$ km from the stellar surface ($0.2 - 0.5\% R_{\rm cs}$). This material extends further from the companion on the egress side of the star than the ingress side, explaining the observed eclipse asymmetry. The ingress and egress durations are 15.2s and 17.5s, respectively (Knight et al., 2022a). Additionally, the material absorbs softer X-rays more efficiently than harder X-rays causing the observed eclipse profiles to depend on energy (see Fig. 2 of Knight et al. 2022a) and be extended in time. These observed features of the X-ray eclipses are analogous to the radio eclipse characteristics of redback and black widow pulsars (Polzin et al., 2020), although, it's important to note that in redbacks and black widows, the radio eclipses typically last a much larger fraction of the orbital period than the X-ray eclipses studied here. At the time of this study, there were

no observations of X-ray or radio pulsations from EXO 0748 (see Jain & Paul 2011 [1] and Ratti et al. 2012), but quiescent studies of the source uncovered spider-like features which led Ratti et al. (2012) and Parikh et al. (2020) to respectively describe EXO 0748 as 'black widow-like' and 'transitional redback-like'. The X-ray eclipses of *Swift* J1858.6–0814 (hereafter Sw J1858) also share several characteristics with EXO 0748, redback and black widow pulsars. While determining the binary inclination ($i \sim 81°$) and mass ratio ($q \sim 0.14$), I uncovered a highly extended, asymmetric ablated layer around the companion star that extends $7000 - 14000$ km from the stellar surface ($1 - 1.6\% R_{\rm cs}$). The duration of the ingress and egress were determined to be $\sim$ 106s and $\sim$ 174s respectively, and the eclipse profiles displayed the same energy dependence as EXO 0748 (see Fig. 2 of Knight et al. 2022b). There are no observations of X-ray or radio pulsations from Sw J1858 at the time of writing.

In addition to the remarkably similar eclipse characteristics shared by both EXO 0748 and Sw J1858 (and by redback and black widow pulsars), they share several non-eclipse similarities including flares, stellar prominences during the ingress and out-of-eclipse dips which occur preferentially during pre-ingress phases (Wolff et al., 2009; Buisson et al., 2021). As such, we group EXO 0748 and Sw J1858 together and refer to them as *false widows*, defined as LMXBs in which the companion star is undergoing ablation. As arachnids, the less aggressive false widows are often mistakenly identified as black widows due to their visual similarity. Thus, the naming of these binaries as false widows refers to the key observable similarity of ablation, but implies a less ablated companion.

In this Chapter, which is adapted from Knight et al. (2023), I present a detailed comparison of the previously uncovered eclipse characteristics of Sw J1858 (Chapter

[1] Jain & Paul (2011) searched for X-ray pulsations in a frequency range based upon the detection of burst oscillations at 45 Hz by Villarreal & Strohmayer (2004). To date, there has not been a published X-ray pulsation search at the burst oscillation frequency of 552 Hz (Galloway et al., 2010), or a published search for radio pulsations at either frequency.

4) and EXO 0748 (Chapter 3) and a phase-resolved spectral analysis of the near-eclipse epochs of both systems. This analysis determines the extent and influence of the ablated material. I also show how the eclipse transition durations change over time, infer the role of the ablated material on these changes and discuss how *false widows* relate to spider pulsars.

5.2 Data Reduction

Three data sets are considered in this work. For Sw J1858 we consider all available archival *NICER* observations of the source between November 2018 and July 2020. For EXO 0748, we consider all archival *RXTE* observations that contain a full eclipse profile (429 out of 746 observations) and a single soft-state outburst observation taken by *XMM-Newton* in April 2005 (Obs-ID 0212480501) (Ponti et al., 2014), which contains four eclipses. As we have previously utilised the *NICER* and *XMM-Newton* data to model the eclipse profiles of each source, the data reduction procedures are detailed in Chapters 3 (Knight et al., 2022b) and 4 (Knight et al., 2022a) respectively. The *RXTE* data reduction pipeline is described below.

5.2.1 *RXTE* Pipeline

Due to the large number of *RXTE* observations considered in this Chapter, we did not manually calibrate the data and extract light curves for each observation containing an eclipse. Instead, we applied the fully automated CHROMOS pipeline[2] (Gardenier & Uttley, 2018): an X-ray spectral-timing analysis code that, for a given list of *RXTE* ObsIDs, downloads the raw observational data from HEASARC, applies all necessary data reduction steps (depending on the observation mode) and extracts light curves at the native time resolution of the data mode in a band made up of energy channels most closely matching the user-defined energy range (which accounts for the changes

[2] `https://github.com/davidgardenier/chromos`

to the *RXTE* channel-to-energy conversion throughout its lifetime). In addition, CHROMOS is capable of calculating more advanced spectral-timing observables, such as power colours and hardnesses. However, given the scope of this work, we run the pipeline up to the light curve extraction. We extract light curves in several different energy bands: $3-6$ keV, $6-10$ keV, $10-16$ keV and $2-15$ keV. All analysed ObsIDs are listed in Table 5.1, including the number of active proportional counter units (PCUs), average $2-15$ keV count rate and hardness, defined as the ratio of the $10-16$ keV to the $6-10$ keV count rate. We note that, while the same energy bands were used for each ObsID, slight differences between the exact energy range may exist between observations due to shifts in the conversion between energy channel and photon energy over time, as well as differences in observing mode. The light curves are re-binned into 1s time bins and normalised by dividing through by the mean out-of-eclipse count rate (such that the mean out-of-eclipse level is 1.0). This normalisation typically results in a mean totality level of 0.2 due to an in-eclipse count rate contributed from the background.

5.3 Phase-Resolved Spectroscopy

We investigate the near-eclipse epochs of the two false widows using phase-resolved spectroscopy to infer how the covering fraction, ionization and column density vary with orbital phase, ϕ.

For each source, we extract a total of 44 spectra; 23 spectra for where $\phi < 0$ for the pre-ingress and ingress spectra, and 21 spectra where $\phi > 0$ for the egress and post-egress spectra. Here, $\phi = 0$ corresponds to the phase at the centre of totality. For EXO 0748 we use *XMM-Newton* spectra, of count rate vs. energy, extracted using 6 energy bands: $0.2-0.5$ keV, $0.5-1.0$ keV, $1.0-2.0$ keV, $2.0-4.0$ keV, $4.0-6.0$ keV and $6.0-8.0$ keV. The ingress and egress spectra are extracted with times bins of 2.5 s and 5.0s respectively, while the pre-ingress and post-egress spectra were both extracted

with 50.0 s time bins. The use of finer time bins during the eclipse transitions is necessary to understand the evolution of material properties during these short times and the difference in bin width accounts for the eclipse asymmetry (e.g. Knight et al., 2022a). Similarly, for Sw J1858, we extract *NICER* spectra (count rate vs. energy) using 6 energy bands: $0.5-1.0$ keV, $1.0-2.0$ keV, $2.0-4.0$ keV, $4.0-6.0$ keV, $6.0-8.0$ and $8.0-10.0$ keV. The ingress and egress spectra are extracted with 25.0 s and 40.0 s time bins respectively. Here, the larger time bins reflect the longer ingress and egress durations in Sw J1858 than EXO 0748 (Buisson et al., 2021; Knight et al., 2022b). The pre-ingress and post-egress spectra for Sw J1858 are both extracted with 50.0 s time bins. Note that the use of 6 wide energy bands in each case ensures a reasonable number of counts per energy bin in the spectra and, for this reason, is preferable to finer energy bins. Despite this, the count rates in several of the spectra are still too low to carry out the modelling using χ^2 statistics. We instead use Cash statistics (Cash, 1979) (the C-stat option within XPSEC), which is more appropriate for low count rate data (see Appendix B of Arnaud 1996). We obtain 1σ error contours using the `steppar` command within XSPEC assuming an appropriate range around the best fitting values, divided into 400 steps (see Appendix 5.8 for full details).

The spectra are modelled using ABSSCA (see Section 2.2.3), with the ratio of free electrons to hydrogen nuclei in the material is set to $n_e/n_H = 1.0$ and the redshift is $z = 0$. We separate absorption arising due to the ionized, ablated material from absorption by the interstellar medium (ISM). We model ISM absorption with the XSPEC model TBABS, assuming the abundances of Wilms et al. (2000). Due to the observed asymmetry in the eclipse profiles of both false widow candidates, we allow f_{cov}, N_H and $\log(\xi)$ to vary across all spectra. Note that this approach differs from our previously published phase-resolved spectroscopy of the ingress and egress of EXO 0748, in which we tied $\log(\xi)$ and f_{cov} across the spectra (Section 3.3; Knight et al. 2022a). This was appropriate since $\log(\xi)$ and f_{cov} are mostly consistent within errors during

the ingress and egress for EXO 0748, and we were only analysing the eclipse transitions. However, here we are modelling spectra across a much wider range of orbital phases, during which $\log(\xi)$ and f_{cov} may change significantly. Therefore, we allow all parameters to vary in this analysis. This does introduce some additional modelling complications, including partial degeneracies between the parameters, which we explore in detail in Appendix 5.8.

The results are respectively shown in Fig. 5.1 and Fig. 5.2 for EXO 0748 and Sw J1858, where we see some similarities. For both sources, the covering fraction (Figs. 5.1A and 5.2A), ionization parameter (Figs. 5.1C and 5.2C) and column density (Figs. 5.1E and 5.2E, black) of the ionized absorber generally increase with proximity to totality during the ingress phases, whereas the column density of ISM absorption (Figs. 5.1E and 5.2E, red) remains constant within uncertainties. These parameter behaviours are roughly mirrored during the egress phases (Figs. 5.1B, D and F and 5.2B, D and F).

Our interpretation of these results is demonstrated schematically in Fig. 5.3. The increase in column density with proximity to the eclipse indicates that the density of the ablated material reduces with distance from the companion, as is expected from simple mass conservation considerations. However, the detection of an ionized absorber for orbital phases beyond the eclipse transitions ($|\phi| \gtrsim 0.2$ rad) indicates that some ablated material is still present far from the companion. The lower covering fraction further from eclipse indicates that the material breaks up into small clumps as it gets further from the companion. Clumpy outflows have been invoked for Vela X-1 and Cyg X-1, both high-mass XRBs, to explain features including variable absorption along the orbit (Hanke et al., 2008; Grinberg et al., 2015, 2017; Diez et al., 2022). In these cases, clumps arise from perturbations in the stellar wind from the OB companion stars, which fragment due to strong shocks in the wind, and variations in temperature and density (Grinberg et al., 2017). While typically associated with

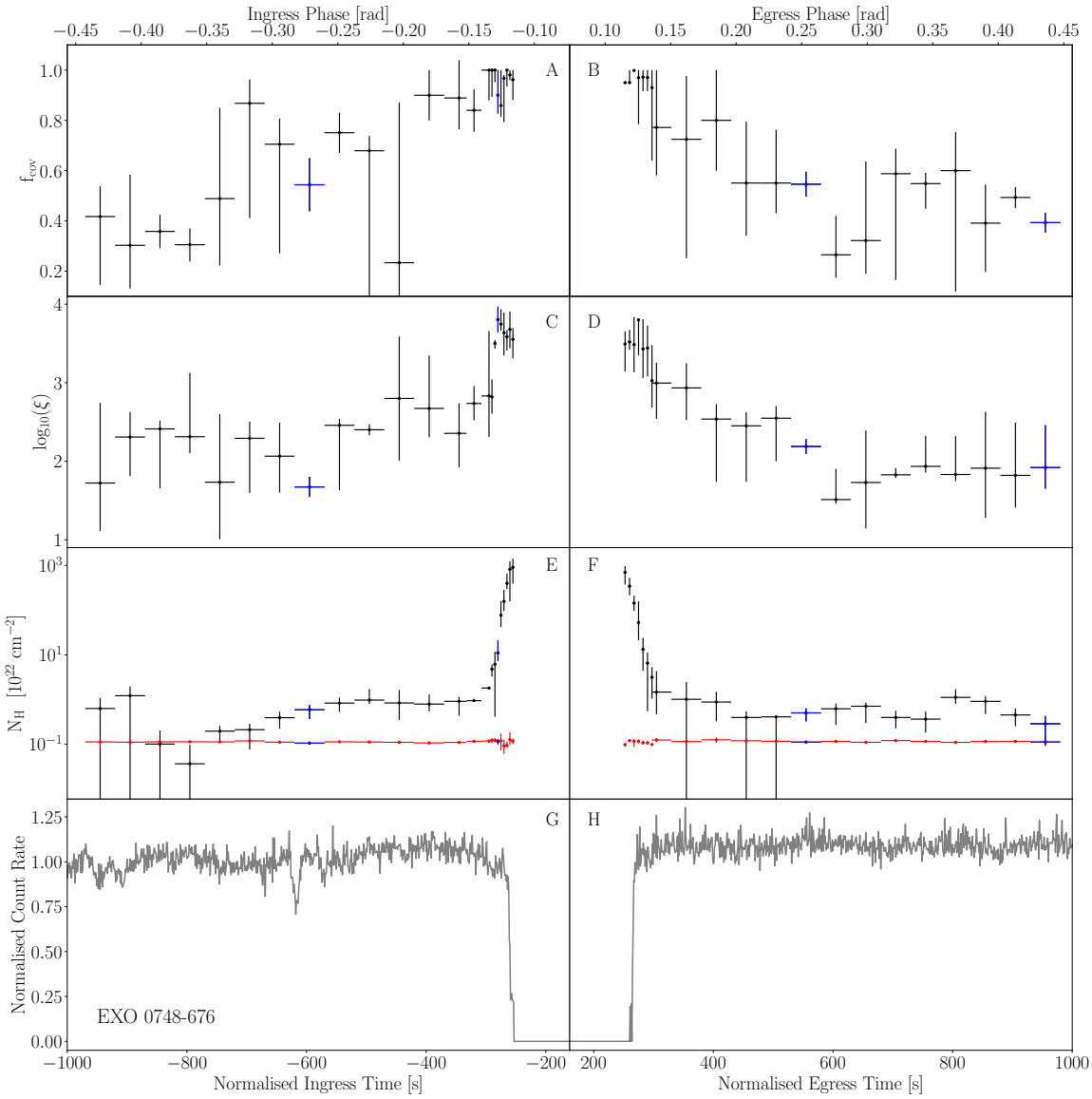

Figure 5.1: Phase-resolved spectroscopy of the near-eclipse epochs in EXO 0748–676 showing how the covering fraction (A and B), log of the ionization parameter defined as $\log(L/(\mathrm{nR}^2))$ (C and D) and column density (E and F) vary as a function of orbital phase. Here the red data points show the measured column density of the ISM. The corresponding *XMM-Newton* eclipse profile is shown in panels G and H. A total of 44 spectra are extracted from 6 non-overlapping energy bands: $0.2-0.5$ keV, $0.5-1.0$ keV, $1.0-2.0$ keV, $2.0-4.0$ keV, $4.0-6.0$ keV and $6.0-8.0$ keV. The ingress and egress spectra are extracted with time bins of 2.5 s and 5.0s respectively, while the pre-ingress and post-egress spectra were both extracted with 50.0 s time bins. The spectra are modelled with our local XSPEC model, ABSSCA (Knight et al., 2022a) using cash-statistics (c-stat) due to the low count rate in several of the spectra. Error bars are 1σ. The blue data points are used to highlight the representative spectra analysed in detail in Appendix 5.8.

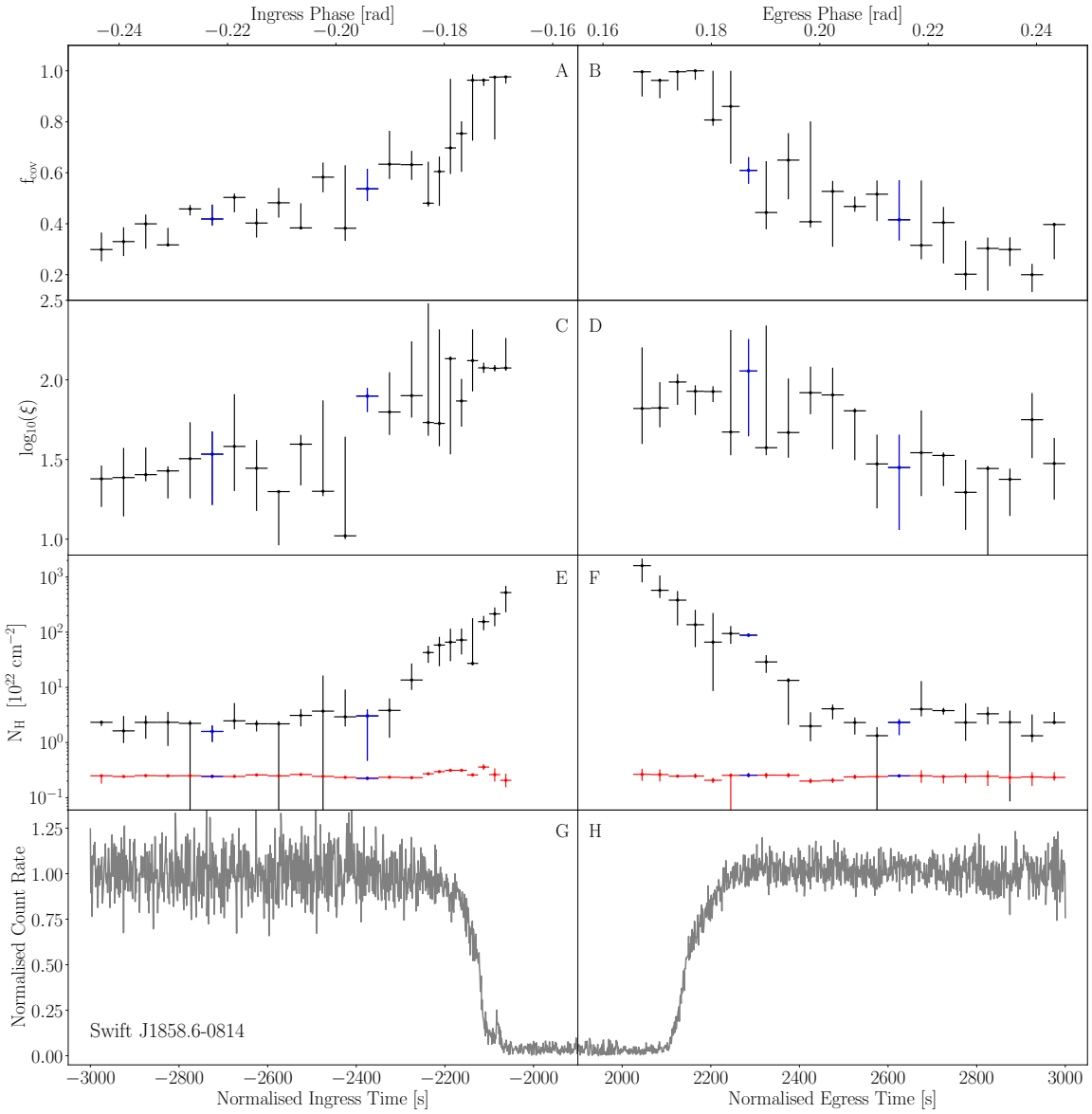

Figure 5.2: Phase-resolved spectroscopy of the near-eclipse regions in *Swift* J1858.6–0814 showing how the covering fraction (A and B), log of the ionization parameter defined as $\log(L/(\mathrm{nR}^2))$ (C and D) and column density (E and F) vary as a function of orbital phase. Here the red data points show the measured column density of the ISM. The corresponding *NICER* eclipse profile is shown in panels G and H. A total of 44 spectra are extracted from 6 non-overlapping energy bands: $0.5-1.0$ keV, $1.0-2.0$ keV, $2.0-4.0$ keV, $4.0-6.0$ keV, $6.0-8.0$ keV and $8.0-10.0$ keV. The ingress and egress spectra are extracted with time bins of 25.0 s and 40.0s respectively, while the pre-ingress and post-egress spectra were both extracted with 50.0 s time bins. The spectra are modelled with our local XSPEC model, ABSSCA (Knight et al., 2022a) using cash-statistics (c-stat) due to the low count rate in several of the spectra. Error bars are 1σ. The blue data points are used to highlight the representative spectra analysed in detail in Appendix 5.8.

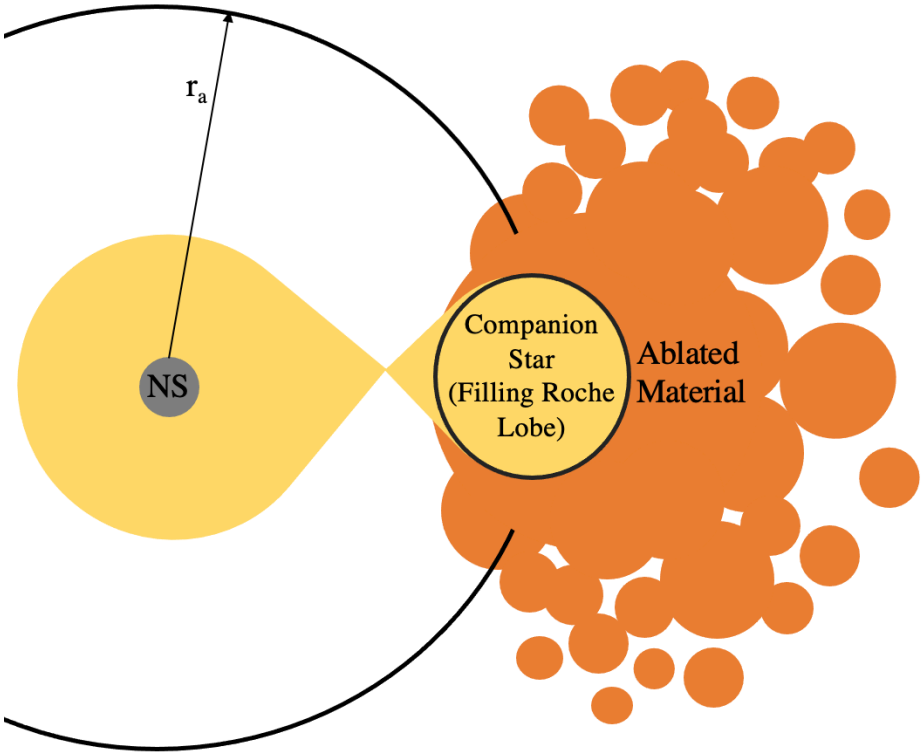

Figure 5.3: A schematic showing the geometry of a *false widow* undergoing ablation. The NS and companion star have an assumed circular orbit with separation, r_a, and the companion star is expected to be filling its Roche lobe. The ablated material is liberated from the companion star by incident X-rays from the NS and accretion disc. The material clumps near to the companion star and then diffuses away such that the density of the material remains high but the overall absorbing column decreases. Note, this schematic is not to scale.

OB stars, radiation-driven outflows may also become clumpy far from low-mass stars (Lagae et al., 2021) which could explain our findings.

The evolution of the ionization parameter with orbital phase implies that material further away from the companion star is also further away from the NS surface (i.e. the material is further from the source of ionizing X-rays), as is pictured in Fig. 5.3. Thus it may appear parabolic in shape like the pulsar wind-driven ablation in spider pulsars. Such a geometry is required to explain how the higher density material closer to the companion star has a higher ionization parameter than the lower density material far from the companion. If we were to assume that the density is simply

proportional to the measured column density, $n \propto N_{\rm H}$, then this increase in distance from the NS would need to be dramatic. For example, the increase in $N_{\rm H}$ by a factor of ~ 1000 in our EXO 0748 fits would require an increase in distance by a factor of $\sim \sqrt{1000} \approx 30$. This seems unlikely to be the case, since the binary motion should cause material far from the centre of mass to become approximately uniform in phase around the binary. However, the column density also depends on the path length of our sight line through the material and on the covering fraction. Our fits indicate that the covering fraction is $\rm f_{cov} \sim 0.5$ far from the companion, and it is natural to assume that the material layer reduces in width with distance from the stellar surface (as is illustrated in Fig. 5.3), meaning that the density drops off less dramatically than would otherwise be inferred. For example, assuming the path length reduces by a factor of 4 far from the companion means that the distance from the NS only needs to increase by a factor ~ 4. In addition, these changes will have an effect on the filling factor, particularly if the material forms clumps as less of the line of sight will contain absorbing material, thus allowing material with a higher density and a lower ξ for a fixed column and overall size. Finally, our fits indicate that the ablated material is asymmetric; the decrease in $\rm N_H$ after the eclipse is longer in duration than the increase before the eclipse. The asymmetry is most likely due to the orbital motion of the binary systems (see Knight et al. 2022a and Knight et al. 2022b), therefore, this is a strong indication that ablated material exists external to the Roche lobe. We refer to this as super-Roche lobe material.

Ablated material will remain gravitationally bound to the binary, but that does not strictly mean that our suggested geometry is enduring, and as suggested above, the ablated structure will governed by the continuous movement of the binary components and ongoing irradiation-driven ablation. Therefore, the geometry depicted in Figure 5.3 should be considered specific to the data analysed here since variations in density and ionization will likely change the ablated structure over month or year-long

timescales.

5.4 Eclipse Analysis

After the onset of a persistent outburst, the ablated material layer is expected to expand until an equilibrium state is reached. During this time, the eclipse transition durations, are expected to increase as a result of increased line-of-sight absorption by the growing ablated layer. Following Knight et al. (2022b) and Knight et al. (2022a), we measure the transition durations by identifying the times t_{90} and t_{10} as the times when the count rate first passes 90 and 10 percent respectively of the mean out-of-eclipse count rate (and stays above/below that level for at least 5 seconds; Knight et al. 2022b). Under this definition, the ingress starts at t_{90} and ends at t_{10} before totality, and the egress starts at t_{10} and ends at t_{90} after totality. Fig. 5.4A shows that the ingress and egress durations of Sw J1858 measured in this way did indeed increase as a function of orbital cycle at the start of the outburst. Here the first orbital cycle of each source's persistent outburst is defined as the zeroth cycle (e.g. Knight et al. 2022b). For Sw J1858, which showed a flaring outburst state prior to its persistent outburst state, this occurs at $\sim$ MJD 58885 (Buisson et al., 2021).

The onset of the persistent emission from EXO 0748 was observed by *EXOSAT*. The eclipse transition durations measured from the eclipses observed by *EXOSAT* between February 1985 and January 1986 were reported by Parmar et al. (1991), who noted their drastic variations and, in some cases, long durations. Parmar et al. (1991) suggested that a cause of this behaviour could be an X-ray heated evaporating wind (ablated stellar material) that enhances the atmospheric scale height of the companion, extending the transition durations. These measurements are shown in Fig. 5.4B for the first 150 orbital cycles of EXO 0748, enabling comparison between the early eclipse transitions of EXO 0748 and Sw J1858. Due to the small number of observed eclipses of Sw J1858 and large variations in the transition durations of the

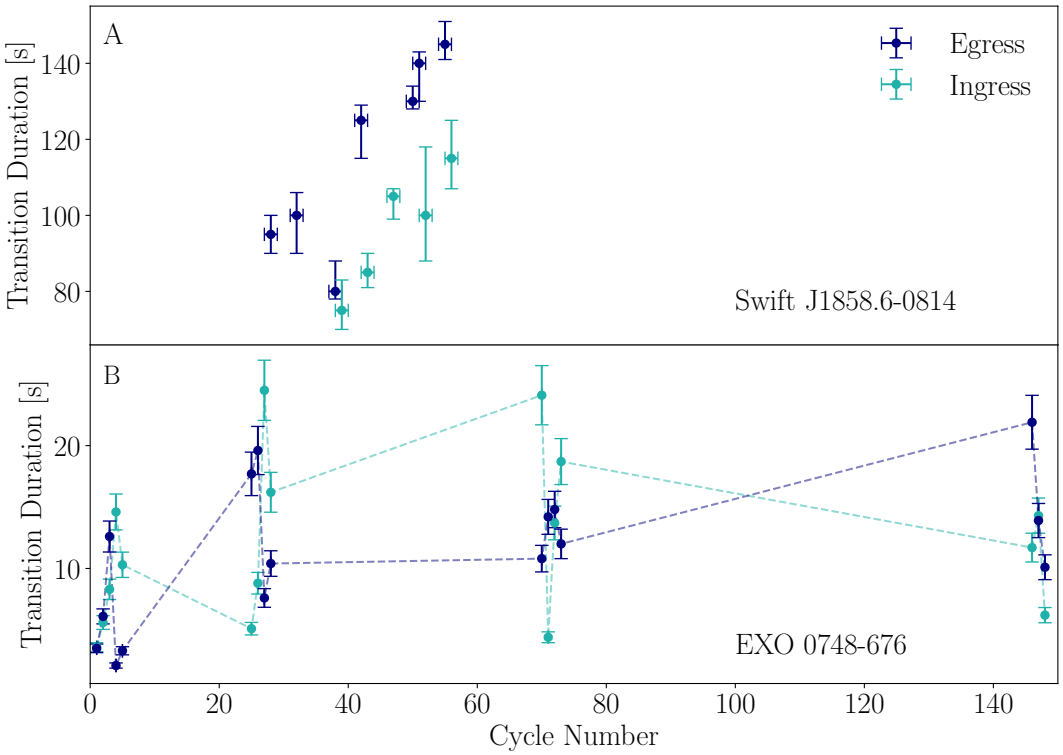

Figure 5.4: Measured eclipse transition durations for eclipses observed within the first 150 orbital cycles of the persistent outburst emission for *Swift* J1858.6–0814 (panel A, *NICER* observations) and EXO 0748–676 (panel B, *EXOSAT* observations, Parmar et al. 1991). In both panels, the light and dark blue points represent the ingress and egress durations respectively. While both *Swift* J1858.6–0814 and EXO 0748–676 show increasing transition durations in this stage, EXO 0748–676 shows very drastic variations attributed to an X-ray heated evaporating wind (Parmar et al., 1991).

EXO 0748 eclipses, making comparisons between the sources is not straightforward, however, both do show increases in transition duration on short timescales. As Sw J1858 is now in quiescence (Saikia et al., 2020; Parikh et al., 2020), we do not know if similar variations to EXO 0748 would have been observed. Also, for this reason, and because of the limited number of observed eclipses of Sw J1858, the analysis presented in the remainder of this section was only possible for EXO 0748.

5.4.1 Evolution of the Eclipse Transitions

After the aforementioned equilibrium state is reached, the eclipse transition durations and how they vary can provide insights into the presence of the absorbing medium

around the companion, its radial extent and its structure. Utilising all available archival *RXTE* observations of EXO 0748–676 that contain full eclipse profiles, we measure the duration of the ingress, egress and totality, thus uncovering how the transitions evolve over time. As there are 429 full *RXTE* eclipses, we chose to fit the observed eclipse profiles with a simple eclipse profile model rather than our previously published eclipse model that describes the absorption by the ablated material layer (see Knight et al. 2022a and Knight et al. 2022b). As *RXTE* does not extend to softer X-rays ($\lesssim$ 2 keV), a simple eclipse model is sufficient as the majority of the absorption by the ablated layer occurs between $0.5 - 2.0$ keV.

Using the re-binned and normalised $2 - 15$ keV *RXTE* eclipse profiles, we first identify the times t_{90} and t_{10} for both the ingress and egress. The durations of the ingress and egress are initially determined as $\Delta t_{\rm in} \approx t_{10,\rm in} - t_{90,\rm in}$ and $\Delta t_{\rm eg} \approx t_{90,\rm eg} - t_{10,\rm eg}$, and the initial duration of totality is determined as $t_{\rm tot} \approx t_{10,\rm eg} - t_{10,\rm in}$. These measurements serve as both initial parameters for our eclipse fits and checks to ensure the eclipses have been correctly identified in each case, particularly for the observations in which the eclipse was not deliberately targeted.

The four eclipse 'contacts', t_1, t_2, t_3 and t_4 which are, respectively, the start of the ingress, start of totality, end of totality and end of the egress (e.g Wolff et al. 2009) are subsequently determined by fitting a simple 'broken-line' eclipse model consisting of 5 parameters to the light curve. The model parameters are the mean pre-ingress count rate, $R_{\rm in}$, the mean post-egress count rate, $R_{\rm eg}$, the mean in-eclipse count rate, $R_{\rm tot}$, the gradient of the ingress $m_{\rm in}$ and the gradient of the egress $m_{\rm eg}$. Since we are working with normalised eclipse profiles, the first three parameters take values between $0.0 - 1.0$ and are used to fit the pre-ingress, post-egress and totality segments of the eclipse profiles. The gradients of the ingress and egress are determined by a linear fit through the predetermined points $\rm t_{90}$ and t_{10}, which are fixed during the fit to the light curve. Each point of intersection between the five fitted lines

thus corresponds to one of the four eclipse contacts. These contacts are related as $t_2 = t_1 + \Delta t_{\rm in}$, $t_4 = t_3 + \Delta t_{\rm eg}$ (e.g. Wolff et al. 2009), where the initial and minimum values of $\Delta t_{\rm in}$ and $\Delta t_{\rm eg}$ are set using the measurements of t_{90} and t_{10}, as described above. Similarly, the totality duration is now determined as $\Delta t_{\rm tot} = t_3 - t_2$ after starting from initial and maximum approximation above and the mid-eclipse time is $t_{\rm mid} = (t_3 - t_2)/2$. An example of a resulting fit is provided in Fig. 5.5. The results of this fitting procedure are presented in Table 5.1 along with a corresponding reduced χ^2 and null-hypothesis probability for each eclipse fit.

The measured ingress, egress and totality durations are displayed as a function of mid-eclipse MJD in Fig. 5.6, panels A, B and C respectively. The colours represent hardness ratio, included to indicate how spectral changes to the system may be influencing in/egress durations and thus, the ablation. Additionally, a 45-point moving average of these durations as a function of mid-eclipse MJD are provided in Fig. 5.7, panels A, B and C respectively, allowing the trends to be seen more clearly. The colours now represent root mean squared (RMS) variability amplitude, which is known to be a good indicator of spectral state (Belloni, 2010; Heil et al., 2015).

The ingress and egress durations for EXO 0748 are found to vary dramatically during the *RXTE* era. The most striking characteristics can be seen in Fig. 5.7. These variations can inform on the quantity and density of ablated material near the companion star; longer transitions indicate gradual X-ray absorption through lower density and/or extended material, while shorter durations indicate steep X-ray absorption through denser and/or less extended material. However, it is also important to consider whether the asymmetrically shaped bulge on the rim of the accretion disc, which arises due to the impact of the accretion stream, could influence the eclipse timings and these observed variations. In this scenario, the disc bulge could partially cover the NS during near-eclipse phases, thus extending the duration of the eclipse transitions. Crucially, the dimensions of these disc features are unknown, so we

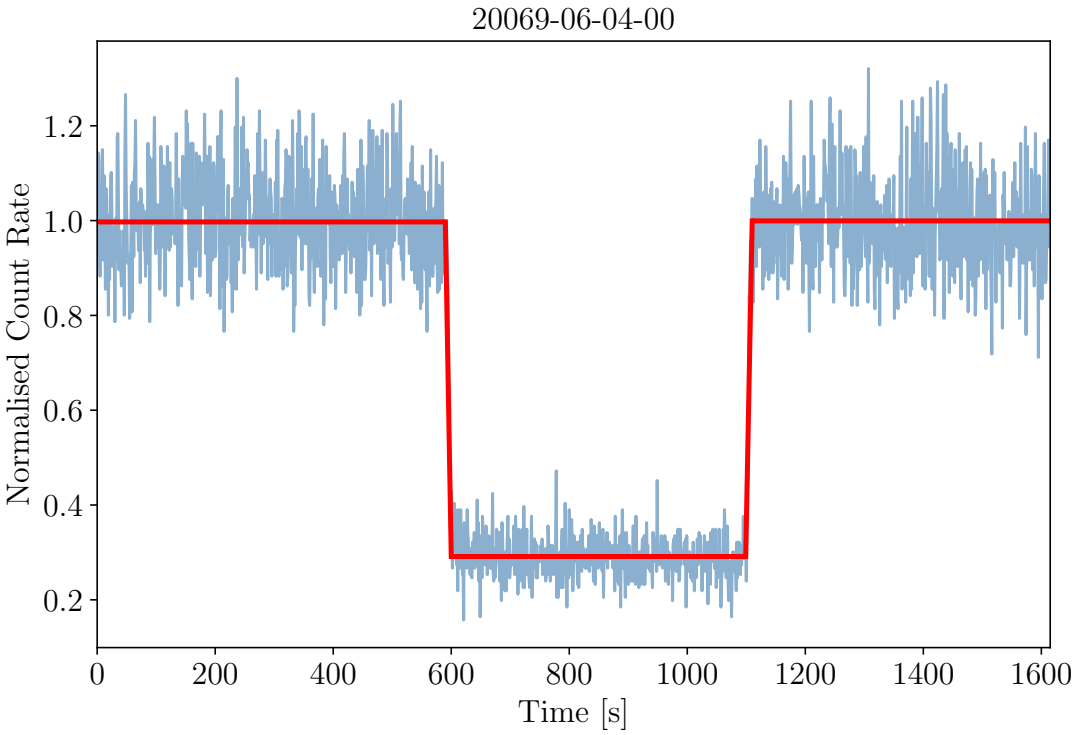

Figure 5.5: Example of a typical eclipse profile fit (red) obtained when fitting the simple eclipse profile model described in Section 5.4 to the $2-15$ keV *RXTE* light curves (blue) shown for ObsID 20069-06-04-00.

cannot determine whether an accretion disc bulge would be visible beyond the ablated material known to be present around the companion star Knight et al. (2022a, 2023). However, van Zyl et al. (2004) has shown that the bulge can extend up to $\sim 90^{\circ}$ in front of the accretion stream impact site for a system with a ~ 17 hr orbital period. Therefore, the bulge could cover a significant portion of the orbit. Despite this, we don't explore this scenario further as an accretion disc bulge extending the eclipse transition durations creates several tensions with our earlier analysis. In particular, it is challenging to reconcile the energy-dependence of the eclipse transitions, the eclipse asymmetry (Chapter 3; Knight et al. 2022a) and the reversal of the eclipse asymmetry (Figure 5.7; Knight et al. 2023) in a scenario where the accretion disc bulge first eclipses the NS.

The ingress duration roughly correlates with fractional RMS (with higher RMS

corresponding to a harder spectral state) and anti-correlates with the egress duration. For most of the *RXTE* era, the egress is longer than the ingress, except for MJD $\sim$ 53000-54000, during which this relationship flips. We illustrate this reversal in Fig. 5.8 by showing the stacked eclipse profiles from two time periods during the *RXTE* era; MJD $50000 - 51000$ (blue) during which the ingress is shorter than the egress and MJD $53000 - 54000$ (red) during which the ingress is longer than the egress. This finding creates further tension with the scenario of an accretion disc bulge contributing to the eclipse transitions. However, it can be explained by the ablated material moving within the gravitationally bound region of the binary and/or by a change in the spectral state of the irradiating source that is driving the outflow from the stellar surface. For example, ablated material trailing behind the companion star due to the binary's orbital motion may 'catch up' with the front of the companion star and extend the ingress duration. Also, a hard spectrum with a drop in the soft X-ray emission should be accompanied by a reduction in the outflow mass loss rate from the companion star. Such a reduction could explain why the egress duration decreases when the system transitions to a harder spectral state (higher RMS). Thus, the eclipse asymmetry reversing is a strong indication that the transition durations are being governed by irradiation driven, super-Roche lobe material.

In eclipsing redback and black widow pulsars the egress is typically longer than the ingress due to the orbital motion of the binary inducing a material trail on the egress side of the star. However, reversal of the eclipse asymmetry has previously been observed. One such case is the black widow pulsar PRS J2051–0827, where Polzin et al. (2019a) uncovered changes in the eclipsing material that occurred on $\sim$ month timescales. Polzin et al. (2019a) studied the evolution of the dispersion measure structure in orbital phases that correspond to the eclipses, during a decade long study. They find the dispersion measure peaks on the ingress side between 2011 and 2014, but later shifts to the egress side, thus implying that the eclipsing material's

structure can change on timescales similar to those observed for EXO 0748.

5.4.2 Totality and Orbital Period Variations

The evolution of the totality duration for EXO 0748 during the *RXTE* era is shown in Fig. 5.6 C, covering a range $\sim 485 - 510$ s, and the corresponding 45-point moving average in Fig. 5.7 C. These measurements are generally consistent with those presented by Wolff et al. (2009), who also studied the variations in the duration of totality (see Fig. 5 of Wolff et al. 2009). The *RXTE* era initially shows a decrease in the totality duration and continues to drop until ~ 52500 MJD. The system is in an a softer state during this period. Following this, the totality duration fluctuates but increases on average. These fluctuations are accompanied by a varying, but overall harder spectral state.

We first investigate if this evolution in totality duration can be explained by evolution of the binary system. If we assume that the companion star is filling its Roche lobe, with no super-Roche lobe material, the duration of totality, t_e, relates to the orbital period, P, mass ratio, $q = M_{\rm cs}/M_{\rm NS}$ and binary inclination, i via Equation 2.4 (Knight et al., 2022a,b). The inclination is unlikely to display the drastic changes needed to explain the observed changes in the totality duration and the orbital period is constant in epochs during which the totality duration varies (Wolff et al., 2009). Therefore, in this picture only the mass ratio can drive the observed changes in totality duration.

The orbital period of EXO 0748 is 3.824 hrs (Parmar et al., 1991; Wolff et al., 2009) and the binary is inclined to $\sim 77^\circ$ (Knight et al., 2022a). For the observed range of totality durations of $\sim 485 - 510$ s, the corresponding range in mass ratio is $q \sim 0.215 - 0.224$ (Knight et al. 2022a measured $q \sim 0.222$). Assuming that the change in mass ratio is driven by accretion onto the NS (i.e. mass transfer > mass loss), then the initial decrease in totality duration from ~ 510 s to ~ 485 s, which

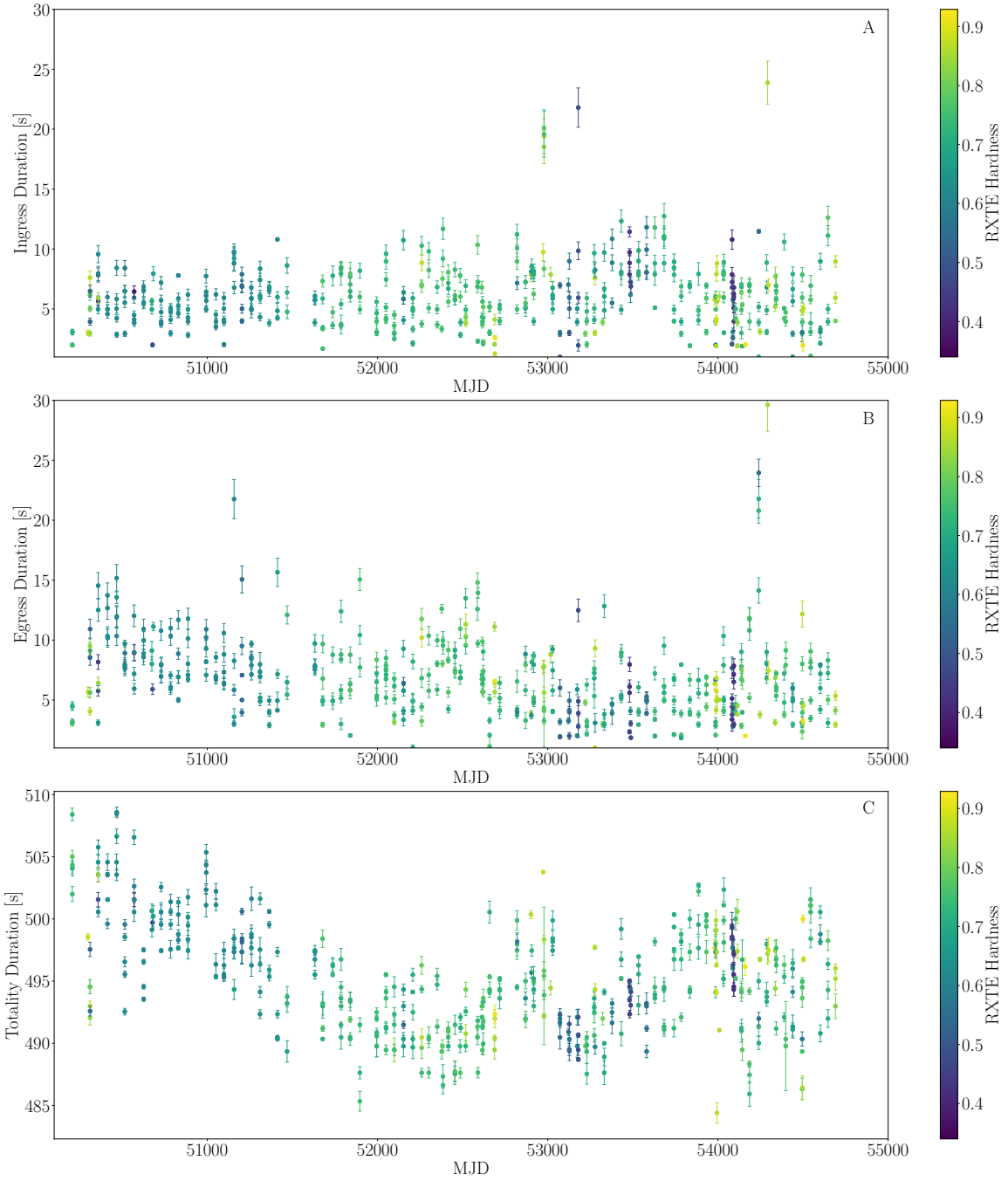

Figure 5.6: Ingress duration (panel A), egress duration (panel B) and totality duration (panel C) as functions of mid-eclipse MJD for all archival *RXTE* observations of EXO 0748–676 that contain a full eclipse profile. The durations are measured by fitting the simple eclipse profile model, described in Section 5.4, to the $2-15$ keV eclipse profiles. Here each data point represents one ObsID. The variations observed in the eclipse transition times are indicative of ablated material clumping or changing structure as a result of the binary's orbital motion. The colour scale represents the *RXTE* hardness, defined as $F_{10-16\mathrm{keV}}/F_{6-10\mathrm{keV}}$.

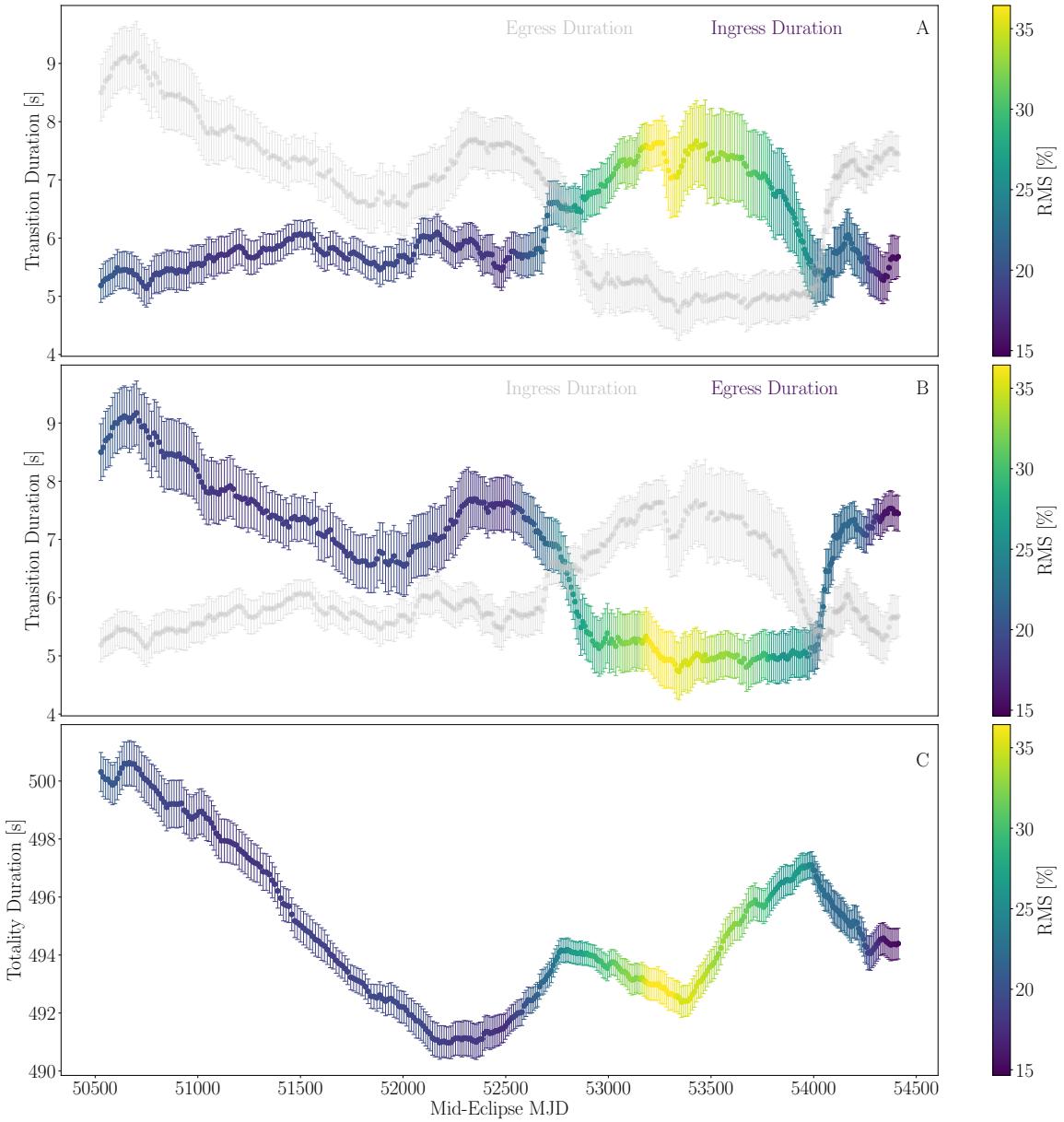

Figure 5.7: 45-point moving averages of eclipse transition durations (Panels A and B) and totality duration (Panel C) as a functions mid-eclipse MJD and of background corrected root mean squared (RMS) variability amplitude (coloured). In Panels A and B respectively, the ingress and egress durations are coloured while the egress and ingress durations are over plot in grey for comparison, clearly showing the observed eclipse asymmetry and anti-correlation between the ingress and egress durations. The egress is typically longer in duration than the ingress, but reverses between $\sim 53000 - 54000$ MJD and seemingly coincides with an increase in RMS (transition to a harder state). In Panel C, the behaviour of the totality duration is determined to arise from changes to the orbital period of EXO 0748. In each panel, error bars correspond to the standard error, $\sigma/\sqrt{n}$ in each 45-point bin. Note that since this a moving average the error bars are not independent.

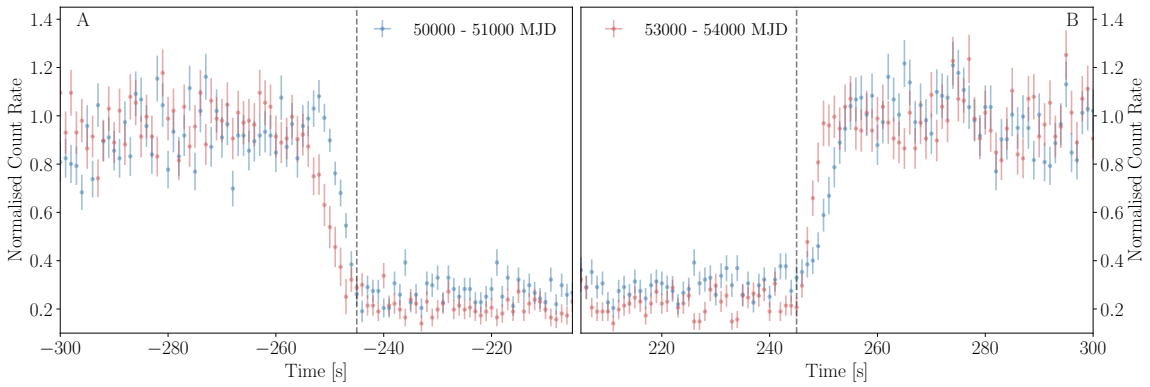

Figure 5.8: Stacked *RXTE* eclipse profiles of EXO 0748–676 for two times periods, $50000 - 51000$ MJD (blue) and $53000 - 54000$ MJD (red). The eclipse profiles are normalised to have a mean out-of-eclipse count rate of ~ 1.0 and shifted horizontally such that the eclipses profiles in panel A (showing the ingress) are aligned at the t_2 times, and t_3 in panel B (showing the egress). In panels A and B respectively, the times t_2 and t_3 are represented by the black dashed lines. Clearly shown are the differences in ingress and egress duration between the two time periods.

occurs over a $\sim$ 5 year period, requires the companion to lose $\sim$ 3.3% of its mass to the NS, which then grows by $\sim$ 0.7%. If $M_{\rm NS} \approx 2\ M_\odot$ (Knight et al., 2022a), this corresponds to a mass transfer rate of $\sim 3 \times 10^{-3}\ M_\odot$/yr. The rest mass energy transferred is therefore $\dot{M}c^2 \approx 1.7 \times 10^{44}$ erg. For a reasonable radiative efficiency, this predicts a luminosity far in excess of what is observed. Therefore, we can rule out the observed changes in totality duration being entirely driven by changes in the Roche potential. Moreover, it would be very difficult to explain t_e *increasing* again because, in this picture, we would require mass to be transferred from the NS to the companion.

An alternative explanation for the variations in totality duration is that a portion of totality is sometimes a result of optically thick material beyond the Roche Lobe of the companion. Specifically, our sight line through the ablated material becomes optically thick near the companion star radius, cutting out all light and extending totality. In this interpretation, the time it actually takes the companion's Roche Lobe to cross our line of sight is $\lesssim$ 491s, with the ablated material adding as much as $\sim$ 9 s to totality in the case of the longest observed eclipses early in the *RXTE*

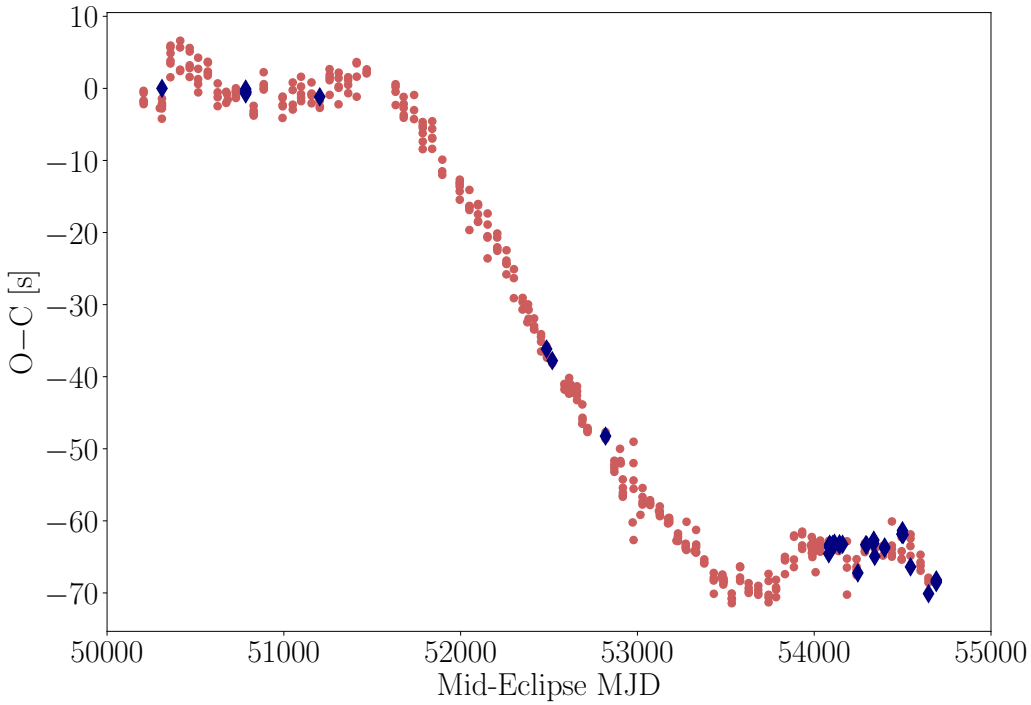

Figure 5.9: Measured O–C residuals of the mid-eclipse times for each of the full eclipses of EXO 0748 observed by *RXTE*. These residuals confirm that EXO 0748–676 showed three constant orbital period solutions during the *RXTE* era, originally uncovered by Wolff et al. (2009). Red dots correspond to ObsIDs originally considered by Wolff et al. (2009) and blue diamonds represent additional ObsIDs considered in this work.

observations. A true totality duration of $\sim$ 491s corresponds to a $\sim$ 2% reduction of t_e assuming an average totality duration of $\sim$ 500s. Following Equations 9 and 17 from Knight et al. (2022a), we see that $M_{\rm NS} \propto (\cos^3(\pi t_e/P))^{-1}$, and t_e does not influence the K-correction (the deviation between the reprocessed light centre and the centre of mass of a Roche lobe-filling star; Munoz-Darias et al. 2005). Therefore, a 2% decrease of t_e corresponds to a 5% increase in $M_{\rm NS}$ which is a negligible change to the NS mass (Knight et al. 2022a present a $\sim$ 14% uncertainty on their NS mass of $2M_\odot$), so this could explain the variations in totality duration. However, totality does not need to correspond to the surface of the Roche lobe. For example, totality could correspond to an interval shorter than the size of the Roche lobe if enough mass can get across the inner Lagrange point to produce the outbursts while the same material

layer seen in the eclipses appears optically thin to X-rays. Calculating this, however, is beyond the scope of this work.

The orbital period of EXO 0748 displayed several sharp transitions between different, seemingly constant values over the course of its outburst (Wolff et al., 2009). Fig. 5.9 shows the O–C residuals[3] as a function of mid-eclipse MJD for the *RXTE* eclipses of EXO 0748. We use our measurements of the mid-eclipse MJD (see Table 5.1) to recreate Figure 3 from Wolff et al. (2009), confirming that during the *RXTE* era there are three separate, constant orbital period solutions. We see that the new O–C measurements are consistent with the previously uncovered relationship. We investigate whether this behaviour can be explained by assuming a constant orbital period with the ablated material causing the totality duration to appear longer or shorter. We define $t_e = t_{\rm bef} + t_{\rm aft}$ as the duration of totality, where $t_{\rm bef} = (t_e/2) - ({\rm O-C})$ and $t_{\rm aft} = (t_e/2) + ({\rm O-C})$. Therefore, by calculating $t_{\rm bef}$ and $t_{\rm aft}$, we can see if $t_{\rm mid}$, the time at the centre of the eclipse, is being shifted by the start or end of totality arriving earlier or later than expected due to excess, optically thick material close to the star's surface. We find that the ablated outflow would need to be responsible for ~ 45 s of the totality duration in order for this hypothesis to be true (see Fig. 5.10), meaning that the true duration of totality would be ~ 455 s. This amount of time is too large to be accounted for by the ablated material layer, especially as the ablated outflow is already responsible for extending the eclipse transitions (which are $\sim 15 - 20$ s long Knight et al. 2022a). This hypothesis also predicts that the O-C residuals correlate with the in/egress durations, however, we do not find any evidence for this. We therefore conclude that the observed O–C residuals really are driven by changes in orbital period, which we speculate could be caused by a circumbinary disc and mass loss from the second Lagrange point (see e.g. Heath & Nixon 2020; Avakyan et al. 2021).

[3]Observed centre of totality minus that predicted for a constant orbital period.

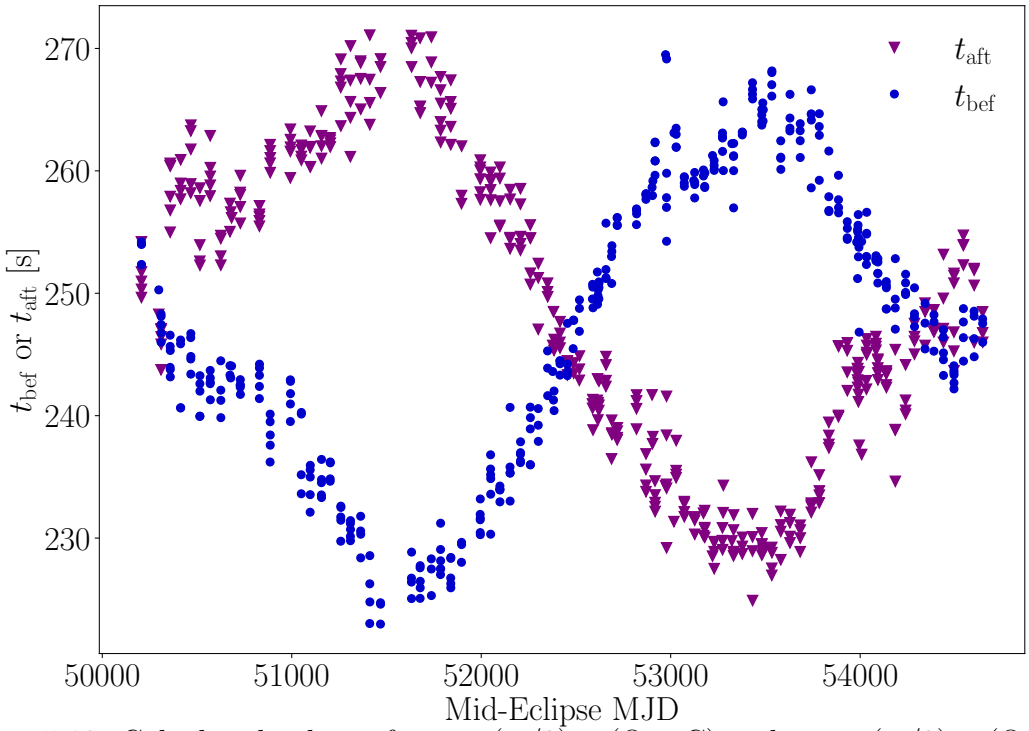

Figure 5.10: Calculated values of $t_{\rm bef} = (t_e/2) - ({\rm O} - {\rm C})$ and $t_{\rm aft} = (t_e/2) + ({\rm O} - {\rm C})$ as a function of mid-eclipse MJD for all full *RXTE* eclipses of EXO 0748–676. Here, the orbital period is defined such that the O–C residuals at the start and end of the *RXTE* era are zero, and the period is constant. As the difference between the maximum and minimum values of both $t_{\rm bef}$ and $t_{\rm aft}$ are ~ 45 s, the ablated material cannot explain the observed O–C residuals.

5.5 Discussion

We have investigated two eclipsing NS LMXBs – EXO 0748 and Sw J1858 – that both show evidence that their companion stars are undergoing ablation by X-ray irradiation from the NS. The physical scenario of ablation was initially suggested by Parmar et al. (1991) to explain the highly variable and extended eclipse transition durations in some *EXOSAT* observations of EXO 0748. The same scenario was later used to explain the eclipse profiles of both EXO 0748 and Sw J1858, as their extended ingress and egress profiles are well described by a model that includes optically thin material around the companion star (Knight et al., 2022a,b). The eclipses of both EXO 0748 and Sw J1858 are asymmetric, respectively, with ingress and egress durations of $\sim$ 15s and $\sim$ 17s and $\sim$ 106s and $\sim$ 174s, which are reproduced well by modelling the

optically thin material around the companion star with an exponential or Gaussian radial density profile (Knight et al., 2022a,b). We can make a simple calculation of the atmospheric scale height of each of the companions stars assuming they have isothermal hydrostatic atmospheres supported by gas pressure. In this case, the density decreases exponentially with height, $\rho \propto \exp(-h/h_{\rm sc})$, as inferred by Knight et al. (2022a) and Knight et al. (2022b). Thus, the scale height of an isothermal companion star atmosphere, in the simplest case, is given by

$$h_{\rm sc} = \frac{R_{\rm cs}^2 kT}{GM_{\rm cs}\mu m_{\rm p}}. \tag{5.1}$$

Here $R_{\rm cs}$ is the Roche lobe radius, k is the Boltzmann constant, T is the temperature of the atmosphere, G is the gravitational constant, $m_{\rm p}$ is the mass of a proton and μ is the mean particle mass in AMU. For 3000K $\leq$ T $\leq$ 7000K, $\mu = 1.0$ and $1.4M_{\odot} \leq M_{\rm NS} \leq 3.0M_{\odot}$, we find that the atmospheric scale heights of both companion stars are far less than the radial extent of the ablated material layers inferred via eclipse mapping (see Figs. 5.11 A and B respectively for EXO 0748 and Sw J1858). Therefore, this simple calculation strongly supports the presence of super-Roche lobe material in both systems and implies that the atmospheric scale height of the companion is negligible when discussing the X-ray absorbing layer. The atmospheric (gas pressure) scale height could still be an important factor if X-ray heating, which is a component of ablation, significantly heats the atmosphere.

Here, we have conducted orbital phase-resolved spectroscopy of both sources to trace the ablated material out to much larger distances from the companion star. For both objects, we find that the ionized absorbing material is still present beyond the eclipses, at orbital phases $|\phi| \gtrsim 0.2$ rad). We find that the column density, ionization and covering fraction drop off with distance from the companion star. These findings inform us that the ablated material remains present at large distances from the companion star and is distinguishable from the ISM. In addition, the measured ionization

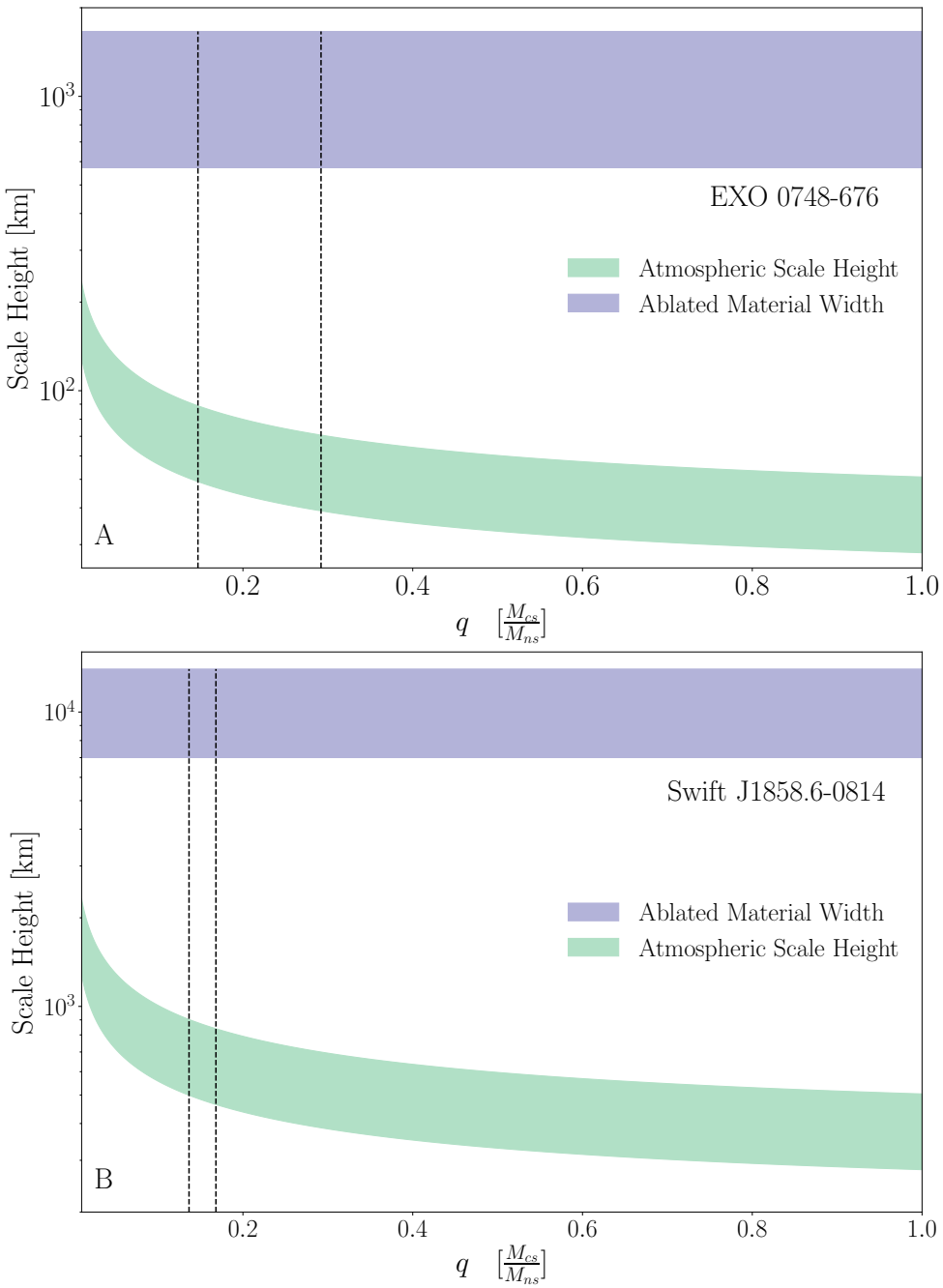

Figure 5.11: The width of the material layer around the companion star measured via eclipse mapping for EXO 0748 (Knight et al., 2022a) (Panel A, blue) and Sw J1858 (Knight et al., 2022b) (Panel B, blue) compared to the width of the companion star atmosphere calculated using Equation 5.1, which assumes the star is in hydrostatic equilibrium (atmosphere is supported by gas pressure) for EXO 0748 (Panel A, green) and Sw J1858 (Panel B, green) respectively. In both sources we conclude the the atmospheric scale height is not sufficient to explain the radial extent of the obscuring material around the companions. In each panel, black dashed lines indicate the mass ratio in each source measured via eclipse mapping (Knight et al., 2022a,b).

is consistent with the outflow being driven by irradiation and the evolution of the covering fraction suggests that the ablated material becomes clumpy when diffusing away from the companion star. This inferred geometry is illustrated in Fig. 5.3.

We have further investigated the long-term evolution of eclipses in both objects. Since there are hundreds of archival eclipses for EXO 0748 and only 12 partial eclipses for Sw J1858, our analysis focuses mainly on the former object. Utilising all available *RXTE* observations of EXO 0748, we find several properties that cannot be explained without the presence of stellar material extending beyond the companion's Roche Lobe. First, the evolution of the totality duration, which cannot be driven by changes to the binary system, but must instead be due to ablated material close to the companion star surface sometimes becoming sufficiently optically thick to extend totality. Second, the evolution of the ingress and egress durations; for most of the time *RXTE* was monitoring EXO 0748's eclipses, the egress was longer than the ingress, indicating that material was being dragged behind the companion star on its orbit. However, for several years this behaviour reversed, with the ingress becoming longer than the egress, similar to the observed behaviour of the known black widow pulsar PRS J2051–0827 (Polzin et al., 2019a). We further find that the ingress and egress durations appear to be anti-correlated with one another and we uncover tentative evidence that the transition durations are correlated with the RMS variability amplitude of the irradiating X-ray signal. This is well known as a good proxy for spectral state (Belloni, 2010; Muñoz-Darias et al., 2010; Heil et al., 2015). We, therefore infer, that the ingress is longer when a harder spectrum is being emitted from the NS vicinity, while longer egresses align with irradiation by a softer spectrum, thus providing further evidence that X-ray irradiation is responsible for the presence of the ionized absorbing material in the vicinity of the companion.

While EXO 0748 and Sw J1858 display remarkably similar eclipse and orbital phase-resolved spectral properties, there are also notable differences between the two

systems. First, eclipse mapping analyses indicates that the companion star in EXO 0748 is consistent with being a main sequence star (mass: $\sim 0.4 M_{\odot}$, radius: $\sim 0.43 R_{\odot}$; Knight et al. 2022a) but implies that the companion star in Sw J1858 is far less compact than a typical main sequence star (mass: $0.183 M_{\odot} \leq M_{\rm cs} \leq 0.372 M_{\odot}$, radius:$1.02 R_{\odot} \leq R_{\rm cs} \leq 1.29 R_{\odot}$; Knight et al. 2022b). Therefore if ablation has influenced the global properties of the companion star in these two objects, it has not caused the companion in EXO 0748 to diverge far from the expected main sequence mass-radius relation.

Secondly, Sw J1858 has a longer orbital period than EXO 0748 ($\sim$ 21.3 hrs versus 3.82 hrs). It is intuitive to associate ablation with more compact systems e.g. short-period binaries since the irradiating X-ray flux is higher for a given source luminosity, so ablation may be more effective in EXO 0748 than in Sw J1858. Podsiadlowski (1991) showed that a low-mass companion star in an accreting binary could be induced to expand by a factor of 2 to 4 and lose mass by an irradiating flux of $\log(F_x/\mathrm{erg\ s^{-1} cm^{-2}}) \approx 11.6$. For reasonable distance estimates to each source (6.8 kpc for EXO 0748 Díaz Trigo et al. 2011 and 12.8 kpc for Sw J1858 Buisson et al. 2020), the irradiating flux can be estimated to be above this threshold for both EXO 0748 ($\log(F_x/\mathrm{erg\ s^{-1}\ cm^{-2}}) \sim 12.8$) and Sw J1858 ($\log(F_x/\mathrm{erg\ s^{-1} cm^{-2}}) \sim 12.1$; Knight et al. 2022b). Therefore, although the orbital period is very different between the two systems, both appear to have enough irradiating flux to drive expansion/bloating of the companion's atmosphere and contribute to mass loss. We therefore suggest that other LMXBs with an irradiating flux $\gtrsim 10^{12}$ erg s^{-1} cm^{-2} could host material ablated from the companion star outside of the Roche-equipotential boundary. Note, however, that these simple calculations assume that the emission is isotropic and have not been averaged over an outburst duty-cycle. As such, these values represent upper limits on the irradiating flux incident on the companion star. Proper consideration of the incident flux requires us to compute the average flux over a timescale rele-

vant to the star's response. However, this is challenging as both EXO 0748 and Sw J1858 have only showed one outburst each, so the duration of each source's outburst cycle is unknown. Reasonable order-of-magnitude estimates for the duty cycles of X-ray transients fall within the range $0.01 - 0.1$ (e.g. Barnard et al., 2014), so the the true irradiating flux required for ablation is likely $< 10^{12}$ erg s^{-1} cm^{-2}. Further observations of ablation in XRBs are required to constrain this flux boundary.

If we assume that the companion star has expanded due to X-ray irradiation, we would also need to consider whether the binary itself has expanded as a result. Such expansion could cause mass transfer to cease (e.g. a transient system) and thus, stop any ongoing irradiation-driven ablation. This scenario may explain the short outburst in Sw J1858 and inferred radius of its companion star, but is overall incompatible with EXO 0748. Furthermore, a bloated/expanded atmosphere remains challenging to reconcile with the large observed eclipse asymmetry. While stellar atmospheres can be asymmetric, this has only been observed in asymptotic giant branch (AGB) stars or pulsating red giants; e.g. Mira A (Vlemmings et al., 2019). Even then, the degree of asymmetry seen for these evolved stars is not sufficient to explain the $t_{\rm in}/t_{\rm eg} \sim 0.6$ asymmetry we observe in Sw J1858 and is even difficult to reconcile with the $t_{\rm in}/t_{\rm eg} \sim 0.87$ asymmetry observed in EXO 0748.

The asymmetric, photon energy-dependent eclipse profiles (compare Fig. 2 of Knight et al. 2022a and Fig. 2 of Knight et al. 2022b), the low-mass companion stars and the presence of ionized, optically thin material ablated from the companion stars in both sources are reminiscent of redback and black widow pulsars, in which the NS with a pulsar wind drives the ablation of the companion star, having previously been spun up by accretion (Fruchter et al., 1988; Alpar et al., 1982; Radhakrishnan & Srinivasan, 1982). While the number of known eclipsing redback and black widow pulsars remains low, the observed radio eclipses (see e.g. Polzin et al. 2018 for discussion of the eclipses observed for J1810+1744) are similar in many ways to the X-ray

eclipses we observe for EXO 0748 and Sw J1858. Additionally, the reversal in eclipse asymmetry that we have uncovered in the *RXTE* eclipses of EXO 0748 is also seen in the known black widow pulsar PRS J2051–0827 (Polzin et al., 2019a). For PRS J2051–0827, the structure of the ablated material changes on $\sim$ month timescales, peaking on the ingress side for $\sim$ 3 years, before reversing and peaking on the egress side. These timescales are comparable to those uncovered for EXO 0748 thus increasing our confidence that super-Roche lobe material is influencing the observed eclipse profiles in both systems. Furthermore, the presence of very broad optical emission lines (Ratti et al., 2012) and a broad C IV (UV) feature (Parikh et al., 2020) observed from EXO 0748 while in quiescence, provide additional evidence that EXO 0748 is spider-like. Ratti et al. (2012) attributed the broad optical emission lines to an outflow driven by X-ray irradiation and/or a pulsar wind, while Parikh et al. (2020) found similarities between the broad C IV (UV) feature and observed features of the known tMSP PSR J1023+0038.

These findings contradict analysis by Church & Bałucińska-Church (2004), who interpret the eclipse ingress and egress of EXO 0748 as being due to the transit by the companion star across a very large X-ray emitting region. Such an interpretation is incompatible with the observed asymmetry and photon energy dependence of the eclipses. Specifically, the eclipse of an extended X-ray emitting region cannot explain how the soft X-ray ingress is observed to start earlier and the egress to finish later than the hard X-ray ingress and egress, while the start and end of totality are both independent of photon energy (see Section 2.3.1 of Knight et al. 2022a). In contrast, the eclipse profiles and phase-resolved spectra are naturally explained by the presence of ionizing material ablated from the companion star.

Despite there being no additional observed similarities between Sw J1858 and black widow pulsars, its evolved companion is consistent with observations of known huntsman pulsars (Strader et al., 2015) suggesting Sw J1858 is huntsman-like. How-

ever, its short orbital period is inconsistent with huntsman systems and is instead, similar to redback systems. Sw J1858 also shares a number of properties with EXO 0748, including but not limited to the X-ray eclipse characteristics, out-of-eclipse flaring and dipping behaviour (Bonnet-Bidaud et al., 2001; Homan et al., 2003; Buisson et al., 2021), type I X-ray bursts (Gottwald et al., 1986; Bonnet-Bidaud et al., 2001; Buisson et al., 2020) and a stellar prominence during some ingresses (Wolff et al., 2007; Buisson et al., 2021). We consider these similarities sufficient to group the two systems at this stage. Interestingly, Church & Bałucińska-Church (2004) identify several other eclipsing NS XRBs with even longer transition durations than those seen in EXO 0748 (see Fig. 2 of Church & Bałucińska-Church 2004), implying that ablation is common in binaries that are compact enough for eclipses to be likely and that it becomes a stronger effect with increasing X-ray luminosity.

The aforementioned similarities between these X-ray observations and the radio observations of eclipsing spider pulsars led us to term EXO 0748 and Sw J1858 as *false widows*. We define a false widow as a LMXB whose companion star is being ablated by X-ray irradiation from the NS and accretion disc and/or a pulsar wind. For EXO 0748, some observations indicate the presence of a pulsar wind (see Díaz Trigo et al. 2011; Parikh et al. 2020), but the response of the transition durations to spectral state strongly suggest that the outflow is irradiation-driven. We further suggest that an irradiating flux on the companion from the primary $\gtrsim 10^{12}$ erg s^{-1} cm^{-2} is sufficient to drive ablation in such systems. Uncovering ablation in other LMXBs will enable us to test this boundary and assess the commonality of ablation in XRBs.

We speculate that false widows may represent progenitors of redback pulsars under the assumption that ablation begins while the source is actively accreting and continues into the rotation powered phase. At the time of writing, the false widows are not known to display pulsations at any wavelength, however the distance to each source ($\approx$ 13 kpc for Sw J1858 (Buisson et al., 2020) and $\approx$ 7 kpc for EXO 0748

(Díaz Trigo et al., 2011)) makes detecting pulsations challenging. The spin of EXO 0748 is known to be 552 Hz (Galloway et al., 2010), which would place it within the millisecond regime, like redbacks and black widows, if it is a pulsar, but the spin of the NS in Sw J1858 is not known at the time of writing. While both sources are in X-ray quiescence we will search for radio pulsations. Additionally spider pulsars are known to harbour some of the most massive NSs (Romani et al., 2012; Linares et al., 2018; Burdge et al., 2022) which is consistent with the $\sim 2M_{\odot}$ NS in EXO 0748 (Knight et al., 2022a). Our speculations could be settled by understanding whether ablation occurs solely in NS XRBs or whether it also occurs in BH XRBs. Evidence for the latter would not only imply that irradiation is driving ablation but also suggest that ablation is ubiquitous among XRBs, thus contradicting our hypothesised link between false widows and redback pulsars. The presence of ablated material is of course harder to infer in the absence of eclipses, but may still be possible to detect with orbital phase-resolved spectroscopy even for non-eclipsing sources and observed changes in $N_{\rm H}(t)$ could constrain the orbital period.

5.6 Conclusions

The X-ray eclipses exhibited by two NS LMXBs, EXO 0748 and Sw J1858, share several characteristics such as asymmetry and photon energy dependence throughout the eclipse transitions. Additionally, the two sources share some out-of-eclipse behaviours such as type I X-ray bursts, dips and flares. We utilised archival data to further explore the similarities between the two systems through phase-resolved spectroscopy of their near-eclipse epochs. We determined that an ionized absorber exists close to the companion star in both systems. The column density and covering fraction of the ionized absorber decreases further from the companion star, implying that the material becomes clumpy at large distances. This is consistent with the optically thin material layer inferred to extend the duration of the eclipse transitions

of both LMXBs (Knight et al., 2022a,b). This clumpy material arises from the ablation of the companion star's atmosphere by X-ray irradiation and/or a pulsar wind, similar to the cannibalistic behaviour exhibited by redback and black widow pulsars. We therefore refer to EXO 0748 and Sw J1858 as *false widows*, defined as an XRB hosting an ablated companion star. We speculate that the false widows may represent progenitors of redback pulsars under the assumption that ablation begins during the accretion-powered phase and continues into the rotation-powered phase. This mechanism could provide a way to create the under-massive companions in short-period binaries like those observed within spider pulsars (Fruchter et al., 1988; Stappers et al., 1996). By modelling all available full eclipse profiles of EXO 0748 from the *RXTE* data archive, we uncover a reversal of the eclipse asymmetry. This appears, tentatively, to depend on the spectral state of the system and could also be influenced by the movement of ablated material within the gravitationally bound region of the binary, similar to observations of the black widow pulsar PRS J2051–0827. We can evidence the link between the false widows and spider pulsars by searching for radio pulsations from the two sources while they are in X-ray quiescence and determining whether ablation is ubiquitous among XRBs.

5.7 Appendix 5A: *RXTE* Eclipse Data Table for EXO 0748 − 676

The *RXTE* data archive contains a total of 746 observations of EXO 0748–676, taken between March 1996 and September 2010, which contain 429 full eclipse profiles. The results of fitting the simple eclipse model described in Section 5.4 to these data are provide in Table 5.1, which details the Obs ID, number of active PCUs (proportional counter units), mid-eclipse MJD, ingress duration, egress duration, totality duration, reduced χ^2, null-hypothesis probability, mean $2 - 15$ keV out-of-eclipse count rate and hardness ratio. Each of the durations are provided with a 1σ confidence interval

and the hardness ratio is calculated as $F_{10-16\mathrm{keV}}/F_{6-10\mathrm{keV}}$.

Table 5.1: Eclipse transition durations and X-ray hardness from all archival *RXTE* observations of EXO 0748–676 containing full eclipse profiles. The full version of this table is available on the MNRAS webpage.

Obs ID	PCU No.	Mid-Eclipse MJD	Ingress Duration [s]	Egress Duration [s]	Totality Duration [s]	χ^2_ν	p	Rate [cts/s]	Hardness $\frac{F_{10-16\mathrm{keV}}}{F_{6-10\mathrm{keV}}}$
10108-01-01-00	5	50206.37478	1.996 ± 0.149	3.179 ± 0.238	508.405 ± 0.508	1.024	0.578	150.3	0.730
10108-01-02-00	5	50206.53410	1.983 ± 0.149	3.055 ± 0.229	505.025 ± 0.505	1.001	0.682	160.6	0.788
10108-01-03-00	5	50206.69343	3.073 ± 0.231	4.455 ± 0.334	502.006 ± 0.602	1.025	0.573	129.8	0.742
10108-01-04-00	5	50206.85277	3.070 ± 0.230	4.514 ± 0.338	504.060 ± 0.604	1.014	0.606	136.6	0.713
10108-01-05-00	5	50207.01211	1.984 ± 0.148	3.141 ± 0.236	504.306 ± 0.647	1.005	0.643	136.9	0.749
10068-03-02-00	5	50298.15333	3.016 ± 0.226	5.666 ± 0.424	498.558 ± 0.257	1.000	0.688	153.3	0.894
10108-01-06-00	5	50310.10367	2.958 ± 0.222	9.497 ± 0.712	492.059 ± 0.591	1.000	0.699	139.4	0.846
10108-01-07-00	5	50310.26303	7.611 ± 0.571	4.057 ± 0.304	493.005 ± 0.391	1.019	0.594	135.4	0.876
10108-01-08-00	5	50310.42237	6.177 ± 0.463	5.612 ± 0.421	494.553 ± 0.568	1.001	0.682	134.0	0.786
10108-01-09-00	4	50310.58170	5.031 ± 0.227	9.098 ± 0.682	494.551 ± 0.566	1.011	0.615	82.84	0.795
10108-01-07-01	5	50310.90039	6.481 ± 0.486	10.92 ± 0.819	492.593 ± 0.395	1.003	0.659	155.3	0.522
10108-01-10-00	4	50310.74106	3.939 ± 0.295	8.536 ± 0.642	497.557 ± 0.572	1.013	0.608	109.2	0.515
10108-01-11-00	5	50358.06446	4.976 ± 0.373	3.100 ± 0.233	504.564 ± 0.580	1.018	0.592	152.2	0.638
10108-01-12-00	5	50358.22379	7.837 ± 0.588	5.758 ± 0.432	501.561 ± 0.576	1.052	0.524	155.3	0.471
10108-01-13-00	5	50358.38312	5.658 ± 0.424	8.169 ± 0.613	503.563 ± 0.578	1.064	0.601	156.7	0.413
10108-01-14-00	5	50358.70179	7.961 ± 0.597	14.54 ± 1.091	500.560 ± 0.375	1.032	0.557	128.4	0.605
10108-01-15-00	5	50358.86113	9.576 ± 0.718	12.51 ± 0.938	505.766 ± 0.581	1.016	0.618	146.5	0.619
10108-01-15-01	5	50359.02048	5.905 ± 0.442	6.417 ± 0.481	503.563 ± 0.578	1.001	0.678	161.9	0.844
20069-01-01-00	5	50413.03601	5.991 ± 0.449	13.73 ± 1.030	499.609 ± 0.387	1.037	0.547	155.2	0.595
20069-01-02-00	5	50413.19536	4.992 ± 0.374	12.67 ± 0.950	503.563 ± 0.178	1.021	0.588	147.6	0.596
20069-01-03-00	5	50413.35465	4.580 ± 0.343	10.33 ± 0.775	504.564 ± 0.675	1.015	0.601	145.9	0.593
20069-01-05-00	4	50413.83268	4.972 ± 0.373	10.17 ± 0.762	501.561 ± 0.149	1.003	0.654	143.2	0.628
20069-02-01-00	5	50466.73285	5.029 ± 0.377	11.90 ± 0.892	504.564 ± 0.657	1.033	0.556	152.7	0.620

5.8 Appendix 5B: Phase-Resolved Spectroscopy

The principal result of this work, respectively shown in Figs. 5.1 and 5.2, is the phase-resolved absorption spectroscopy of the near-eclipse epoch of the two false widows EXO 0748–676 and *Swift* J1858.6–0814. From this analysis we uncover evidence for an ionized absorbing medium surrounding the companion star in both LMXBs which supports our hypothesis that in both EXO 0748–676 and *Swift* J1858.6–0814, the companion stars are experiencing irradiation driven ablation. For each source, we have modelled 44 phase-resolved spectra within XSPEC using our local absorption model ABSSCA, which introduces the hydrogen column density, $N_{\rm H}$, the log of the ionization, $\log(\xi)$ and covering fraction as properties of the companion star's outflow. Any absorption from the ISM is modelled separately using the XSPEC model TBABS, assuming the abundances of Wilms et al. (2000). The three parameters introduced by ABSSCA each create subtly different changes to the spectra. The material hydrogen column density, $N_{\rm H}$, alters the transmission factor such that higher values of $N_{\rm H}$ increase the material optical depth by an energy-independent factor. Since the absorption cross-section typically decreases with energy, increasing $N_{\rm H}$ typically has the effect of preferentially suppressing soft X-rays. The ionization parameter, $\log(\xi)$, impacts the number of bound atomic species in the absorber which in turn impacts the energy-dependence of the absorption cross-section. The covering fraction, $\rm f_{cov}$, changes the absorption fraction such that lower covering fractions allow more photons to pass through and thus increases the peak of the spectrum. Since each of these effects are only subtly different, we must determine whether all three parameters can be individually constrained, particularly if the spectra are not of high quality.

We begin by assessing the quality of each spectrum by checking the count rate for each bin of each spectrum. While we have opted for wide energy bands to increase the number of counts per bin (see Section 5.3), in some cases the number of counts remains too low to perform the fits using chi-squared statistics. Indeed, when testing

the chi-squared fits we often found very tight, unbelievable parameter constraints or that a comparable fit could be found with entirely different parameters. We instead opt to use C-statistics (hereafter c-stat) within XSPEC as it is more appropriate for fitting lower quality data with fewer counts (Arnaud, 1996) and did not encounter the aforementioned issues. Note, that while binning the data to ensure a reasonable number of counts per bin is not required when fitting with c-stat, we do not re-bin the data into finer energy bands. This ensures consistency between the analysis presented here and our earlier phase-resolved spectral analyses of the same sources (Knight et al., 2022a,b). For each source, we then select four spectra, two from the ingress or pre-ingress phases and two from the egress or post-egress phases to represent the spectral fits and investigate the partial parameter degeneracies.

For each representative spectrum and each parameter, we perform a 1-dimensional `steppar` analysis within XSPEC to check how well each parameter is constrained and whether a better fit (one with an overall lower C-statistic) could be found. The results of each `steppar` are shown by the 1-dimensional contour plots in Figs. 5.12 and 5.14 respectively for EXO 0748–676 and *Swift* J1858.6–0814. In these plots, the solid red line highlights the best-fitting parameter value and the dashed red lines indicate the 1σ confidence interval. Here, we clearly see that each parameter *can* be individually constrained in each of the representative spectra, although in some cases this is a broad constraint. While these contours are informative, they do not necessarily prove that partial parameter degeneracies have been avoided, nor do they highlight any parameter correlations. Therefore, for each representative spectra, we also include a corner plot showing the parameter distributions obtained by running a Markov-Chain Monte-Carlo (MCMC) simulation within XSPEC, using the Goodman-Weare algorithm. We use a chain length of 307200, 256 walkers and a burn-in period of 19998 to produce the corner plots in Figs. 5.13 and 5.15 respectively for the representative spectra of EXO 0748–676 and *Swift* J1858.6–0814. These 2-dimensional parameter

Spectra	N_H $[10^{22}]$	$\log(\xi)$	f_{cov}
EXO 0748: 8 (h)	0.4252 - 0.8167	1.5456 - 1.8013	0.4379 - 0.6494
EXO 0748: 8 (f)	0.5907 - 0.6020	1.7407 - 1.7572	0.5323 - 0.5359
EXO 0748: 18 (h)	7.2929 - 21.016	3.6398 - 3.9675	0.8272 - 1.000
EXO 0748: 18 (f)	11.659 - 13.209	4.2809 - 4.3117	0.8852 - 0.9414
EXO 0748: 36 (h)	0.3721 - 0.6823	2.0941 - 2.2819	0.4963 - 0.5954
EXO 0748: 36 (f)	0.5176 - 0.5309	2.1958 - 2.2080	0.5029 - 0.5330
EXO 0748: 44 (h)	0.1452 - 0.4820	1.6512 - 2.4598	0.3537 - 0.4326
EXO 0748: 44 (f)	0.4969 - 0.5649	1.4883 - 1.5697	0.3488 - 0.3722
Sw J1858: 6 (h)	1.1347 - 2.1545	1.2148 - 1.6768	0.3931 - 0.4749
Sw J1858: 6 (f)	1.6074 - 1.6609	1.5521 - 1.6106	0.4149 - 0.4249
Sw J1858: 13 (h)	2.1031 - 5.6160	1.7689 - 1.9189	0.4889 - 0.6157
Sw J1858: 13 (f)	3.0193 - 3.0544	1.8774 - 1.8929	0.5309 - 0.5354
Sw J1858: 30 (h)	85.744 - 91.901	1.6461 - 2.2557	0.5571 - 0.6612
Sw J1858: 30 (f)	90.251 - 92.546	2.0730 - 2.0899	0.6085 - 0.6089
Sw J1858: 37 (h)	1.9995 - 3.2778	1.0589 - 1.6548	0.3349 - 0.5705
Sw J1858: 37 (f)	2.9559 - 2.9979	1.3049 - 1.3211	0.3493 - 0.3509

Table 5.2: 1σ confidence intervals for each of the three key ABSSCA model parameters; the material column density N_H, the log of the ionization parameter, $\log(\xi)$ and the material covering fraction, f_{cov}, for each of the eight representative spectra. We compare these intervals for the cases where the spectra are heavily (h) binned into the six energy bands (see Section 5.3) and finely (f) binned to have one count per bin. The parameters are found to be mostly consistent within 1σ confidence bounds. All fits were carried out using c-stat.

distributions largely support the conclusion from our 1-dimensional contours that each parameter can be individually constrained for each spectrum. Note that individually constraining each parameter was only possible when performing the analysis using c-stat, as is appropriate for the quality of our spectra. No strong parameter correlations are present, although in a few spectra tentative correlations do appear; e.g. Fig 5.13C. If such correlations appeared in all corner plots it would be obvious that some parameter degeneracies were impacting our results, however, they are not a consistent feature. Therefore, we remain confident that each parameter in our modelling can be constrained in each spectrum and that the behaviours found in Figs. 5.1 and 5.2 are real.

Finally, we ensure that our choice to keep the data binned in six wide energy bands,

thus maintaining consistency between this analyses and our earlier investigations of the same sources, does not impact our findings. For each of the eight representative spectra, we rebin the data to have one count per bin and repeat the fitting procedure. While the data do not necessarily need to be binned at all when modelling with c-stat, unbinned data are known to show biases that are not present when the data are finely binned (Arnaud, 1996). We compare the results of the finely binned spectra to those of the heavily binned spectra used in Section 5.3 in Table 5.2, finding that the best fitting parameters are generally consistent within 1σ confidence intervals for the two binning procedures. While our choice to heavily bin the data does not appear to have influenced our findings, we note that more precise results are possible with finer binned spectra.

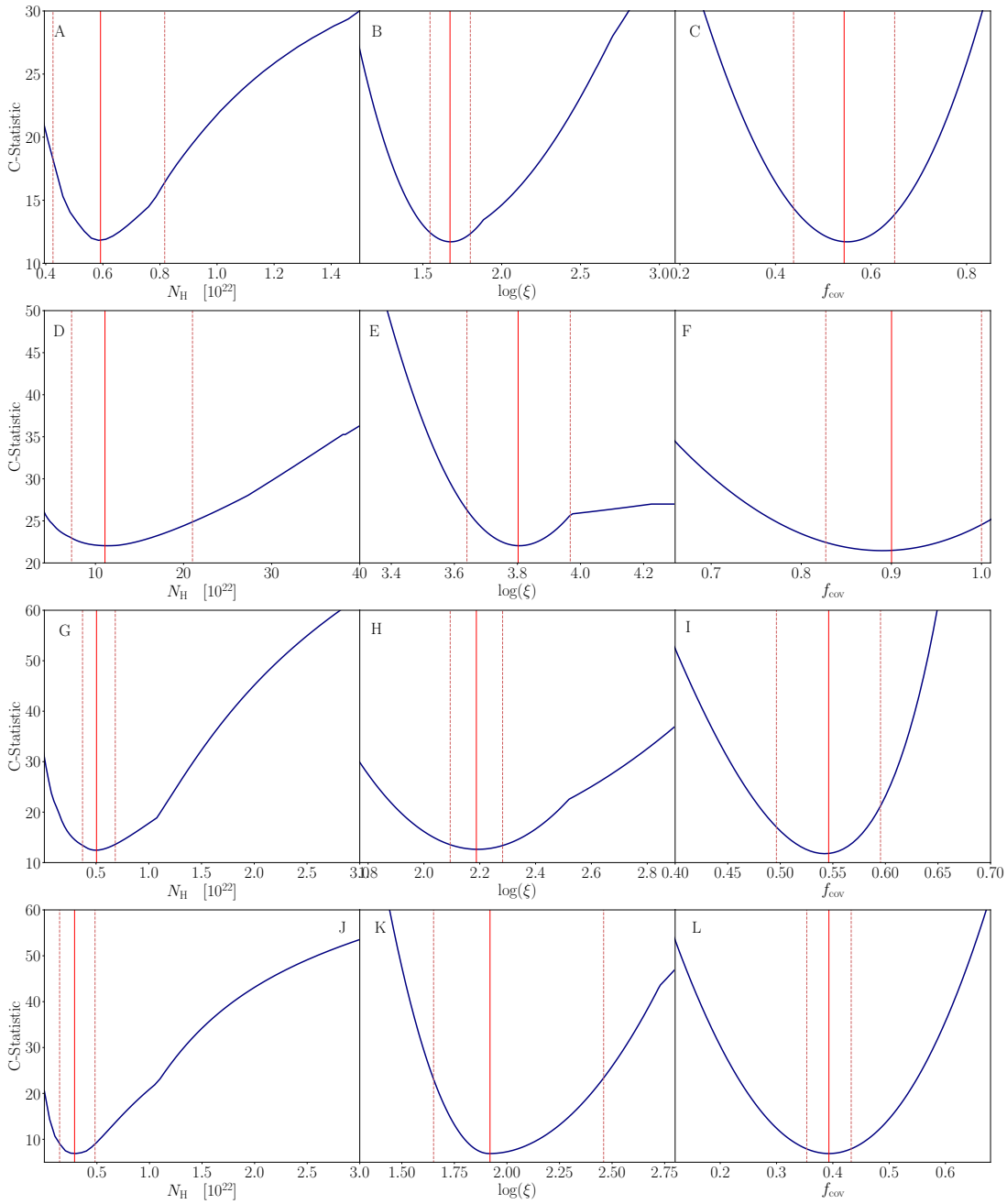

Figure 5.12: 1D parameter contours (blue) for four different phase-resolved spectra of EXO 0748 obtained by running `steppar` analysis within XSPEC. Respectively, panels A-C, D-F, G-I and J-L correspond to Spectra 8, 18, 36 and 44, following a left to right numbering convention for the spectral fits in Fig. 5.1. For each spectra log(ξ), $f_{\rm cov}$ were respectively varied in the ranges $1.0-3.0$ and $0.05-0.95$ using 400 steps, except panel E, which instead used a range of $2.5-4.5$. For each spectra, $N_{\rm H}$ is varied through a range of values surrounding the best fitting values, again using 400 steps. For panels A, D and J this range is $1.0\times10^{-5}-5.0$ while the range used in panel G is $0.1-50.0$. In each panel the best fitting parameter value is shown by the solid red line while the dashed red lines represent 1σ contours.

A) EXO 0748–676: Spectrum 8

B) EXO 0748–676: Spectrum 18

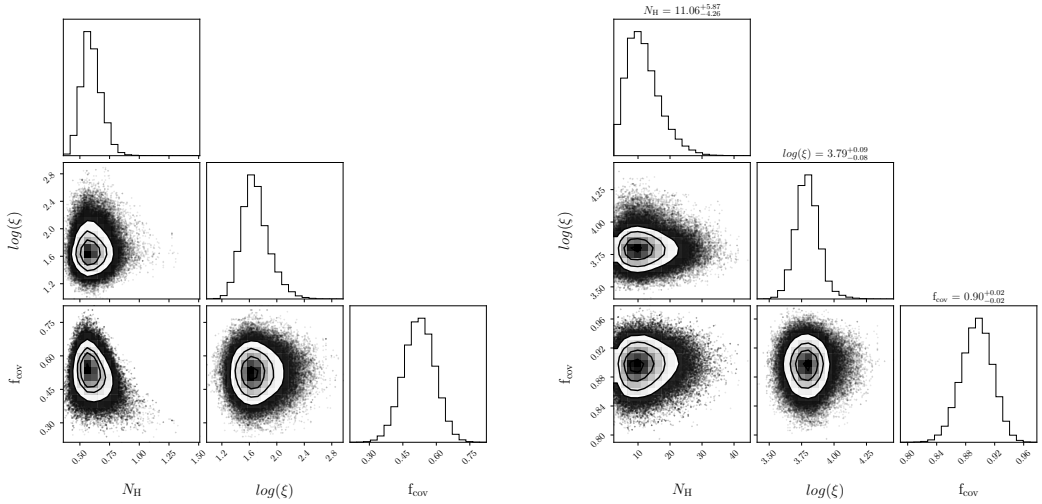

C) EXO 0748–676: Spectrum 36

D) EXO 0748–676: Spectrum 44

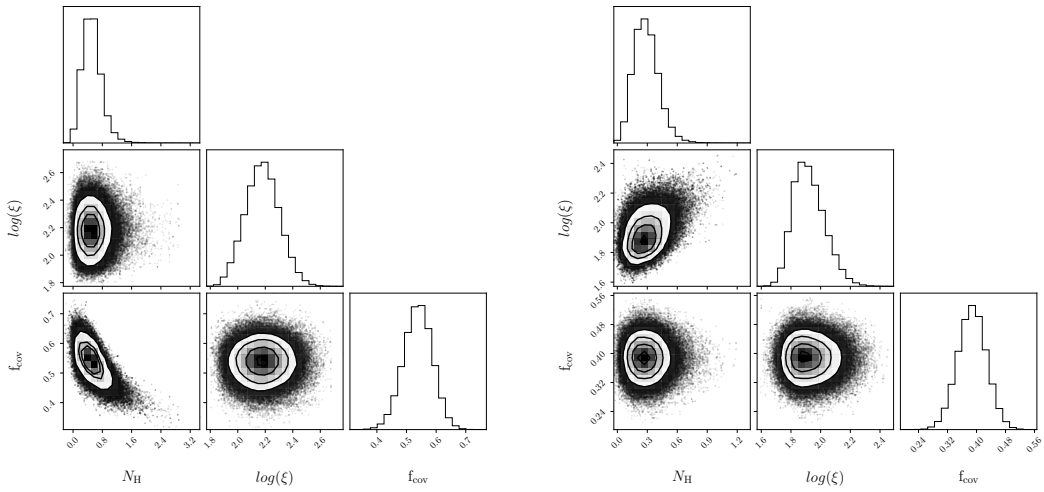

Figure 5.13: Distributions of $N_{\rm H}$, $\log(\xi)$ and $f_{\rm cov}$ for four different phase-resolved spectra of EXO 0748 obtained by running an MCMC simulation of ABSSCA within XSPEC. Spectra are numbered following a left-to-right convention of the spectral fit in Fig. 5.1. The chains are run using the Goodman-Weare algorithm, using a length of 307200, 256 walkers and a burn-in period of 19998. For the 2D histograms, 1σ, 2σ and 3σ contours are shown by the solid black lines. The 1D histograms are displayed with their y-axes in arbitrary units.

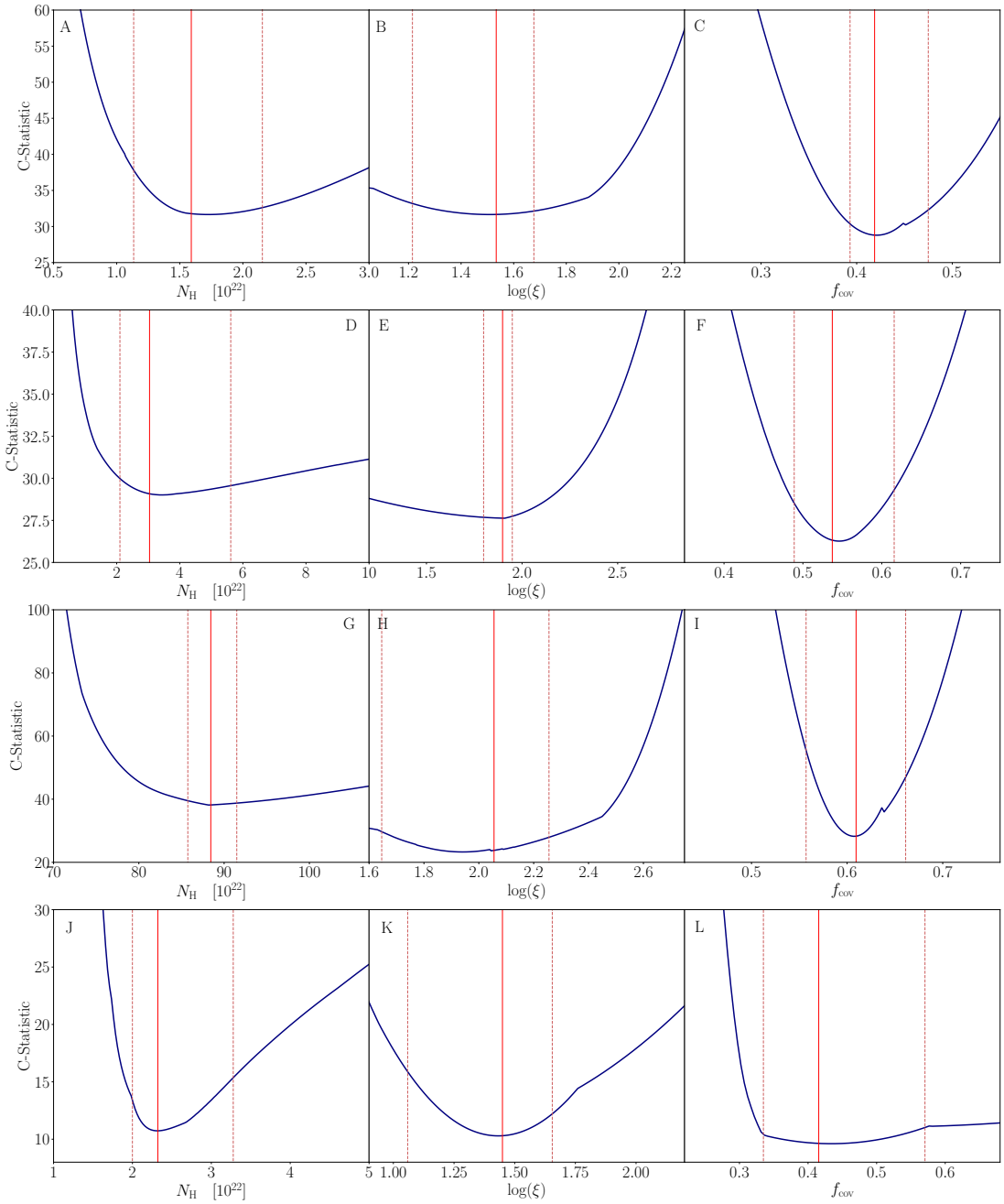

Figure 5.14: 1D parameter contours (blue) for four different phase-resolved spectra of Sw J1858 obtained by running `steppar` analysis within XSPEC. Respectively, panels A-C, D-F, G-I and J-L correspond to Spectra 6, 13, 30 and 37, following a left to right numbering convention for the spectral fits in Fig. 5.2. For each spectra log(ξ), f_{cov} were respectively varied in the ranges $0.75 - 3.0$ and $0.05 - 0.95$ using 400 steps. For each spectra, $N_{\rm H}$ is varied through a range of values surrounding the best fitting values, again using 400 steps. For panels A this range is $1.0 \times 10^{-5} - 5.0$. For panel D and J the range used is $0.1 - 30.0$ and for panel G the range used is $50.0 - 200.0$. In each panel the best fitting parameter value is shown by the solid red line while the dashed red lines represent 1σ contours.

A) *Swift* J1858.6–0814: Spectrum 6

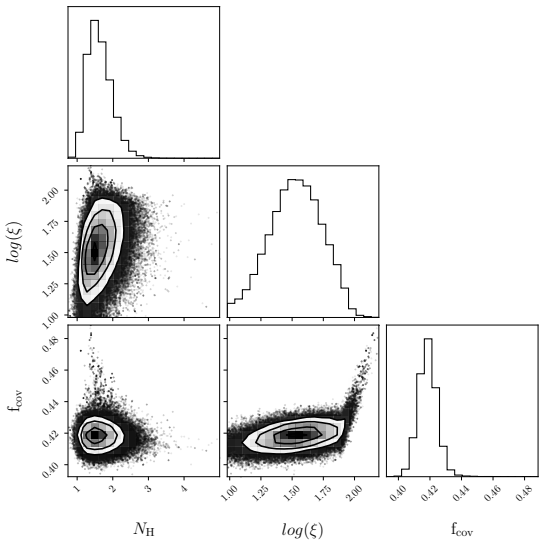

B) *Swift* J1858.6–0814: Spectrum 13

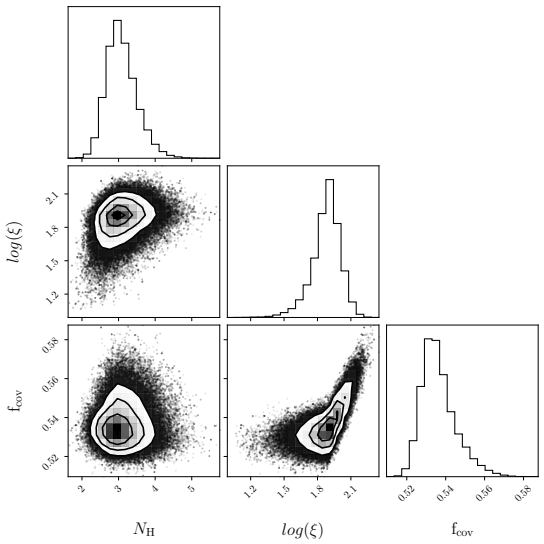

C) *Swift* J1858.6–0814: Spectrum 30

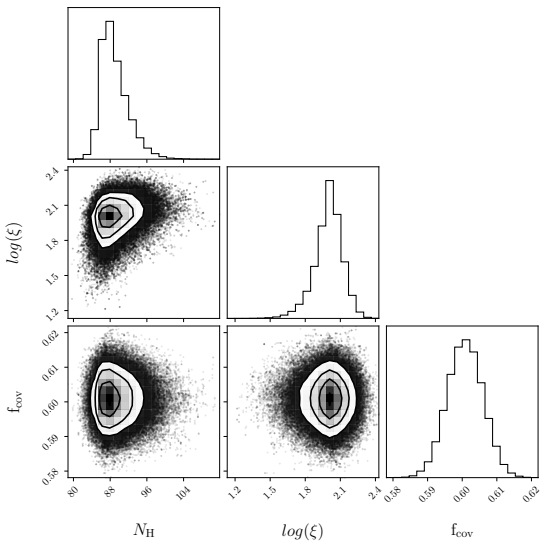

D) *Swift* J1858.6–0814: Spectrum 37

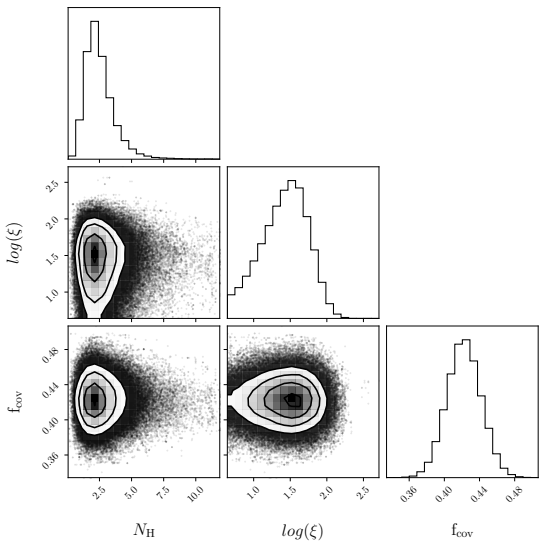

Figure 5.15: Distributions of $N_{\rm H}$, log(ξ) and $f_{\rm cov}$ for four different phase-resolved spectra of Sw J1858 obtained by running an MCMC simulation of ABSSCA within XSPEC. Spectra are numbered following a left-to-right convention of the spectral fit in Fig. 5.2. The chains are run using the Goodman-Weare algorithm, using a length of 307200, 256 walkers and a burn-in period of 19998. For the 2D histograms, 1σ, 2σ and 3σ contours are shown by the solid black lines. The 1D histograms are displayed with their y-axes in arbitrary units.

Chapter 6

Searching for Radio Pulsations in EXO 0748–676

6.1 Introduction

The *false widow link* (Chapter 5) between NS LMXBs and spider pulsars speculates that in some short-period NS LMXBs, X-ray irradiation is sufficient to trigger ablation, thus depleting the mass of the companion star. This hypothesised connection expands on the well-established evolutionary connection between XRBs and radio MSPs, known as the recycling scenario (Backer et al., 1982; Alpar et al., 1982), which fails to explain all of the observed properties of spider pulsars (Fruchter et al., 1988).

Spider pulsars are characterised by significantly ablated, very low-mass companion stars, short orbital periods (Fruchter et al., 1988; Stappers et al., 1996; Roberts, 2012a) and more massive NSs (Romani et al., 2012; Linares et al., 2018; Burdge et al., 2022). One suggestion to explain these observational properties is that the companion star's mass becomes so low due to ablation by the energetic pulsar wind. Subsequently, this led to the hypothesis that spider pulsars form part of the evolutionary pathway towards isolated MSPs (stage 3 to stage 4 in Figure 6.1), assuming that the companion star is eventually entirely ablated by the incident pulsar wind (Ruderman et al., 1989a). Ablation does explain some spider pulsar properties; for example, the accretion of ablated material can contribute to the growth of the NS

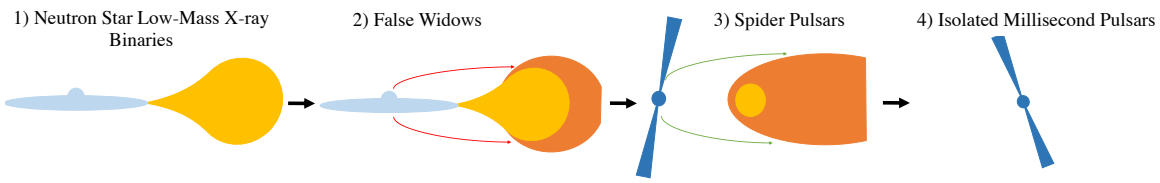

Figure 6.1: A schematic showing the expected evolutionary path from neutron star (NS) low-mass X-ray binaries (LMXBs) to isolated millisecond pulsars (MSPs). Here the X-ray bright NS and accretion disc are shown in light blue and the companion star is yellow. The ablated outflow from the companion star is orange. The radio-bright NS is dark blue and the red and green arrows represent the X-ray photons or pulsar wind particles that bombard and ablate the companion star.

(Knight et al., 2022a, 2023). It also explains several of the eclipse properties of spider pulsars. However, ablation by a pulsar wind was determined to be an inefficient mass-loss mechanism, so it cannot be solely responsible for forming the very low-mass companions observed in spider pulsars (Polzin et al., 2018, 2020).

In Chapters 3, 4 and 5, I uncovered evidence that some NS LMXBs undergo ablation driven by X-ray irradiation (Knight et al., 2022a,b), raising questions regarding the connection between NS XRBs and spider pulsars (Knight et al., 2023). In Chapter 5, I termed NS LMXBs experiencing ablation *false widows* and speculated that they comprise part of the evolutionary pathway between NS LMXBs and spider pulsars (Knight et al., 2023). The premise of this connection is that, while in an XRB phase, the companion star loses masses via accretion *and* X-ray-driven ablation. The NS can accrete material transferred via RLOF and any nearby ablated material, and the binary separation may also decrease due to mass loss from the system. Ultimately, this mechanism paves the way toward systems with spider pulsar-like configurations so that when accretion ceases, the false widow transitions into a spider pulsar (see Fig. 6.1).

In this Chapter, I test this hypothesised connection by searching for radio pulsations from the false widow, EXO 0748–676 (hereafter EXO 0748), using recent observations from the Parkes Radio Telescope (hereafter Parkes) while the system is

in X-ray quiescence. EXO 0748 hosts an irradiated, $0.4M_{\odot}$ M-dwarf star in a 3.824 hr orbit with a $\sim 2.0M_{\odot}$ NS (Knight et al., 2022a). During EXO 0748's outburst, the companion star recurrently eclipsed the NS and accretion disc. The eclipse properties are highly variable and show extended, energy-dependent, and asymmetric eclipse transitions (ingress and egress) (Parmar et al., 1991; Wolff et al., 2009; Knight et al., 2022a, 2023). The eclipse transitions vary on long and short timescales, lasting between $1 - 30$ s (Parmar et al., 1991; Knight et al., 2023). These features, which are analogous to the observed characteristics of the radio eclipses exhibited by spider pulsars, led to my discovery of X-ray driven ablation in EXO 0748 (Knight et al., 2022a) and its subsequent false widow classification (Knight et al., 2023). The detection of broad lines in quiescent optical and UV spectra further support the spider-like diagnosis (Ratti et al., 2012; Parikh et al., 2020). Most recently, the discovery of the reversal of the eclipse asymmetry (see Figures 5.7 and 5.8; Knight et al. 2023), which is only otherwise exhibited by the black widow pulsar PSR J2051–0827 (Polzin et al., 2019b), strongly implies that ablated material is present in and around the binary. EXO 0748 is at a distance of approximately 7 kpc (Díaz Trigo et al., 2011), and the spin frequency of the NS is within a few Hertz of the type I X-ray burst oscillation frequency of 552 Hz (Galloway et al., 2010).

Detecting radio pulsations from EXO 0748 would indicate that the system has transitioned from an accretion-powered false widow (stage 2 in Figure 6.1) to a rotation-powered spider pulsar (stage 3 in Figure 6.1) and support the false widow hypothesis. In this Chapter, I discuss proprietary data from ongoing investigations by my False Widow Collaboration, and the results presented here are preliminary.

6.2 Quasi-Simultaneous X-ray and Radio Observations

We obtained a 2 ks X-ray observation of EXO 0748 on 25th August 2022 using *Swift*-XRT to confirm that the source had not begun actively accreting again. Since entering quiescence in late 2009, all X-ray observations of EXO 0748 have identified X-ray emissions caused by the cooling of the NS surface (Parikh et al., 2021). However, radio pulsations are only observable if the source is truly in quiescence. Therefore, to test the false widow hypothesis, it is necessary to determine that no low-level accretion is occurring. Within the 2 ks observation, *Swift*-XRT detected a faint thermal source coincident with the coordinates of EXO 0748. The observed spectrum and flux are consistent with the cooling NS surface, and the observation uncovered no evidence of active accretion. Thus, EXO 0748 is the ideal candidate for this radio pulsation search.

To demonstrate the feasibility of an accelerated search for radio pulsations in false widow candidates, we prepared a pilot study to search for radio pulsations from the false widow EXO 0748 using Parkes. Through a DDT proposal, we obtained 1 hour of observing time which we divided into four ten-minute pointings to ensure that at least three pointings avoided the eclipse phases, with the remainder allocated for overheads. We observed on 8th September 2022 using the Ultra Wide-band Low receiver and recorded data on the MEDUSA backend. The known 552 Hz (Galloway et al., 2010) spin frequency and source distance of $\sim$7 kpc (Díaz Trigo et al., 2011) (corresponding to a dispersion measure of $\sim$88 $\mathrm{cm^{-3}pc}$ using the NE2001 model Cordes & Lazio 2002) govern our chosen sampling rate and spectral resolution. Respectively, these are 1μs and 128 channels per sub-band, each 1 MHz wide.

6.3 PRESTO Search

The data are analysed using the PulsaR Exploration and Search TOolkit (PRESTO), a suite of pulsar search and analysis software (Ransom, 2001). This open-source software efficiently searches for MSPs in data taken by various radio telescopes. Instead of concatenating the four pointings, we divide them into 2 minutes segments to reduce the likelihood of smearing any radio pulsations due to the distance to the source or the varying orbital dispersion measure. The latter of which is contributed by ablation (Chapter 5; Knight et al. 2023).

We begin by searching for instances of prominent RFI by running the command `rfifind -time 0.75 -o mask_filename input_filename -psrfits`, where the `-psrfits` specifies the data type. `rfifind` identifies cases of strong narrow-band or broadband RFI and creates a mask (`mask_filename`) to replace RFI by median values, which we apply to the data during de-dispersion. `-time` specifies the integration times and should be no more than a few seconds. The returned number of bad intervals should be less than 20 per cent. Persistent low-level RFI is identifiable by running the command `prepdata -nobary -o output_filename-DM0.00 -dm 0.0 -mask mask_filename input_filename -psrfits`. Subsequently, the output file is Fourier transformed and searched, in the Fourier domain, for instances of persistent RFI using `accelsearch`. The RFI instances are collated in the *birds* file (birds are periodic interference in the power spectra) and are removed at a later stage.

The data are dedispersed at user-specified dispersion measures with `prepsubband`. Since the dispersion measure contribution of the ablated material in EXO 0748 is unknown, we dedisperse the data multiple times at dispersion measures between $1-150$, in steps of 1. The previously identified low-level RFI (birds) is removed from the data using `zapbirds`. The data are Fourier transformed and searched for pulsations in the Fourier domain using `accelsearch -zmax 200`. We then fold promising candidates with the `prepfold`.

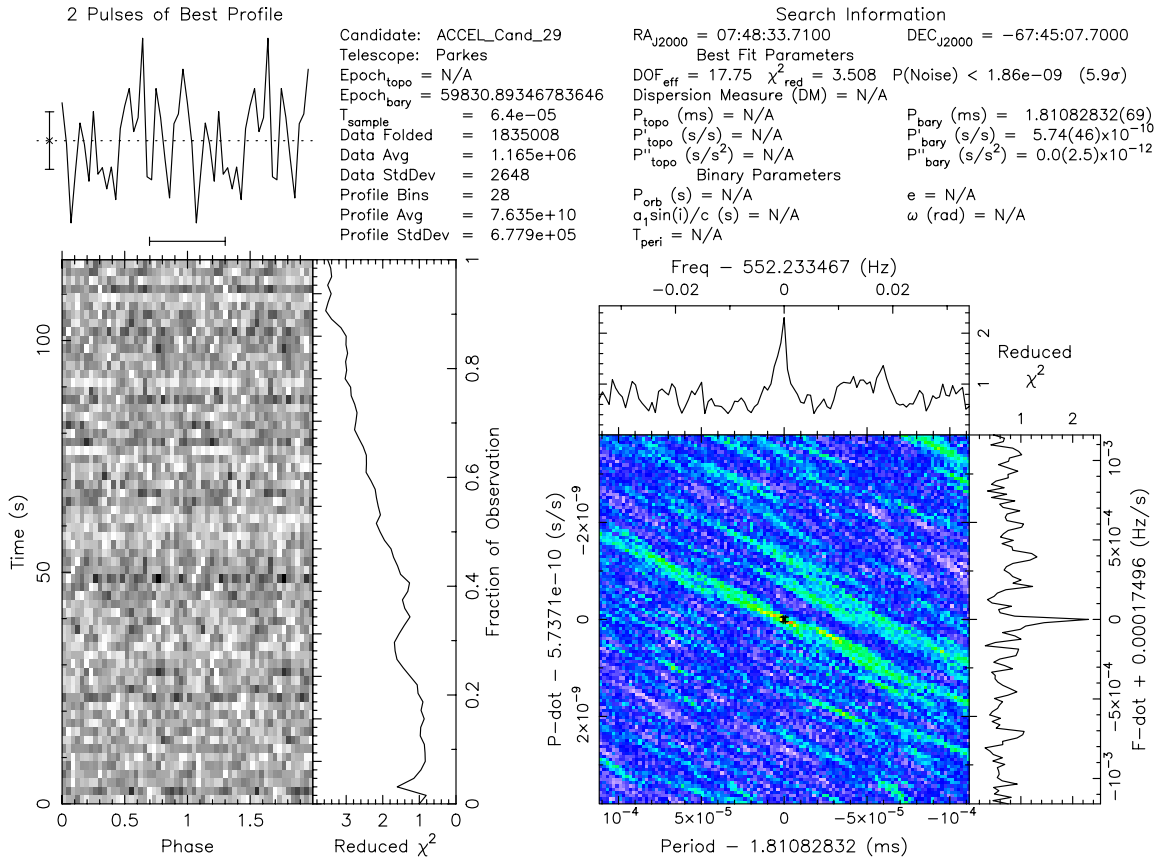

Figure 6.2: A 552.2 Hz candidate pulse from the false widow, EXO 0748–676. This candidate was identified through an acceleration search using PRESTO on pilot observations taken with the Parkes Radio Telescope.

6.3.1 Pulse Candidates

Our pilot search uncovered several exciting candidates at $551 - 554$ Hz, consistent with the known NS spin frequency (Galloway et al., 2010). These pulse candidates (see Fig. 6.2 for an example at 552.2 Hz) are recurrently identified in 2-minute segments of the 40-minute pilot observation, each with a significance of $\leq 2\sigma$. While this means we cannot confidently state that EXO 0748 has transitioned to a MSP, it does suggest that a transition occurred, and it is evident that higher sensitivity observations of EXO 0748 are necessary to determine the exact NS spin frequency, improve confidence in these detections and thus confirm the false widow link. The dispersion measure at which the candidates are identified changes around the orbit

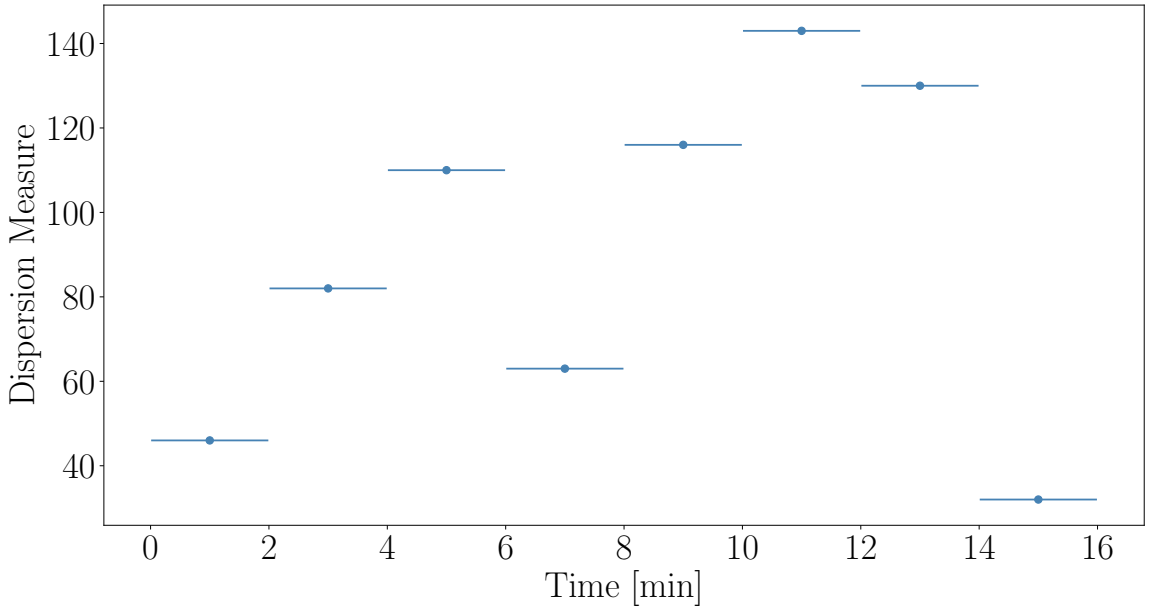

Figure 6.3: The dispersion measure of radio pulsation candidates identified from EXO 0748 – 676 as a function of time for the first sixteen minutes of our forty-minute pilot observation with the Parkes Radio Telescope.

in a manner consistent with the known changes in the column density of the ablated material (Knight et al., 2022a, 2023), enabling the study of irradiation-driven ablated outflows after the false widow transitions into a spider pulsar. As shown in Figure 6.3, the increases and decreases in dispersion measure are reminiscent of the changes in $N_{\rm H}$ seen in the phase-resolved spectroscopy of the near eclipse epochs of EXO 0748. However, as the orbital ephemeris of EXO 0748 is constrainable from X-ray eclipse timing (Wolff et al., 2009), we determine that these observations are at an orbital phase reasonably far removed from the eclipse ($\phi \sim 0.76$ rad, where $\phi = 0$ is the centre of totality). Therefore, we predict that the observed changes in dispersion measure are due to clumped ablated material trailing behind the companion star as it orbits. This scenario is increasingly likely if EXO 0748 is now a rotation-powered pulsar exhibiting an energetic pulsar wind that is now driving ablation, but is confirmable with confident detections of the radio pulsations.

Finally, it is necessary to note that the candidates reported here are not the only

ones discovered during our search. High sigma candidates emerge from our Fourier domain acceleration search in each 2-minute segment. These candidates occur at various frequencies (the frequencies are different in each segment) and are high on the list of candidates, with values of sigma reaching the thousands. We identify these candidates as artefacts or interference but are yet to determine their cause. Doing so is necessary such that we can amend our analysis procedure appropriately to ensure that the ~ 552 Hz candidates remain.

6.4 Discussion and Future Plans

We completed a Fourier domain acceleration search of 40 minutes of data, taken with the Parkes radio telescope, of the X-ray quiescent false widow EXO 0748 to assess the feasibility of searching for radio pulsations from false widow candidates and determine an observational strategy for future proposals.

We prepared, searched and folded the data using PRESTO (Ransom, 2001), which uncovered several exciting candidates consistent with the known NS spin frequency of 552 Hz (Galloway et al., 2010). All identified candidates are low sigma, likely due to the distance to the source or the ablated outflow from the companion star increasing the local dispersion measure. Therefore, we cannot confidently confirm that EXO 0748 is now a rotation-powered spider pulsar and have submitted a proposal to the MeerKat radio telescope in the latest open-time call, as the higher sensitivity available with MeerKat will be valuable when determining if these candidates are real. In addition, the dispersion measure at which the candidates are identified changes around the orbit in a manner consistent with the known changes in the column density of the ablated material (Knight et al., 2022a, 2023), enabling the study of irradiation-driven ablated outflows after the false widow transitions into a spider pulsar. We determine that our Parkes DDT observations are at an orbital phase reasonably far removed from the eclipse. Therefore, the observed changes in dispersion measure are likely

due to clumped ablated material trailing behind the companion star as it orbits. If EXO 0748 is now a rotation-powered pulsar exhibiting an energetic pulsar wind that is driving ablation, this scenario is probable.

Evidencing the false widow evolutionary phase creates many lines of exploration that will further our understanding of the processes contributing to this unique evolution. Firstly, monitoring the known false widows using X-ray and radio facilities is necessary to determine if the transition between false widows and spider pulsars is permanent or alternates and indicate the timescales upon which these transitions occur. Based on the knowledge of tMSPs (Archibald et al., 2009), the initial switch can take several years, but subsequent transition timescales can be as short as weeks. Similar transitions to tMSPs are possible in false widows. However, it is only determinable through long-term monitoring. In particular, the false widow EXO 0748 experienced a 24-year outburst and has been in X-ray quiescence since late 2009. Intermittent monitoring by X-ray facilities has not uncovered evidence for any other transitions implying that, for EXO 0748, the change may be permanent.

Furthermore, the small population of known false widows restricts our understanding. We cannot fully understand their evolution without knowing how many systems experience ablation and how many evolve into spider pulsars. Searching for false widows using archival X-ray observations and methods independent of the viewing angle, such as phase-resolved spectroscopy (Knight et al., 2022a, 2023) utilises the entire catalogue of X-ray binaries. Such a search would specifically probe local variations in density and ionisation that indicate irradiation-driven ablation. Therefore, we can identify new false widows and establish whether ablation is ubiquitous among XRBs.

In each stage in Fig. 6.1, the companion star is losing mass. However, there are open questions regarding the exact mass-loss processes occurring and their efficiencies. Examining the roles of accretion, ablation, and CBDs in false widows thus determines whether these processes are sufficiently efficient to form short-period binaries with

very low-mass companion stars. CBDs are discs of stellar material around the entire binary system. They are a crucial yet relatively unexplored line of enquiry since they are known to drain mass and angular momentum from binaries. As part of an ongoing investigation, I am simulating CBDs around false widows using PHANTOM, an SPH code for smoothed particle hydrodynamics and magneto-hydrodynamics. These simulations can uncover the properties of the CBDs and divulge their role in the evolution of binary systems. CBDs have not been directly observed but likely exist around several interesting systems like the false widow, EXO 0748–676 (Wolff et al., 2009; Knight et al., 2022a) and the XRBs XTE J1710–281 (Jain & Paul, 2011) and MXB 1658–298 (Jain et al., 2017). Thus, exploring the role of CBDs can advance our understanding of XRB evolution on multiple fronts.

Chapter 7

Type I X-ray Bursts *in* the X-ray Eclipses of EXO 0748–676

7.1 Introduction

While analysing the *RXTE* eclipses of EXO 0748–676 in Chapter 5, I discovered several unusual light curves that weren't compatible with my eclipse model. These observations all hosted what appeared to be a type I X-ray burst *in* the X-ray eclipses. Initially, I suggested that these few unusual events were instrumentation faults. However, as my eclipse model progressed through the *RXTE* archive, more light curves showed these events.

Here, I present the discovery of type I X-ray bursts *in* the X-ray eclipses of EXO 0748–676. I assess which events are physical and which are due to PCU errors and complete some statistical analysis of the population of bursts for EXO 0748–676 to understand these unique events. Finally, I present an initial spectral analysis of the in-eclipse X-ray bursts and hypothesise that they originate from reflection off of the ablated outflow.

7.2 In-Eclipse Thermonuclear X-ray Bursts

EXO 0748–676 was extensively monitored by *RXTE* and *XMM-Newton* during its 24-year-long outburst. As such, we utilise all archival *RXTE* and *XMM-Newton*

observations of EXO 0748–676 in this Chapter. The *RXTE* observations were considered in Chapter 5, which details the full data reduction procedure. However, a short overview is included below.

7.2.1 Data Reduction

We apply the fully automated CHROMOS pipeline[1] (Gardenier & Uttley, 2018) to all archival *RXTE* observations of EXO 0748–676. The CHROMOS pipeline applies all necessary data reduction steps before extracting light curves at the native time resolution of the data mode. We extract light curves in several energy bands: $3-6$ keV, $6-10$ keV, $10-16$ keV and $2-15$ keV. Each band comprises energy channels most closely matching the user-defined energy range, which accounts for the changes to the *RXTE* channel-to-energy conversion throughout its lifetime. We utilise the $2-15$ keV light curves, rebinned into 1 s time bins, to identify type I X-ray bursts.

7.2.2 Burst Identification

Since there are hundreds of observations, we do not manually inspect each light curve. Instead, we search each time series for count rates that are ≥ 1.4 times the average count rate in 100 s segments of the light curve. These events are flagged and appended to an index of features, specifying its ObsID, MJD of the features, number of active PCUs, peak count rate, in-eclipse exposure time and out-of-eclipse exposure time for the full ObsID. We manually assessed these features to determine their nature and whether other features were flagged nearby (e.g. doublets). During this, I noticed some features resembling type I X-ray bursts coinciding with the X-ray eclipses. Subsequently, we repeated the search with a 20% count rate threshold to ensure we captured any faint in-eclipse features.

[1] `https://github.com/davidgardenier/chromos`

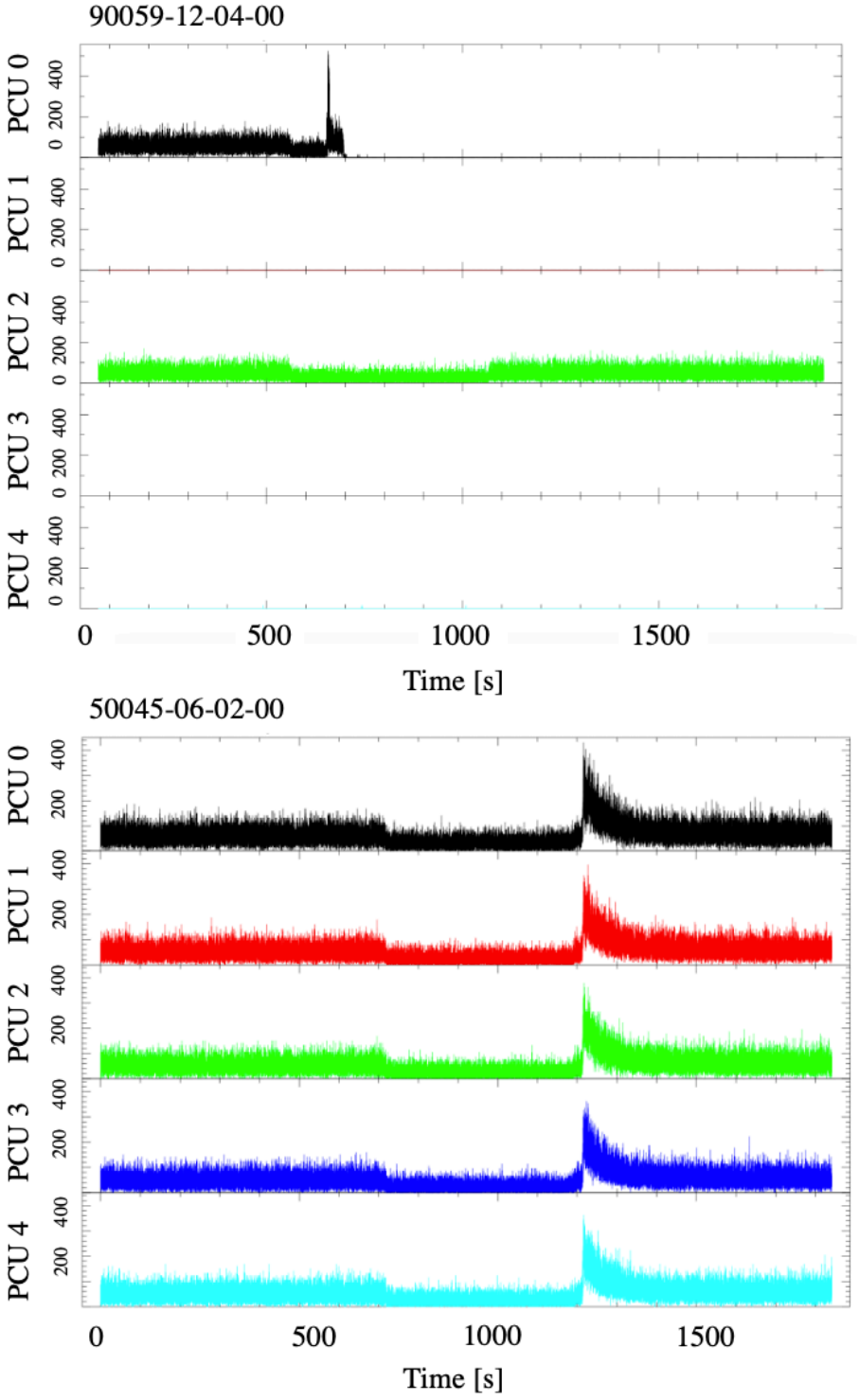

Figure 7.1: *RXTE* light curves of EXO 0748–676 per PCU for ObsIDs 90059-12-04-00 (top) and 50045-06-02-00 (bottom). The top panel shows the behaviour of a malfunctioning PCU, which creates an X-ray burst-like event in only one PCU before switching off. The feature in the bottom panel is physical.

7.2.3 Burst Classification

During an X-ray eclipse, the companion star blocks the X-rays from the NS and accretion disc. Therefore, it is somewhat unlikely that we are directly observing X-ray burst emission from the surface of the NS during eclipse phases. As such, it is prudent to determine that all identified features are physical.

To robustly establish which features are physical, we look at the light curve of the observation per PCU. Some *RXTE* light curves include instrumental features that resemble X-ray bursts, which occur when a PCU malfunctions, for example. In such cases, the malfunctioning PCU exhibits a flare and then turns off. This behavioural pattern (see Figure 7.1) is unique and highly unlikely to occur in two PCUs simultaneously. Therefore, we check whether the burst pattern occurs in multiple PCUs. Even in observations with only one active PCU, the behaviour of that PCU can indicate whether the feature is real. If a burst-like event occurs and the PCU stays active, the burst is probably real, whereas if the PCU switches off, the burst is likely instrumental.

We filter the list of features using the PCU behaviour, positively identifying 165 thermonuclear X-ray bursts, 20 of which coincide with an X-ray eclipse (see Figures 7.2 and 7.3). We classify the X-ray bursts into three groups: 1) In-eclipse bursts, where the entire burst profile occurs within eclipse totality (Figure 7.2). 2) Split bursts, where the burst starts in the later stages of totality and continues its decay phase after the egress or starts just before ingress and is interrupted when ingress begins (Figure 7.3). 3) Out-of-eclipse bursts do not interrupt an eclipse at all. Subsequently, we determine that all in-eclipse and split X-ray bursts occur while the EXO 0748 is in the hard spectral state.

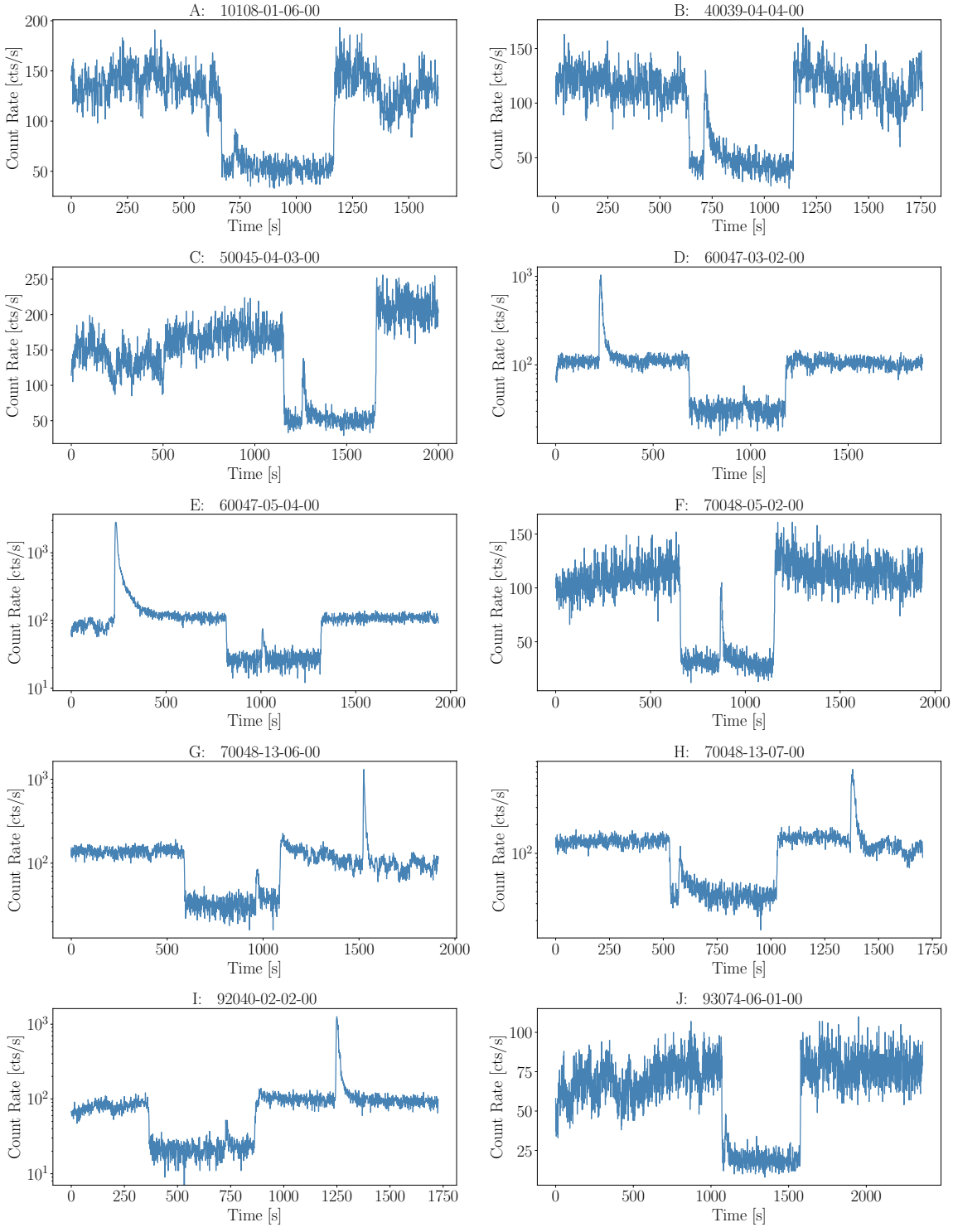

Figure 7.2: $2-15$ keV *RXTE* light curves showing all 10 instances in which type I X-ray bursts occur during the X-ray eclipses in EXO 0748–676. We refer to these as *in-eclipse bursts*. All 10 instances were observed by *RXTE* between $1996-2008$. The ObsIDs are detailed in each panel. Note that the y-axes are in log scale on some panels to improve the visual clarity of the in-eclipse bursts.

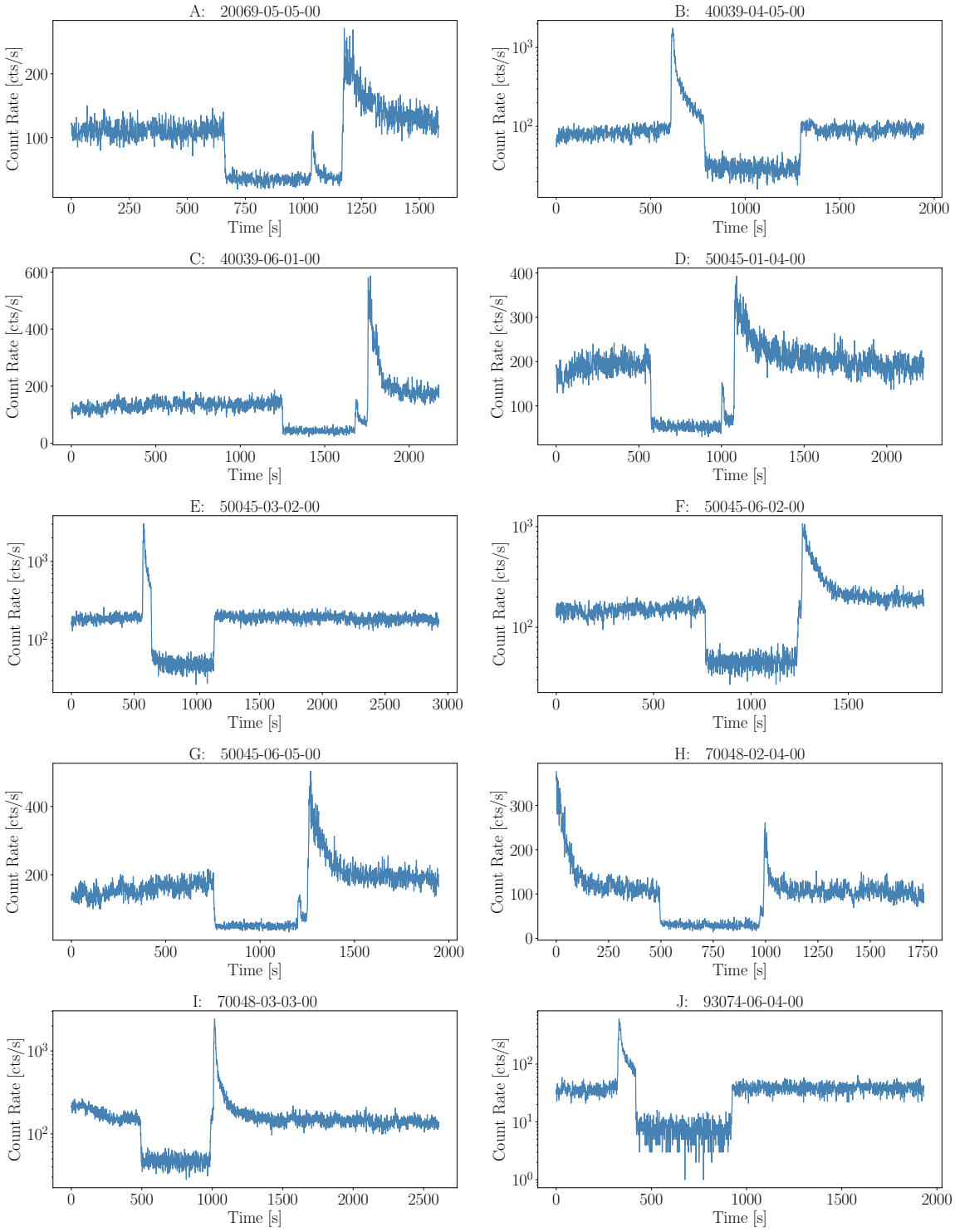

Figure 7.3: $2-15$ keV *RXTE* light curves showing all 10 instances in which type I X-ray bursts are interrupted by an eclipse transition (ingress or egress) in EXO 0748–676. We refer to these as *split bursts*. All 10 instances were observed by *RXTE* between $1996-2008$. The ObsIDs are detailed in each panel. Note that the y-axes are in log scale on some panels to improve the visual clarity of the in-eclipse bursts.

7.2.4 *XMM-Newton* Observations

We reduced all *XMM-Newton* observations of EXO 0748–676 listed in the XMM-Master data archive with the XMM-Newton Science Analysis Software, XMM-SAS to determine whether another instrument captured any in-eclipse or split X-ray bursts. We begin by creating an EPIC-PN event file for each ObsID using `epproc`, from which we extract a high-energy light curve to search for flaring events using `evselect` with the selection expression `#XMMEA_EP && (PI>10000&&PI<12000) && (PATTERN==0)`. Note that the high-energy extraction only uses energies up to 12 keV to avoid mistakenly identifying hot pixels as very high-energy events. We obtain the corresponding good time intervals (GTI) using `tabgtigen` with the rate expression determined by identifying a count/second threshold just above the low, steady background level. These filters are applied using `evselect` with the selection expression `#XMMEA_EP && gti(gti_filename,TIME) && (PI>150)`, where `gti_filename` is the output of `tabgtigen`. We barycentre the data with `barycen` and apply standard filters using `evselect` with the selection expression `(FLAG==0)&&(PATTERN<=4)&&(PI in [200:15000])&&#XMMEA_EP'`. For each ObsID, we extract an image and use DS9 to select appropriate source and background regions. For observations in imaging mode, the regions are circular, while in timing mode, the region is rectangular. Finally, light curves are extracted from the filtered and barycentric event lists in the energy range of $0.2 - 10.0$ keV and manually inspected for type I X-ray bursts. We do not confidently find any in-eclipse or split bursts in these light curves. However, we note two cases, shown in Figure 7.4, where burst-like features coincide with the X-ray eclipses. The high variability in these light curves and the lower peak fluxes of in-eclipse and split bursts prevent a confident identification of these features, so we do not consider these observations further.

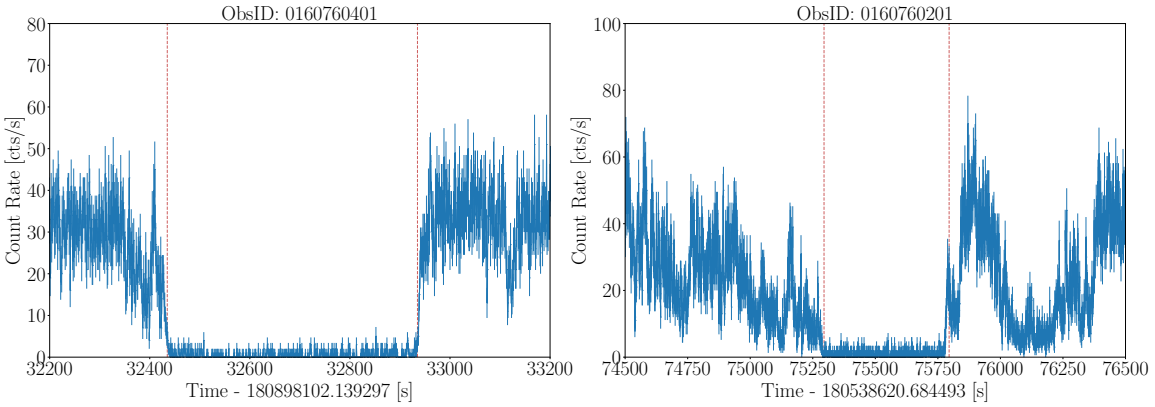

Figure 7.4: $0.5 - 10$ keV *XMM-Newton* light curves showing the two instances in which X-ray burst-like features interrupted by an eclipse transition (ingress or egress) in EXO 0748–676. In ObsID 0160760401 a burst-like feature occurs during the ingress and in ObsID 0160760201 a burst-like feature occurs during the egress. The red dashed lines show the expected totality duration.

7.3 Burst Statistics

We can make inferences about the nature of the in-eclipse bursts by analysing the number of in-eclipse (ec) and out-of-eclipse (ooe) bursts detected, and their relative peak count rates. Here, we complete several statistical tests to further understand these unique events.

7.3.1 The Expected Number of In-Eclipse Bursts

We detect $N_{\rm ooe} = 145$ out-of-eclipse bursts, $N_{\rm ec} = 10$ in-eclipse bursts, $N_{\rm eg} = 7$ egress-split bursts and $N_{\rm in} = 3$ ingress-split bursts, and show this population of bursts in Figure 7.5. The expected number of in-eclipse bursts *occurring* during one of the observed eclipses is $N_{\rm expect} = (T_{\rm ec}/T_{\rm ooe})N_{\rm ooe}$, where $T_{\rm ec}$ and $T_{\rm ooe}$ are in-eclipse exposure time and the out-of-eclipse exposure time respectively.

For each observation, we identify if any eclipses are present using our previously published, simple eclipse model (Knight et al., 2023). The in-eclipse exposure time is $t_3 - t_2$ (see Chapter 5). If observations contained partial eclipses, we manually adjusted the eclipse contacts, t_2 and t_3. Thus, the out-of-eclipse exposure time is the

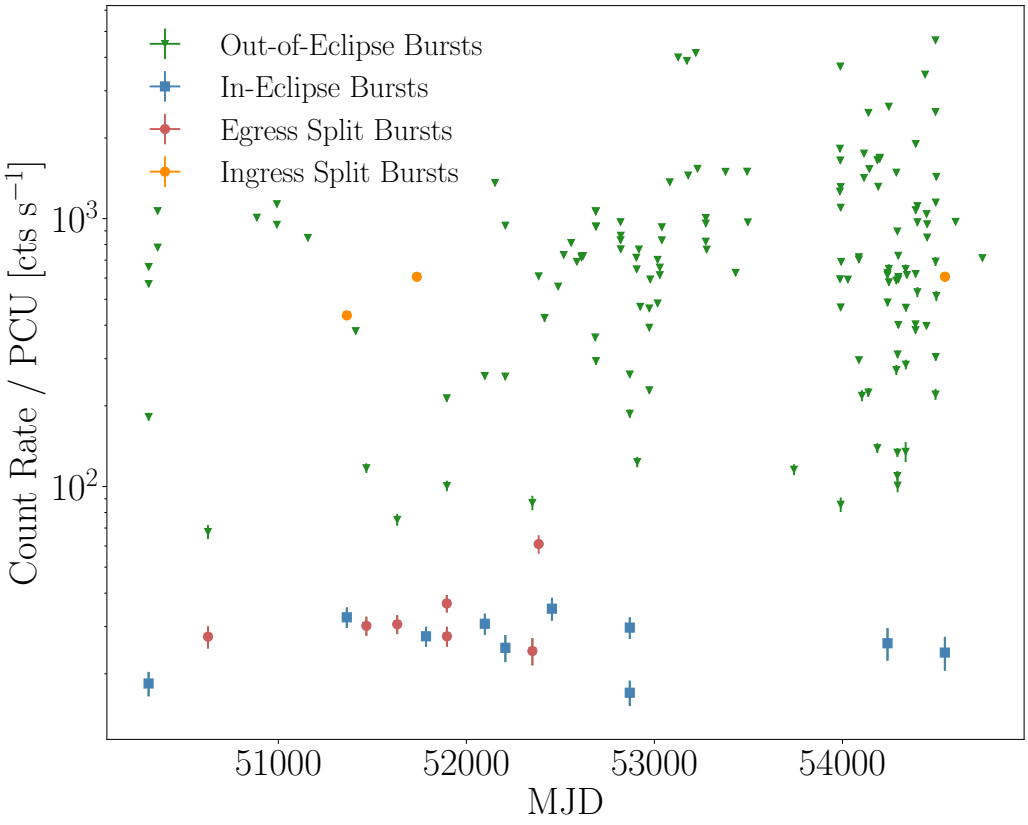

Figure 7.5: The distribution of the different classes of thermonuclear X-ray bursts identified in the archival *RXTE* data of EXO 0748–676.

total exposure time minus the in-eclipse exposure and any time lost to dropouts. To the nearest second, the total in-eclipse exposure time is $T_{\rm ec} \sim 46171$ s and the total out-of-eclipse exposure is $T_{\rm ooe} \sim 696499$ s. Subsequently, we determine $N_{\rm expect} = (46171/696499) \times 145 = 10.04$. Here the ratio of exposure times also accounts for any observational bias arising from the large number of observations of EXO 0748 that targeted the eclipses (Wolff et al., 2009).

Although the actual number of observed in-eclipse bursts (10) is comparable with the expected number occurring (10.04), we do not necessarily *see* all of the bursts that occur during eclipses. It is natural to suspect that some in-eclipse X-ray bursts are too dim to detect, particularly as the later *RXTE* observations have fewer active PCUs (due to PCU failures), so we may only observe the brightest bursts. Let us assume that we instead see a fraction, f, of the in-eclipse bursts that occur such that

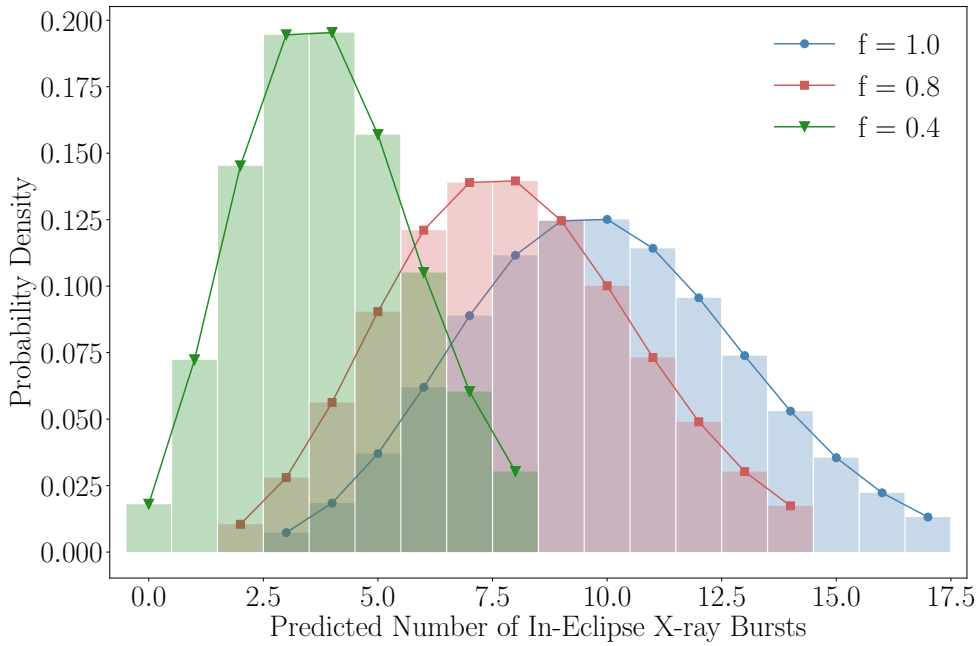

Figure 7.6: Poisson distributions with expectation values, fN_{expect}, describe the probability distribution function for the predicted number of observed in-eclipse X-ray bursts. Here f is the observed fraction of the in-eclipse bursts that occurred and N_{expect} is the number of in-eclipse bursts we expect to actually occur.

the number of in-eclipse bursts we're predicted to see is fN_{expect}. To compare this to the number of observed in-eclipse bursts N_{ec}, we consider the probability distribution function for the predicted number of observed in-eclipse bursts N_{predict}, which is a Poisson distribution with an expectation value of fN_{expect} as shown in Figure 7.6 for $f = 1$, $f = 0.8$ and $f = 0.4$. To determine the likelihood of observing at least N_{ec} in-eclipse bursts for a given value of f, we integrate this distribution from $N_{\text{predict}} = N_{\text{ec}}$ to $N_{\text{predict}} = \infty$ for $0 \leq f \leq 1.0$ in 101 steps. We plot the calculated probability of seeing at least $N_{\text{ec}} \sim 10$ against f in Figure 7.7, which shows that the chance of actually observing all ~ 10 in-eclipse bursts (i.e. $f = 1$) is $\sim 55\%$. The $1, 2$ and 3σ contour lines (red, green and orange respectively) correspond to scenarios whereby 12 ($f = 0.83$), 19 ($f = 0.54$) and 30 ($f = 0.33$) in-eclipse bursts actually occurred, but only 10 were observed. This also demonstrates that $f > 0.42$ with 99% statistical confidence.

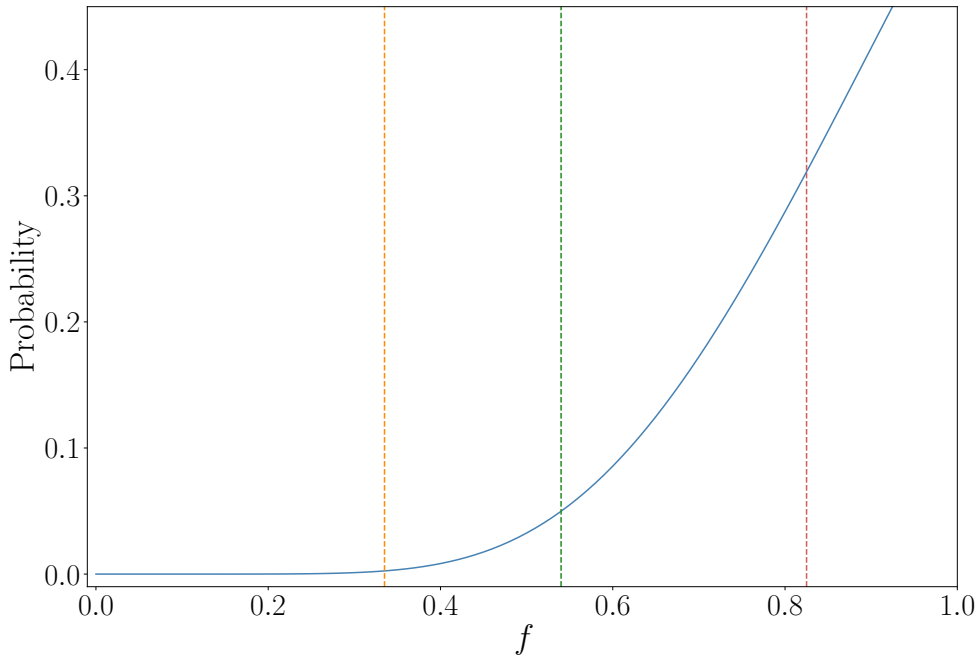

Figure 7.7: The fraction of predicted bursts we observe (f) as a function of the probability of observing all in-eclipse X-ray bursts. Here the red, green and orange lines are $1, 2$ and 3σ contours, corresponding to scenarios whereby, 12 ($f = 0.83$), 19 ($f = 0.54$) and 30 ($f = 0.33$) in-eclipse X-ray bursts occur but only 10 are observed. The probability of 10 in-eclipse bursts occurring *and* 10 being observed is $\sim 55\%$.

7.3.2 Flux Distributions

To further understand the different classes of X-ray bursts, we consider Figure 7.5, which shows the peak flux of the bursts against its MJD. Here, the different colours represent different classifications of X-ray bursts, as labelled in the Figure. We uncover a dichotomy between the in-eclipse (blue) and egress split (red) bursts and the out-of-eclipse (green) and ingress split (orange) bursts. The former two classes both have burst peaks during the totality, so their peak count rates are relatively low. In contrast, the latter two classes have their peaks during out-of-eclipse phases, so the count rates are comparatively high. We note that the low peak count rates exhibited by some of the out-of-eclipse bursts are due to either consecutive events, for example, doublets and triplets (see Figure 1.7) or observations that captured the burst shortly after the peak e.g. Figure 7.3 H.

Despite consistent monitoring of EXO 0748 during the *RXTE* era, we note a lack of observed X-ray bursts bewteen $53000 - 54000$ MJD, when the eclipse asymmetry reversed (when the ingress was longer than the egress; see Chapter 5). We suggested that this reversal was governed by the movement of the gravitationally bound ablated material in the system. Thus, we must consider whether the presence of the ablated material influences the in-eclipse bursts, or even scatters the burst emission into our line of sight. In this scenario, a fraction of the burst emission reflects into our line of sight while another fraction is absorbed and remitted at longer wavelengths. To estimate the reflection fraction, we compute the ratio of the mean peak count rate of bursts that peak during totality and the mean peak count rate of the out-of-eclipses bursts as $R_{\rm ec} = C_{\rm ec}/C_{\rm ooe} \approx 97/2462 = 0.0394$. On average, therefore, an in-eclipse burst has a peak count rate $\sim 4\%$ of an average out-of-eclipse burst.

Since the ablated material governs the ingress and egress, we hypothesise that the peak count rate of the bursts occurring closer to an eclipse transition should be higher than those coinciding with the centre of totality. We assess this for all bursts that peak during the eclipse in Figure 7.8, where we see tentative evidence for this trend. Here, $\phi = 0.0$ rad denotes the centre of totality, and the burst's peak count rates display increases on either side. While inconclusive, this analysis does indicate that the in-eclipse bursts further depend on the ablated material and could even be the reflector. The reflection fraction of egress split bursts is, $R_{\rm eg} = C_{\rm eg}/C_{\rm ooe} \approx 136/2462 = 0.0552$. Therefore an egress split burst has a peak count rate $\sim 6\%$ of an average out-of-eclipse burst, which is 1.6% higher than for in-eclipse bursts and supports the hypothesis that bursts are brighter further from the centre of totality. In contrast, the ratio of the average totality count rate to the average out-of-eclipse count rate in the absence of bursts is $R = C_{\rm tot}/C \approx 0.0167$.

The analysis, determines that $R_{\rm ec}$ is larger than R. This implies that that bursts are special, such that more flux is scattered during a burst than otherwise. However,

this could be alternatively understood if we only observe the brightest bursts in-eclipse, such that the fraction of flux from each burst that leaks through during totality is $R_{\rm burst} < R_{\rm ec}$. Here, $R_{\rm burst}$ is calculated as the mean peak flux of the observed in-eclipse bursts divided by the mean peak flux of the K brightest out of eclipse bursts, such that the fraction of out of eclipse bursts observable during eclipse is $f = K/N_{\rm ooe}$. Let us consider the value of f, which we denote as $f_{\rm burst}$, required for $R_{\rm burst} = R$. To find $f_{\rm burst}$, we iteratively calculate the mean flux of the K brightest out-of-eclipse bursts, reducing K from a maximum of $N_{\rm ooe}$ in integer steps until $R_{\rm burst} = R$. We determine that at $R_{\rm burst} = R$, $K = 31$, and $f_{\rm burst} = 0.21$, which we can strongly rule out based on the large number of in-eclipse bursts we observe, and the corresponding probability is $p = 2 \times 10^{-5}$. This implies that we observe a greater fraction of the burst flux during an eclipse than the non-burst flux. Therefore, extra scattering of the burst emission into our line of sight is necessary to explain the fraction of the in-eclipse bursts we observe and could be explained if there is an increase in $N_{\rm H}$ during the X-ray bursts (e.g. Albayati et al. 2023).

7.4 Spectral Analysis

For each of the in-eclipse and split bursts, we extract $2 - 15$ keV PCU2 spectra for a time range matching the peak of the X-ray burst. For each ObsID, our code creates a filter file using `xtefilt` and a GTI file from the user-specified time range using `timetrans`. We generate corresponding standard-2 background files using `runpcabackest` and extract separate standard-2 source and background spectra using `saextract`. We correct for deadtime and create appropriate response matrices using `pcarsp`. When modelling, we do not utilise the background spectra resulting from our code. Instead, we extract spectra for in-eclipse portions of each light curve to serve as background, as these spectra more accurately represent the background at the time of an in-eclipse X-ray burst.

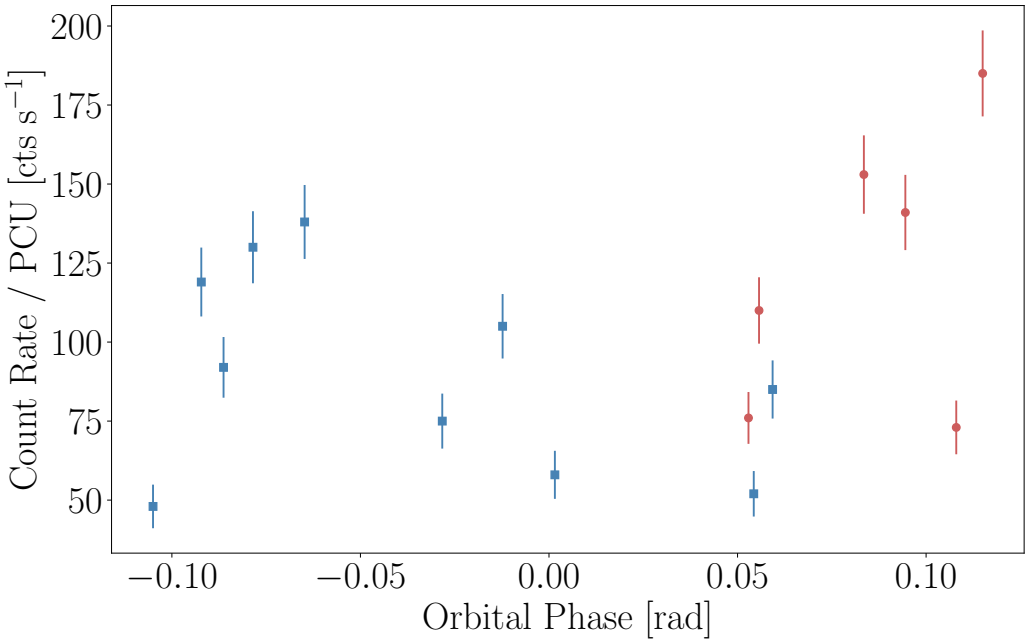

Figure 7.8: The peak count rate of in-eclipse (blue) and egress split bursts (red) as a function of orbital phase. Here the orbital phase, 0.0, marks the centre of totality. Further from the centre of totality, the bursts appear to reach higher peak count rates.

We fit each spectrum using XSPEC with three different models as we attempt to understand their origin and properties. These models are: 1) TBABS*(DISKBB+ BBODYRAD) 2) TBABS*ZXIPCF*PEXRIV and 3) TBABS*ZXIPCF*XILLVERNS. Here TBABS calculates the cross section for X-ray absorption by the ISM. DISKBB is a multi-temperature accretion disc blackbody spectrum, and BBODYRAD is a NS surface blackbody spectrum with the normalisation proportional to the surface area of the emitter. ZXIPCF considers absorption by an ionised material with partial covering, which we have previously utilised to model the ablated outflow in EXO 0748 (see Chapters 3 and 5). PEXRIV and XILLVERNS are both models for reflection spectra. The former is a reflected power law for an ionised material, while the latter is a more sophisticated reflection model that also considers flouresence lines (García et al., 2013, 2014)

We present the results of these fits for the representative in-eclipse burst, ObsID

40039-04-04-00, and the representative egress-split burst, ObsID 20069-05-05-00, in Figure 7.9, which demonstrates that the quality of the in-eclipse and egress-split burst spectra do not allow the models to be separated statistically. When comparing the reduced chi-squares and null hypothesis probabilities of each fit, we can favour the two reflection models (models 2 and 3), and tentatively prefer model 3 since it is the more physical model, but we cannot confidently separate them. We note that stacking similar in-eclipse and egress-split peak burst spectra didn't improve the signal-to-noise.

The fits using model 1 feature a negligible contribution from an accretion disc. Across all model 1 fits, the strength of DISKBB components are consistent with zero, including the egress-split bursts where we might otherwise expect the disc to reemerge, suggesting that even if the accretion disc extended beyond the companion star, the disc emission doesn't reach the observer and supporting my earlier analysis (Chapters 3 and 5), in which I suggest ablated material surrounds the companion star in EXO 0748. Further support for the presence of ablated material in the system comes from the results from models 2 and 3, which are mostly consistent. Both models imply that the ionisation of the reflector is high ($\log(\xi) \sim 3.5$), and the inferred ionisations are compatible with the ionisation of the ablated outflow measured from my eclipse mapping analysis (Knight et al., 2022a). Overall, these findings suggest the in-eclipse X-ray bursts are arising due to reflection off the ablated outflow rather than the accretion disc and/or the bursts are increasing the amount of scattering material (Albayati et al., 2023). We explore this further in Section 7.5.

7.5 Possible Origins of the In-Eclipse X-ray Bursts

We begin by assessing whether the in-eclipse X-ray bursts in EXO 0748 could arise due to reflection off of the outer accretion disc and calculate how much of the disc is visible at different orbital phases. Let us assume a spherical companion star with a radius

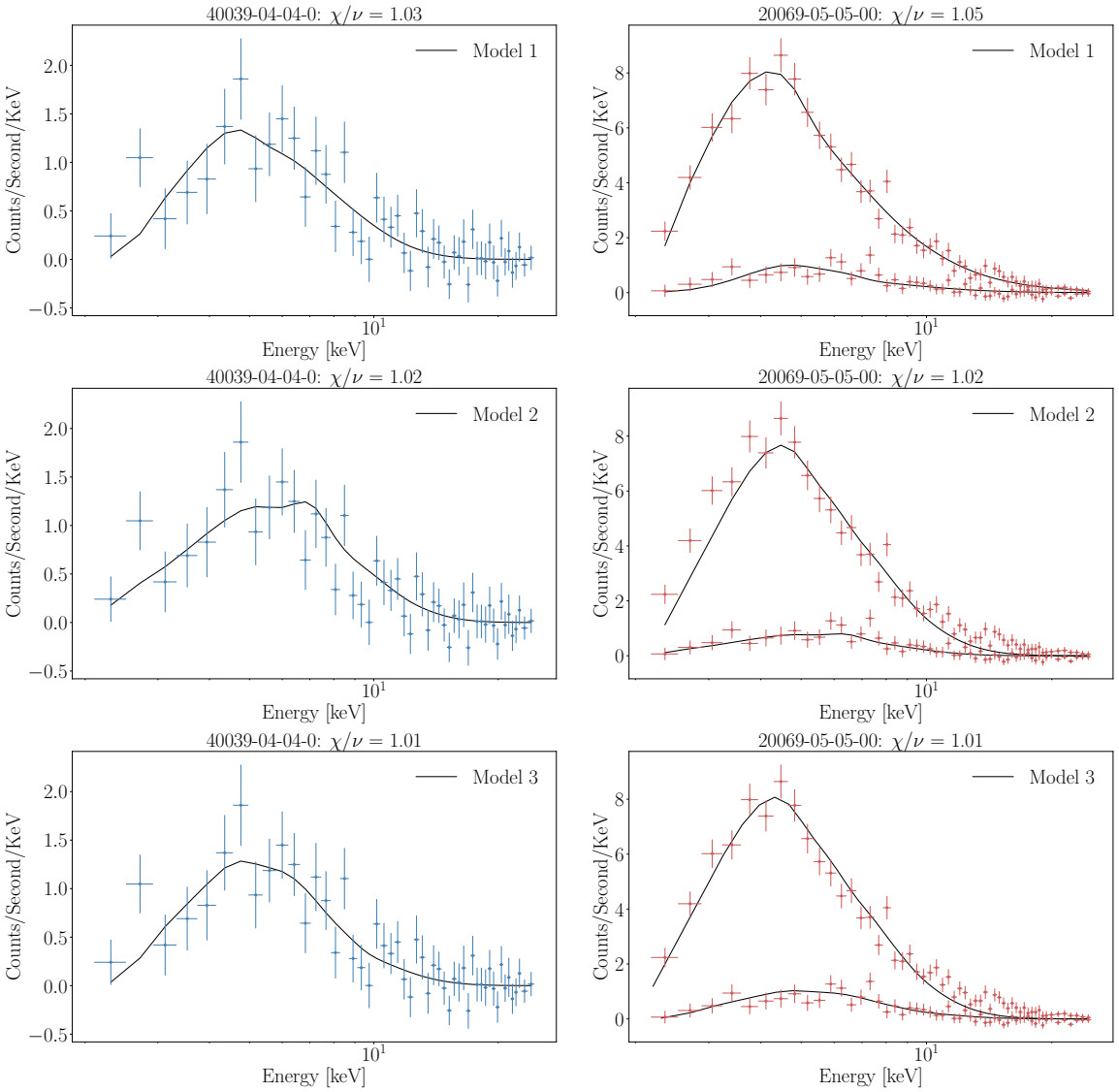

Figure 7.9: Spectral fits to the in-eclipse burst, ObsID 40039-04-04-00, and the egress-split burst, ObsID 20069-05-05-00, using 3 different models. These models are: 1) TBABS*(DISKBB+BBODYRAD) 2) TBABS*ZXIPCF*PEXRIV and 3) TBABS*ZXIPCF*XILLVERNS. The spectra are extracted from the peak of the X-ray bursts, and in the case of the split bursts, also the brightest point out of eclipses.

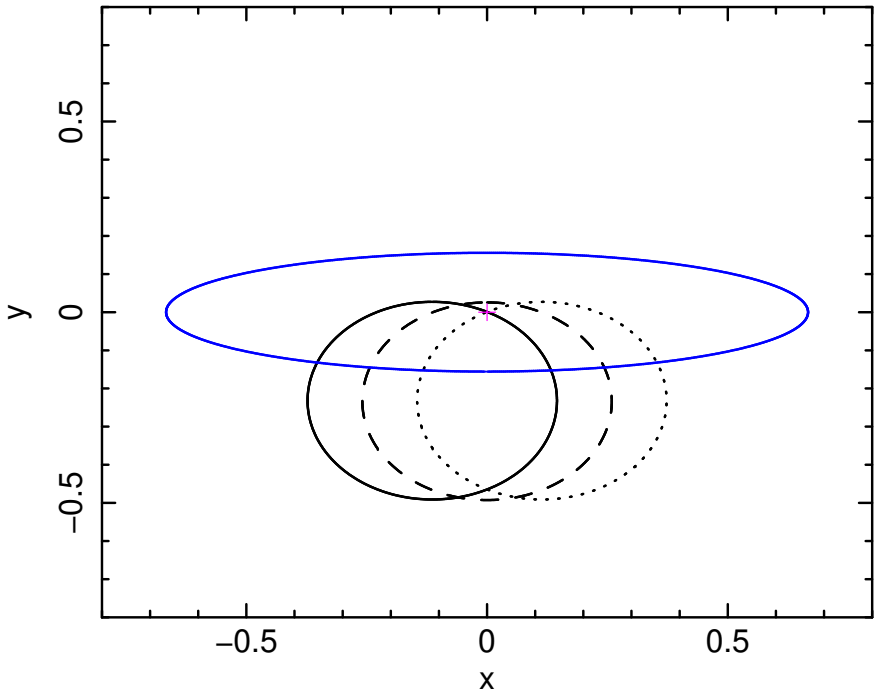

Figure 7.10: Simple image of the accretion disc (blue) and the companion star (black) at three orbital phases: the beginning of totality (solid), the centre of totality (dashed), and the end of totality (dotted). The neutron star (which dominates the X-ray flux) is at the origin (magenta cross). Note that x and y axes are in units of the semi-major axis, a.

given by Equation 2.3 and approximate the accretion disc as tidally truncated at ~ 0.9 its own Roche Lobe radius (Mushtukov et al., 2019), which we will approximate as $a - r_{\rm cs}$, such that the outer disc radius is $r_{\rm out} = 0.9(a - r_{\rm cs})$. The image of the accretion disc (blue), under these assumptions, is in Figure 7.10. Here, the solid, dashed and dotted circles represent the position of the companion star at the start, centre and end of totality. We assume $q = 0.222$ and viewer inclination angle $i = 76.5°$, as is appropriate for EXO 0748 (Knight et al., 2022a). Overall, we see that, even at the centre of totality, we can see some of the outer accretion disc. Despite the regions dominating the X-ray signal being blocked, some fraction of the X-ray emission still reaches the observer. This analysis creates some tension with my earlier analysis of the X-ray eclipses (see Chapter 3). However, the assumption of an X-ray point source is still reasonable because the emissivity is centrally peaked.

X-rays from the outer disc originate from reflection of X-rays originally emitted from the inner regions. For this, we assume a simple model which ignores relativistic effects and assumes a point like isotropic 'lamppost' source, a height h above the NS, is the illuminator. For a flat accretion disc, the reflected flux we observe per unit disc radius, as a fraction of the direct flux is

$$\frac{dF}{dr} = 2\cos i \frac{hr}{(h^2 + r^2)^{3/2}}. \tag{7.1}$$

Integrating this from an inner radius equal to the NS radius, $r_{\rm NS}$, to an outer radius of infinity gives

$$F = \int_{r_{\rm NS}}^{\infty} \frac{dF}{dr}\, dr = 2\cos i \frac{h}{(h^2 + r_{\rm NS}^2)^{1/2}}. \tag{7.2}$$

For $r_{\rm NS} = 12$ km and $h = r_{\rm NS}$, $F = 0.33$. However, this assumes the entire accretion disc is visible. For a partially visible accretion disc, we instead compute the above integral numerically in a grid of r and ϕ. For each point on the grid, we calculate the projected distance on the observer's image plane between the centre of a disc patch and the centre of the companion star. If this distance exceeds the radius of the companion star, we include the flux from that patch in the integral. We repeat the calculation for a range of orbital phases.

The black line in Figure 7.11 shows the result of this calculation. In out-of-eclipse phases, the reflected flux is 0.33 times the out-of-eclipse direct flux, as expected from the above integration. At the centre of totality, the reflected emission reaching an observer is instead $\approx 3 \times 10^{-5}$ times the out-of-eclipse direct flux. At other orbital phases, the companion star doesn't cover as much of the disc, so we see a greater X-ray flux. Therefore this simple model predicts that the in-eclipse bursts should have a peak flux $\sim 3 \times 10^{-5} - 10^{-4}$ times the peak flux of the out-of-eclipse bursts. The observed number is $\sim 4\%$ (with a 99% confidence lower limit of $\sim 2.2\%$), so reflection from the outer edge of a flat accretion disc does not confidently explain the observed in-eclipse X-ray bursts.

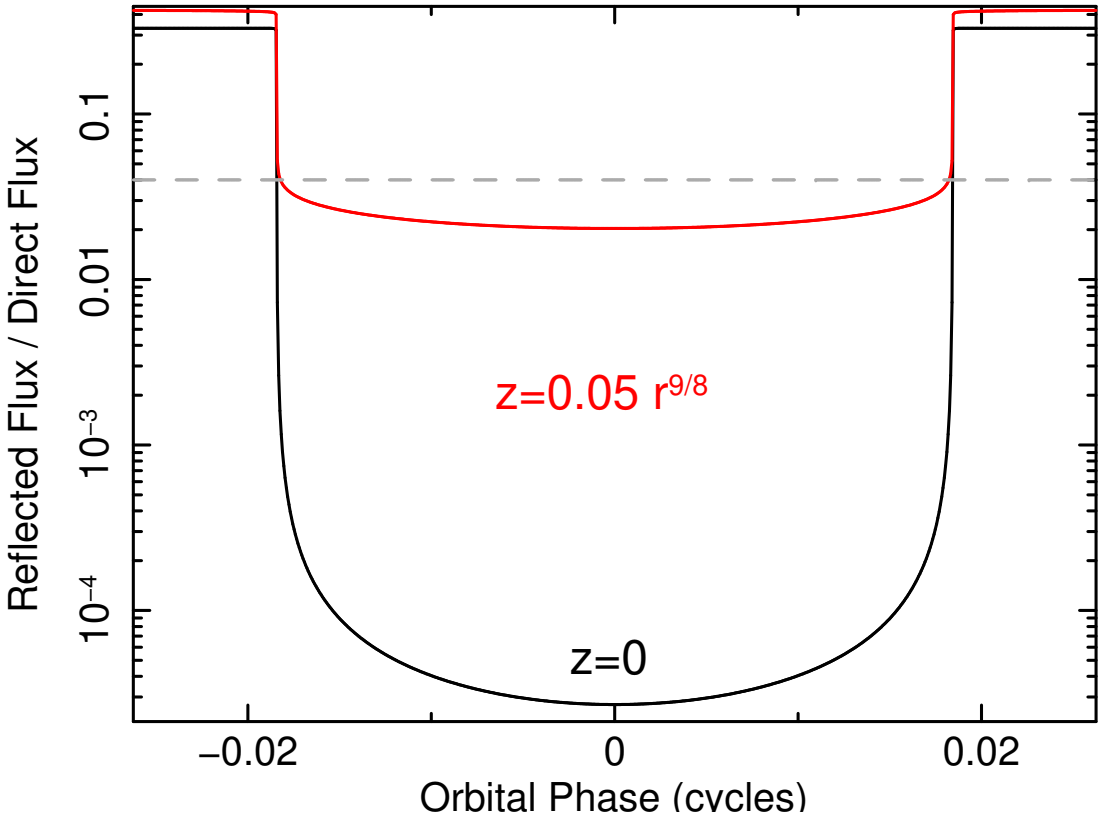

Figure 7.11: Ratio of reflected flux to out-of-eclipse direct flux as a function of orbital phase for a disc being illuminated by a lamppost source at $h = r_{\rm ns}$. For the black line, the disc is flat ($z = 0$) and for the red line, it is flared ($z \propto r^{9/8}$). The grey dashed line indicates a 4% ratio of in-eclipse burst peak flux to out-of-eclipse burst peak flux. We see that the flared disc cannot reproduce this observed ratio for reasonable parameters.

For the case of a flared disc with height $z(r)$, as is illustrated in Figure 7.12, Equation (7.1) generalises to

$$\frac{dF}{dr\ d\phi} = \frac{r\ \mathrm{MAX}\left\{\left(r\ dz/dr + h - z\right), 0\right\} \mathrm{MAX}\left\{\left(\cos i - \sin i\ \cos\phi\ dz/dr\right), 0\right\}}{\pi\left[r^2 + (h-z)^2\right]^{3/2}\left[(dz/dr)^2 + 1\right]^{1/2}}. \quad (7.3)$$

Here, the disc azimuthal angle ϕ is zero for disc patches that lie in the unique plane defined by the observer's line of sight and the disc rotation axis, and r is the *cylindrical* radial polar coordinate of the disc. The red line in Figure 7.11 shows the result of this calculation, assuming the maximum, $z(r) = 0.05r^{9/8}$ (for a thicker

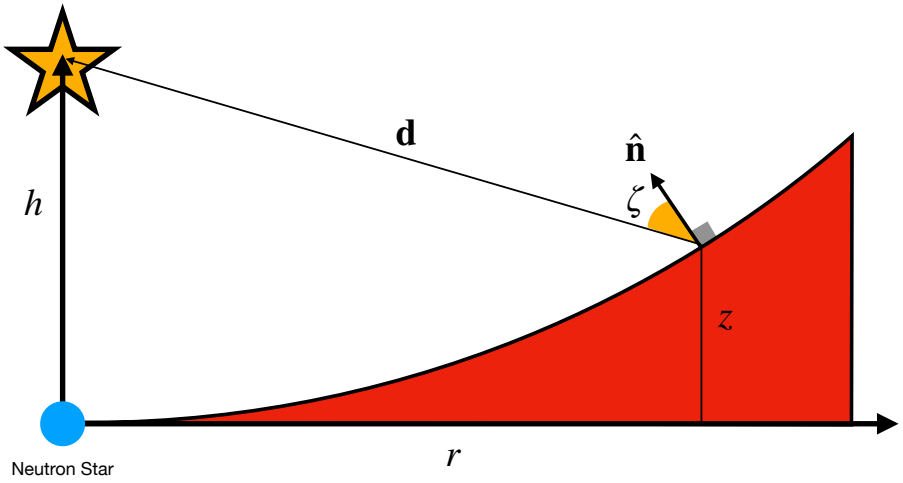

Figure 7.12: Schematic of a flared disc being illuminated by a lamppost source. A given disc patch is at height $z(r)$ and cylindrical polar radius r. The illuminating flux depends on the distance d from the source to the patch and the angle ζ between the vector $\mathbf{d}$ and the disc normal $\hat{\mathbf{n}}$.

disc than this, the outer edges of the disc would completely block our view of the NS). Here, the power-law index is consistent with zone C of the Shakura & Sunyaev (1973) disc model. The out-of-eclipse reflected flux agrees with that of the flat disc case (0.35 vs 0.33) because the reflection from the inner disc is unchanged. However, the in-eclipse reflected flux is higher than for a flat disc, increasing to $\sim 2\%$. This increase is because the back of the outer disc now subtends a larger solid angle to both the observer and the lamppost source. Therefore, reflection off of the outer accretion disc alone cannot account fot the presence of the in-eclipse X-ray bursts, but likely contributes some flux during the eclipses.

An alternative scenario, which we consider likely, assumes that the in-eclipse bursts arise due to reflection off the ablated material surrounding the companion star (or, more accurately, reflection off ablated material dominates over reflection off the outer disc, which we expect to also be present). While we cannot say definitively, our spectral analysis implies that the accretion disc is not visible during phases where in-eclipse and egress-split bursts occur, despite showing that the disc extends radially beyond the companion star earlier in this discussion. We attribute this to the presence

of ablated material around the system that is required to explain the behaviour and variation of the observed X-ray eclipses. From the fits to the peak burst spectra with models 2 and 3 (reflection models), we determine that the ionisation of the reflector is high and the inferred ionisations are compatible with the ionisation of the ablated outflow measured from my eclipse mapping analysis (Knight et al., 2022a). The presence of ablated material can also explain the lack of in-eclipse X-ray bursts observed by *XMM-Newton* since the softer X-rays that *XMM-Newton* is sensitive to will be absorbed by the ablated wind.

Thus far, our findings suggest the in-eclipse and split X-ray bursts arise due to reflection off the ablated outflow rather than the accretion disc itself. However, our analysis of these unique bursts and their origins is ongoing, and one likely scenario we are yet to explore is the in-eclipse X-ray bursts arise from reflection of off the irradiated accretion disc atmosphere. Much like the ablated material, the material in the accretion disc is bombarded with X-ray irradiation from the NS, creating an atmosphere above the disc that can scatter the X-ray bursts into our line of sight. Crucially, if present above a flared accretion disc, this atmosphere could allow the reflection fraction to surpass the 4% threshold and thus be a viable explanation. Furthermore, an accretion disc atmosphere is compatible with the high ionisation we infer for the reflector (an irradiated atmosphere is likely to be highly ionised) and can also explain the in-eclipse continuum level, which is known to be $\sim 4\%$ Parmar et al. (1991). Therefore, it is evident that we must explore this possibility.

Chapter 8

Concluding Remarks

In this thesis, I have investigated eclipsing X-ray binaries using X-TREC, a model I designed to accurately map the shape and duration of X-ray eclipse profiles, enabling precise constraints on the binary inclination angle and mass ratio. While simple straight-line models for X-ray eclipses can determine the eclipse duration (e.g. Wolff et al. 2009), a physical model can extract far more information from the eclipse profiles than can be inferred solely from the totality duration. Therefore, it is necessary to develop an eclipse model capable of capturing the eclipse features in high-resolution data. Furthermore, X-ray binaries do not typically display sharp eclipse transitions due to outflowing material from the companion star extending their duration and creating asymmetric eclipse profiles. We cannot learn about these outflows using simple eclipse models. My model overcomes this by determining how the local material absorbs the X-ray emission using different absorption models, each described by a radial density profile. These profiles act as a fantastic diagnostic tool for the type of outflow exhibited by the companion star and are fundamental when modelling the shape of the X-ray eclipses.

I demonstrated the abilities of X-TREC in Chapters 3 and 4, in which I applied it to archival *XMM-Newton* data of EXO 0748−676 and archival *NICER* data of *Swift* J1858.6−0814, respectively. By modelling the energy-dependent eclipse profiles of EXO 0748−676, I measured the mass ratio, $q \sim 0.2$ and the binary inclination

angle $i \sim 77°$, and I combined these measurements with the previously measured binary mass function to constrain the neutron star mass. Using the Doppler-mapping derived semi-amplitude of the Hα emission line, $K_{\rm em} \approx 410$ km/s (Bassa et al., 2009), yields $M_{\rm ns} \sim 2\ M_{\odot}$, even when using the most conservative (closest to unity) K-correction to account for the fact that this line originates from the irradiated face of the companion (Munoz-Darias et al., 2005). In this case, the canonical NS mass of $M_{\rm ns} = 1.4\ M_{\odot}$ is outside of the 3σ confidence contour, and use of a more realistic K-correction ($K_{\rm corr} \sim 0.8$) pushes the posterior NS mass distribution into the $3-5 M_{\odot}$ mass gap. Alternatively, using the Bowen blend (Mikles & Hynes, 2012) permits the canonical NS mass, but the peak-posterior value for a realistic K-correction is still $M_{\rm ns} \sim 2 M_{\odot}$. Despite the advances of X-TREC to the technique of eclipse mapping, it is evident that the constraints on the compact object mass heavily depend on quiescent observations accurately measuring the radial velocity curve. Future observations of spectral lines emitted directly from the companion star's surface, combined with our inclination and mass ratio constraints, would yield a precision measurement of the neutron star's mass. Nonetheless, we measure a neutron star mass consistent with prior research (Özel, 2006) and our results agree that the companion star is a low-mass main sequence star (Parmar et al., 1991).

Similarly, by modelling the energy-dependent eclipse profiles of *Swift* J1858.6–0814 in multiple energy bands, I constrain the binary inclination, $i \sim 81°$, and mass ratio, $q \sim 0.14$. I combined these measurements with neutron star masses in the range $1.4\ M_{\odot} \leq M_{\rm ns} \leq 2.5\ M_{\odot}$ to infer that the companion star has a low mass, $0.183 M_{\odot} \leq M_{\rm cs} \leq 0.372 M_{\odot}$, and a large radius, $1.02 R_{\odot} \leq R_{\rm cs} \leq 1.29 R_{\odot}$. A star with a mass in the inferred range would have a main-sequence lifetime above the Hubble time. Therefore, the large radius likely arises from binary interactions, and a common envelope phase likely contributed to the ejection of mass from the system and the reduction in the orbital period, thus forming a short-period binary with a

low-mass companion, and future spectroscopic studies could confirm this possibility.

Thus far, X-TREC has been successfully applied to eclipsing neutron star low-mass X-ray binaries, where assuming circular orbits is reasonable. My model, however, has not yet been applied to eclipsing high-mass X-ray binaries, systems with eccentric orbits or systems hosting black holes. These are all under active investigation; I am developing X-TREC to include eccentric orbits and a preliminary application of X-TREC to *Chandra* observations of the eclipsing black hole high-mass X-ray binary M33 X−7, indicate the success of the accelerating stellar wind absorption model. As our observational capabilities and understanding of stellar outflows increase, the next step is to apply X-TREC to various systems to improve its capabilities and accuracy.

An interesting result from the eclipse mapping studies in Chapters 3 and 4 was the diagnosis of an ablated outflow from the companion stars in both EXO 0748−676 and *Swift* J1858.6−0814. Their X-ray eclipses share several characteristics, such as asymmetry and photon energy dependence throughout the eclipse transitions, and they share some out-of-eclipse behaviours like type I X-ray bursts, dips and flares. For both sources, X-TREC required an irradiation-driven outflow model to recreate the extended shape of their X-ray eclipses, and the outflow must extend further from the companion on the egress side of the star to map the eclipse asymmetries. The discovery of these irradiation-driven ablated outflows raises questions regarding their connection to the only other neutron star systems known to undergo ablation - the spider pulsars (Fruchter et al., 1988; Stappers et al., 1996).

As such, it was necessary to explore the connections between EXO 0748−676, *Swift* J1858.6−0814 and spider pulsars, which led to the work presented in Chapter 5. I use archival data to explore the similarities between the two X-ray binaries through phase-resolved spectroscopy of their near-eclipse epochs, determining that an ionized absorber exists close to the companion star in both systems. The column density and covering fraction of the ionized absorber decreases further from the companion

star, implying that the material becomes clumpy at large distances, and proved consistent with the optically thin material layer inferred to extend the duration of the eclipses of both EXO 0748−676 and *Swift* J1858.6−0814 (Knight et al., 2022a,b). This clumpy material arises from the ablation of the companion star's atmosphere by X-ray irradiation or a pulsar wind, similar to the cannibalistic behaviour exhibited by redback and black widow pulsars. Therefore, I termed EXO 0748−676 and *Swift* J1858.6−0814 as *false widows*, defined as X-ray binaries hosting ablated companion stars, and speculate that the false widows may represent progenitors of redback pulsars under the assumption that ablation begins during the accretion-powered phase and continues into the rotation-powered phase. This mechanism could provide a way to create under-massive companions in short-period binaries like those observed within spider pulsars (Fruchter et al., 1988; Stappers et al., 1996), but requires further investigation. Furthermore, by modelling all available eclipse profiles of EXO 0748−676 from the *RXTE* data archive, I noticed a reversal of the eclipse asymmetry that is tentatively correlated with the spectral state of the system and potentially influenced by the movement of ablated material within the gravitationally bound region of the binary, similar to observations of the black widow pulsar PSR J2051−0827 (Polzin et al., 2019a). This picture is also consistent with my discovery of thermonuclear X-ray bursts during the X-ray eclipses in EXO 0748−676, which require a large amount of material to be present in the system to scatter emission from the neutron star around the companion, into our line of sight.

Based on these findings, I created the false widow collaboration to investigate these unique systems. Our initial focus is to evidence the link between the false widows and spider pulsars by searching for radio pulsations from EXO 0748−676 while it is in X-ray quiescence. The preliminary results from this collaboration are in Chapter 6, which highlights exciting radio pulsation candidates at frequencies consistent with the known spin period of the neutron star. The candidates are all low-sigma, and their

dispersion measure varies around the orbit. While promising, we cannot yet confirm the false widow link, and further observations with a higher sensitivity instrument are necessary.

To fully understand the evolutionary role of false widows, some key questions must be answered: How common are false widow binaries? What mechanism drives ablation? How do short-period binaries with very-low mass companion stars form? My collaboration is working to address these open questions, and in addition to searching for radio pulsations, we are searching for additional false widow candidates using archival observations and methods independent of the viewing angle, such as phase-resolved spectroscopy (Knight et al., 2022a,b), allowing us to search the entire catalogue of X-ray binaries and investigate whether ablation is ubiquitous among X-ray binaries. Also, there are several open questions regarding the exact mass-loss processes occurring in false widows and their efficiencies. By examining the roles of accretion, ablation and circumbinary discs in false widows, I aim to determine whether these processes are sufficiently efficient to form short-period binaries with very low-mass companion stars. Simulations of circumbinary discs around false widows could uncover the properties of the circumbinary discs and divulge their role in the evolution of these binary systems. From this, the temperature of the circumbinary disc material and its distance from the binary's centre of mass is determinable, which could inform an observational approach to image a circumbinary disc.

Much of the work presented in this thesis is ongoing. My discovery of false widows could explain the evolution of compact binary systems but has raised several questions which I intend to answer as I lead the false widow collaboration through our upcoming investigations and observations. As a post-doctoral researcher at the University of Durham, I will explore the population of ultra-luminous X-ray sources, including those undergoing eclipses, and the role of circumbinary discs on their evolution.

Bibliography

Abbott B. P., et al., 2020a, The Astrophysical Journal Letters, 892, L3

Abbott R., et al., 2020b, The Astrophysical Journal Letters, 896, L44

Alabarta K., et al., 2021, Monthly Notices of the Royal Astronomical Society, 507, 5507

Albayati A. C., et al., 2023, Thermonuclear Type-I X-ray Bursts and Burst Oscillations from the Eclipsing AMXP Swift J1749.4-2807 (`arXiv:2306.11440`)

Alpar M. A., et al., 1982, Nature, 300, 728

An H., Romani R. W., Kerr M., 2018, The Astrophysical Journal Letters, 868, L8

Antoniadis J., et al., 2016, arXiv e-prints, p. arXiv:1605.01665

Archibald A. M., et al., 2009, Science, 324, 1411

Arnaud K. A., 1996, in Jacoby G. H., Barnes J., eds, Astronomical Society of the Pacific Conference Series Vol. 101, Astronomical Data Analysis Software and Systems V. p. 17

Arons J., Tavani M., 1993, The Astrophysical Journal, 403, 249

Astashenok A., et al., 2021, Physics Letters B, 816, 136222

Avakyan A. L., et al., 2021, Astronomy Letters, 47, 377

Baade W., Zwicky F., 1934, Proceedings of the National Academy of Sciences, 20, 259

Backer D. C., et al., 1982, Nature, 300, 615

Baglio M. C., et al., 2018, The Astronomer's Telegram, 12180, 1

Bahramian A., Degenaar N., 2022, Low-Mass X-ray Binaries. Springer Nature Singapore, Singapore, pp 1–62, doi:10.1007/978-981-16-4544-0˙94-1

Bahramian et al., 2018, The Astrophysical Journal, 864, 28

Bardeen J. M., Press W. H., Teukolsky S. A., 1972, The Astrophysical Journal, 178, 347

Barnard R., et al., 2014, The Astrophysical Journal, 791, 33

Bassa, C. G. et al., 2006, Astronomy and Astrophysics, 456, 295

Bassa C. G., et al., 2009, Monthly Notices of the Royal Astronomical Society, 399, 2055

Bauböck M., et al., 2015, The Astrophysical Journal, 799, 22

Becker W., 2009, X-Ray Emission from Pulsars and Neutron Stars. Springer Berlin Heidelberg, Berlin, Heidelberg, pp 91–140, doi:10.1007/978-3-540-76965-1˙6

Belczynski K., et al., 2012, The Astrophysical Journal, 757, 91

Belloni T. M., 2010, States and Transitions in Black Hole Binaries. Springer Berlin Heidelberg, pp 53–84, doi:10.1007/978-3-540-76937-8˙3

Belloni et al., 2005, Astronomy and Astrophysics, 440, 207

Beskin V. S., et al., 2015, Space Science Reviews, 191, 207

Bhattacharya D., van den Heuvel E. P. J., 1991, Physics Reports, 203, 1

Bildsten L., 2002, The Astrophysical Journal, 577, L27

Bildsten L., et al., 1997, The Astrophysical Journal Supplement Series, 113, 367

Bogdanov S., Grindlay J. E., Rybicki G. B., 2006, The Astrophysical Journal, 648, L55

Bogdanov S., Rybicki G. B., Grindlay J. E., 2007, The Astrophysical Journal, 670, 668

Bonnet-Bidaud et al., 2001, A&A, 365, L282

Braje T. M., Romani R. W., Rauch K. P., 2000, The Astrophysical Journal, 531, 447

Buisson D. J. K., et al., 2020, Monthly Notices of the Royal Astronomical Society, 499, 793

Buisson D. J. K., et al., 2021, Monthly Notices of the Royal Astronomical Society, 503, 5600

Burderi L., King A. R., 1998, The Astrophysical Journal, 505, L135

Burdge K. B., et al., 2022, Nature, 605, 41

Burke M. J., Gilfanov M., Sunyaev R., 2017, Monthly Notices of the Royal Astronomical Society, 466, 194

Cadeau C., et al., 2007, The Astrophysical Journal, 654, 458

Callanan P. J., Garnavich P. M., Koester D., 1998, Monthly Notices of the Royal Astronomical Society, 298, 207

Casares J., et al., 2014, Nature, 505, 378

Casella P., et al., 2008, The Astrophysical Journal, 674, L41

Cash W., 1979, The Astrophysical Journal, 228, 939

Castro Segura N., et al., 2022, Nature, 603, 52

Chakrabarty D., Morgan E. H., 1998, Nature, 394, 346

Chen W., 2017, A&A, 606, A60

Chen H.-Y., Chatziioannou K., 2020, The Astrophysical Journal Letters, 893, L41

Chen H.-L., et al., 2013, The Astrophysical Journal, 775, 27

Church M. J., Bałucińska-Church M., 2004, Monthly Notices of the Royal Astronomical Society, 348, 955

Church, M. J. Halai, G. S. Baluci´nska-Church, M. 2006, Astronomy and Astrophysics, 460, 233

Clark C. J., et al., 2023, Nature Astronomy, 7, 451

Collier Cameron A., 1991, Memorie della Societa Astronomica Italiana, 62, 337

Cominsky L. R., Wood K. S., 1984, The Astrophysical Journal, 283, 765

Condon J. J., Ransom S. M., 2016, Essential Radio Astronomy

Cook G. B., Shapiro S. L., Teukolsky S. A., 1994, The Astrophysical Journal, 424, 823

Cordes J. M., Lazio T. J. W., 2002, arXiv e-prints, pp astro–ph/0207156

Cromartie H. T., et al., 2020, Nature Astronomy, 4, 72

Damen E., et al., 1990, Astronomy and Astrophysics, 237, 103

Degenaar N., et al., 2011, Monthly Notices of the Royal Astronomical Society, 412, 1409

Demircan O., Kahraman G., 1991, Astrophysics and Space Science, 181, 313

Dewi J. D. M., Pols O. R., 2003, Monthly Notices of the Royal Astronomical Society, 344, 629

Dewi J. D. M., et al., 2002, Monthly Notices of the Royal Astronomical Society, 331, 1027

Díaz Trigo et al., 2011, A&A, 528, A150

Dietrich T., et al., 2020, Science, 370, 1450

Diez C. M., et al., 2022, Astronomy & Astrophysics, 660, A19

Done C., 2014, in González Martínez-País I., Shahbaz T., Casares Velázquez J., eds, Canary Islands Winter School of Astrophysics, Accretion Processes in Astrophysics. Cambridge University Press, pp 184–226, doi:10.1017/CBO9781139343268.007

Done C., Gierliński M., 2003, Monthly Notices of the Royal Astronomical Society, 342, 1041

Done C., Gierliński M., Kubota A., 2007, The Astronomy and Astrophysics Review, 15, 1

Eggleton P. P., 1983, The Astrophysical Journal, 268, 368

Essick R., Landry P., 2020, The Astrophysical Journal, 904, 80

Evans A., Wood J. H., eds, 1996, Slingshot Prominences During Dwarf Nova Outbursts? Springer Netherlands, Dordrecht

Fabian A. C., et al., 1989, Monthly Notices of the Royal Astronomical Society, 238, 729

Fabian A. C., et al., 2000, The Publications of the Astronomical Society of the Pacific, 112, 1145

Fender R., Gallo E., 2014, Space Science Reviews, 183, 323

Fender R., Muñoz-Darias T., 2016, The Balance of Power: Accretion and Feedback in Stellar Mass Black Holes. Springer International Publishing, Cham, pp 65–100, doi:10.1007/978-3-319-19416-5˙3, https://doi.org/10.1007/978-3-319-19416-5_3

Fender R. P., Belloni T. M., Gallo E., 2004, Monthly Notices of the Royal Astronomical Society, 355, 1105

Ferreira J. M., 2000, Monthly Notices of the Royal Astronomical Society, 316, 647

Fonseca E., et al., 2021, The Astrophysical Journal Letters, 915, L12

Fragos T., et al., 2010, The Astrophysical Journal, 719, L79

Frank J., King A., Raine D. J., 2002, Accretion Power in Astrophysics: Third Edition

Fruchter A. S., Stinebring D. R., Taylor J. H., 1988, Nature, 333, 237

Fruchter A. S., et al., 1990, The Astrophysical Journal, 351, 642

Fujimoto M. Y., Taam R. E., 1986, The Astrophysical Journal, 305, 246

Galloway D. K., Keek L., 2021, Thermonuclear X-ray Bursts. Springer Berlin Heidelberg, Berlin, Heidelberg, pp 209–262, doi:10.1007/978-3-662-62110-3˙5, https://doi.org/10.1007/978-3-662-62110-3_5

Galloway D. K., et al., 2008, The Astrophysical Journal Supplement Series, 179, 360

Galloway D. K., et al., 2010, The Astrophysical Journal Letters, 711, L148

García J., et al., 2013, The Astrophysical Journal, 768, 146

García J., et al., 2014, The Astrophysical Journal, 782, 76

Gardenier D. W., Uttley P., 2018, Monthly Notices of the Royal Astronomical Society, 481, 3761

Ghosh P., Lamb F. K., 1979, The Astrophysical Journal, 234, 296

Ghosh P., Lamb F. K., 1991, in Ventura J., Pines D., eds, NATO Advanced Study Institute (ASI) Series C Vol. 344, Neutron Stars. p. 363

Gianolli V. E., et al., 2023, Monthly Notices of the Royal Astronomical Society

Gierliński M., Poutanen J., 2005, Monthly Notices of the Royal Astronomical Society, 359, 1261

Gierliński M., et al., 1999, Monthly Notices of the Royal Astronomical Society, 309, 496

Gierliński M., Done C., Barret D., 2002, Monthly Notices of the Royal Astronomical Society, 331, 141

Ginzburg S., Quataert E., 2020, Monthly Notices of the Royal Astronomical Society, 500, 1592

Gottlieb E. W., Wright E. L., Liller W., 1975, The Astrophysical Journal Letters, 195, L33

Gottwald M., et al., 1986, The Astrophysical Journal, 308, 213

Grinberg et al., 2015, Astronomy & Astrophysics, 576, A117

Grinberg V., et al., 2017, Astronomy & Astrophysics, 608, A143

Grindlay J., et al., 1976, The Astrophysical Journal Letters, 205, L127

Grindlay J. E., et al., 2002, The Astrophysical Journal, 581, 470

Güver T., et al., 2010a, The Astrophysical Journal, 712, 964

Güver T., et al., 2010b, The Astrophysical Journal, 719, 1807

Hanke M., et al., 2008, The Astrophysical Journal, 690, 330

Hare J., et al., 2020, The Astrophysical Journal, 890, 57

Hasinger G., van der Klis M., 1989, Astronomy and Astrophysics, 225, 79

Heath Nixon 2020, A&A, 641, A64

Heil L. M., Uttley P., Klein-Wolt M., 2015, Monthly Notices of the Royal Astronomical Society, 448, 3339

Hewish A., et al., 1967, Nature, 217, 709

Higginbottom N., et al., 2018, Monthly Notices of the Royal Astronomical Society, 479, 3651

Hjellming R. M., Johnston K. J., 1981, The Astrophysical Journal Letters, 246, L141

Homan Wijnands, R. van den Berg, M. 2003, A&A, 412, 799

Horne K., 1985, Monthly Notices of the Royal Astronomical Society, 213, 129

Hui C. Y., Li K. L., 2019, Galaxies, 7

Ingram A. R., Motta S. E., 2019, New Astronomy Reviews, 85, 101524

Jackson J. D., 1998, Classical Electrodynamics, 3rd Edition. Wiley, New York

Jain C., Paul B., 2011, Research in Astronomy and Astrophysics, 11, 577

Jain C., et al., 2017, Monthly Notices of the Royal Astronomical Society: Letters, 468, L118

Jiménez-Ibarra F., et al., 2017, Monthly Notices of the Royal Astronomical Society, 474, 4717

Johns-Krull C. M., Valenti J. A., 1996, The Astrophysical Journal, 459, L95

Jonker P. G., et al., 2000, The Astrophysical Journal, 537, 374

Kaltenegger L., Traub W. A., 2009, The Astrophysical Journal, 698, 519

Kerr R. P., 1963, Physical Review Letters, 11, 237

Kippenhahn R., Weigert A., Weiss A., 2012, Final Explosions and Collapse. Springer Berlin Heidelberg, Berlin, Heidelberg, pp 449–472, doi:10.1007/978-3-642-30304-3˙36, https://doi.org/10.1007/978-3-642-30304-3_36

Kluzniak W., et al., 1988, Nature, 334, 225

Knight A. H., et al., 2022a, Monthly Notices of the Royal Astronomical Society, 510, 4736

Knight A. H., et al., 2022b, Monthly Notices of the Royal Astronomical Society, 514, 1908

Knight A. H., et al., 2023, Monthly Notices of the Royal Astronomical Society, 520, 3416

Kochukhov O., 2020, The Astronomy and Astrophysics Review, 29, 1

Krimm H. A., et al., 2018, The Astronomer's Telegram, 12151, 1

Lagae et al., 2021, A&A, 648, A94

Laor A., 1991, The Astrophysical Journal, 376, 90

Laplace, E. et al., 2020, A&A, 637, A6

Lattimer J. M., Prakash M., 2001, The Astrophysical Journal, 550, 426

Lazarus P., et al., 2013, Monthly Notices of the Royal Astronomical Society, 437, 1485

Lecavelier des Etangs, A. et al., 2010, Astronomy and Astrophysics, 514, A72

Lewin W. H. G., van Paradijs J., Taam R. E., 1993, Space Science Reviews, 62, 223

Linares M., 2014, The Astrophysical Journal, 795, 72

Linares M., Shahbaz T., Casares J., 2018, The Astrophysical Journal, 859, 54

Lindblom L., 1992, The Astrophysical Journal, 398, 569

Longair M. S., 2011, High Energy Astrophysics

Lorimer D. R., Kramer M., 2004, Handbook of Pulsar Astronomy. Cambridge Observing Handbooks for Research Astronomers Vol. 4, Cambridge University Press, Cambridge, UK

Lyne A. G., Graham-Smith F., 2006, Pulsar Astronomy, 3 edn. Cambridge Astrophysics Vol. 1, Cambridge University Press, Cambridge, UK

Majczyna A., Madej J., 2005, Acta Astronomica, 55, 349

Marco B. D., Ponti G., 2016, The Astrophysical Journal, 826, 70

Marsden D., White N. E., 2001, The Astrophysical Journal, 551, L155

Marsh T. R., Robinson E. L., Wood J. H., 1994, Monthly Notices of the Royal Astronomical Society, 266, 137

Masetti N., et al., 2000, Astronomy and Astrophysics, 363, 188

Mikles V. J., Hynes R. I., 2012, The Astrophysical Journal, 750, 132

Miller M. C., Lamb F. K., 1998, The Astrophysical Journal, 499, L37

Miller L., et al., 2006, A&A, 453, L13

Miller M. C., et al., 2019, The Astrophysical Journal Letters, 887, L24

Miller M. C., et al., 2021, The Astrophysical Journal Letters, 918, L28

Mirabel, I. F. Rodrigues, I. 2003, A&A, 398, L25

Miraval Zanon, A. et al., 2021, Astronomy and Astrophysics, 649, A120

Mondal A. S., et al., 2017, Monthly Notices of the Royal Astronomical Society, 474, 2064

Moore T. E., Horwitz J. L., 2007, Reviews of Geophysics, 45

Motta S. E., et al., 2017, Monthly Notices of the Royal Astronomical Society, 468, 981

Muno M. P., Özel F., Chakrabarty D., 2002, The Astrophysical Journal, 581, 550

Muñoz-Darias T., et al., 2009, Monthly Notices of the Royal Astronomical Society: Letters, 394, L136

Muñoz-Darias T., Motta S., Belloni T. M., 2010, Monthly Notices of the Royal Astronomical Society, 410, 679

Muñoz-Darias T., et al., 2014, Monthly Notices of the Royal Astronomical Society, 443, 3270

Munoz-Darias T., Casares J., Martinez-Pais I. G., 2005, The Astrophysical Journal, 635, 502

Mushtukov A. A., et al., 2019, Monthly Notices of the Royal Astronomical Society, 486, 4061

Nathan E. J. R., 2022, PhD thesis, University of Oxford

Nättilä, J. et al., 2017, Astronomy and Astrophysics, 608, A31

Novikov I. D., Thorne K. S., 1973, in Black Holes (Les Astres Occlus). pp 343–450

Oppenheimer J. R., Volkoff G. M., 1939, Phys. Rev., 55, 374

Orosz J. A., et al., 2007, Nature, 449, 872

Özel F., 2006, Nature, 441, 1115

Özel F., 2013, Reports on Progress in Physics, 76, 016901

Özel F., Freire P., 2016, Annual Review of Astronomy and Astrophysics, 54, 401

Özel F., Psaltis D., 2009, Phys. Rev. D, 80, 103003

Papitto A., Martino D. d., 2022, Transitional Millisecond Pulsars. Springer International Publishing, Cham, pp 157–200, doi:10.1007/978-3-030-85198-9˙6, https://doi.org/10.1007/978-3-030-85198-9_6

Papitto, A. et al., 2011, Astronomy and Astrophysics, 526, L3

Papitto A., et al., 2013, Nature, 501, 517

Parikh A. S., Wijnands R., Altamirano D., 2020, The Astronomer's Telegram, 13725, 1

Parikh A. S., et al., 2021, Monthly Notices of the Royal Astronomical Society, 501, 1453

Parker M. L., et al., 2019, Monthly Notices of the Royal Astronomical Society, 484, 1202

Parmar A. N., et al., 1986, The Astrophysical Journal, 308, 199

Parmar A. N., et al., 1991, The Astrophysical Journal, 366, 253

Patruno A., Watts A. L., 2021, Accreting Millisecond X-ray Pulsars. Springer Berlin Heidelberg, Berlin, Heidelberg, pp 143–208, doi:10.1007/978-3-662-62110-3˙4, https://doi.org/10.1007/978-3-662-62110-3_4

Patruno A., et al., 2008, The Astrophysical Journal, 690, 1856

Pearson K. J., et al., 2006, The Astrophysical Journal, 648, 1169

Pechenick K. R., Ftaclas C., Cohen J. M., 1983, The Astrophysical Journal, 274, 846

Podsiadlowski P., 1991, Nature, 350, 136

Podsiadlowski P., 2014, The evolution of binary systems. Cambridge University Press, pp 45–88, doi:10.1017/CBO9781139343268.003

Pols O., 2011, Stellar Structure and Evolution. Astronomical Institute Utrecht, https://books.google.co.uk/books?id=sawHtAEACAAJ

Pols O. R., et al., 1998, Monthly Notices of the Royal Astronomical Society, 298, 525

Polzin E. J., et al., 2018, Monthly Notices of the Royal Astronomical Society, 476, 1968

Polzin E. J., et al., 2019a, Monthly Notices of the Royal Astronomical Society, 490, 889

Polzin E. J., et al., 2019b, Monthly Notices of the Royal Astronomical Society, 490, 889

Polzin E. J., et al., 2020, Monthly Notices of the Royal Astronomical Society, 494, 2948

Ponti G., et al., 2012, Monthly Notices of the Royal Astronomical Society: Letters, 422, L11

Ponti G., Muñoz-Darias T., Fender R. P., 2014, Monthly Notices of the Royal Astronomical Society, 444, 1829

Postnov K. A., Yungelson L. R., 2014, Living Reviews in Relativity, 17, 3

Poutanen J., 2006, Advances in Space Research, 38, 2697

Poutanen J., Gierliński M., 2003, Monthly Notices of the Royal Astronomical Society, 343, 1301

Poutanen, Juri Veledina, Alexandra Zdziarski, Andrzej A. 2018, Astronomy and Astrophysics, 614, A79

Providência C., 2019, AIP Conference Proceedings, 2127, 020022

Psaltis D., Özel F., 2014, The Astrophysical Journal, 792, 87

Psaltis D., Özel F., DeDeo S., 2000, The Astrophysical Journal, 544, 390

Puls J., Vink J. S., Najarro F., 2008, The Astronomy and Astrophysics Review, 16, 209

Radhakrishnan V., Srinivasan G., 1982, Current Science, 51, 1096

Raithel C. A., Sukhbold T., Özel F., 2018, The Astrophysical Journal, 856, 35

Ransom S. M., 2001, New search techniques for binary pulsars, https://ui.adsabs.harvard.edu/abs/2001PhDT.....123R

Rapisarda S., et al., 2016, Monthly Notices of the Royal Astronomical Society, 462, 4078

Ratti E. M., et al., 2012, Monthly Notices of the Royal Astronomical Society, 420, 75

Revnivtsev et al., 2002, A&A, 391, 1013

Riley T. E., et al., 2019, The Astrophysical Journal Letters, 887, L21

Roberts M. S. E., 2012a. Proceedings IAU Symposium No. 291. Cambridge University Press, p. 127, http://www.pulsarastronomy.net/IAUS291/proceedings/iaus291-procs-2012.12.10.pdf

Roberts M. S. E., 2012b, Proceedings of the International Astronomical Union, 8, 127

Roberts M. S., et al., 2017, Proceedings of the International Astronomical Union, 13, 43

Romani R. W., et al., 2012, The Astrophysical Journal, 760, L36

Ruderman M., Shaham J., Tavani M., 1989a, The Astrophysical Journal, 336, 507

Ruderman M., et al., 1989b, The Astrophysical Journal, 343, 292

Rybicki G. B., Lightman A. P., 1979, Radiative processes in astrophysics

Saikia P., et al., 2020, The Astronomer's Telegram, 13719, 1

Salvo T. D., Sanna A., 2022, Accretion Powered X-ray Millisecond Pulsars. Springer International Publishing, Cham, pp 87–124, doi:10.1007/978-3-030-85198-9˙4, https://doi.org/10.1007/978-3-030-85198-9_4

Sanna, A. et al., 2018, Astronomy and Astrophysics, 616, L17

Schwarzschild K., 1916, Abh. Konigl. Preuss. Akad. Wissenschaften Jahre 1906,92, Berlin,1907, 1916, 189

Sen D., 2019, PhD thesis

Shakura N. I., Sunyaev R. A., 1973, Astronomy and Astrophysics, 24, 337

Shulyak, D. et al., 2019, Astronomy and Astrophysics, 626, A86

Somero, A. et al., 2012, Astronomy and Astrophysics, 539, A111

Stappers B. W., et al., 1996, The Astrophysical Journal Letters, 465, L119

Steeghs D., Casares J., 2002, The Astrophysical Journal, 568, 273

Steiner A. W., Lattimer J. M., Brown E. F., 2010, The Astrophysical Journal, 722, 33

Strader J., et al., 2015, The Astrophysical Journal Letters, 804, L12

Strohmayer T., Bildsten L., 2006, New views of thermonuclear bursts. Cambridge University Press, Cambridge, pp 113–156, doi:DOI: 10.1017/CBO9780511536281.004, https://www.cambridge.org/core/books/compact-stellar-xray-sources/new-views-of-thermonuclear-bursts/AF210903A212AC941233372BF85E4684

Strohmayer T. E., et al., 1996, The Astrophysical Journal, 469, L9

Strohmayer T. E., Zhang W., Swank J. H., 1997, The Astrophysical Journal, 487, L77

Sukhbold T., Woosley S. E., Heger A., 2018, The Astrophysical Journal, 860, 93

Suleimanov, V. Poutanen, J. Werner, K. 2011, A&A, 527, A139

Swihart S. J., et al., 2018, The Astrophysical Journal, 866, 83

Sztajno M., et al., 1987, Monthly Notices of the Royal Astronomical Society, 226, 39

Tan C., 2021, Journal of Physics: Conference Series, 2012, 012119

Tetarenko B. E., et al., 2016, The Astrophysical Journal Supplement Series, 222, 15

Tolman R. C., 1939, Phys. Rev., 55, 364

Van Oeveren E. D., Friedman J. L., 2017, Phys. Rev. D, 95, 083014

Vanderburg A., et al., 2015, Nature, 526, 546

Vasilopoulos G., Bailyn C., Milburn J., 2018, The Astronomer's Telegram, 12164, 1

Venter C., et al., 2015, The Astrophysical Journal, 807, 130

Verbunt F., 1993, Annual Review of Astronomy and Astrophysics, 31, 93

Villarreal A. R., Strohmayer T. E., 2004, The Astrophysical Journal, 614, L121

Vlemmings Khouri, T. Olofsson, H. 2019, A&A, 626, A81

Voisin G., et al., 2020, A&A, 638, A24

Wade R. A., Horne K., 1988, The Astrophysical Journal, 324, 411

Walton D. J., et al., 2017, The Astrophysical Journal, 839, 110

Wang, J. et al., 2011, Astronomy and Astrophysics, 526, A88

Wang L., et al., 2016, Monthly Notices of the Royal Astronomical Society, 466, 2261

Wang J., et al., 2021, The Astrophysical Journal Letters, 910, L3

Wargelin B. J., Drake J. J., 2002, The Astrophysical Journal, 578, 503

Watts A. L., 2012, Annual Review of Astronomy and Astrophysics, 50, 609

Wijnands R., van der Klis M., 1998, Nature, 394, 344

Wijnands R., van der Klis M., 2000, The Astrophysical Journal, 528, L93

Wilms J., Allen A., McCray R., 2000, The Astrophysical Journal, 542, 914

Wolff M. T., et al., 2005, The Astrophysical Journal, 632, 1099

Wolff M. T., Wood K. S., Ray P. S., 2007, The Astrophysical Journal, 668, L151

Wolff M. T., et al., 2009, The Astrophysical Journal Supplement Series, 183, 156

Yamada S., et al., 2013, Publications of the Astronomical Society of Japan, 65

Yang H., East W. E., Lehner L., 2018, The Astrophysical Journal, 856, 110

Yoon S. C., et al., 2012, Astronomy & Astrophysics, 544, L11

Zasche, P. Henzl, Z. Masek, M. 2021, A&A, 652, A81

Zavlin V. E., 2006, The Astrophysical Journal, 638, 951

Zavlin V. E., 2007, Astrophysics and Space Science, 308, 297

Zdziarski A. A., Johnson W. N., Magdziarz P., 1996, Monthly Notices of the Royal Astronomical Society, 283, 193

Zhang Z., et al., 2014, Publications of the Astronomical Society of Japan, 66

van Paradijs J., 1979, The Astrophysical Journal, 234, 609

van Straaten S., van der Klis M., Méndez M., 2003, The Astrophysical Journal, 596, 1155

van Zyl et al., 2004, Astronomy and Astrophysics, 428, 935

van den Eijnden J., et al., 2020, Monthly Notices of the Royal Astronomical Society, 496, 4127

van der Klis M., 1989, in Hunt J., Battrick B., eds, ESA Special Publication Vol. 1, Two Topics in X-Ray Astronomy, Volume 1: X Ray Binaries. Volume 2: AGN and the X Ray Background. p. 203

van der Klis M., 2004, arXiv e-prints,

van der Klis M., 2006, in Lewin W., van der Klis M., eds, Cambridge Astrophysics, Vol. 39, Compact stellar X-ray sources. Cambridge University Press, pp 39–112

van der Sluys M., 2006, PhD thesis, Utrecht University